

Reducing drop friction on liquid repellent polydimethylsiloxane-coated surfaces



MAX PLANCK INSTITUTE
FOR POLYMER RESEARCH



JOHANNES GUTENBERG
UNIVERSITÄT MAINZ

Dissertation

zur Erlangung des Grades

“Doktor der Naturwissenschaften”

im Promotionsfach Chemie

am Fachbereich Chemie, Pharmazie, Geographie und Geowissenschaften der Johannes

Gutenberg-Universität Mainz und in Kooperation mit dem Max-Planck-Institut für

Polymerforschung Mainz

Xiaoteng Zhou

Geboren in Nanyang / P. R. China

On the recommendation of Prof. Dr. Hans-Jürgen Butt, MPIP

Mainz, 2023

Diese Dissertation wurde am Max-Planck-Institut für Polymerforschung erstellt Sep. 2019 bis Oct. 2023 unter der Leitung von Professor Hans-Jürgen Butt. Nach bestem Wissen und Gewissen versichere ich dem Leser, dass es sich um eine Originalrecherche handelt vorgelegt wird und kein Plagiat begangen wurde. Nach bestem Wissen und Gewissen werden Quellen genannt meines Wissens. Aus anderen Veröffentlichungen stammendes Material wurde mit den entsprechenden Angaben wiedergegeben Berechtigungen.

Oct. 2023

1. Berichterstatter:

2. Berichterstatter:

Tag der mündlichen Prüfung:

Dissertation an der Johannes Gutenberg-Universität Mainz

"You can't cross the sea merely by standing and staring at the water."

— Rabindranath Tagore

Abstract

Liquid repellent surfaces are a kind of surface on which liquid drops can detach or shed from them without residue. Based on such properties, they are promising materials to be used for self-cleaning, enhancing condensation, reducing ice adhesion, thermal cooling and water harvesting. Extra low drop friction is necessary for this surface to have a good liquid repellency in these applications. Polydimethylsiloxane (PDMS) is one kind of environmentally friendly polymerized organosilicon. They are usually used as a coating to enhance the liquid repellency of the hydrophilic substrate. Due to its low glass transition temperature (T_g), it is usually considered to be a soft and flexible material at room temperature.

In this thesis, we focus on the open question on three different PDMS-coated surfaces:

1. A partially cross-linked PDMS coating is the one most common coating with a weak liquid repellency. A ridge forms when drops are placed on it due to the high softness of PDMS. It results in discontinuous stick-slip motion at the three-phase contact line. After being deformed, the formed cracks will also result in a high resistance for drop moving. How to endow a better liquid repellency to it with low drop friction is still a challenge.

2. Liquid PDMS can be used as a lubricant to enhance the liquid repellency on porous surfaces. It is used to fabricate liquid repellent oil-infused surfaces. However, this infusing PDMS layer is usually thick, and it will result in a ridge formation at the three-phase contact line. Combined with the viscous flow near the liquid-liquid interface, moving drops on this oil layer will dissipate more energy than moving at an ideal low-friction surface. Reducing the friction from such dissipation is still a problem.

3. Linear or approximately linear PDMS chain can be anchored on a flat surface to have a nano-scale PDMS coating. They are called PDMS brush or pseudo-brush. Due to its high mobility at room temperature, the surface shows repellency to both water and low-surface tension liquids. Nowadays, there is a lack of work to prepare a highly linear PDMS chain by a fast grafting-from method. Moreover, even though such surfaces prepared from different methods or precursors are reported all to be liquid repellent, the layer properties will vary. It will result in dynamic friction difference when drop sliding off them. Key questions are: on which sample the drop will have the lowest friction? How does the PDMS layer affect the drop friction?

In this thesis, **Chapter 1** will give a brief introduction to the basic wetting theory on both rigid and soft surfaces, and the background and concepts in liquid repellent surface design.

Chapter 2.1 is related to the first kind of PDMS. We try to improve the liquid repellency on a cross-linked PDMS coated highly stretchable substrate by adding a rough structure on top of it. In our case, PDMS is coated on a polyisoprene substrate to have a high stretchability (tension strain can be larger than 300 %). The PDMS layer is used as an adhesion layer to fix two-level fluorinated nanofilament structures on it. Water and low-surface-tension liquids can be quickly shed from the surface even though the surface is stretched to a tensile strain of ~ 225 %.

Chapter 2.2 investigates water drop behavior on the liquid PDMS infused surface. Liquid-infused surfaces are one kind of liquid repellent surface which highly reduces static friction. Drops can start to slide off the surface with low extra traction. However, a large liquid ridge formed on the thick infusing liquid PDMS layer and the viscous flow near the liquid-liquid interface is high. It increases the dynamic friction force during the drop sliding process. We highly decrease the oil layer on top of the structure by infusing a volatile PDMS/solvent mixture into a porous PDMS modified structure. Since the lubricant layer is thin and fixed by the anchored pre-coated PDMS, ridge formation and interfacial flow are suppressed. It leads to low drop sliding friction and fast drop shedding.

In **Chapter 2.3** and **2.4**, we focus on nano-scale PDMS coatings. We first report a one-step grafting-from approach to rapidly fabricate linear PDMS brushes on surfaces through spontaneous polymerization of dichlorodimethylsilane. It shows low values of contact angle hysteresis (less than 5°) with most liquids. Then, I tried to study the drop motion on these nano-scale PDMS brush surfaces which are prepared by both the grafting-from and grafting-to methods reported before. The difference in coating thickness resulting from the preparation is found to be the main factor that determines the drop dynamic friction. 4-5 nm thick PDMS layers showed the lowest dynamic friction. Layer inhomogeneities and the PDMS chain stretch are found to be two main mechanisms to affect the friction with the varied thickness.

In conclusion, the reduction of drop friction on soft PDMS-coated surfaces can be achieved through careful design to control energy dissipation during drop shedding, ultimately enhancing the liquid repellency of these surfaces in practical applications. The findings from these studies will inspire us to develop low-friction PDMS-coated surfaces with improved performance across various industrial applications, including microfluidics, biomedical devices, and heat transfer processes in polymer packaging circuits.

Zusammenfassung

Unter flüssigkeitsabweisenden Oberflächen versteht man eine Art Oberfläche, auf der sich Flüssigkeitstropfen rückstandsfrei ablösen bzw. ablösen können. Aufgrund dieser Eigenschaften sind sie vielversprechende Materialien für die Selbstreinigung, die Verbesserung der Kondensation, die Reduzierung der Eisanhaftung, die thermische Kühlung und die Wassergewinnung. Damit diese Oberfläche bei diesen Anwendungen eine gute Flüssigkeitsabweisung aufweist, ist eine besonders geringe Tropfenreibung erforderlich. Polydimethylsiloxan (PDMS) ist eine Art umweltfreundliches polymerisiertes Organosilicium. Sie werden üblicherweise als Beschichtung verwendet, um die Flüssigkeitsabweisung des hydrophilen Substrats zu verbessern. Aufgrund seiner niedrigen Glasübergangstemperatur (T_g) gilt es bei Raumtemperatur üblicherweise als weiches und flexibles Material.

In dieser Arbeit konzentrieren wir uns auf die offene Frage auf drei verschiedene PDMS-beschichtete Oberflächen:

1. Eine teilweise vernetzte PDMS-Beschichtung ist die häufigste Beschichtung mit schwacher Flüssigkeitsabweisung. Aufgrund der hohen Weichheit von PDMS bildet sich ein Grat, wenn Tropfen darauf fallen. Es kommt zu einer diskontinuierlichen Stick-Slip-Bewegung an der dreiphasigen Kontaktlinie. Nach der Verformung führen die gebildeten Risse auch zu einem hohen Widerstand gegen die Bewegung des Tropfens. Es ist immer noch eine Herausforderung, ihm eine gute Flüssigkeitsabweisung bei geringer Tropfenreibung zu verleihen.

2. Flüssiges PDMS kann als Schmiermittel verwendet werden, um die Flüssigkeitsabweisung auf porösen Oberflächen zu verbessern. Es wird zur Herstellung flüssigkeitsabweisender, ölgetränkter Oberflächen verwendet. Diese infundierende PDMS-Schicht ist jedoch normalerweise dick und führt zu einer Gratbildung an der Dreiphasen-Kontaktlinie. In Kombination mit der viskosen Strömung nahe der Flüssigkeits-Flüssigkeits-Grenzfläche verbrauchen bewegte Tropfen auf dieser Ölschicht mehr Energie als die Bewegung auf einer idealen Oberfläche mit geringer Reibung. Die Reduzierung der Reibung durch eine solche Verlustleistung ist immer noch ein Problem.

3. Eine lineare oder annähernd lineare PDMS-Kette kann auf einer flachen Oberfläche verankert werden, um eine PDMS-Beschichtung im Nanomaßstab zu erhalten. Sie werden PDMS-Pinsel oder Pseudo-Pinsel genannt. Aufgrund der hohen Beweglichkeit bei Raumtemperatur ist die Oberfläche sowohl gegenüber Wasser als auch gegenüber Flüssigkeiten mit geringer Oberflächenspannung abweisend. Heutzutage mangelt es an Arbeiten zur Herstellung einer

hochlinearen PDMS-Kette durch eine schnelle Grafting-from-Methode. Auch wenn von solchen Oberflächen, die mit unterschiedlichen Methoden oder Vorläufern hergestellt wurden, berichtet wird, dass sie alle flüssigkeitsabweisend sind, variieren die Schichteigenschaften. Dies führt zu einem dynamischen Reibungsunterschied, wenn der Tropfen von ihnen abrutscht. Die Schlüsselfragen sind: Auf welcher Probe weist der Tropfen die geringste Reibung auf? Wie beeinflusst die PDMS-Schicht die Tropfenreibung?

In dieser Arbeit gibt **Kapitel 1** eine kurze Einführung in die grundlegende Benetzungstheorie sowohl auf starren als auch auf weichen Oberflächen sowie in den Hintergrund und die Konzepte des flüssigkeitsabweisenden Oberflächendesigns.

Kapitel 2.1 befasst sich mit der ersten Art von PDMS. Wir versuchen, die Flüssigkeitsabweisung auf einem mit vernetztem PDMS beschichteten, hoch dehnbaren Substrat zu verbessern, indem wir darauf eine raue Struktur hinzufügen. In unserem Fall wird PDMS auf ein Polyisopren-Substrat aufgetragen, um eine hohe Dehnbarkeit zu gewährleisten (die Zugspannung kann mehr als 300 % betragen). Die PDMS-Schicht dient als Haftschrift, um darauf zweistufige fluorierte Nanofilamentstrukturen zu fixieren. Wasser und Flüssigkeiten mit geringer Oberflächenspannung können schnell von der Oberfläche abgeführt werden, selbst wenn die Oberfläche auf eine Zugspannung von $\sim 225\%$ gedehnt wird.

Kapitel 2.2 untersucht das Verhalten von Wassertropfen auf der mit flüssigem PDMS infundierten Oberfläche. Mit Flüssigkeit durchtränkte Oberflächen sind eine Art flüssigkeitsabweisender Oberflächen, die die Haftreibung stark reduzieren. Bei geringer zusätzlicher Traktion können Tropfen beginnen, von der Oberfläche zu rutschen. Allerdings bildete sich auf der dicken PDMS-Schicht der infundierenden Flüssigkeit ein großer Flüssigkeitsrücken und die viskose Strömung in der Nähe der Flüssigkeit-Flüssigkeit-Grenzfläche ist hoch. Es erhöht die dynamische Reibungskraft beim Tropfengleitvorgang. Wir verringern die Ölschicht auf der Oberseite der Struktur erheblich, indem wir eine flüchtige PDMS/Lösungsmittel-Mischung in eine poröse PDMS-modifizierte Struktur infundieren. Da die Schmiermittelschicht dünn ist und durch das verankerte vorbeschichtete PDMS fixiert wird, werden Gratbildung und Grenzflächenströmung unterdrückt. Dies führt zu einer geringen Tropfengleitreibung und einem schnellen Tropfenabwurf.

In **Kapitel 2.3** und **2.4** konzentrieren wir uns auf nanoskalige PDMS-Beschichtungen. Wir berichten zunächst über einen einstufigen Grafting-from-Ansatz zur schnellen Herstellung linearer PDMS-Bürsten auf Oberflächen durch spontane Polymerisation von Dichlordimethylsilan. Es zeigt bei den meisten Flüssigkeiten niedrige Werte der Kontaktwinkelhysterese (weniger als

5°). Dann habe ich versucht, die Tropfenbewegung auf diesen nanoskaligen PDMS-Bürstenoberflächen zu untersuchen, die sowohl durch die zuvor beschriebenen Grafting-from- als auch Grafting-to-Methoden hergestellt wurden. Der Unterschied in der Schichtdicke, der sich aus der Vorbereitung ergibt, ist der Hauptfaktor, der die dynamische Tropfenreibung bestimmt. 4–5 nm dicke PDMS-Schichten zeigten die geringste dynamische Reibung. Es wurde festgestellt, dass Schichtinhomogenitäten und die Dehnung der PDMS-Kette zwei Hauptmechanismen sind, die die Reibung bei unterschiedlicher Dicke beeinflussen.

Zusammenfassend lässt sich sagen, dass die Reduzierung der Tropfenreibung auf weichen PDMS-beschichteten Oberflächen durch sorgfältiges Design zur Kontrolle der Energiedissipation während des Tropfenabwurfs erreicht werden kann, was letztendlich die Flüssigkeitsabweisung dieser Oberflächen in praktischen Anwendungen verbessert. Die Erkenntnisse aus diesen Studien werden uns dazu inspirieren, reibungsarme PDMS-beschichtete Oberflächen mit verbesserter Leistung für verschiedene industrielle Anwendungen zu entwickeln, darunter Mikrofluidik, biomedizinische Geräte und Wärmeübertragungsprozesse in Polymerverpackungskreisläufen.

Table of content

Chapter 1. State of the art.....	1
1.1 Introduction and motivation.....	1
1.2 Wetting phenomena	2
1.2.1 Wetting on ideal solid surfaces.....	2
1.2.2 Contact angle hysteresis	3
1.2.3 Wetting on soft surface.....	5
1.3 Liquid repellent surfaces	9
1.3.1 Super liquid repellent surfaces	9
1.3.1.1 Wetting on rough surfaces	9
1.3.1.2 Overhanging structures and superamphiphobicity	12
1.3.1.3 Super liquid repellent surface prepared from organosilicon.....	13
1.3.1.4 Stretchable super liquid repellent surfaces	16
1.3.2 Liquid-infused surfaces (LIS).....	18
1.3.2.1 Wetting on LIS	20
1.3.2.2 Drop movement on LIS.....	21
1.3.3 Combination of LIS and superhydrophobic surface	22
1.3.4 Covalently attached liquid surfaces (CALS).....	24
1.4 References	27
Chapter 2. Selected publications	33
2.1 X. Zhou, et al. <i>Adv. Mater.</i> , 2022.	33
2.2 X. Zhou et al. <i>Droplet</i> , 2022.	61
2.3. J. Liu, Y. Sun, X. Zhou et al. <i>Adv. Mater.</i> , 2021.	95
2.4. X. Zhou et al. <i>Submitted</i> , 2023.	125
Chapter 3. Conclusion and outlook	159
Chapter 4. Acknowledgement	161
Chapter 5. Curriculum vitae	163
Chapter 6. List of publications and contributions.....	165

Chapter 1. State of the art

1.1 Introduction and motivation

Wetting is usually the spreading of liquids on solid substrates. It also includes any motion of a liquid with a dry/wet front.^[1] The quest for a physical understanding of this started two centuries ago.^[1a] However, the description and use of wetting precedes its academic understanding. For example, 1300 years ago, a Chinese poet, named Xin Li, wrote in a temple to give a precise observation of that water droplets have a quite low adhesion on lotus leaves (Figure 1.1).^[2] It is called lotus effect^[3] which means water drop can maintain a spherical shape on the surface and roll off the surface easily. The surface on which water has a low friction like the lotus leaves is called a liquid repellent surface.

**Never get caught in water,
purify your original mind.**

— Qi Li



(690 – 751 AD)



Figure 1.1. The Chinese ancient poetry to describe the water-repellency of a lotus leaf.^[2a, 4]

Similar to the lotus effect in nature, in 1936, Wenzel first observe a spherical shape of water drop on a rough surface made of stearone and wax.^[5] Water has a low adhesion on such surface. Subsequently, in 1967, Dettre and Johnson reported the water drop moving on three rough surfaces with a rapid detach process.^[6] Nearly thirty years, due to the high demand in waterproofing in industry, inspired by this lotus effect,^[3] the preparation of such liquid repellent surfaces are widely studied. An overhanging structure imaged by scanning electron microscope (SEM) is first reported in 1989^[7] and has been widely fabricated since 1996.^[8] Rapid drop shedding velocity resulting from low friction and adhesion on such surfaces make them a promising material to achieve self-cleaning,^[9] enhanced heat transfer,^[10] anti-fouling^[11] and water harvesting.^[12]

Thousands of papers have reported to realize this target e.g. super-repellent surfaces (1. Superhydrophobic surface, repel water; 2. Superoleophobic surface, repel low-surface-tension liquids, and 3. Superamphiphobic surface, repel both water and low-surface-tension liquids) with fast drop shedding velocity based on the lotus effect.^[13] Following the super liquid repellent surface, low-surface-tension liquid can be infused into these rough structures to have liquid-infused surfaces (LIS).^[14] Covalently attached liquid coated surfaces (CALS) were then fabricated based on the same strategy that building a highly mobile interface.^[15] These two surfaces with a lubricated layer shows low drop adhesion when drop detached from them and low tilting angles. They can be also considered as liquid repellent surfaces.

These liquid repellent surfaces are usually fabricated on rigid substrates e.g. glass slides, silicon wafers to reduce the high adhesion or friction of drops on them. However, liquid repellency of soft surfaces is less investigated. For example, soft polydimethylsiloxane (PDMS) is usually used as a main composition of a soft liquid repellent surface. Due to its high hydrophobicity, it can resist water penetration. However, soft surfaces are usually easily deformed. Drop friction will be varied on them due to such deformation. It also limits a fast drop shedding as that on a super liquid repellent surface. Reducing drop friction to enhance the liquid repellency on them is meaningful in various situations such as flexible electronics,^[16] artificial skin,^[17] textile dressings,^[18] and liquid manipulation.^[19]

With respect to such elastic deformation, several theories have been developed to describe it. It usually results in a higher static friction force when a drop starts to slide off a soft surface than that on a rigid liquid repellent surface. Moreover, when a drop moves on the surface with a soft interface e.g. PDMS-water interface, the friction of the contact line will result in a more obvious drop shape change with the velocity. It means more resistance with the increasing drop velocity. Open questions are: how can one reduce such high resistance for a drop moving on the soft, stretchable cross-linked PDMS substrate? How can one reduce it on the liquid PDMS/water interface? And does such deformation also affect the friction on a nano-scale soft PDMS coating? They are still not answered.

1.2 Wetting phenomena

1.2.1 Wetting on ideal solid surfaces

An ideal solid surface here means the surface is ideally rigid (no deformation), smooth (no roughness) and homogeneous. When a liquid drop contacts such solid surface, the degree to which the solid is wetted by the liquid is decided by the interfacial energies of these two phases.

The liquid can either spread on a surface (“wetting”) or form a defined contact angle (“no wetting”). Marangoni first imaged a construction that a film spreads from a reservoir of liquid onto an ideal rigid solid (Figure 1.2a), provided that the solid/air surface tension which entrains this film is larger than the sum of the solid/liquid and liquid/air surface tensions which both resist the spreading.^[20] In 1805, Thomas Young derived the basic relationship between the interfacial energies (γ)* of a liquid drop on an ideally flat, homogeneous, solid surface when liquid wet the surface in an equilibrium state (Figure 1.2b)^[1a]:

$$\gamma_{LA} \cos \theta = \gamma_{SA} - \gamma_{SL} \quad (1.1)$$

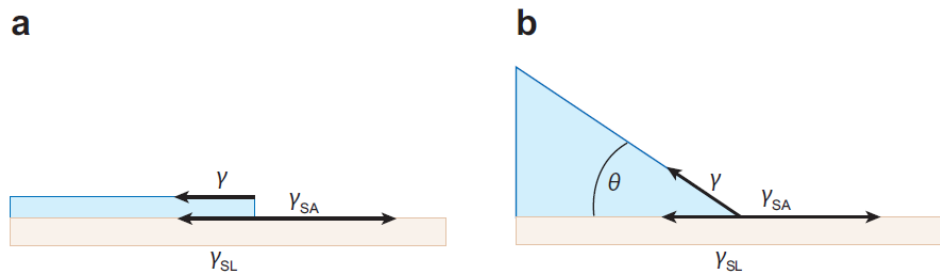


Figure 1.2. Classical wetting phenomenon on an ideal material. (a) A liquid film spreads, drawn by the solid/air surface tension (γ_{SA}), despite the action of the liquid/air (γ or γ_{LA}) and solid/liquid (γ_{SL}) tensions. (b) The balance of surface tensions determines the contact angle θ when wetting is only partial.^[20a] Copyright 2008, Annual Reviews, Inc.

Here, γ_{LA} , γ_{SA} , and γ_{SL} are liquid/vapor, solid/vapor and solid/liquid interfacial tension, respectively, and θ is the angle at which the liquid contacts the surface at the liquid/air/solid contact line (“three phase contact line”). On a common smooth surface, a solid/liquid surface tension tends to be smaller than a solid/air one. Therefore, in most situations, this angle lies between 0° and 90° (hydrophilic surfaces). On hydrophobic flat solids (e.g. fluorinated surface), the maximum contact angle of water never exceeds approximately 120° . Only if we increase the surface roughness, the gap between 120° and 180° will be filled and the surface is supposed to be super-liquid-repellent.

1.2.2 Contact angle hysteresis

Ideally, when the drop contact line (Figure 1.3a, static case) moves or the whole drop slides (Figure 1.3b, dynamic case) on the surface, the contact angle in the front and rear of the drop are the same as the equilibrium contact angle Θ if there is no resistance to the drop movement.

* Mathematics symbols are independent for each chapter.

However, in real situations, there will be a difference between the advancing (Θ_a) and receding (Θ_r) contact angles (Figure 1.3c and d). This difference is called contact angle hysteresis $\Delta\Theta$:

$$\Delta\Theta = \Theta_a - \Theta_r \quad (1.2)$$

Contact angle hysteresis exists because contact lines usually do not slide freely due to interfacial friction. Friction is caused by the varied energy dissipation process^[21] which arise from hydrodynamic viscous force^[22], thermal activation of liquid molecules^[23], pinning/de-pinning by surface inhomogeneity^[24], elastocapillary deformation on soft surfaces^[25], surface adaptation^[26], and electrostatic force from slide electrification^[27].

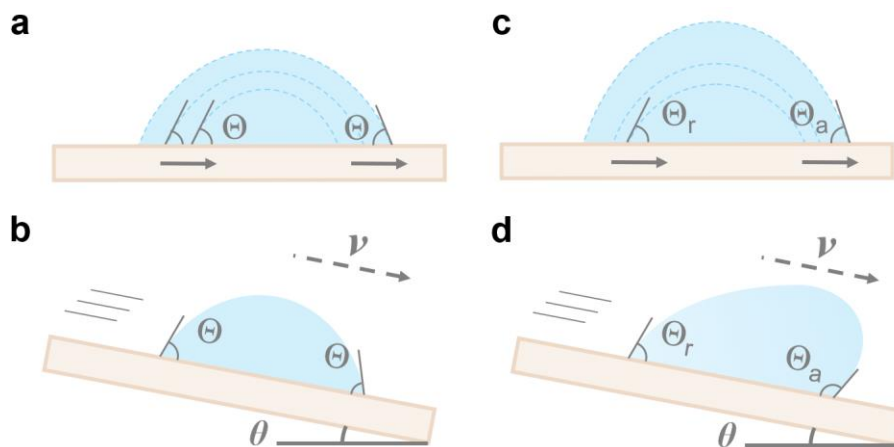


Figure 1.3. Static and dynamic contact angle hysteresis. The ideal case for contact line moving (a) and (b) drop sliding with unchanged contact angles. The real case for contact line moving (c) and (d) drop sliding with a difference between advancing and receding contact angles due to the interfacial friction.

Contact angle hysteresis can be measured with any technique available to measure both the advancing and receding contact angles.^[28] Commonly, these contact angles can be observed by moving the contact line including the capillary rise by the Wilhelmy plate moving from the liquid,^[29] a sessile drop placed on the surface while the drop is inflated or deflated via a micropipette^[30] (Figure 1.4a and b), or by moving the whole drop by gravity or centrifugal force,^[31] for example, on a tilted plate or a centrifuge (Figure 1.4c and d). The force to move the drop can also be carried out by dragging it using a thin pipette^[32] or an air flow^[33] (Figure 1.4e and f). For all these methods, the advancing and receding contact angles can be recorded by a camera and then being fitted and analyzed.^[28]

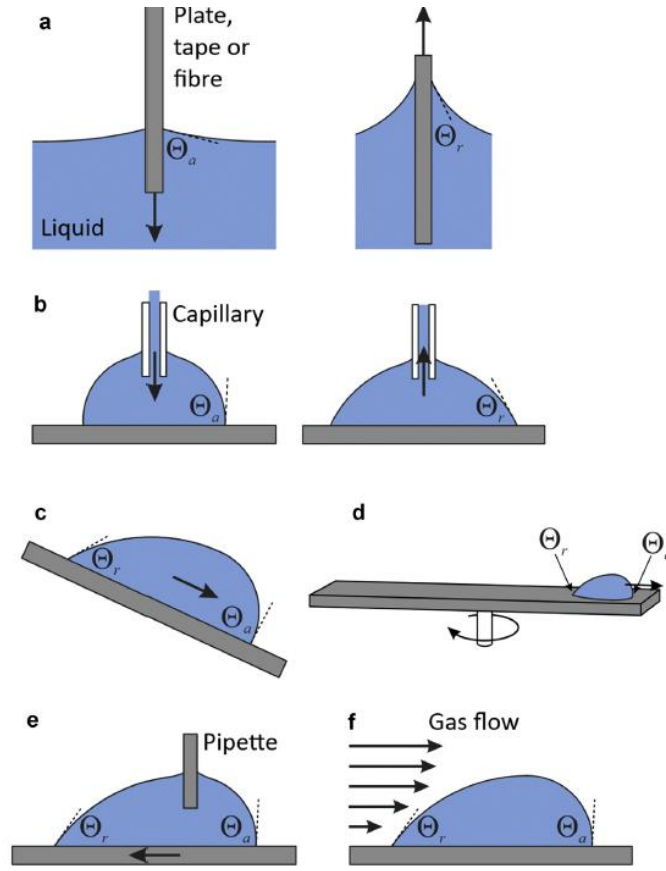


Figure 1.4. The scheme shows the methods we usually use to measure advancing and receding contact angles. (a) Moving a plate or tape into a liquid or pulling it out of the liquid, (b) inflating and deflating a sessile drop, (c) tilted plate, (d) centrifuge, (e) drop adhesion forces instrument, and (f) aerodynamic drag.^[28] Copyright 2022, Elsevier Ltd.

The contact angle hysteresis mainly comes from the contact line friction in a wedge area. The viscous dissipation in the bulk is usually low. From the contact angle hysteresis, we can easily calculate the friction force according to the capillary force F_c near the contact line by Furmidge–Kawasaki equation:^[31a]

$$F \approx F_c = w\gamma k (\cos \Theta_r - \cos \Theta_a) \quad (1.3)$$

Here, w is the drop width, γ is the surface tension of the liquid, $k \approx 1$ is a geometrical drop shape factor.

1.2.3 Wetting on soft surface

A liquid drop sitting on an ideal solid does not induce any significant deformation of the surface. However, for soft surfaces, the softness of them needs to be considered. They deform under the

effect of the liquid surface tension. In general, elastic deformation of a solid is described by the shear modulus G (Figure 1.5). G is defined as the ratio of shear stress τ_{xy} to the shear strain γ_{xy} :

$$G = \frac{\tau_{xy}}{\gamma_{xy}} = \frac{F/A}{\Delta x/l} = \frac{Fl}{A\Delta x} \quad (1.4)$$

Here, F is the force acting on the body, A is the area on which the force acts, Δx is the transverse displacement, l is the initial length in the vertical direction.^[34] At the same time, Young's modulus E which evaluate the elasticity in the vertical direction can be calculated by: $E = 2G(1+\nu)$ (for isotropic and homogeneous materials, ν is Poisson's ratio).

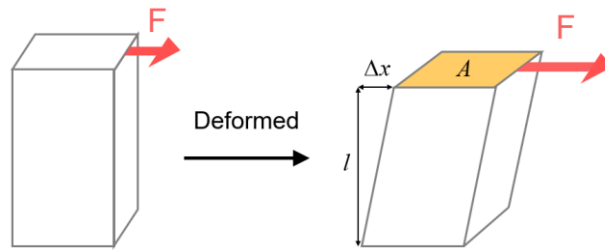


Figure 1.5. The scheme shows the calculation for shear modulus as the ratio of shear stress to shear strain.

When the length scale defined by the ratio of surface tension to shear modulus (γ_{LA}/G) enters the molecular interaction range (γ_{LA}/G is above the width of the interface $a \sim 10^{-9}$ m which obtained from the simulation result^[35]), the traditional wetting phenomena described by Young's law need to be replaced by Neumann's law (Figure 1.6):

$$\gamma_{LA}t_{LA} + \gamma_{SA}t_{SA} + \gamma_{SL}t_{SL} = 0 \quad (1.5)$$

Here, t is the tangent vectors along different interfaces.^[36] This phenomenon is usually called elastocapillary phenomena or soft wetting.

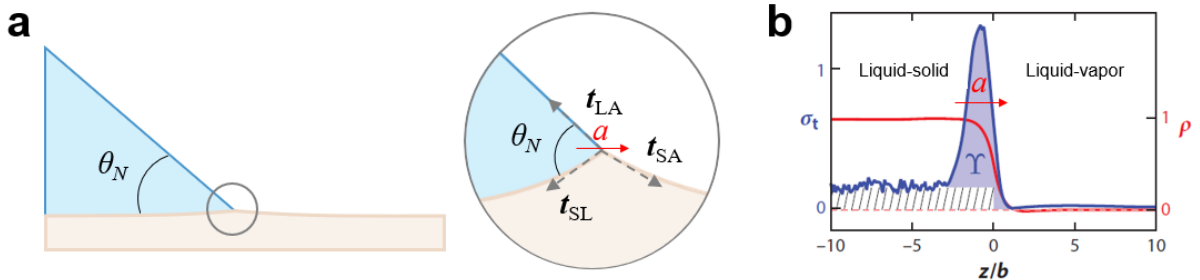


Figure 1.6. The three-phase contact line in soft wetting phenomenon. (a) The scheme to show the wetting phenomena on soft surface described by Neumann's law. (b) The transition of liquid-

solid interface to liquid-vapor interface at the three-phase contact line. a is the nanometric solid-vapor interface width. ρ in the red line is the monomer density, indicating the location of the solid-vapor interface (the position is z expressed in terms of monomer size b). σ_t in the blue line is the profile of the stress anisotropy across a stretched film. The effect of surface tension manifests itself as the peak of σ_t , located inside the liquid-solid interface (the integral gives Υ). The hatched region is the bulk elastic stress. Copyright 2020, Annual Reviews, Inc.

Elastocapillary phenomena can be adjusted in terms of length scales (Figure 1.7).^[37] By tuning the substrate softness, γ_{LA}/G can be varied from sub-molecular up to millimeter scales. When comparing this length to the nanometric interface width a and to the macroscopic parameters e.g. the drop size R and the thickness e of the elastic substrate, the wetting phenomenon and drop shape will vary due to the relationship between them.

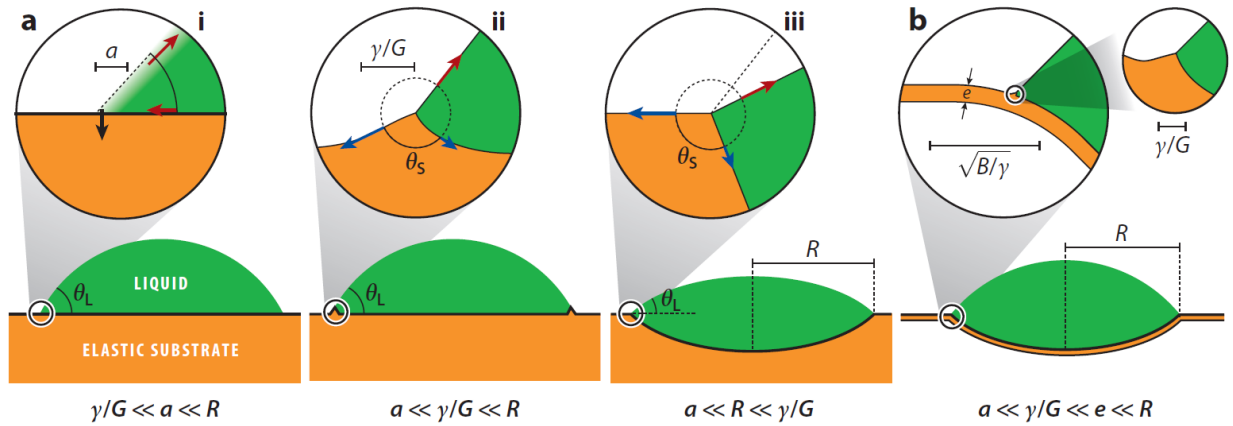


Figure 1.7. Scales of elastocapillarity, γ here represent the liquid-air interfacial tension γ_{LA} . (a) Drops on thick elastic substrates of different softness, tracking the change of the liquid angle θ_L and of the solid angle θ_S (insets). The elastocapillary length γ_{LA}/G must be compared to the width of the interface a and the drop size R . (b) Typical case for a thin membrane of thickness e . The capillary-induced bending remains smooth at the bending length scale, B/γ_{LA} . Copyright 2020, Annual Reviews, Inc.

When water drops move on surfaces, the energy dissipation changes with velocity. One reason is that the advancing and receding contact angle changes with velocity. Then, according to equation 1.3, the friction force also changes. On a rigid surface, the dynamic contact angle $\Theta_{a/r}(U)$ change with the velocity following such relationship when we use a hydrodynamic mode from Cox and Voinov:

$$\Theta_{a/r}^3(U) = (\Theta_{a/r}^0)^3 + \left(\frac{9\eta U}{\gamma_{LA}}\right) \kappa \quad (1.6)$$

where $\Theta_{a/r}^0$ is the static advancing or receding contact angles, η is the drop viscosity, κ is the factor related to the ratio of outer region (where the apparent contact angle is measured), to the inner region (where surface effects, such as slip, are allowed) and U is the drop velocity. When the energy is dissipated during drop moving, it results in an increasing difference between advancing and receding contact angles ($\Delta\theta$).

For soft materials, a small ridge forms at the contact line as shown in Figure 1.7 when $\gamma_{LA}/G \ll R$. When the liquid spreads, this ridge will affect the motion of the contact line by a stick-slip motion of soft material e.g. cross-linked PDMS substrate with $G = 2\text{kPa}$.^[38] This motion means if the drop is only driven by gravity (drop velocity is not so high), when drop moves on the soft surface with a displacement, the contact line is pinned at a certain position and then suddenly slips forward (Figure 1.8).^[39]

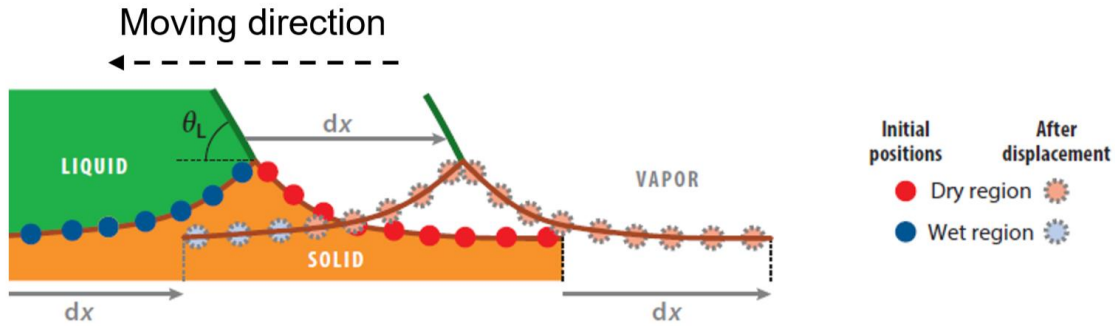


Figure 1.8. Drop moving on a soft surface with a displacement. The liquid contact angle θ_L can be obtained from a global displacement dx of the contact line. The region close to the contact line remains unchanged, and the changes in (elastic and capillary) energy occur at the edge of the indicated contour.^[40] Copyright 2020, Annual Reviews, Inc.

Due to the stick-slip motion, a certain amount of energy is dissipated when the contact line is moving. When drop moves on one soft surface with a shear modulus G at a velocity U , the contact angle change $\delta\theta$ from the equilibrium contact angle will be:^[40]

$$\delta\theta \sim \left(\frac{U\tau}{\gamma/G} \right) \quad (1.7)$$

where τ is the relaxation time of polymer coating.^[41] Because we consider shear modulus G in this equation, when the change of velocity is only from 10^{-7} to 10^{-6} m/s, a 10° contact angle difference can be obtained (Figure 1.9b). The water contact angle hysteresis change is much more sensitive to the drop velocity than that on a rigid surface (Figure 1.9). This rapid change of the contact angle

illustrates a higher drop friction during drop moves on a soft surface which will result from more energy dissipation during the movement.

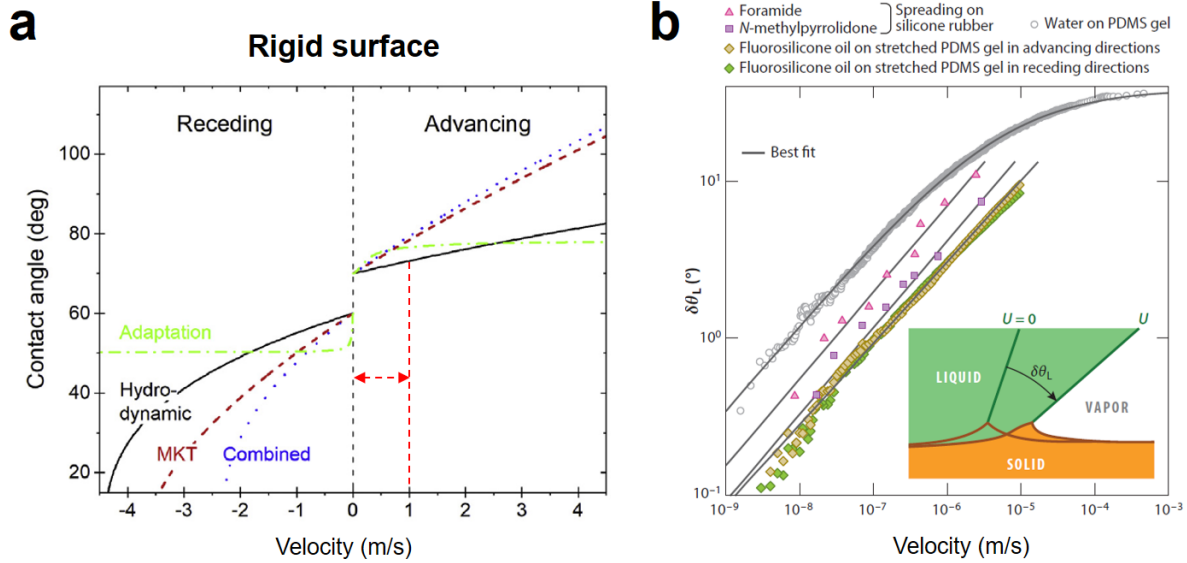


Figure 1.9. Energy dissipation difference when drop moves on rigid and soft surfaces. (a) Energy dissipation of a moving contact line on a rigid surface. Dynamic contact angles are calculated for static contact angles $\theta_a^0 = 70^\circ$ and $\theta_r^0 = 60^\circ$ on a rigid PET (polyethylene terephthalate) surface with hydrodynamic theory, MKT theory, the combined MKT/hydrodynamic theory and adaptation theory. Copyright 2022, Elsevier Ltd. (b) Energy dissipation inside a moving wetting ridge on different soft surfaces. The plots show variation of the liquid angle $\delta\theta$ as a function of the contact line velocity in different liquid–solid wetting experiments. The solid gray lines show the best fits by power laws, and the upper gray curve includes phenomenologically the saturation at large velocity. Copyright 2020, Annual Reviews, Inc.

Due to such higher energy dissipation, designing a soft liquid repellent surface (e.g. PDMS coated surfaces) with low drop friction is usually a problem for real applications. In the next section, I will give a brief introduction about the design of previous liquid repellent surfaces. To understand and then avoid the resistance from the elastowetting on soft surfaces is important to design liquid repellent surfaces with efficient drop shedding.

1.3 Liquid repellent surfaces

1.3.1 Super liquid repellent surfaces

1.3.1.1 Wetting on rough surfaces

When a drop is placed on a rough surface, it will spread until it finds a meta stable configuration (Figure 1.10). The apparent contact angle θ^* is different from the Young angle θ . The roughness factor r was introduced by Wenzel to account for surface roughness:^[5] $r = \text{Actual surface}/\text{Apparent surface area}$. When the contact line moves on the dry solid, it is assumed that each piece of liquid/air interface will get replaced by a solid/liquid interface of the same surface area. The surface energy variation dE can be calculated by using an apparent displacement dx (Figure 1.10):

$$dE = r(\gamma_{SL} - \gamma_{SA}) dx + \gamma_{LA} dx \cos \theta^* \quad (1.8)$$

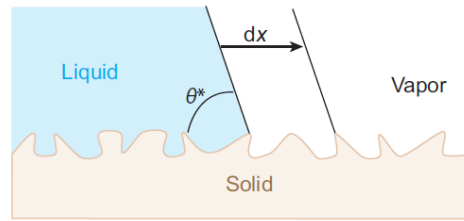


Figure 1.10. The Wenzel model of a rough solid. One can obtain the apparent contact angle θ^* by considering a small apparent displacement of the contact line and looking at the corresponding variation in surface energy.^[20a] Copyright 2008, Annual Reviews, Inc.

When $dE = 0$, if the solid is flat ($r = 1$), $\cos \theta^* = \cos \theta$; if not, there will be a relationship between apparent contact angle θ^* and the Young's angle θ :

$$\cos \theta^* = r \cos \theta \quad (1.9)$$

If the factor $r > 1$ (the surface is rough), a hydrophilic solid ($\theta < 90^\circ$) becomes more hydrophilic ($\theta^* < \theta$) and a hydrophobic solid ($\theta > 90^\circ$) shows an increased hydrophobicity ($\theta^* > \theta$). When the roughness factor $r \gg 1$, a complete drying state can be realized in theory ($\cos \theta^* < -1$).

In Wenzel model, the liquid will conform to the rough solid surface. However, if the roughness is high enough, solid air pockets should form below the liquid (Figure 1.11). This is the so-called Cassie or Cassie-Baxter state.^[42] Pillar surface is an ideal model to describe the Cassie-state drop motion on a rough surface with air pockets and where Φ_s (solid fraction) is used to describe the pillar density. The variation of interfacial energy can be calculated by a moving (new liquid/solid and liquid/vapor interfaces will be created) distance of the contact line dx (Figure 1.11):

$$dE = \Phi_s(\gamma_{SL} - \gamma_{SA}) dx + (1 - \Phi_s) \gamma_{LA} dx + \gamma_{LA} dx \cos \theta^* \quad (1.10)$$

At equilibrium, $dE = 0$, the relationship between the apparent angle θ^* and Young's angle θ is:

$$\cos \theta^* = -1 + (1 - \Phi_s) \cos \theta \quad (1.11)$$

If one surface has a Young's contact angle θ of 110 to 120° (the material is hydrophobic) and Φ_s value of 5% to 10%, we will get liquid apparent angles of 160 to 170°. In addition to a large contact angle, this kind of surface will also have a small contact angle hysteresis because of the air cushion. This kind of surface is called super liquid repellent with a reduced liquid friction and improved liquid repellency.

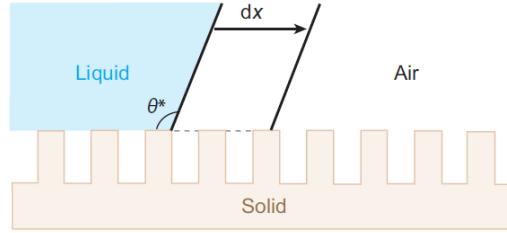


Figure 1.11. Displacing the contact line in the Cassie regime. The dynamic energy balance includes the creation of liquid/air interfaces below the drop, as indicated by the dotted lines.^[20a] Copyright 2008, Annual Reviews, Inc.

How both the surface structure (the roughness factor r and the solid fraction Φ_s) and the Young's angle θ affect the apparent angle θ^* can be illustrated in a wetting diagram (Figure 1.12). The dashed line in the middle is from $\cos \theta^* = r \cos \theta$ which is used to describe the Wenzel state. The critical angle θ^* (θ' in the diagram) for obtaining Cassie state can be calculated by:

$$\cos \theta^* = (\Phi_s - 1) / (r - \Phi_s) \quad (1.12)$$

Using this equation, super liquid repellent surface can be designed by choosing an intrinsic hydrophobic material and increasing the roughness. For water, the maximum Young's contact angle θ (θ_Y in the diagram) is about 120°. Therefore, using ideal pillar-like surfaces, only a narrow-hatched area (green part) is expected to show a composite state (where drop is suspended on tips of a surface texture with the air pockets trapped under the drop) for water ($-0.5 < \cos \theta < (\Phi_s - 1)/(r - \Phi_s)$).

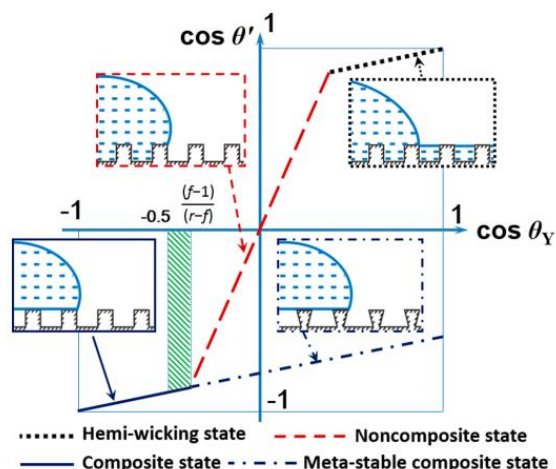


Figure 1.12. Schematic of a wetting diagram for textured surfaces.^[43] Copyright 2019, American Chemical Society.

However, in some experimentals,^[44] the liquid drop also has the possibility to keep the composite wetting state with materials that are moderately hydrophobic ($((\Phi_s - 1)/(r - \Phi_s) < \cos \theta < 0^\circ)$) or even hydrophilic ($\cos \theta > 0^\circ$). Re-entrant structures like multi-curvature pillar (Figure 1.13) are used to fabricate super liquid repellent surfaces even with a high surface energy.^[45]

1.3.1.2 Overhanging structures and superamphiphobicity

In 2014, Liu and Kim give three model structures to illustrate the functionality of the overhanging part in the re-entrant structures when fabricating super liquid repellent surfaces.^[45d] Commonly, a designed pillar structure with a low surface energy can suspend water drop due to a high Young's contact angle (Figure 1.13a). Compared to the pillar surface, for re-entrant structure, it didn't need a high Young's contact angle θ to suspend the water due to a horizontal overhanging part (Figure 1.13b). For low-energy liquids, such as oils or organic solvents, they have a low Young's contact angle ($< 90^\circ$), a roughness with overhanging topology was necessary to make the surface repel them. If the overhanging structure can be fabricated in 3D dimensions to have double re-entrant structure, even if the liquid fully wet the solid with $\theta \sim 0^\circ$, the liquid drop can still have a high contact angle on the surface (Figure 1.13c). Such kinds of super liquid repellent surface which could repel both water with high θ and low-surface-tension liquids with low θ are called superamphiphobic surfaces. By plotting equation 1.11 in Figure 1.13d, we can see that for low-surface-tension liquid, a much less solid fraction is needed to have the same apparent contact angle as that of a high-surface-tension liquid. For the overhanging structures, due to the topography, we can more easily

reduce the solid fraction even if the surface roughness is the same as that on a pillar surface. This is beneficial to repel the low-surface-tension liquid.

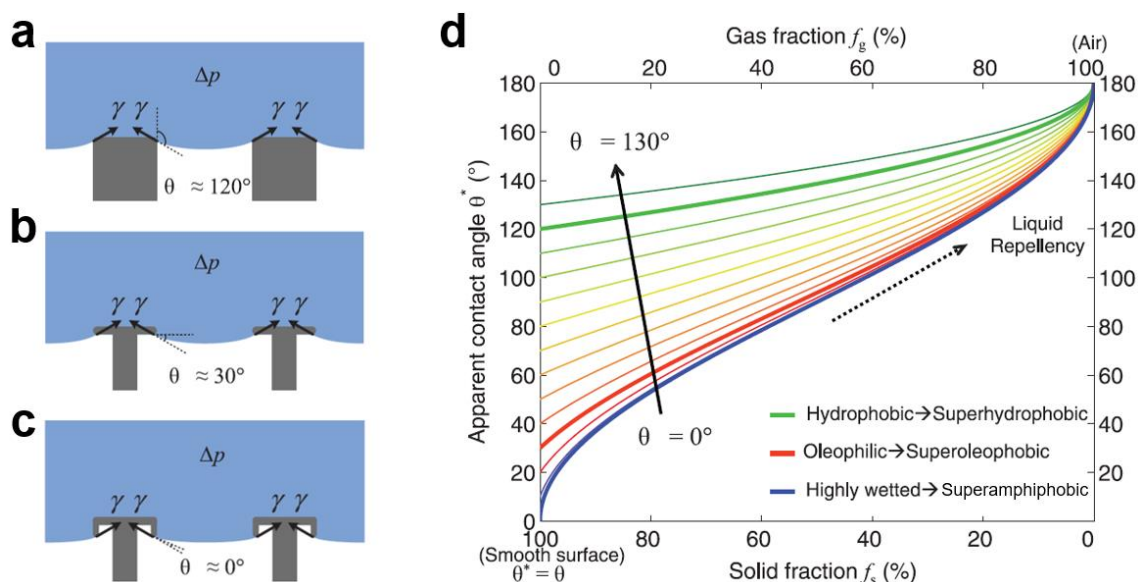


Figure 1.13. Model structures for fabricating super liquid repellent surface. (a) Simple structures require Young’s contact angle $\theta > 90^\circ$ to suspend water. Δp , is the pressure difference between the liquid and air. (b) Re-entrant structures with a horizontal overhanging part allow $\theta < 90^\circ$ to suspend oils or solvents. (c) Doubly re-entrant structures with both horizontal and vertical overhanging part allow $\theta \sim 0^\circ$ to suspend any liquid, as surface tension acts on the vertical overhangs with a substantial vertical component. (d) Relation between apparent contact angle θ^* and solid fraction f_s (the same as Φ_s we mentioned before) for ideal Cassie-state droplets with intrinsic contact angle θ as a parameter. The three bold lines correspond to the three cases in the left (a: green, b: red, c: blue). Copyright 2014, reprinted with permission from AAAS.

1.3.1.3 Super liquid repellent surface prepared from organosilicon

Silicone is not a natural material and the major source of silicon, SiO_2 , was recognized as a separate substance in the 17th century and referred to as vitrifiable earth. The name for the element, ‘silicium’ from the latin silex, meaning rock which is used to reflect the sources of silicon. In World War I, the reactive nature of silicon halides was recognized. This reaction between water and silicon-chlorine bond is the primitive method to produce the starting materials required for the organosilicon compounds. The difference of chemical composition between the organosilicon and the natural silicon (SiO_2) is the silicon-carbon bond which is the key to organosilicon chemistry. Therefore, a transfer reagent which can add an alkyl or an aryl group to the silicon center easily is in need. The first organosilicon derivative was obtained by Friedel and Crafts by heating Et_2Zn

and SiCl_4 together at 140-160 °C^[46] and tetramethylsilane was made similarly from Me_2Zn at 200 °C.^[47] In 1940, Kipping used Hyde's research^[48] to obtain some "sticky messes" product and then gave the material the name "silicones". In 1945, Rochow in General Electric company published a direct process reaction between elemental silicon and an organic halide to obtain Me_2SiCl_2 (the most important monomer in the silicones industry) by using the copper as the catalyst.^[49] After the Me_2SiCl_2 can be large-scale synthesized, the silicone started to be used in industrial area. In 1943 during World War II, Dow Corning was formally established as a joint venture between the American conglomerates Dow Chemical and Corning Glass to explore the potential of silicone for industrial use. The "silicones" are straight or branched linear polymers in which the difunctional $\text{—O—Si(R}_2\text{)—O—}$ or trifunctional —O—Si(R)(O)—O— siloxane elements form a system of extended chains and both ends of the chain are capped with a monofunctional residue $\text{R}_3\text{SiO—}$ or with some other reactive groups (-H, -OH, -OR). Silicone oils, silicone resins and silicone rubber are the three main kinds of silicone products in our daily life nowadays. Silicones have thermal stability, resistance to weathering, high electrical resistivity, flexibility at extremely low temperatures and physiological inertness which make them to be important in many applied fields nowadays.

Due to their low price and fast reaction process, they are usually used to fabricate coatings in real applications. The double re-entrant structures are easy to build from the direct hydrolysis of the organosilicon or the deposition of organosilicon on a template. Two main kinds of reported super liquid repellent structures are reported based on this including silicone nanofilament surface,^[50] and candle-soot template surface.^[51] These organosilicon-based surfaces give us an opportunity to prepare super liquid repellent surfaces in a low-cost and easy way.

The process of modifying the surface of an inorganic material with a reactive alkylsilane has become widely used in both research and technology and has been studied to great extent.^[52] When a surface with hydroxyl (-OH) groups is exposed to reactive mono-, di- or trifunctional organosilicons, several reaction products can be formed, depending on the reaction conditions.

Coating a substrate with polyalkylsilsesquioxane filaments (named as silicone nanofilaments, SNF), first reported in 2004, represents an economical and efficient way to prepare a super-liquid-repellant surface.^[53] Trichloromethylsilane (TCMS) will hydrolyze when there is water in the solvent (e.g. toluene).^[52a-d, 54] During the process, the methylsilanols produced from the hydrolysis of TCMS form a partially cross-linked polysiloxane^[52b, 52d]. The polymethylsilsesquioxane nanofilaments is then formed because of the cross-linking part existing in this kind of polysiloxane.^[50] Because of the cross-linking part, it is possible for the polysiloxane in the solvent

to form filament shape when it grows following one direction when we carefully control the water concentration in the solvent during the reaction (Figure 1.14) [50, 55].

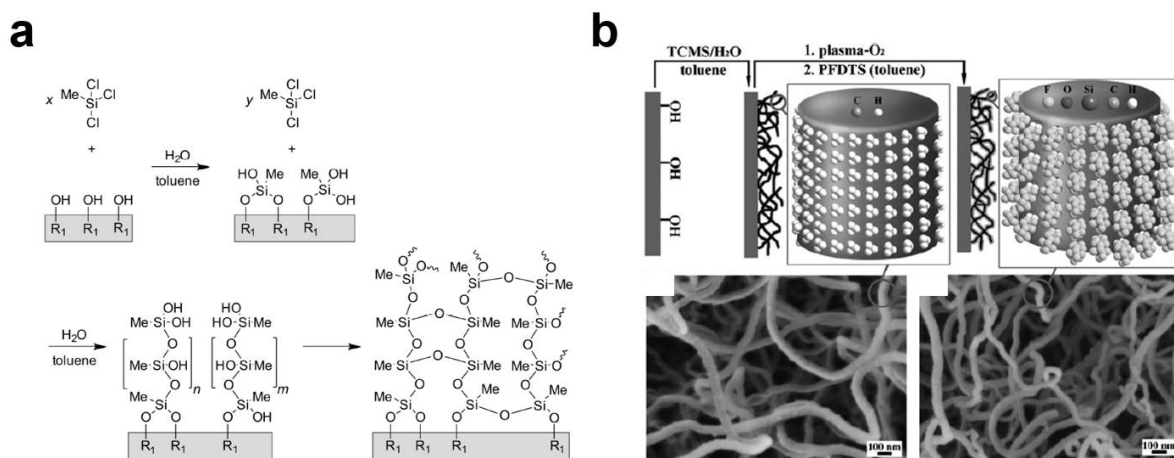


Figure 1.14. Nanofilament coated super liquid repellent surfaces. (a) Possible reaction scheme for the formation of nanofilaments. (b) Growth of silicone nanofilaments onto glass slides and the corresponding SEM images.^[55a] Copyright 2011, John Wiley and Sons.

Thin filaments are the main feature of the surface topography (Figure 1.14b). These filament structures are irregularly bent and hooked which supports a random re-entrant structure. Small filaments have diameters ranging from 20 to 50 nm. The length of these fibers range from very short, nearly spherical bases up to about 1 μm . Occasionally, much larger filaments of a similar shape to the smaller ones are also found on the surface. These are up to 150 nm in diameter and several micrometers in length. Water drops on nanofilament-coated substrates show a high static contact angles ($> 150^\circ$) and on most of the substrates, they also show a low sliding angle ($< 10^\circ$ when coated on polished rigid surface, $< 20^\circ$ when coated on soft polymer substrate, water drop volume is 10 μL).^[50] By changing the concentration of water in the solvent, after fluorination, the nanofilament-coated surface can also be superamphiphobic (a low sliding angle 5° for *n*-decane whose surface tension is 23.8 mN m^{-1}). Because of the easy grafting method, nanofilament-coated surface is one of the widely used surfaces in the super liquid repellent surface preparation.

Soot coated surfaces, which are generated from candle flame, also have an double re-entrant structure (a loose, fractal-like network, Figure 1.15a).^[56] A water drop on the surface shows a contact angle above 160° and rolls off easily. However, when water rolls off the surface, soot particles will be carried by the drop and when the soot deposit is removed, the drop undergoes a wetting transition.^[51] Candle-soot template surface is prepared by the deposition of one

hydrolyzed organosilicon (i.e. tetraethoxysilane) on the soot coated substrates (glass or silicon).^[51] In this way the soot is stabilized by a coating of SiO₂.

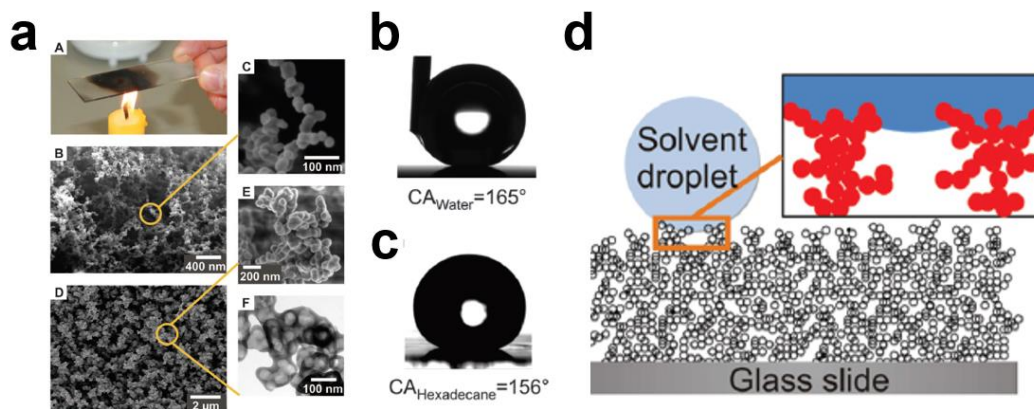


Figure 1.15. Candle-soot template super liquid repellent surfaces. (a) The preparation procedure of the soot-template surface. (A) Photograph depicting sample preparation. A glass slide is held in the flame of a candle until a soot layer a few micrometers thick is deposited. (B) Scanning electron microscope (SEM) image of the soot deposit. (C) High-resolution SEM image showing a single particle chain made up of almost spherical carbon beads 40 ± 10 nm in diameter. (D) SEM image of the deposit after being coated with a silica shell. (E) High-resolution SEM image of a cluster after the carbon core was removed by heating for 2 hours at 600°C. (F) High-resolution TEM image of a cluster after calcination, revealing the silica coating with holes that were previously filled with carbon particles. The silica shell is 20 ± 5 nm thick. (b) (c) A 2 ml water drop (b) and 5 ml hexadecane drop (c) deposited on the surface possess a static contact angle of $165^\circ \pm 1^\circ$ and $156^\circ \pm 1^\circ$, respectively. (d) Scheme of a liquid drop deposited on the fractal-like composite interface.^[51] Copyright 2011, reprinted with permission from AAAS.

After removing the carbon core at 600 °C (Figure 1.15a) and being fluorinated, the surface will be transparent, and it will repel even low surface tension liquid (e.g. n-hexadecane) (Figure 1.15b and c). Because of the silica shell, the coating has a better mechanical resistance compared to the original soot-coated substrate. Moreover, the structure of the candle soot hence provides multiple overhangs which need to be overcome before the substrate is fully wetted (Figure 1.15d) which makes candle soot-templated surfaces an efficient and simple strategy to fabricate superamphiphobic surfaces.

1.3.1.4 Stretchable super liquid repellent surfaces

Super liquid repellent coating can endow a liquid repellency to a soft even stretchable substrate by isolating the substrate and drops using low-surface-energy textured structures. The first stretchable superhydrophobic surface was reported as using the “pre-stretching” method by Genzer et al. in 2000 (Figure 1.16a). The surface can have a quite low contact angle hysteresis of less than 10° when they prepared the surface in a certain ratio of around 60% (Figure 1.16b).

Based on that, various kinds of surfaces such as tunable surface patterns,^[57] stretchable superhydrophobic surface,^[58] hierarchically wrinkled surface^[59] were then developed. Water drops can easily slide off or rebound from these surfaces in a relaxed or stretched state. It avoids the extra energy dissipation from the surface deformation due to the extremely low contact area and adhesion.

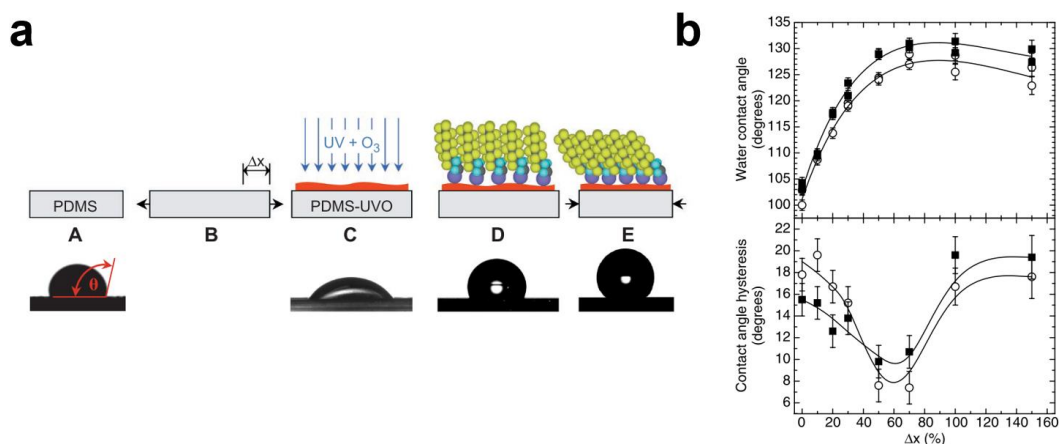


Figure 1.16. First reported work on fabrication of a stretchable superhydrophobic surface. (a) The preparation process of this surface: (A) A pristine PDMS network is prepared by casting a mixture of PDMS and a cross-linker into a thin film and curing it for about 1 hour. (B) The film is mechanically stretched by a certain length, Δx . (C) Subsequent exposure to a UVO treatment produces hydrophilic PDMS surfaces (PDMS-UVO) composed mainly of hydroxyl groups. (D) The SF trichlorosilanes molecules are deposited from vapor onto this stretched substrate and form an organized self-assembled monolayer. (E) Finally, the strain is released from the PDMS-UVO film, which returns to its original size, causing the grafted molecules to form a densely organized mechanically assembled monolayer (MAM). (b) The dependence of the water contact angle and contact angle hysteresis on F6H2-MAM (circles) and F8H2-MAM (squares) samples on the degree of stretching of the PDMS substrate before the UVO treatment, Δx . Copyright 2000, reprinted with permission from AAAS.

However, most of the water drops in real applications are not pure water. There will be some solutes in the water drop, especially for some biological liquids e.g. blood, tissue fluid or protein dispersion, the surface tension of these liquids will be low which results in a drop pinning due to a failure of the liquid-repellency. Therefore, a superamphiphobic stretchable surface is needed to repel low-surface-tension liquid on a highly elastic substrate which can be easily deformed.

Water has a relatively high surface tension. It will result in a high Young's contact angle. The air-liquid interface as shown in Figure 1.17a has a certain distance away from the non-textured substrate. Even though we stretch the surface to a certain tensile strain, the height of such interface decreases but the liquid component will not touch the substrate. However, if the liquid drop has a low surface tension, the corresponding low Young's contact angle will make the air-liquid interface much closer to the substrate (Figure 1.17b). After a slight stretch of the surface, the oil will easily contact and wet the smooth part of the substrate. Water on the surface transits from Cassie state to Wenzel state. Therefore, currently existing superamphiphobic surfaces easily lose their super-liquid-repellency to non-polar liquids with a low surface tension under small deformation, in particular when being stretched.^[60] The breakup of the surface structures during stretching usually cause the low-surface-tension liquids on. Till now, there is no effective way proposed to solve this problem that the loss of superamphiphobicity due to stretching.

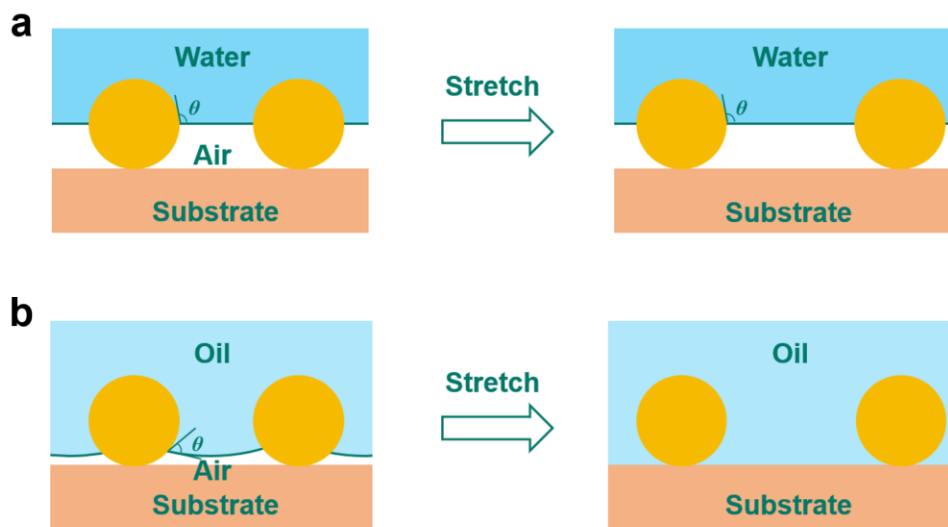


Figure 1.17. The scheme to show why the stretchable super-liquid repellent surface fails when the surface is stretched. (a) Water drop with a high surface tension ($\sim 72 \text{ mN m}^{-1}$) placed on the surface. (b) Oil drop with a low surface tension ($< 30 \text{ mN m}^{-1}$) placed on the surface.

1.3.2 Liquid-infused surfaces (LIS)

Liquid-Infused surface (LIS) is another kind of liquid repellent surface which is inspired from the Nepenthes pitcher plant (Figure 1.18).^[61] On a liquid-infused surface, the drop has a low contact angle. Still, the contact angle hysteresis is less than 5° . They have attracted a lot of attention since they were first reported in research literature.^[62] A liquid-infused surface is a combination of a liquid layer and an underneath scaffold stabilizing the liquid. To create a liquid-infused surface, three main design principles must be met: 1. the lubricant and the placed liquid must be immiscible; 2. the lubricating oil prefers to wet and spread onto the solid substrate; 3. the solid substrate must have higher affinity for the lubricating liquid over the probing liquid.^[14] For such a surface, when liquid drops are placed on it, there will be a soft liquid/liquid interface. The drop is considered to contact a soft matter part instead of the rigid structure underneath.

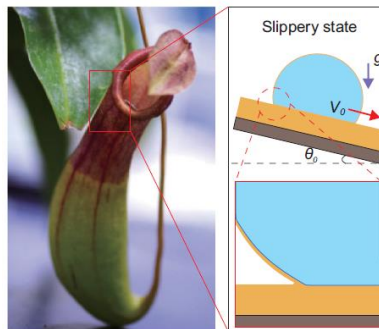


Figure 1.18. Liquid-infused surface inspired from the Nepenthes pitcher plant.^[63] Copyright 2020, Oxford University Press.

The most common case of a liquid-infused surface is the combination of a solid rough textured substrate with micro- and nanoscale topography and an oil-based lubricant (Figure 1.19a). It is called slippery liquid-infused porous surface (SLIPS).^[62a] Such kind of surface was first reported by Aizenberg et al. in 2011. Different from the lotus effect, their approach uses the microstructured substrate to lock the infused lubricating in place (Figure 1.19b). They will have a smooth lubricate-water interface when water drops are placed on or sliding off such surface (Figure 1.19a). An oil cloak and an oil ridge are usually formed which will induce the oil depletion from the textured structures.^[64]

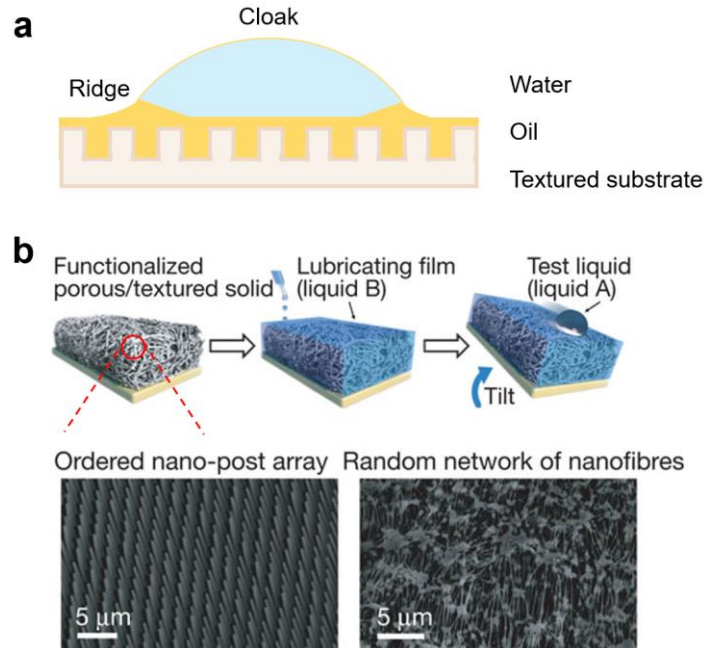


Figure 1.19. Slippery liquid-infused porous surface. (a) The scheme to show the most common composition of a SLIPS. (b) The first work related to SLIPS reported by Aizenberg et al. in 2011. A liquid B by which the solid prefer to wet is infused as a lubricated layer. Copyright 2011, Springer Nature.

1.3.2.1 Wetting on LIS

A ridge at the contact line and the a cloak surrounding the drop could appear (Figure 1.20)^[65] due to the different wetting situations for the liquid-liquid (red frame) and liquid-air interface (black frame) and the interfacial energy difference between the different phases. Smith et al. described the details related to the different thermodynamic conditions which describe this four-phase system.^[65] For example, if the droplet in Figure 1.20 is water, the lubricant is a fluorinated “oil”, and the other two phases are air and the solid, then, a water droplet will be completely encapsulated by the oil (an oil cloak will surround the drop) if the spreading parameter $S_{ow(a)} > 0$ or lays on top (no cloak formation) if $S_{ow(a)} < 0$, as shown in Figure 1.20, left and right, respectively. The spreading factor $S_{ow(a)}$, where “o”, “w”, and “a” are represented by oil, water, and air, correspondingly, is defined by:

$$S_{ow(a)} = \gamma_{wa} - \gamma_{ow} - \gamma_{oa} \quad (1.13)$$

where γ_{wa} is the water–air surface tension, γ_{ow} is the oil–water surface tension, and γ_{oa} is the oil–air surface tension. Depending on the four-phase system at hand, the oil will completely wet (encapsulate) the surface, partially wet, or will not be present under thermodynamic conditions by

comparing the total interface energy per unit area E_i for different cases. The derivations can be checked in the original publication.^[65]

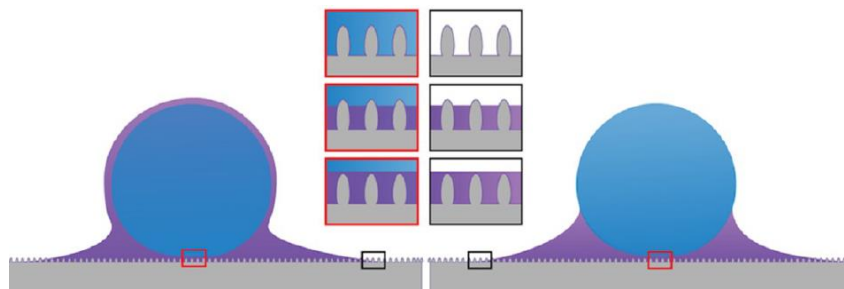


Figure 1.20. Different wetting process for a four-phase system (air, liquid-1: water, liquid-2: lubricate, solid). Red frame inset represents possible wetting states near the droplet–lubricant interface. Here, the droplet can completely wet the surface (top), partially wet the surface (middle), or a completely lubricated structure (bottom). The black inset represents the wetting of the lubricant on a surface in the presence of an air phase. Here, the structure can lack any lubricant (top), be partially wetted (middle), or be fully impregnated (bottom) by the lubricant.^[14] Copyright 2019, American Chemical Society.

1.3.2.2 Drop movement on LIS

Even though the drop adhesion is quite low on the liquid-liquid interface, the drop movement is usually slow on such surfaces. Compared to the drop sliding off a smooth rigid surface or a superhydrophobic surface, the source of the friction will be more complicated (Figure 1.21). The drop friction is hypothesized to come from their viscous effects due to flow near the liquid-liquid interface (Figure 1.21d) and leading or lagging oil menisci (Figure 1.21e and f) at the three-phase contact line.

The drop velocity will be affected by the viscosity η_0 of the infusing oil and the meniscus size at the contact lines. Keiser et al.^[66] suggested a model to calculate the velocity on SLIPS:

$$U = \frac{(\rho g)^{2/3} R^3}{\gamma_0^{1/2} \beta \eta_0} \sin^{3/2} \alpha \quad (1.14)$$

They assumed that the oil viscosity is bigger than that of water. Here, ρ is the drop density, γ_0 is the oil surface tension, U is the drop velocity, R is the radius of the drop, $\beta = \ln \frac{l}{h}$, with l being the typical size of meniscus and h being the oil layer thickness, is the numerical factor reflecting the singular dissipation at the wedge tip. They estimate it to be an order of 10 if the particle size of the porous structure underneath the oil is around 30 nm.^[66] The velocity value calculated by such an equation is usually 3 times lower than that on the superhydrophobic surface in magnitude. Up

to now, how to achieve a high drop velocity on SLIPS versus a mobile contact line and low drop adhesion together is still a problem for fabricating such kind of surface.

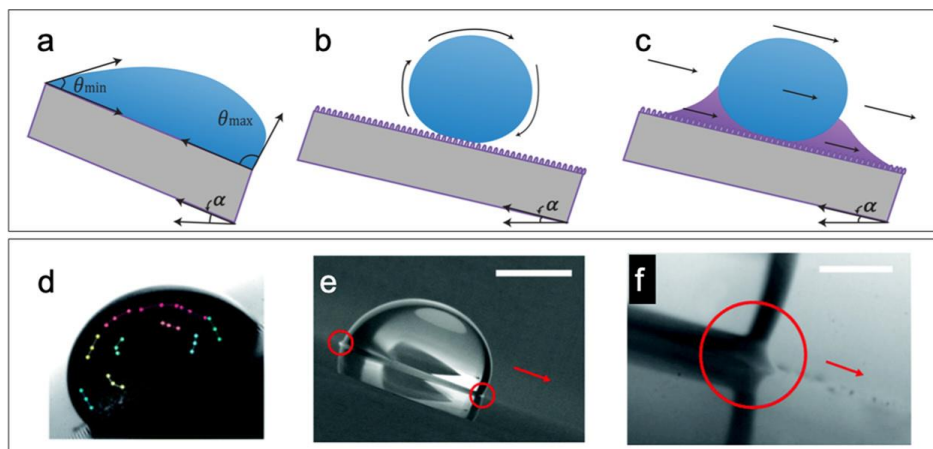


Figure 1.21. Rolling and contact line deformation of a drop moving on SLIPS. The schemes for (a) sliding of a droplet on a flat surface, (b) rolling of a droplet on a superhydrophobic surface and (c) droplet sliding on a liquid-infused surface. (d) Trajectories mapping of coffee particles within a water droplet on SLIPS demonstrating droplet rolling. (e,f) Observations of leading and lagging wetting ridge on SLIPS caused by surface tensions between droplet and lubricant. Scale bar represents 2 and 0.4 mm in (e,f), respectively. Copyright 2019, American Chemical Society.

1.3.3 Combination of LIS and superhydrophobic surface

Recently, the development of slippery superhydrophobic surfaces has provided a promising avenue for achieving a balance between rapid drop shedding and sufficient stability in practical applications. The concept of a slippery Cassie state (Figure 1.22), where drops maintain a Cassie state, was initially introduced by Brian et al. in 2013.^[67] Subsequently, several model surfaces with slippery superhydrophobic properties have been constructed, exhibiting unique characteristics such as low drop pull-off force,^[68] reduced lateral adhesion^[63, 69], switchable wetting property^[70] and self-propelled droplet transport^[71].

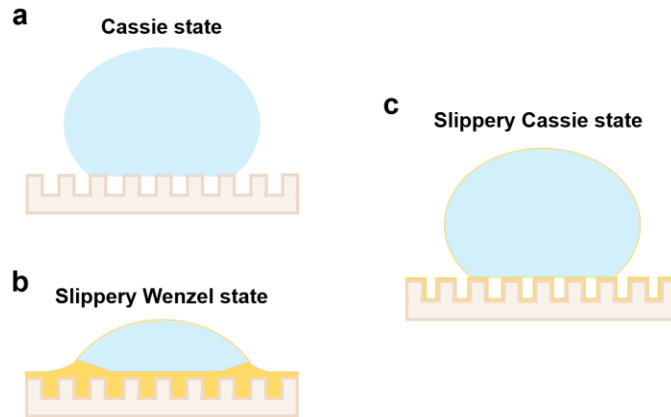


Figure 1.22. Diagram of possible wetting states on textured surfaces. (a) Cassie state: a layer of air separates most of the water from the surface. (b) Slippery Wenzel state: a layer of an immiscible liquid separates the water from the surface. (c) Slippery Cassie state: a layer of air separates most of the water from the surface, which is coated with a second liquid.

Liquid-infused super liquid repellent surface (sometimes is also called slippery super liquid repellent surface) is a concept that the surface is a combination of a superhydrophobic surface and a slippery lubricant-infused porous surface. The oil layer can be infused in the top part of the porous hydrophobic structures e.g. a pillar surface with a PDMS cap (Figure 1.23a)^[63] and a doubly re-entrant micropillar (Figure 1.23b).^[68] Because of the infused oil layer, the superhydrophobic surface will have an increased stability against pressure and impact, and enhanced lateral mobility of water drops as well as reduced hydrodynamic drag.

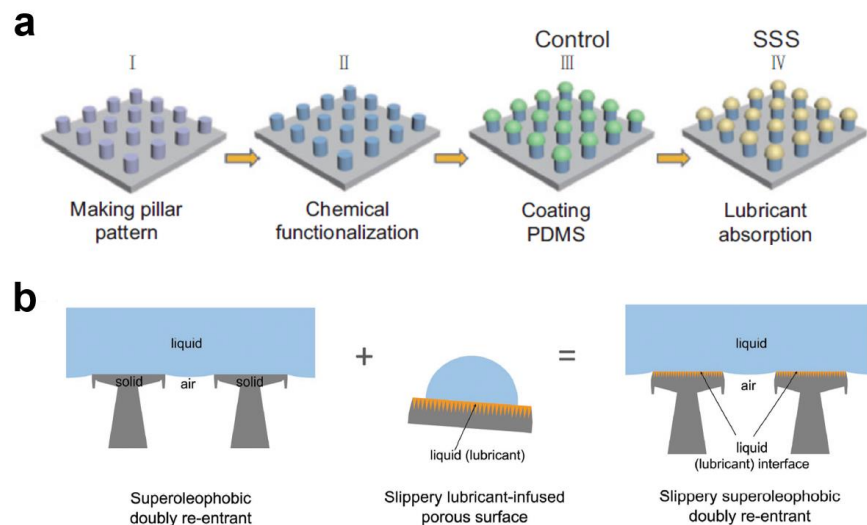


Figure 1.23. Liquid-infused super liquid repellent surfaces. (a) Fabrication process and topological structure of the Salvinia-like slippery surface (SSS).^[63] Copyright 2020, Oxford

University Press. (b) Blueprint for a slippery superoleophobic surface formed via combination of a doubly re-entrant structure and a slippery lubricant-infused porous surface.^[68] Copyright 2018, John Wiley and Sons.

Currently, the methods for preparing surface for slippery superhydrophobic surfaces are complex and technically demanding. It is hard to use them in real applications. And even though the air gap between the structures will reduce the friction, the micrometer-thick oil layer ^[63, 67-68, 71] may result in a meniscus near the contact line preventing the rapid drop shedding. To date, no work has achieved a rapid drop shedding process on a slippery superhydrophobic surface as observed on a dry superhydrophobic surface (defined here as a surface without any liquid component).

1.3.4 Covalently attached liquid surfaces (CALs)

Besides the liquid-infused surfaces, recently, covalently attached liquid surfaces (CALs) are widely reported as another kind of slippery surface.^[72] Both water and most solvents have low values of contact angle hysteresis (CAH, less than 5°) on them. Despite their nanoscale thickness (less than 10 nm), CALs exhibit behavior similar to liquid-infused surfaces, including high droplet mobility and the ability to prevent icing and fouling.^[72c, 73] To date, CALs have primarily been obtained using grafted polydimethylsiloxane (PDMS), though there are also examples of polyethylene oxide (PEO),^[74] perfluorinated polyether (PFPE),^[75] and short-chain alkane.^[76] When liquid drops are placed on such surfaces, there will be an interface composed of a soft-matter (liquid-like) and a liquid. For such kind of surfaces, they have several advantages. First, their liquid-like nature endows liquid repellency to smooth solid surfaces, without relying on surface texturing. Second, they do not have the problem of the interface instability of air-mediated or liquid-mediated liquid repellent surfaces due to air or lubricant loss, since the molecule layer is covalently bonded which makes it not easily washed away or depleted. Third, the CALs have unique characteristics, such as reduced friction and adhesion which is meaningful in real applications.^[15]

To date, most of the work on CALs has been conducted on PDMS systems. PDMS CALs have been prepared via several mechanisms, which here are grouped into three families: grafting-from methods using chlorosilanes, grafting-from methods using methoxysilanes, and grafting-to methods using high molecular weight PDMS.

Such a kind of surface is considered to be 'liquid-like'. This 'liquid-like' concept had been proposed previously in studies on polymer glasses, which found that the molecular chains are many orders of magnitude more mobile on the surface than in the interior. There are three physical states for

amorphous polymers because of temperature-dependent chain mobility: the glassy state, the rubbery state and the fluid state. Glass transition temperature (T_g) can also be defined as the temperature when grafted polymers change from the solid-like state to the liquid-like. Some highly flexible polymers with extremely low T_g (less than $-100\text{ }^\circ\text{C}$), such as PDMS ($T_g = -127\text{ }^\circ\text{C}$) are liquid and highly mobile at room temperature. While one end of the polymer chain is fixed on the surface by the covalent bond, the rest is free to rotate, bend and stretch (Figure 1.24). The dynamic chain nature of grafted flexible polymers gives solid surfaces liquid-like qualities at ambient temperature and unprecedented liquid repellency (ultralow CAH).

This kind of surface structure reduces CAH in two ways. First, CALS is self-smoothing and chemically homogeneous, due to the high mobility of grafted molecular layers mask the chemical or physical defects on the solid surfaces. Second, the grafted molecule chains are rotationally flexible, which helps to overcome the energy barriers for moving the contact lines of the drops.

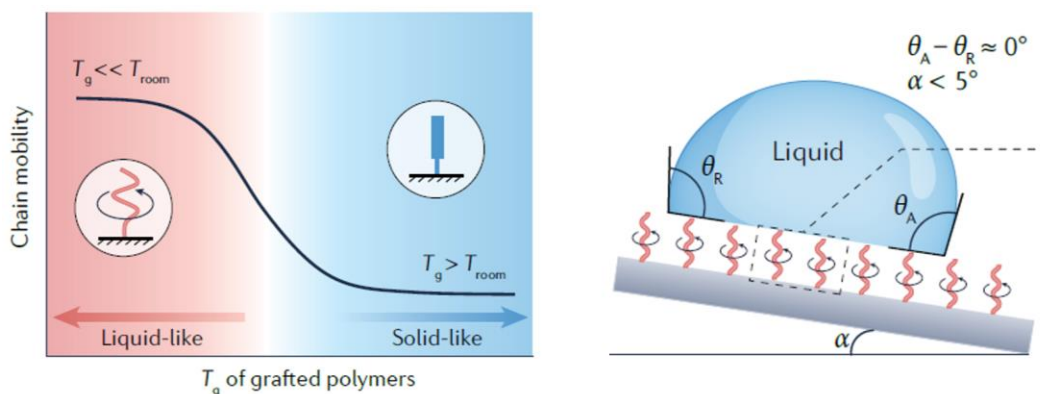


Figure 1.24. The left curve shows the chain nature of the surface-grafted polymers with different values of T_g . When the T_g of polymer is far less than the room temperature (T_{room}), typically less than $-100\text{ }^\circ\text{C}$, the grafted polymer layer exhibits a unique liquid-like nature. The right schematic illustrates the low contact angle hysteresis and sliding angles (α) on the liquid-like surface, and the high mobility of covalently bonded polymer chains of the attached liquid.^[15] Copyright 2023, Springer Nature.

The comprehension of drop motion and friction on liquid-like CALS remains challenging, primarily due to factors such as chain rearrangement, chain stretching and molecule reordering occurring at the polymer/liquid interface.^[77] Because the polymer layer is highly soft and flexible, nano-scale deformation can also happen on the CALS even though the coating thickness ($< 10\text{ nm}$) is much thinner than that of a bulk soft matter.

This kind of nano-scale deformation can be the main source of this energy dissipation on CALS even though the drop friction is low. In prior research, Kristina et al. observed a nano-scale elastic deformation at the contact line when good solvent of PDMS e.g. decane moving on PDMS brushes by the contact angle difference in different scales (Figure 1.25).^[41, 78]

Fredrickson et al. give a theory to calculate the minimum work W we need to deform a thin polymer layer:^[79]

$$W \approx -\frac{192\epsilon^3 R^2 \mu_0}{\pi^2 h_0^3} \quad (1.15)$$

where ϵ is the perturbation amplitude, R is the radius of the spherical tip which give the force to the layer, μ_0 is the shear modulus, h_0 is the layer thickness. It gives us the impression that both thickness and the shear modulus of layer will affect the contact line deformation of the nano-scale CALS. For poor solvents like water with polarity, such nano-scale CALS coating layer may rearrange in it to create patches of chemical groups susceptible to hydrogen bonding resulting in a higher force between drop and the soft coating at the three-phase contact line. Up to now, it is still unclear how this kind of deformation affects the drop moving on CALS.

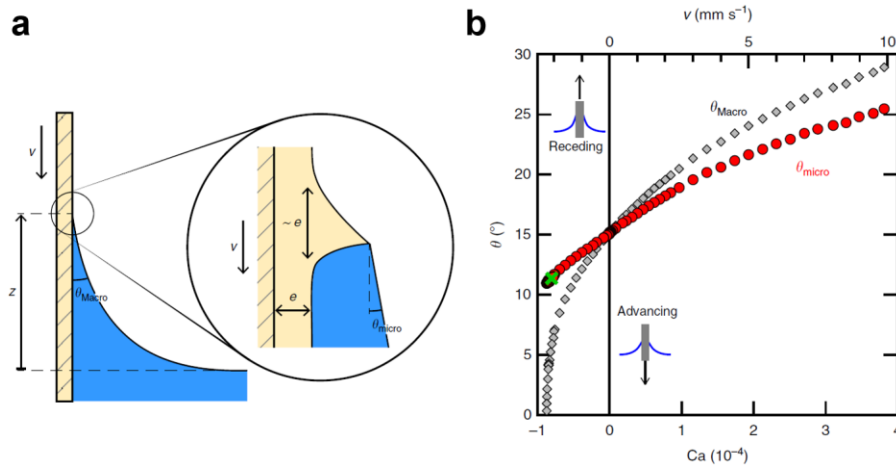


Figure 1.25. Observation of nano-scale deformation at the contact line when liquid decane moves on a pseudo-brush surface.^[41] (a) Dip-coating experiment and definitions of the contact angles on a CAL. Due to the viscous bending of the liquid–vapor interface, on a viscoelastic surface e.g. PDMS brush, the force exerted by the fluid produces a deformation of the layer immediately below the contact line. (b) The difference between the dynamics micro-scale receding contact angle θ_{micro} and macro-scale receding contact angle θ_{macro} reflects the response of the cusp-shaped deformation when the contact line is moving. Copyright 2016, Springer Nature.

1.4 References

- [1] a) T. Young, *Philosophical Transactions of the Royal Society of London* **1805**, 95, 65; b) A. B. D. Cassie, *Discussions of the Faraday Society* **1948**, 3, 11; c) P. G. de Gennes, *Reviews of Modern Physics* **1985**, 57, 827; d) F. B.-W. Pierre-Gilles Gennes, David Quéré, *Capillarity and Wetting Phenomena: Drops, Bubbles, Pearls, Waves*, Springer New York, NY **2004**.
- [2] a) 中. 编辑部, *全唐诗*, 中华书局, **1999**; b) M. Zhao, *Université Paris sciences et lettres* **2017**.
- [3] W. Barthlott, C. Neinhuis, *Planta* **1997**, 202, 1.
- [4] Lotus Leaf Inspires Equipment Upgrade, <https://www.foodmanufacturing.com/home/news/21100076/lotus-leaf-improves-food-equipment-sanitation>
- [5] R. N. Wenzel, *Industrial & Engineering Chemistry* **1936**, 28, 988.
- [6] R. H. Dettre, R. E. J. Johnson, in *Contact Angle, Wettability, and Adhesion*, Vol. 43, American chemical society, 1964, 8.
- [7] M. Morra, E. Occhiello, F. Garbassi, *Langmuir* **1989**, 5, 872.
- [8] T. Onda, S. Shibuichi, N. Satoh, K. Tsujii, *Langmuir* **1996**, 12, 2125.
- [9] a) S. Wu, Y. Du, Y. Alsaïd, D. Wu, M. Hua, Y. Yan, B. Yao, Y. Ma, X. Zhu, X. He, *Proc. Natl. Acad. Sci. USA* **2020**, 117, 11240; b) W. S. Y. Wong, T. P. Corrales, A. Naga, P. Baumli, A. Kaltbeitzel, M. Kappl, P. Papadopoulos, D. Vollmer, H.-J. Butt, *ACS Nano* **2020**, 14, 3836.
- [10] N. Miljkovic, R. Enright, E. N. Wang, *ACS Nano* **2012**, 6, 1776.
- [11] a) G. Luo, L. Wen, K. Yang, X. Li, S. Xu, P. Pi, X. Wen, *Chem. Eng. Sci.* **2020**, 383, 123125; b) F. Geyer, M. D'Acunzi, C.-Y. Yang, M. Müller, P. Baumli, A. Kaltbeitzel, V. Mailänder, N. Encinas, D. Vollmer, H.-J. Butt, *Adv. Mater.* **2019**, 31, 1801324.
- [12] a) L. Zhai, M. C. Berg, F. Ç. Cebeci, Y. Kim, J. M. Milwid, M. F. Rubner, R. E. Cohen, *Nano Lett.* **2006**, 6, 1213; b) R. Ghosh, A. Baut, G. Belleri, M. Kappl, H.-J. Butt, T. M. Schutzius, *Nature Sustainability* **2023**, n/a, n/a.
- [13] W. Zhang, D. Wang, Z. Sun, J. Song, X. Deng, *Chem. Soc. Rev.* **2021**, 50, 4031.
- [14] M. Villegas, Y. Zhang, N. Abu Jarad, L. Soleymani, T. F. Didar, *ACS Nano* **2019**, 13, 8517.
- [15] L. Chen, S. Huang, R. H. A. Ras, X. Tian, *Nature Reviews Chemistry* **2023**, 7, 123.
- [16] a) B. Choi, J. Lee, H. Han, J. Woo, K. Park, J. Seo, T. Lee, *ACS Appl. Mater. Interfaces* **2018**, 10, 36094; b) L. Li, Y. Bai, L. Li, S. Wang, T. Zhang, *Adv. Mater.* **2017**, 29, 1702517.
- [17] a) J. N. Wang, Y. Q. Liu, Y. L. Zhang, J. Feng, H. Wang, Y. H. Yu, H. B. Sun, *Adv. Funct. Mater.* **2018**, 28, 1800625; b) R. Shimizu, Y. Nonomura, *J. Oleo. Sci.* **2018**, 67, 47.

- [18] a)L. Xiong, L. L. Kendrick, H. Heusser, J. C. Webb, B. J. Sparks, J. T. Goetz, W. Guo, C. M. Stafford, M. D. Blanton, S. Nazarenko, D. L. Patton, *ACS Appl. Mater. Interfaces* **2014**, 6, 10763; b)H. Zou, S. Lin, Y. Tu, F. Li, J. Hu, G. Liu, S. Hu, G. Yang, Z. Yu, *Adv. Mater. Interfaces* **2016**, 3, 1500693.
- [19] a)S. Y. W. William, L. Guanyu, T. Antonio, *Small* **2017**, 13, 1603688; b)J.-Y. Huang, Y.-K. Lai, F. Pan, L. Yang, H. Wang, K.-Q. Zhang, H. Fuchs, L.-F. Chi, *Small* **2014**, 10, 4865.
- [20] a)D. Quéré, *Annual Review of Materials Research* **2008**, 38, 71; b)C. Marangoni, P. Stefanelli, *Il Nuovo Cimento (1869-1876)* **1873**, 9, 236.
- [21] X. Li, F. Bodziony, M. Yin, H. Marschall, R. Berger, H.-J. Butt, *Nat. Commun.* **2023**, 14, 4571.
- [22] H.-Y. Kim, H. J. Lee, B. H. Kang, *Journal of colloid and interface science* **2002**, 247, 372.
- [23] T. Blake, J. Haynes, *Journal of colloid and interface science* **1969**, 30, 421.
- [24] J. Joanny, P.-G. De Gennes, *The journal of chemical physics* **1984**, 81, 552.
- [25] B. Andreotti, J. H. Snoeijer, *Annual review of fluid mechanics* **2020**, 52, 285.
- [26] a)H.-J. r. Butt, R. d. Berger, W. Steffen, D. Vollmer, S. A. Weber, *Langmuir* **2018**, 34, 11292; b)R. Tadmor, *Langmuir* **2021**, 37, 6357; c)X. Li, S. Silge, A. Saal, G. Kircher, K. Koynov, R. Berger, H.-J. Butt, *Langmuir* **2021**, 37, 1571.
- [27] a)X. Li, P. Bista, A. Z. Stetten, H. Bonart, M. T. Schür, S. Hardt, F. Bodziony, H. Marschall, A. Saal, X. Deng, *Nature Physics* **2022**, 1; b)D. Díaz, X. Li, P. Bista, X. Zhou, F. Darvish, H.-J. Butt, M. Kappl, *Physics of Fluids* **2023**, 35, 017111.
- [28] H.-J. Butt, J. Liu, K. Koynov, B. Straub, C. Hinduja, I. Roismann, R. Berger, X. Li, D. Vollmer, W. Steffen, M. Kappl, *Current Opinion in Colloid & Interface Science* **2022**, 59, 101574.
- [29] R. E. Johnson, R. H. Dettre, D. A. Brandreth, *J. Colloid Interface Sci.* **1977**, 62, 205.
- [30] T. Huhtamäki, X. Tian, J. T. Korhonen, R. H. A. Ras, *Nature Protocols* **2018**, 13, 1521.
- [31] a)C. G. L. Furnidge, *Journal of Colloid Science* **1962**, 17, 309; b)R. Goodwin, D. Rice, S. Middleman, *J. Colloid Interface Sci.* **1988**, 125, 162.
- [32] N. Gao, F. Geyer, D. W. Pilat, S. Wooh, D. Vollmer, H.-J. Butt, R. Berger, *Nat. Phys.* **2018**, 14, 191.
- [33] J. Fan, M. C. T. Wilson, N. Kapur, *J. Colloid Interface Sci.* **2011**, 356, 286.
- [34] D. H. Allen, *Introduction to the Mechanics of Deformable Solids*, Springer New York, NY, **2013**.
- [35] H. Liang, Z. Cao, Z. Wang, A. V. Dobrynin, *ACS Macro Lett.* **2018**, 7, 116.
- [36] A. Marchand, S. Das, J. H. Snoeijer, B. Andreotti, *Phys. Rev. Lett.* **2012**, 109, 236101.

- [37] R. D. Schroll, M. Adda-Bedia, E. Cerda, J. Huang, N. Menon, T. P. Russell, K. B. Toga, D. Vella, B. Davidovitch, *Phys. Rev. Lett.* **2013**, 111, 014301.
- [38] J. H. Snoeijer, E. Rolley, B. Andreotti, *Phys. Rev. Lett.* **2018**, 121, 068003.
- [39] T. Kajiya, A. Daerr, T. Narita, L. Royon, F. Lequeux, L. Limat, *Soft Matter* **2013**, 9, 454.
- [40] B. Andreotti, J. H. Snoeijer, *Annual Review of Fluid Mechanics* **2020**, 52, 285.
- [41] R. Lhermerout, H. Perrin, E. Rolley, B. Andreotti, K. Davitt, *Nat. Commun.* **2016**, 7, 12545.
- [42] A. B. D. Cassie, S. Baxter, *Transactions of the Faraday Society* **1944**, 40, 546.
- [43] J. Ou, G. Fang, W. Li, A. Amirfazli, *J. Phys. Chem. C* **2019**, 123, 23976.
- [44] a)J.-L. Liu, X.-Q. Feng, G. Wang, S.-W. Yu, *Journal of Physics: Condensed Matter* **2007**, 19, 356002; b)Y. Ma, X. Cao, X. Feng, Y. Ma, H. Zou, *Polymer* **2007**, 48, 7455.
- [45] a)A. Ahuja, J. A. Taylor, V. Lifton, A. A. Sidorenko, T. R. Salamon, E. J. Lobaton, P. Kolodner, T. N. Krupenkin, *Langmuir* **2008**, 24, 9; b)A. Marmur, *Langmuir* **2008**, 24, 7573; c)A. Tuteja, W. Choi, G. H. McKinley, R. E. Cohen, M. F. Rubner, *MRS Bulletin* **2008**, 33, 752; d)T. L. Liu, C.-J. C. Kim, *Science* **2014**, 346, 1096.
- [46] C. F. a. J. M. Crafts, *Ann.* **1863**, 127, 28.
- [47] C. F. a. J. M. Crafts, *Ann.* **1865**, 136, 203.
- [48] M. J. Hunter, E. L. Warrick, J. F. Hyde, C. C. Currie, *J. Am. Chem. Soc.* **1946**, 68, 2284.
- [49] E. G. Rochow, *J. Am. Chem. Soc.* **1945**, 67, 963.
- [50] G. R. J. Artus, S. Jung, J. Zimmermann, H. P. Gautschi, K. Marquardt, S. Seeger, *Adv. Mater.* **2006**, 18, 2758.
- [51] X. Deng, L. Mammen, H.-J. Butt, D. Vollmer, *Science* **2012**, 335, 67.
- [52] a)G. E. Maciel, M. J. Sullivan, D. W. Sindorf, *Macromolecules* **1981**, 14, 1607; b)K. A. Andrianov, T. V. Vasil'eva, N. M. Katashuk, T. V. Snigireva, B. I. D'Yachenko, *Polymer Science U.S.S.R.* **1976**, 18, 1457; c)M. Trau, B. S. Murray, K. Grant, F. Grieser, *J. Colloid Interface Sci.* **1992**, 148, 182; d)C. P. Tripp, M. L. Hair, *Langmuir* **1995**, 11, 149; e)L. Gao, T. J. McCarthy, *J. Am. Chem. Soc.* **2006**, 128, 9052.
- [53] Z. Chu, S. Seeger, *Chem. Soc. Rev.* **2014**, 43, 2784.
- [54] A. Y. Fadeev, T. J. McCarthy, *Langmuir* **2000**, 16, 7268.
- [55] a)J. Zhang, S. Seeger, *Angew. Chem. Int. Ed.* **2011**, 50, 6652; b)J. Zimmermann, G. R. J. Artus, S. Seeger, *Journal of Adhesion Science and Technology* **2008**, 22, 251; c)J. Zhang, L. Li, B. Li, S. Seeger, *RSC Advances* **2014**, 4, 33424.
- [56] C. M. Megaridis, R. A. Dobbins, *Combustion Science and Technology* **1990**, 71, 95.
- [57] C. Cao, H. F. Chan, J. Zang, K. W. Leong, X. Zhao, *Adv. Mater.* **2014**, 26, 1763.

- [58] J. Ju, X. Yao, X. Hou, Q. Liu, Y. S. Zhang, A. Khademhosseini, *J. Mater. Chem. A* **2017**, 5, 16273.
- [59] K. Efimenko, J. Finlay, M. E. Callow, J. A. Callow, J. Genzer, *ACS Appl. Mater. Interfaces* **2009**, 1, 1031.
- [60] a)S. Pan, R. Guo, M. Björnmalm, J. J. Richardson, L. Li, C. Peng, N. Bertleff-Zieschang, W. Xu, J. Jiang, F. Caruso, *Nat. Mater.* **2018**, 17, 1040; b)W. Li, Y. Zong, Q. Liu, Y. Sun, Z. Li, H. Wang, Z. Li, *Prog. Org. Coat.* **2020**, 147, 105776; c)W. Hujun, Z. Zhihui, W. Zuankai, L. Yunhong, C. Zhenquan, Z. Jie, L. Xiujuan, R. Luquan, *ACS Appl. Mater. Interfaces* **2019**, 11, 28478; d)A. Grigoryev, I. Tokarev, K. G. Kornev, I. Luzinov, S. Minko, *J. Am. Chem. Soc.* **2012**, 134, 12916; e)W. Wang, J. Salazar, H. Vahabi, A. Joshi-Imre, W. E. Voit, A. K. Kota, *Adv. Mater.* **2017**, 29, 1700295.
- [61] F. Bohn Holger, W. Federle, *Proc. Natl. Acad. Sci. USA* **2004**, 101, 14138.
- [62] a)T. S. Wong, S. H. Kang, S. K. Y. Tang, E. J. Smythe, B. D. Hatton, A. Grinthal, J. Aizenberg, *Nature* **2011**, 477, 443; b)A. Lafuma, D. Quéré, *EPL (Europhysics Letters)* **2011**, 96, 56001.
- [63] X. Li, J. Yang, K. Lv, P. Papadopoulos, J. Sun, D. Wang, Y. Zhao, L. Chen, D. Wang, Z. Wang, X. Deng, *National Science Review* **2021**, 8, nwaa153.
- [64] M. J. Kreder, D. Daniel, A. Tetreault, Z. Cao, B. Lemaire, J. V. I. Timonen, J. Aizenberg, *Physical Review X* **2018**, 8, 031053.
- [65] J. D. Smith, R. Dhiman, S. Anand, E. Reza-Garduno, R. E. Cohen, G. H. McKinley, K. K. Varanasi, *Soft Matter* **2013**, 9, 1772.
- [66] A. Keiser, L. Keiser, C. Clanet, D. Quéré, *Soft Matter* **2017**, 13, 6981.
- [67] E. Jenner, B. D'Urso, *Applied Physics Letters* **2013**, 103.
- [68] Z. Dong, M. F. Schumann, M. J. Hokkanen, B. Chang, A. Welle, Q. Zhou, R. H. A. Ras, Z. Xu, M. Wegener, P. A. Levkin, *Adv. Mater.* **2018**, 30, 1803890.
- [69] Y. Tan, J. Yang, Y. Li, X. Li, Q. Wu, Y. Fan, F. Yu, J. Cui, L. Chen, D. Wang, X. Deng, *Adv. Mater.* **2022**, 34, 2202167.
- [70] Y. Huang, B. B. Stogin, N. Sun, J. Wang, S. Yang, T.-S. Wong, *Adv. Mater.* **2017**, 29, 1604641.
- [71] G. Launay, M. S. Sadullah, G. McHale, R. Ledesma-Aguilar, H. Kusumaatmaja, G. G. Wells, *Scientific Reports* **2020**, 10, 14987.
- [72] a)J. W. Krumpfer, T. J. McCarthy, *Faraday Discuss.* **2010**, 146, 103; b)L. Wang, T. J. McCarthy, *Angew. Chem. Int. Ed.* **2016**, 55, 244; c)X. Zhao, B. Khatir, K. Mirshahidi, K. Yu, J. N. Kizhakkedathu, K. Golovin, *ACS Nano* **2021**, 15, 13559.

- [73] J. Wang, L. Wang, N. Sun, R. Tierney, H. Li, M. Corsetti, L. Williams, P. K. Wong, T.-S. Wong, *Nature Sustainability* **2019**, 2, 1097.
- [74] A. Papra, N. Gadegaard, N. B. Larsen, *Langmuir* **2001**, 17, 1457.
- [75] A. Y. Fadeev, T. J. McCarthy, *Langmuir* **1999**, 15, 3759.
- [76] M. Soltani, K. Golovin, *Adv. Funct. Mater.* **2022**, 32, 2107465.
- [77] a)H. J. Butt, R. Berger, W. Steffen, D. Vollmer, S. A. L. Weber, *Langmuir* **2018**, 34, 11292; b)Q. Xu, N. Zhu, H. Fang, X. Wang, R. D. Priestley, B. Zuo, *ACS Macro Lett.* **2021**, 10, 1; c)L. I. S. Mensink, J. H. Snoeijer, S. de Beer, *Macromolecules* **2019**, 52, 2015; d)M. Geoghegan, G. Krausch, *Progress in Polymer Science* **2003**, 28, 261.
- [78] R. Lhermerout, K. Davitt, *Colloids and Surfaces A: Physicochemical and Engineering Aspects* **2019**, 566, 148.
- [79] G. H. Fredrickson, A. Ajdari, L. Leibler, J. P. Carton, *Macromolecules* **1992**, 25, 2882.

Chapter 2. Selected publications

2.1 X. Zhou, et al. *Adv. Mater.*, 2022.

Fabrication of Stretchable Superamphiphobic Surfaces with Deformation-Induced Rearrangeable Structures

Xiaoteng Zhou,^{1,2} Jie Liu,^{1,2} Wendong Liu,¹ Werner Steffen,¹ and Hans-Jürgen Butt¹

¹Max Planck Institute for Polymer Research, Ackermannweg 10, 55128, Mainz, Germany.

²Key Laboratory of Green Printing, Beijing National Laboratory for Molecular Science, Institute of Chemistry, Chinese Academy of Sciences, Beijing 100190, PR China

Published in:

Advanced Materials

Reproduced with permission from *Advanced Materials* 2022, 34, 2107901. Copyright © 2022 The Authors. *Advanced Materials* published by Wiley-VCH GmbH.

Author Contribution:

Xiaoteng Zhou, Jie Liu, and Hans-Jürgen Butt designed and performed research. Xiaoteng Zhou, Jie Liu, and Wendong Liu did the surface preparation. Xiaoteng Zhou, Jie Liu, Wendong Liu, and Werner Steffen contributed new reagents/analytic tools. Xiaoteng Zhou, Jie Liu, and Hans-Jürgen Butt analyzed data. Xiaoteng Zhou, Jie Liu, Wendong Liu, Werner Steffen, and Hans-Jürgen Butt wrote the paper. All authors have approved the final version of this manuscript.

Fabrication of Stretchable Superamphiphobic Surfaces with Deformation-Induced Rearrangeable Structures

Xiaoteng Zhou, Jie Liu,* Wendong Liu, Werner Steffen, and Hans-Jürgen Butt

Stretchable superamphiphobic surfaces with a high deformation resistance are in demand to achieve liquid-repellent performance in flexible electronics, artificial skin, and textile dressings. However, it is challenging to make mechanically robust superamphiphobic coatings, which maintain their superliquid repellency in a highly stretched state. Here, a stretchable superamphiphobic surface is reported, on which the microstructures can rearrange during stretching to maintain a stable superamphiphobicity even under a high tensile strain. The surface is prepared by spray-coating silicone nanofilaments onto a prestretched substrate (e.g., *cis*-1,4-polyisoprene) with poly(dimethylsiloxane) (PDMS) layer as a binder. After subsequent fluorination, this surface keeps its superamphiphobicity to both water and *n*-hexadecane up to the tensile strain of at least 225%. The binding PDMS layer and rearrangeable structures maximize the deformation resistance of the surface during the stretching process. The superamphiphobicity and morphology of the surface are maintained even after 1000 stretch–release cycles. Taking advantage of the mentioned benefits, a liquid manipulation system is designed, which has the potential for fabricating reusable and low-cost platforms for biochemical detection and lab-on-a-chip systems.

1. Introduction

Liquid-repellent surfaces are of interest for basic research and industrial use in self-cleaning,^[1] antifouling,^[2] corrosion resistance,^[3] and droplet manipulation.^[4] To achieve superliquid-repellency, the liquid needs to be in the Cassie state, in which a layer of air is entrapped between the liquid and the substrate.^[5] For liquids with low surface tension (γ), the Cassie state with a static contact angle larger than 150° can be achieved on superamphiphobic surfaces with microscopic overhanging morphologies, sometimes called a re-entrant geometry.^[6] Surfaces such as silicone nanofilaments^[6c] or template candle soot^[6d] have been reported to achieve superamphiphobicity by having a sub-micrometer inward curved surface morphology. Although

we now profit from an improved understanding of the mechanisms of a superamphiphobic surface, a less complex method of preparation and a high mechanical stability of the surface are still two of the main challenges that have hindered its widespread adoption.^[7]

Recently, superliquid-repellent surfaces with deformation-resistant performance are becoming increasingly significant in various situations such as flexible electronics,^[8] artificial skin,^[9] textile dressings,^[10] and liquid manipulation.^[11] Currently existing superamphiphobic surfaces appear to lose their superliquid-repellency to nonpolar liquids under small deformation, in particular when being stretched.^[12] The breakup of the surface structures during stretching usually cause the low-surface-tension liquids on the surface transiting from the Cassie state to the Wenzel state (fully wetted) easily. Pan et al. reported an excellent textile which repels the wetting of liquid nitrogen with surface

tension of 8.8 mN m⁻¹, yet it loses the superoleophobicity when being stretched to 20%.^[12a] Even till now, there is no effective way proposed to solve this problem that the loss of superamphiphobicity due to stretching.

In this work, we fabricated a stretchable surface whose superamphiphobicity is maintained during stretching via construction of spontaneously rearrangeable microstructures, and which is fabricated by spray-coating silicone nanofilament (NF) on a pre-stretched elastic substrate. A single NF usually has a diameter of the order of 10 nm and can form on the overhanging structures due to its round, spaghetti-like shape.^[6c] After spray-coating process, the NFs together with their assembly lead to a re-entrant geometry from tens of nanometer to hundreds of micrometers providing the underlying structure for a superamphiphobic surface. Releasing the tension of the substrate after fabrication leads to relatively compacted structures. During the surface stretching process, we observed the rearrangement of these structures in situ. The rearrangement of the structures includes the breakup of the largest NF clusters and the movement of the structures with respect to each other due to surface stretching. Through monitoring the size and density of the structure, the reason why the surface remains its superamphiphobicity in a high strain was understood. This surface was further utilized to fabricate a programmable liquid manipulation system to achieve drop coalescences and synthesis of asymmetric hydrogels.

X. Zhou, J. Liu
Key Laboratory of Green Printing, Institute of Chemistry
Chinese Academy of Sciences
Beijing 100190, China

X. Zhou, J. Liu, W. Liu, W. Steffen, H.-J. Butt
Max Planck Institute for Polymer Research
Ackermannweg 10, 55128 Mainz, Germany
E-mail: liujie@mpip-mainz.mpg.de

 The ORCID identification number(s) for the author(s) of this article can be found under <https://doi.org/10.1002/adma.202107901>.

DOI: 10.1002/adma.202107901

2. Results and Discussion

Spray-coating is a simple and effective method to construct hierarchical micro/nanostructures, but using nanoparticles in spray-coating to prepare superamphiphobic surfaces is usually a complex process. Particles size, concentration, spray pressure, droplet size, and solvent all need to be optimized in order to obtain a re-entrant structure.^[10a,13] Silicone nanofilaments (NF) synthesized by cross-linking of hydrolyzed trichloromethylsilane (TCMS)^[14] can easily form sub-microscale re-entrant structures, which are one of the most effective superamphiphobic coatings with ultralow sliding angles of liquids.^[6c,15] However, direct growth of NF on the surface usually needs to be carried out under specific conditions including rinsing the surface in organic solvent or in vacuum. This significantly reduces the area that can be covered and the efficiency to modify the surface, thus limiting its widespread use.

To overcome the limits of NF direct growth and to reduce the complexity of the preparation, we use pre-prepared nanofilaments as the substitute of nanoparticles in spray-coating. Only a low spray pressure (27 kPa) is applied, as compared to the high spray pressure (150–300 kPa) that is normally used,^[8b,16] which further facilitates the process. A poly(dimethylsiloxane) (PDMS, Sylgard184) layer is used as the binder to fix the NF layer on the substrate.^[17] To achieve stretching stability of the superamphiphobicity, the pre-stretching of the substrate was carried out to ensure the surface to be covered by NF with a high density after spray-coating. The “pre-stretching” method of preparing stretching resistant superliquid-repellent surfaces was first proposed by Genzer et al.,^[18] based on which various kinds of surfaces such as tunable surface patterns,^[19] stretchable superhydrophobic surface,^[20] hierarchically wrinkled surface^[21] were developed. As a model substrate, a commercial *cis*-1,4-polyisoprene tape (Figure S1a,b, Supporting Information) was elongated to the tensile strain ε ($\varepsilon = (L - L_0)/L_0 \times 100\%$, in which L_0 is the original length of the relaxed surface and L is the stretched length) of 200% (Figure 1a). The solution of PDMS oligomers and curing agent (10:1) in n-hexane (4.2 wt%) was spray-coated on the stretched substrate (Figure S1c,d, Supporting Information). The thickness of the PDMS layer was $0.85 \pm 0.10 \mu\text{m}$ (Figure S2, Supporting Information). Then the NF dispersion (0.1 wt% in toluene) was spray-coated onto the PDMS layer immediately. After curing at 80 °C for 2 h, the sample was fluorinated with trichloro(1H,1H,2H,2H-heptadecafluorodecyl)silane) by chemical vapor deposition after activating the surface with oxygen plasma. The surface was always held in tension during the preparation. A permanent strain of 10.5% remained when releasing the surface to the relaxed state after pre-stretching to 200% (Figure S3, Supporting Information). We define the tensile strain of the relaxed surface after this permanent deformation as $\varepsilon_0 = 0\%$ for following tests. The permanent strain of the surface depends on the selected substrate, and might be improved by optimizing materials or preparation techniques.^[22]

The nanofilament-structured and stretchable superamphiphobic (NFSS) surface shows a hierarchical micro/nanostructure (Figure 1b,c). To clearly present the morphology and the composition of the surface, we further observed the

cross-section of the NFSS surface by SEM (Figure S4, Supporting Information). Comparing to the porous nanofilament structure on the top of the NF clusters, we observed a different morphology at a certain region close to the substrate. The nanofilament structure in this region is denser than that in the upper side. This dense layer is the binding layer composed of both nanofilament and cross-linked PDMS. The thickness is around $1.5 \pm 0.5 \mu\text{m}$, which is much lower than the thickness ($45 \pm 20 \mu\text{m}$) of the nanofilament layer. For the gaps existing on the substrate, the NF structure can only partially cover them. As the gaps are so small that extra nanofilaments cannot fill in them (Figure S5, Supporting Information).

As the NFSS surface is fabricated by keeping the substrate under tension, the NF microstructures become more compacted after the surface is released (Figure 1d). Thereby the NFSS surface at the relaxed state exhibits both advancing (Θ_{ACA}) and receding (Θ_{RCA}) contact angles of water and n-hexadecane that are larger than 150° (Figure S6, Supporting Information). In the preparation, we use pre-prepared nanofilaments as the substitute of nanoparticles in spray-coating. The NF dispersions for spray-coating were prepared when the air humidity changed from 20% to 40% (Figure S7, Supporting Information). At such humidity region, the superamphiphobic NFSS surface is easy to be reproduced. For comparison, the same process was also used to spray-coat SiO_2 particles on the stretchable substrate. After fluorination, the surface was only superhydrophobic, while the receding contact angle of n-hexadecane on such a surface is almost 0° (Figure S6, Supporting Information). Thus, spray-coating NFs rather than nanoparticles leads to a better liquid repellency and it means our method has obviously reduced the complexity of preparation of the stretchable superamphiphobic surface.

Drop impact experiments show the mechanical stability of the surface against droplet impalement in the relaxed state. Both water (Weber number $We = 7.1$; $We = \rho U_0^2 R / \gamma$, where ρ is the density, U_0 is the impacting velocity, R is the radius of the drop and γ is the liquid–air surface tension) and n-hexadecane ($We = 11.1$) bounce from the relaxed NFSS surface ($\varepsilon = 0\%$) with no retention (Figure 1e,f). The porous microstructure increases the impalement pressure of the surface and prevents the three-phase contact line from moving downward on the structure. Moreover, given a stable superamphiphobicity, both water and n-hexadecane sessile drops maintain spherical shapes on the stretched NFSS surface, even at a strain $\varepsilon \approx 200\%$ (Figure 1g).

The NFSS surface in the stretched state exhibits stable superliquid-repellent performance to both water and n-hexadecane (Figure 2a). To avoid the effects of the inhomogeneous tensile strength on the stretched NFSS surface,^[23] the advancing and receding contact angles (Θ_{ACA} and Θ_{RCA}) and the roll-off angles ($\alpha_{\text{toll-off}}$) of liquids were all measured in the middle area. The surface maintains high receding contact angles ($\Theta_{\text{RCA}} > 150^\circ$) for both water and n-hexadecane and low roll-off angles (10 μL water, $\alpha_{\text{toll-off}} \leq 1.2^\circ$ and 10 μL hexadecane, $\alpha_{\text{toll-off}} \leq 3.3^\circ$) up to $\varepsilon \leq 225\%$. At $\varepsilon = 250\%$, the NFSS surface was still superhydrophobic. However, both Θ_{ACA} and Θ_{RCA} of n-hexadecane are lower than 150° (Figure S8, Supporting Information). Nevertheless, 10 μL n-hexadecane drops still rolled off the surface at a low tilting angle of $3.4^\circ \pm 0.3^\circ$ when $\varepsilon \approx 250\%$. In contrast, if the NFSS surface is fabricated without pre-stretching, the

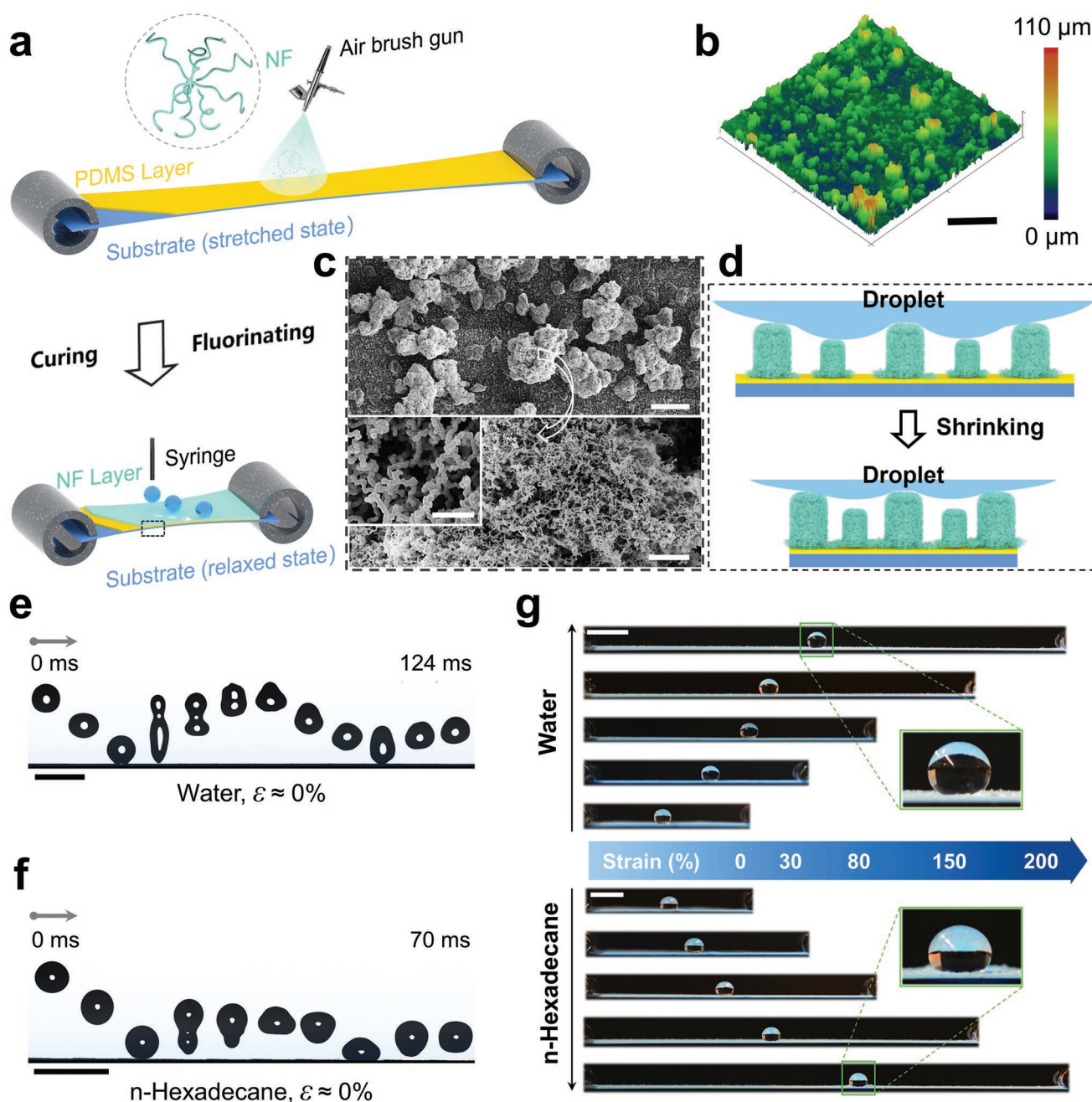


Figure 1. The nanofilament-structured and stretchable superamphiphobic surface. a) Schematic of the fabrication process of the nanofilament-structured and stretchable superamphiphobic (NFSS) surface. b) 3D images taken by Nanofocus μ surf 3D confocal surface measurement system of the NFSS surface at $\epsilon \approx 0\%$. Scale bar: 200 μm . c) Scanning electronic microscopy (SEM) images of the NFSS surface at $\epsilon \approx 0\%$. Scale bar: 50 μm (top), 2 μm (bottom), and 500 nm (inset). d) Schematic to illustrate the changing of microstructures on the NFSS surface after releasing the surface. e) Image series show the impact and bouncing of one 6 μL water drop on the NFSS surface ($\epsilon \approx 0\%$). Drop release height: 2 cm, scale bar: 5 mm. f) Image series show the impact and bouncing of one 3 μL n-hexadecane drop on the NFSS surface ($\epsilon \approx 0\%$). Drop release height: 2 cm, scale bar: 5 mm. g) Optical images of spherical shapes of 6 μL water and n-hexadecane drops on the NFSS surface under various strains ranging from 0 to 200%. Scale bar: 5 mm.

surface loses its superamphiphobicity at $\epsilon \geq 50\%$ (Figure S9, Supporting Information).

The accessibility of the surface superamphiphobicity during stretching is determined by the liquid entry or impalement pressure P_{LEP} .^[24] P_{LEP} represents the pressure required to force the transition from the nonwetting Cassie state to the fully

wetted Wenzel state. For a particular liquid, the microstructure size and spacing usually affect the value of P_{LEP} .^[25] Here, we use the average distance between adjacent edges of two NF clusters to illustrate the average structure spacing. When the NFSS surface is stretched, the separation and rearrangement of the structure allow slight changes in both the spacing and the

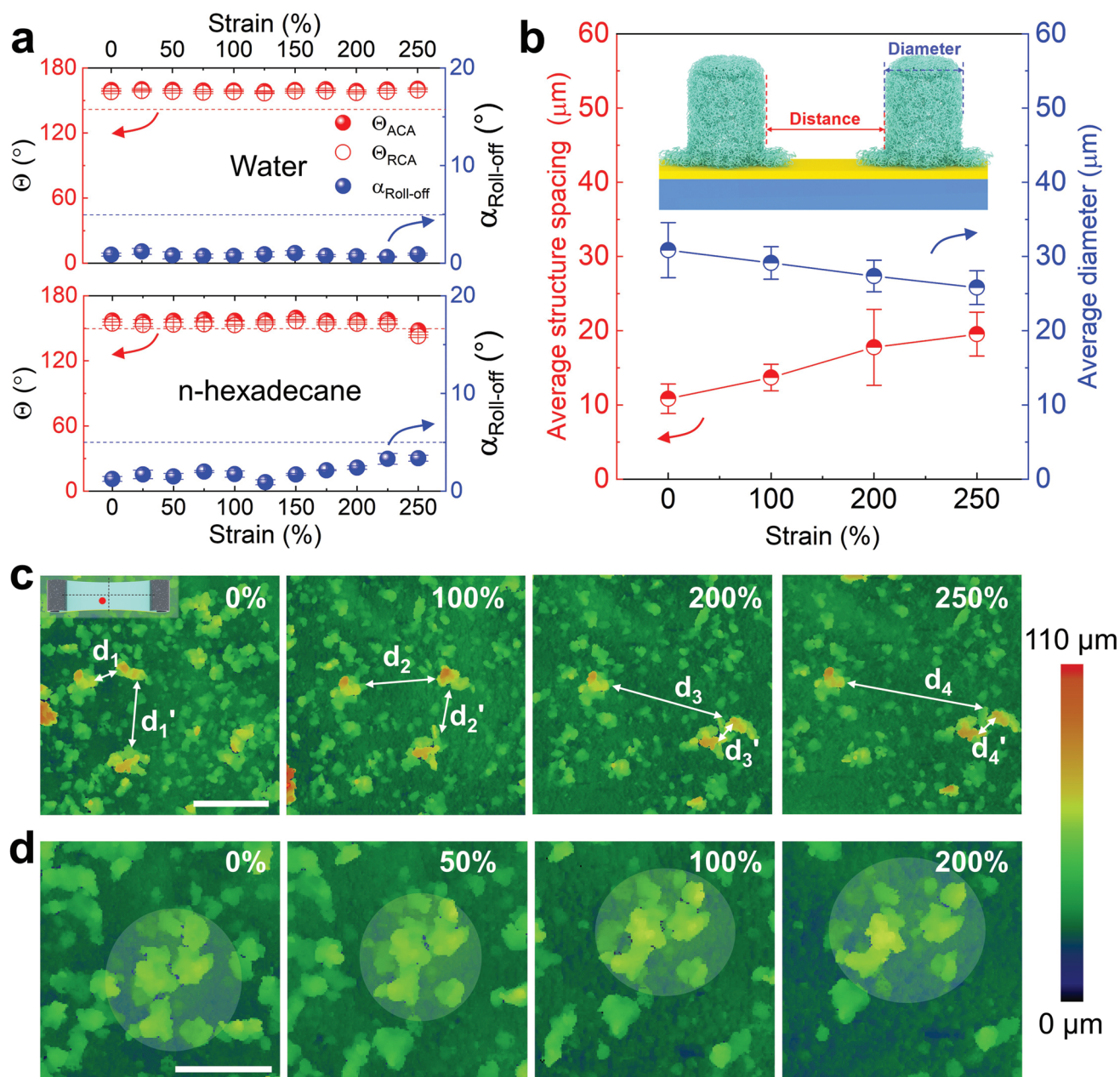


Figure 2. Superamphiphobicity of the stretched NFSS surface. a) Advancing and receding contact angles (Θ_{ACA} and Θ_{RCA}) and roll-off angles ($\alpha_{roll-off}$) of water and n-hexadecane on the NFSS surface with different tensile strains. Drop volume used in roll-off angle measurement was 10 μL . b) Evolution of the average structure spacing (distance between two NF clusters) and the average cluster size (diameter of the NF cluster) with the change of the surface tensile strain. c) Images using a Nanofocus μsurf 3D confocal surface measurement system illustrate variation of the morphologies when the NFSS surface was stretched. Strain: 0%, 100%, 200%, and 250%. The inset illustrates the measurement position (red dot) of the NFSS surface. Scale bar: 200 μm . d) Images show a rearranging process of the compacted microstructures after stretching from 0% to 200%. Scale bar: 200 μm . The color bar to the right of (c) and (d) illustrates the measured height.

cluster size (Figure 2b). As a result, the NFSS surface exhibits a quite stable superamphiphobicity resisting stretching because of the slightly changed liquid entry pressure.

A Nanofocus μsurf 3D confocal surface measurement system (Nanofocus AG, Oberhausen, Germany) was used to monitor the topography of the NFSS surface in situ during the stretching process (Figure 2c,d). The result shows that when the surface was stretched in one direction, and

the distances of NF clusters along the stretching direction increased (e.g., $d_1 < d_2 < d_3 < d_4$) with the strain increasing from 0% to 250%, while the distance of the clusters vertical to the stretching direction decreased (e.g., $d_1' > d_2' > d_3' > d_4'$) (Figure 2c). Some compacted structures split and rearrange at high strain (Figure 2d), and thereby the average diameter of the NF cluster decreases with the increasing tensile strain. In our view, the splitting of the structures into smaller clusters and the

rearrangement of them during the stretching process prevent breakup of the NF coating layer and the formation of big cracks to ensure that thus the surface maintains a stable superamphiphobicity. Finally, the surface loses its superamphiphobicity due to the low coverage of the NF cluster at a high tensile strain, in our case at $\epsilon \approx 250\%$.

A continuous and alternating stretch–release test was conducted to illustrate the mechanical durability of the NFSS surface (Figure S10a, Supporting Information). The surface

was repeatedly stretched along one direction with a speed of 0.4 cm s^{-1} to $\epsilon \approx 100\%$ and then released to $\epsilon \approx 0\%$ with the same speed again. During stretch–release cycles, both water and n-hexadecane rebounded and rolled off the surface (Figure S10b,c, Movie S1, Supporting Information). After 1000 cycles, both water and n-hexadecane still have a high receding contact angle ($\Theta_{\text{RCA}} > 150^\circ$) and low contact angle hysteresis (Figure 3a). Here, Θ_{ACA} and Θ_{RCA} were measured when the tensile strain of the NFSS surface was 0% and

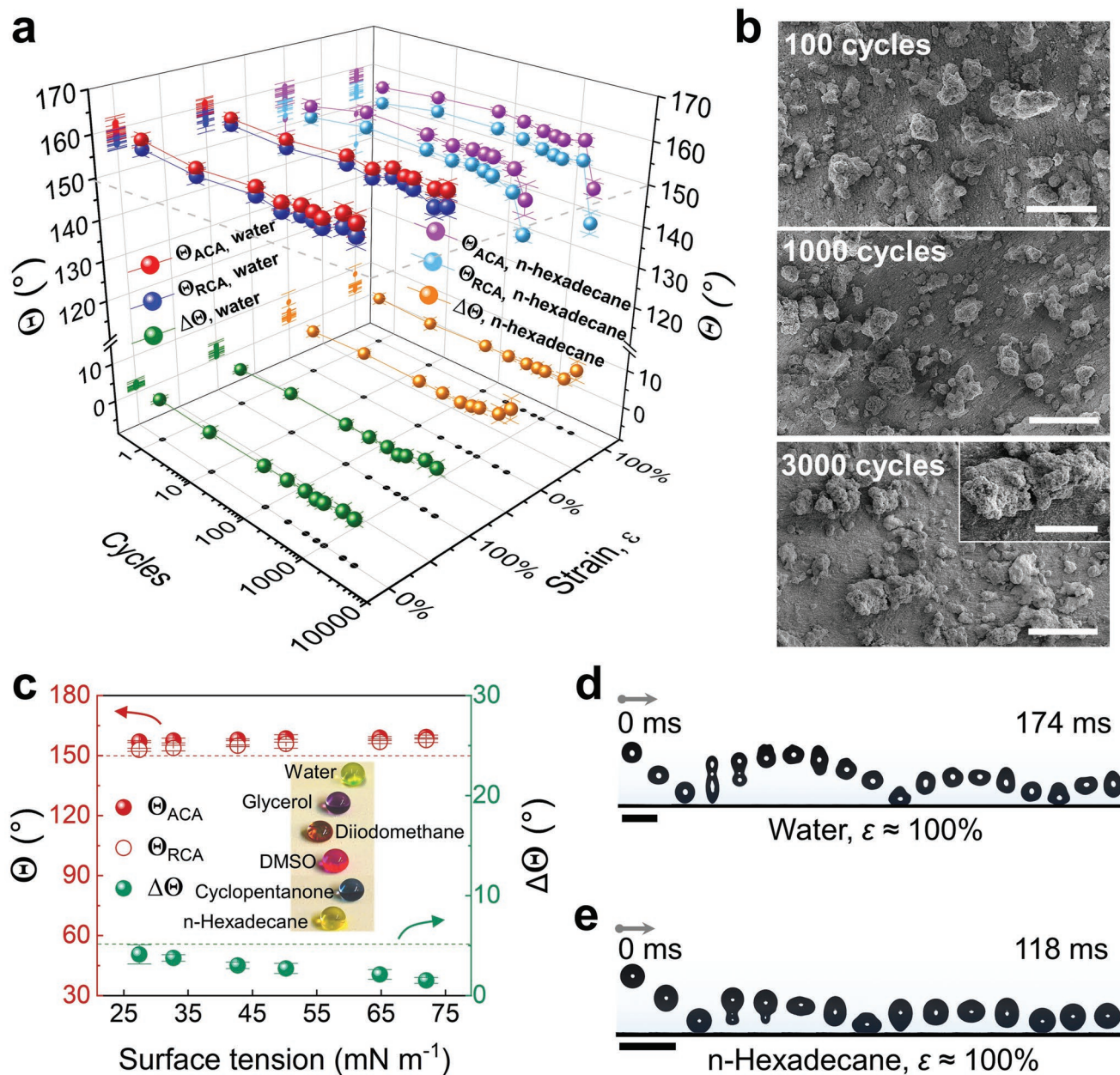


Figure 3. Durability of the NFSS surface after repeated stretching. a) Θ_{ACA} , Θ_{RCA} , and $\Delta\Theta$ of water and n-hexadecane on the NFSS surface after different stretch–release cycles. The contact angles were measured at $\epsilon \approx 0\%$ and $\epsilon \approx 100\%$, respectively. b) SEM images of the NFSS surface after 100, 1000, and 3000 stretch–release cycles. Scale bar: 100 and $50 \mu\text{m}$ (inset). c) Θ_{ACA} , Θ_{RCA} , and $\Delta\Theta$ of various liquids on the stretched NFSS surface ($\epsilon \approx 100\%$) after 1000 cycles of test. Inset shows the image of sessile drops ($10 \mu\text{L}$) of corresponding liquids on the stretched NFSS surface. d) Image series showing the impact and bouncing of a $6 \mu\text{L}$ water drop on the surface. Release height: 2 cm; scale bar: 5 mm; $\epsilon \approx 100\%$. e) Image series of the impact and bouncing of a $3 \mu\text{L}$ n-hexadecane drop on the surface. Drop release height: 2 cm; scale bar: 5 mm; $\epsilon \approx 100\%$.

100%, respectively. According to the SEM images (in random positions), the morphologies of the surface after 100 and 1000 stretch–release cycles seem not to change qualitatively (Figure 3b). After 1000 cycles, the NFSS surface is still superamphiphobic to a wide range of liquids even if it is stretched to 100% (Figure 3c). Besides water ($\gamma = 72.2 \text{ mN m}^{-1}$) and hexadecane ($\gamma = 27.4 \text{ mN m}^{-1}$), other liquids including glycerol ($\gamma = 64.8 \text{ mN m}^{-1}$), diiodomethane ($\gamma = 50.2 \text{ mN m}^{-1}$), dimethyl sulfoxide (DMSO, $\gamma = 42.7 \text{ mN m}^{-1}$) and cyclopentanol ($\gamma = 32.7 \text{ mN m}^{-1}$) all maintain spherical shapes on the surface with high receding contact angles ($\Theta_{\text{RCA}} > 150^\circ$) and low contact angle hysteresis ($\Delta\Theta = \Theta_{\text{ACA}} - \Theta_{\text{RCA}} < 5^\circ$). The surface can still withstand liquid drop impact after 1000 cycles of stretch–release test (Figure 3d,e). When ε was about 100%, both water ($We = 7.1$) and n-hexadecane ($We = 11.1$) drops rebounded at least three times. No retention caused by the impact was observed on the surfaces. This enduring repellency is likely due to the high coverage of the re-entrant structures. Although the surface is still superhydrophobic after 3000 stretch–release cycles, contact angle measurements show that the NFSS surface starts to lose the superoleophobicity. This is reflected by the receding contact angle of hexadecane on both relaxed and stretched surfaces being lower than 150° (Figure 3a). The rearrangement seems to be irreversible after 3000 cycles as big cracks happen on the cluster because of a failing regrouping process (Figure 3b, 3000 cycles inset).

Besides the stretch durability, we further characterized the mechanical stability of the NFSS surface against sand abrasion (Figure S11, Supporting Information). After testing for more than 5 min, the appearance of the coating changed little. Drops of water (30 μL) and n-hexadecane (20 μL) still easily slide off the surface with tilting angle of 45° . According to the contact angle measurements, the superamphiphobicity of the surface does not change with receding contact angles being larger than 150° when the surface is in both relaxed and stretched states after the test. A sandpaper abrasion test was further conducted, in which NFSS loaded with a weight of 30 g were placed face down on a sandpaper (Starcke P1000) (Figure S12, Supporting Information). The abrasion area was about 4.2 cm^2 and thereby the loaded pressure during the test was around 0.72 kPa which is within the range of the pressure values previously reported.^[26] We define a movement of 10 cm of the surface along the ruler as one abrasion cycle. After 10 cycles of abrasion, the surface still maintains its superhydrophobicity, but has lost its superoleophobicity. The receding contact angle of water remained around 155° , while the contact angle of n-hexadecane decreased from 153° to 140° . From the SEM images, we observed that after 10 cycles of abrasion, the NFSS morphology was destroyed into pieces and no obvious compact cluster could be observed anymore. Nevertheless, the remained structures fixed by the binding layer were still superhydrophobic. The NFSS surface with a good mechanical stability against both deformation and abrasion has potential real applications including artificial skin, flexible electronics and dressings.

By taking advantage of the repellency to low-surface-tension liquids and the stretchability of the NFSS surface, we developed a setup that can help achieve repetitive drops coalesce in a controlled way (Figure 4a). Two drops were placed side by side onto a stretched NFSS surface. When the surface was

gradually released, the decreasing distance between the drops finally led to the drops coming into contact and coalescing. Two water drops (15 μL) or two n-hexadecane drops (10 μL) can be placed on a stretched NFSS surface with $\varepsilon = 100\%$ (Figure S13, Movie S2 and S3, Supporting Information). Releasing the surface, drops coalesced and formed a merged spherical drop. After removing the merged drop, the drop coalescing process can repetitive occur if two new drops are placed on the NFSS surface which is stretched again. Since even small water drops have a low roll-off angle ($\alpha_{\text{roll-off}} \leq 1^\circ$), placing and keeping them on the surface is difficult. Therefore, poly(vinyl alcohol) hydrophilic dots (diameter: 0.5 mm) were introduced on the stretchable surface to fix the water drops (Figure S14a, Supporting Information). For hexadecane drops with their higher roll-off angle ($\alpha_{\text{roll-off}} \approx 3^\circ$), no hydrophilic dots were necessary (Figure S14b, Supporting Information).

A programmable coalescence of a sequence of drops was then orchestrated. We define programmable manipulation here as the coordinated approach to control the movement and the coalescing sequence of droplets. As an example, a trapezoidal arrangement of water drops was controlled to coalesce on the NFSS surface ($\varepsilon \approx 100\%$) (Figure 4b). When the surface was gradually released, the two middle drops coalesce. Subsequently, coalescence with the drops on the left and right hand side respectively of the merged drop occurs (Movie S4, Supporting Information). This is because the distance between the two drops in the middle was smaller than the distance between the drop on the outside and one of the middle drops. Furthermore, four n-hexadecane drops were linearly arranged on a stretched NFSS surface ($\varepsilon \approx 100\%$) in the stretching direction (Figure 4c). When the surface was released, these drops merged in a certain order from left to right (Movie S5, Supporting Information). This programmable drop manipulation method provides a possible one-by-one reaction process which could be described as $A+B \rightarrow A+B+C \rightarrow A+B+C+D$. It is noted that the NFSS surface based liquid manipulation system can be reusable due to its low adhesion to liquids.

The programmable coalescence of drops on this stretchable superamphiphobic surface was not limited to miscible liquids. One n-hexadecane and two water drops were placed on a stretched NFSS surface (Figure 4d) at appropriate distances. After coalescence, a merged drop with a dumbbell-like shape formed with an apparent interface between these two different drops. This led us to synthesize asymmetric or Janus particles by manipulating drop coalescence with two immiscible liquids. As an example, we synthesized asymmetric hydrogels with two reactive liquid drops (Figure 4e and Figure S15, Supporting Information). Drops of sodium alginate aqueous solution (0.05 wt%) and iron chloride (FeCl_3) aqueous solution (1.00 wt%) were placed on the NFSS surface. The reaction of sodium alginate and FeCl_3 started when the drops came into contact, after which the iron ions diffused rapidly in the alginate drop (Figure S15a, Supporting Information). As a result, the alginate drop became a hydrogel in a short time, while the FeCl_3 drops remained liquid. After removing the FeCl_3 drops, hydrogels with different shapes were prepared. We controlled the coalescence of two, three, and four drops. Depending on the numbers and relative position of the drops, hemispherical, cylinder-like, and triangular prism-like hydrogels have been

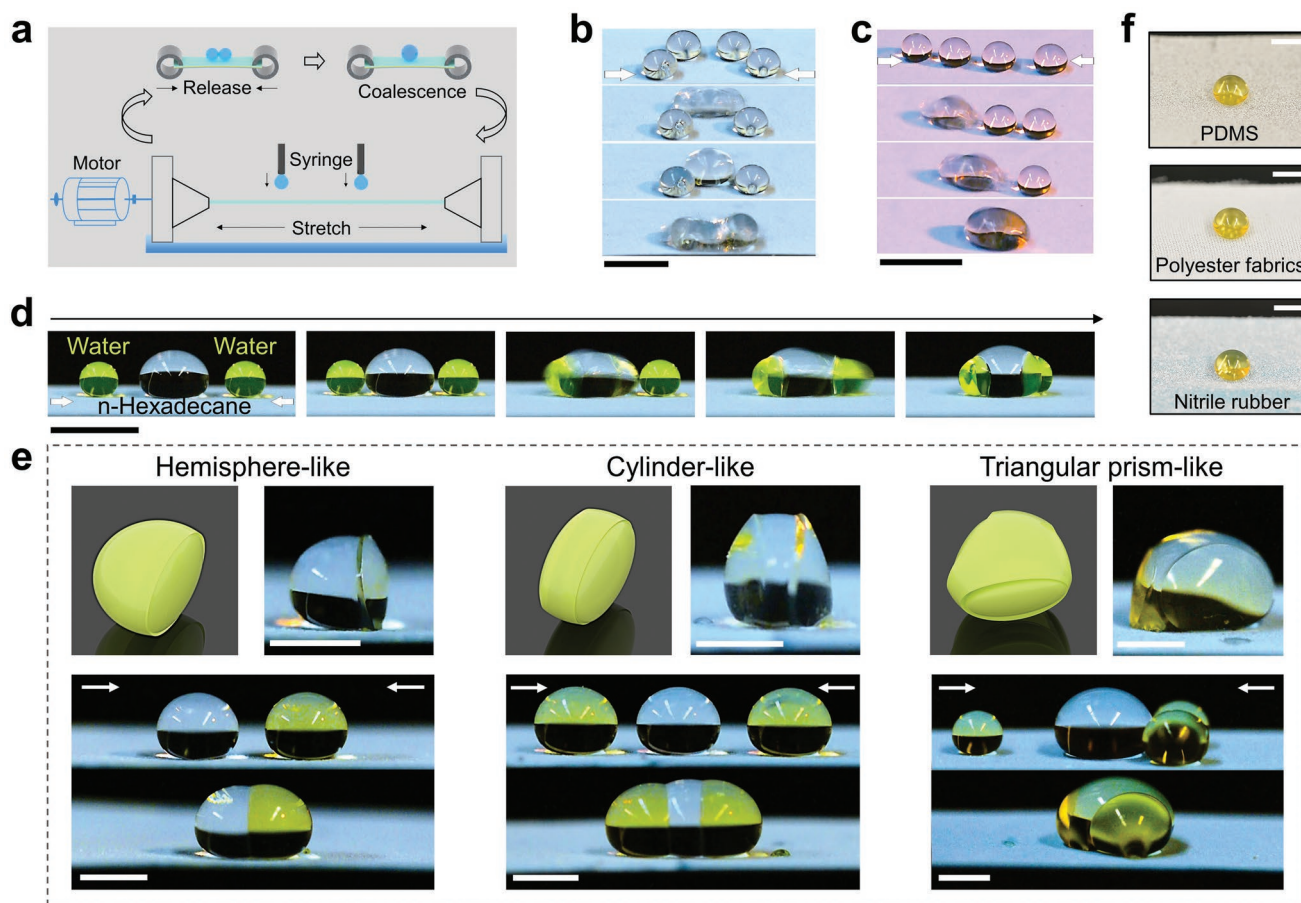


Figure 4. Programmable manipulation of drop coalescences and synthesis of asymmetric hydrogels. a) Schematic to show the setup with a controllable motor to manipulate drop coalescences repetitively. Drops on the surface coalesce via controlled release of the stretched NFSS surface. b) Programmable coalescence of four water drops (15 μL) with a trapezoidal arrangement. Scale bar: 5 mm. c) Programmable coalescence of four n-hexadecane drops (10 μL) with a linear arrangement. Scale bar: 5 mm. d) Coalescence of one n-hexadecane drop (colorless) and two water drops (light green) on the NFSS surface. Scale bar: 5 mm. e) Fabrication of asymmetric hydrogels with specific shapes. One alginate sodium aqueous solution drop (colorless) and different numbers (from left to right: 1, 2, and 3) of FeCl_3 aqueous solution drops (yellow) are used in the hydrogel fabrication process. The top schemes and images present three gels with distinct shapes (from left to right): hemispherical, cylinder-like, and triangular prism-like. The lower images show the coalescence of the drops. Volumes of the alginate drops (from left to right): 20, 20, and 30 μL . Volumes of the FeCl_3 drops (from left to right): 20, 20, and 15 μL . Scale bar: 2.5 mm. f) Images show spherical n-hexadecane drop (10 μL) on three different flexible substrates spray-coated with silicone nanofilaments. From top to bottom the substrates are PDMS, PE fabrics, and nitrile rubber. Scale bar: 2 mm.

fabricated. By adjusting the volume ratios of the sodium alginate drop to the FeCl_3 drop, it is possible to make more kinds of variably shaped hydrogels (Figure S15b,c, Supporting Information).

We further illustrate the fabrication of other three stretchable superamphiphobic surfaces with substrates of cross-linked poly(dimethylsiloxane) (PDMS), polyester (PE) fabrics, and nitrile rubber, in turn. All these surfaces were pre-stretched to their maximum strains during the coating process. Hexadecane drops show high static contact angles ($\Theta > 150^\circ$), low contact angle hysteresis ($\Delta\Theta < 5^\circ$) and roll-off angles ($\alpha_{\text{roll-off}} < 5^\circ$) on all these surfaces (Figure 4f and Figure S16, Supporting Information).

3. Conclusion

We have fabricated a stretchable superamphiphobic surface by spray-coating nanofilaments on a pre-stretched substrate. After

drying, annealing, and fluorination, the surfaces were able to withstand at least one thousand stretch–release cycles between $\varepsilon \approx 0\%$ and $\varepsilon \approx 100\%$ with no loss of superamphiphobicity. By using the stretching property, we were able to control the coalescence of miscible and immiscible liquid drops on the surface. We demonstrated that stretchable superamphiphobic surfaces can be applied to let drops react in a programmable manner. This outcome offers us the potential of using stretchable superamphiphobic surfaces to fabricate low-cost, reusable, and programmable droplet-based microfluidic systems which could help to study the reactions or interactions of multidrops.

4. Experimental Section

Preparation of Silicone Nanofilament Dispersion: 1.6 mL of trichloromethylsilane (TCMS, 99.0%, Merck Chemicals GmbH, Germany) was dissolved in 400 mL of toluene (water concentration is

about 150 ppm). The vessel with a narrow mouth was left open to the air (at about 30% relative humidity). Under stirring for more than 12 h, silicone nanofilaments were formed in toluene. The final dispersion was diluted to 0.1 wt% and sonicated for about 30 min.

Fabrication of a Nanofilament-Structured and Stretchable Superamphiphobic (NFSS) Surface: A commercial *cis*-1,4-polyisoprene tape (length: 3.8 cm, width: 1.8 cm, thickness: 0.5 mm, Melloc Handelsgesellschaft and Agentur GmbH, Germany) was used as the substrate. The tape was then stretched to a tensile strain of 200%. After treatment with oxygen plasma (Femto low-pressure plasma system, Diener electronic GmbH, Germany. Treating time is 5 min, the pressure is 0.4 mbar and the power is 200 W, 100%), the stretched substrate was spray-coated with a layer of PDMS oligomers (the ratio of monomer to curing agent is 10:1, Sylgard184, Dow Europe GmbH, Germany) by using a spray gun with a nozzle diameter of 0.2 mm at a spraying pressure of 27 kPa. The sprayed PDMS solution was prepared by dissolving 1.0 g of monomer and 0.1 g curing agent in 20 mL of *n*-hexane. Subsequently, the nanofilament dispersion was spray-coated onto the substrate by using the same spray gun and spraying pressure. Afterward, the surface held under tension was heated at 80 °C to cure the PDMS layer for 2 h. Then, the surface was cooled to room temperature and treated with oxygen plasma. The surface was further fluorinated with 5 μ L trichloro(1H,1H,2H,2H-heptadecafluorodecyl)silane (Alfa Aesar, 96%) by chemical vapor deposition in a vacuum desiccator (Pyrex Labware borosilicate vacuum desiccator, Fisher Scientific GmbH. The desiccator was evacuated to less than 100 mbar.) for 12 h. Finally, the tensile force was removed and the tape was allowed to relax.

Morphology Characterization: The samples were coated with a thin layer of platinum (7 nm) by a sputtering process, and then the samples were imaged by scanning electron microscopy (SEM, Hitachi SU8000). The *in situ* images of the morphologies of this surface with different tensile strains were characterized by a Nanofocus μ surf 3D confocal surface measurement system (Nanofocus AG, Oberhausen, Germany). The light of Nanofocus confocal system was focused through a multipinhole disk (MPD) and the objective lens onto the sample surface. The reflected light was detected by the camera to obtain confocal images. Each confocal image was a horizontal and nanometer-range-resolution slice through the topography of the sample. Capturing the images at different focal heights gave hundreds of confocal images which could be reconstructed an exact 3D height image of the sample by Gwyddion.^[27] For calculating the average structure spacing and average diameter, the microstructures were marked by circles with comparable size in the Nanofocus confocal images. The Feret diameter (*D*) of each cluster was obtained by measuring the diameter of the circles. The average structure spacing was measured according to the distance between the edges of the circles.

Wetting Properties: Advancing and receding contact angles as well as the roll-off angles of various liquids on the surfaces were measured by DataPhysics OCA 35 goniometer (DataPhysics Instruments). Each data point was the average of at least three individual measurements on the middle area of the surfaces. Impinging dynamics of water and *n*-hexadecane drops were recorded by a Photron Fastcam Mini UX100 high-speed camera (4000 fps) with a 2 \times lens.

Test of the Stretching Robustness: Two sides of a rectangular NFSS surface (length: 4.2 cm, width: 1.8 cm, thickness: 0.5 mm) were fixed and then moved by an electric motor in one direction. Alternatively control of the strain of the surface to be 100% and 0% by the motor. Water or *n*-hexadecane were dropped on the surface once during each stretch-release cycle, so that it could be checked if the surface still has a good superamphiphobicity. The dynamics were recorded by a Nikon D7100 digital camera (60 fps). After a certain number of stretch-release cycles, the contact angles of water and *n*-hexadecane were measured on the surface with strain of 0% and 100%, respectively.

Manipulation of Drop Coalescence: A rectangular NFSS surface (length: 4.2 cm, width: 1.8 cm, thickness: 0.5 mm) was fixed at two sides in the motor-controlled stretching setup. Drops were placed on a stretched NFSS surface (typical strain \approx 100%) with specific distances. Different drops with different components were used. When the surface was

released, drops coalesce in turn. The process was recorded by a Nikon D7100 digital camera (60 fps). For the synthesis of asymmetric hydrogel, drops of sodium alginate aqueous solution (0.05 wt%) and iron chloride (FeCl₃) aqueous solution (1.00 wt%) were placed on the NFSS surface.

Supporting Information

Supporting Information is available from the Wiley Online Library or from the author.

Acknowledgements

This project received funding from the European Research Council (ERC) under the European Union's Horizon 2020 research and innovation program (grant agreement No 883631, DYNAMO). The authors are also grateful for the financial support from the European Union's Horizon 2020 research and innovation program under grant agreement No 801229. X.Z. is sponsored by the China Scholarship Council (CSC). Helma Burg and Andreas Best are acknowledged for the technical support.

Conflict of Interest

The authors declare no conflict of interest.

Author Contributions

X.Z. and J.L. designed and performed research. X.Z., J.L., W.L., W.S., and H.-J.B. contributed new reagents/analytic tools. X.Z. and J.L. analyzed data. X.Z., J.L., W.L., W.S., and H.-J.B. wrote the paper. All authors have approved the final version of this manuscript.

Data Availability Statement

The data that support the findings of this study are available from the corresponding author upon reasonable request.

Keywords

deformation resistance, liquid manipulation, stretchable surfaces, superamphiphobicity, wetting

Received: October 2, 2021

Revised: December 21, 2021

Published online: January 31, 2022

[1] a) S. Wu, Y. Du, Y. Alsaïd, D. Wu, M. Hua, Y. Yan, B. Yao, Y. Ma, X. Zhu, X. He, *Proc. Natl. Acad. Sci. USA* **2020**, *117*, 11240; b) W. S. Y. Wong, T. P. Corrales, A. Naga, P. Baumli, A. Kaltbeitzel, M. Kappl, P. Papadopoulos, D. Vollmer, H.-J. Butt, *ACS Nano* **2020**, *14*, 3836.

[2] a) G. Luo, L. Wen, K. Yang, X. Li, S. Xu, P. Pi, X. Wen, *Chem. Eng. Sci.* **2020**, *383*, 123125; b) F. Geyer, M. D'Acunzi, C.-Y. Yang, M. Müller, P. Baumli, A. Kaltbeitzel, V. Mailänder, N. Encinas, D. Vollmer, H.-J. Butt, *Adv. Mater.* **2019**, *31*, 1801324.

- [3] a) S. Masoud Emarati, M. Mozammel, *Chem. Eng. Sci.* **2020**, 387, 124046; b) N. Valipour Motlagh, F. C. Birjandi, J. Sargolzaei, N. Shahtahmassebi, *Appl. Surf. Sci.* **2013**, 283, 636.
- [4] a) H. Han, J. S. Lee, H. Kim, S. Shin, J. Lee, J. Kim, X. Hou, S.-W. Cho, J. Seo, T. Lee, *ACS Nano* **2018**, 12, 932; b) Z. Cheng, H. Liu, H. Lai, Y. Du, K. Fu, C. Li, J. Yu, N. Zhang, K. Sun, *ACS Appl. Mater. Interfaces* **2015**, 7, 20410.
- [5] P. Papadopoulos, L. Mammen, X. Deng, D. Vollmer, H. J. Butt, *Proc. Natl. Acad. Sci. USA* **2013**, 110, 3254.
- [6] a) A. Tuteja, W. Choi, M. Ma, J. M. Mabry, S. A. Mazzella, G. C. Rutledge, G. H. McKinley, R. E. Cohen, *Science* **2007**, 318, 1618; b) E. M. Domingues, S. Arunachalam, J. Nauruzbayeva, H. Mishra, *Nat. Commun.* **2018**, 9, 3606; c) J. Zhang, S. Seeger, *Angew. Chem., Int. Ed.* **2011**, 50, 6652; d) X. Deng, L. Mammen, H.-J. Butt, D. Vollmer, *Science* **2012**, 335, 57.
- [7] a) D. Wang, Q. Sun, M. J. Hokkanen, C. Zhang, F.-Y. Lin, Q. Liu, S.-P. Zhu, T. Zhou, Q. Chang, B. He, Q. Zhou, L. Chen, Z. Wang, R. H. A. Ras, X. Deng, *Nature* **2020**, 582, 55; b) H. Bellanger, T. Darmanin, E. Taffin de Givenchy, F. Guittard, *Chem. Rev.* **2014**, 114, 2694; c) Z. Chu, S. Seeger, *Chem. Soc. Rev.* **2014**, 43, 2784; d) J. Yong, F. Chen, Q. Yang, J. Huo, X. Hou, *Chem. Soc. Rev.* **2017**, 46, 4168.
- [8] a) B. Choi, J. Lee, H. Han, J. Woo, K. Park, J. Seo, T. Lee, *ACS Appl. Mater. Interfaces* **2018**, 10, 36094; b) L. Li, Y. Bai, L. Li, S. Wang, T. Zhang, *Adv. Mater.* **2017**, 29, 1702517.
- [9] a) J. N. Wang, Y. Q. Liu, Y. L. Zhang, J. Feng, H. Wang, Y. H. Yu, H. B. Sun, *Adv. Funct. Mater.* **2018**, 28, 1800625; b) R. Shimizu, Y. Nonomura, *J. Oleo Sci.* **2018**, 67, 47.
- [10] a) L. Xiong, L. L. Kendrick, H. Heusser, J. C. Webb, B. J. Sparks, J. T. Goetz, W. Guo, C. M. Stafford, M. D. Blanton, S. Nazarenko, D. L. Patton, *ACS Appl. Mater. Interfaces* **2014**, 6, 10763; b) H. Zou, S. Lin, Y. Tu, F. Li, J. Hu, G. Liu, S. Hu, G. Yang, Z. Yu, *Adv. Mater. Interfaces* **2016**, 3, 1500693.
- [11] a) S. Y. W. William, L. Guanyu, T. Antonio, *Small* **2017**, 13, 1603688; b) J.-Y. Huang, Y.-K. Lai, F. Pan, L. Yang, H. Wang, K.-Q. Zhang, H. Fuchs, L.-F. Chi, *Small* **2014**, 10, 4865.
- [12] a) S. Pan, R. Guo, M. Björnalm, J. J. Richardson, L. Li, C. Peng, N. Bertleff-Zieschang, W. Xu, J. Jiang, F. Caruso, *Nat. Mater.* **2018**, 17, 1040; b) W. Li, Y. Zong, Q. Liu, Y. Sun, Z. Li, H. Wang, Z. Li, *Prog. Org. Coat.* **2020**, 147, 105776; c) W. Hujun, Z. Zhihui, W. Zuankai, L. Yunhong, C. Zhenquan, Z. Jie, L. Xiujuan, R. Luquan, *ACS Appl. Mater. Interfaces* **2019**, 11, 28478; d) A. Grigoryev, I. Tokarev, K. G. Kornev, I. Luzinov, S. Minko, *J. Am. Chem. Soc.* **2012**, 134, 12916; e) W. Wang, J. Salazar, H. Vahabi, A. Joshi-Imre, W. E. Voit, A. K. Kota, *Adv. Mater.* **2017**, 29, 1700295.
- [13] W. S. Y. Wong, G. Y. Liu, N. Nasiri, C. L. Hao, Z. K. Wang, A. Tricoli, *ACS Nano* **2017**, 11, 587.
- [14] a) A. Y. Fadeev, T. J. McCarthy, *Langmuir* **2000**, 16, 7268; b) C. P. Tripp, M. L. Hair, *Langmuir* **1995**, 11, 149; c) G. E. Maciel, M. J. Sullivan, D. W. Sendorf, *Macromolecules* **1981**, 14, 1607; d) K. A. Andrianov, T. V. Vasil'eva, N. M. Katashuk, T. V. Snigireva, B. I. D'Yachenko, *Polym. Sci. U.S.S.R.* **1976**, 18, 1457.
- [15] S. Liu, X. Zhang, S. Seeger, *ACS Appl. Mater. Interfaces* **2019**, 11, 44691.
- [16] a) W. Tao, L. Chang, J. Lvlu, H. Xia, W. Sheng, *ACS Appl. Mater. Interfaces* **2020**, 12, 49155; b) S. Dong, B. Li, J. Zhang, A. Wang, *Adv. Mater. Interfaces* **2018**, 5, 1701520.
- [17] a) Z. Li, M. Cao, P. Li, Y. Zhao, H. Bai, Y. Wu, L. Jiang, *Matter* **2019**, 1, 661; b) Z. Nie, E. Kumacheva, *Nat. Mater.* **2008**, 7, 277; c) B. Zdyrko, V. Klep, I. Luzinov, *Mater. Matters* **2008**, 3, 44.
- [18] a) J. Genzer, K. Efimenko, *Science* **2000**, 290, 2130; b) K. Efimenko, M. Rackaitis, E. Manias, A. Vaziri, L. Mahadevan, J. Genzer, *Nat. Mater.* **2005**, 4, 293.
- [19] C. Cao, H. F. Chan, J. Zang, K. W. Leong, X. Zhao, *Adv. Mater.* **2014**, 26, 1763.
- [20] J. Ju, X. Yao, X. Hou, Q. Liu, Y. S. Zhang, A. Khademhosseini, *J. Mater. Chem. A* **2017**, 5, 16273.
- [21] K. Efimenko, J. Finlay, M. E. Callow, J. A. Callow, J. Genzer, *ACS Appl. Mater. Interfaces* **2009**, 1, 1031.
- [22] a) Y. Ma, K.-I. Jang, L. Wang, H. N. Jung, J. W. Kwak, Y. Xue, H. Chen, Y. Yang, D. Shi, X. Feng, J. A. Rogers, Y. Huang, *Adv. Funct. Mater.* **2016**, 26, 5345; b) V. Tanrattanakul, N. Sungthong, P. Raksa, *Polym. Test.* **2008**, 27, 794.
- [23] J. Genzer, D. A. Fischer, K. Efimenko, *Adv. Mater.* **2003**, 15, 1545.
- [24] A. K. Kota, Y. Li, J. M. Mabry, A. Tuteja, *Adv. Mater.* **2012**, 24, 5838.
- [25] a) A. Tuteja, W. Choi, G. H. McKinley, R. E. Cohen, M. F. Rubner, *MRS Bull.* **2008**, 33, 752; b) S. S. Chhatre, W. Choi, A. Tuteja, *Langmuir* **2010**, 26, 4027.
- [26] a) H. Cho, D. Kim, C. Lee, W. Hwang, *Curr. Appl. Phys.* **2013**, 13, 762; b) M. Li, Y. Li, F. Xue, X. Jing, *Appl. Surf. Sci.* **2019**, 480, 738; c) J. Song, Y. Li, W. Xu, H. Liu, Y. Lu, *J. Colloid Interface Sci.* **2019**, 541, 86; d) P. Wang, B. Sun, T. Yao, M. Chen, X. Fan, H. Han, L. Li, C. Wang, *Chem. Eng. Sci.* **2017**, 326, 1066; e) L. Chen, X. Sun, J. Hang, L. Jin, D. Shang, L. Shi, *Adv. Mater. Interfaces* **2016**, 3, 1500718; f) P. Varshney, S. S. Mohapatra, *Tribol. Int.* **2018**, 123, 17; g) D. Zhang, L. Li, Y. Wu, B. Zhu, H. Song, *Appl. Surf. Sci.* **2019**, 473, 493; h) P. Wang, B. Sun, Y. Liang, H. Han, X. Fan, W. Wang, Z. Yang, *J. Mater. Chem. A* **2018**, 6, 10404; i) A. Davis, S. Surdo, G. Caputo, I. S. Bayer, A. Athanassiou, *ACS Appl. Mater. Interfaces* **2018**, 10, 2907.
- [27] D. Nečas, P. Klapetek, *Open Phys.* **2012**, 10, 181.

ADVANCED MATERIALS

Supporting Information

for *Adv. Mater.*, DOI: 10.1002/adma.202107901

Fabrication of Stretchable Superamphiphobic Surfaces
with Deformation-Induced Rearrangeable Structures

Xiaoteng Zhou, Jie Liu, Wendong Liu, Werner Steffen,
and Hans-Jürgen Butt*

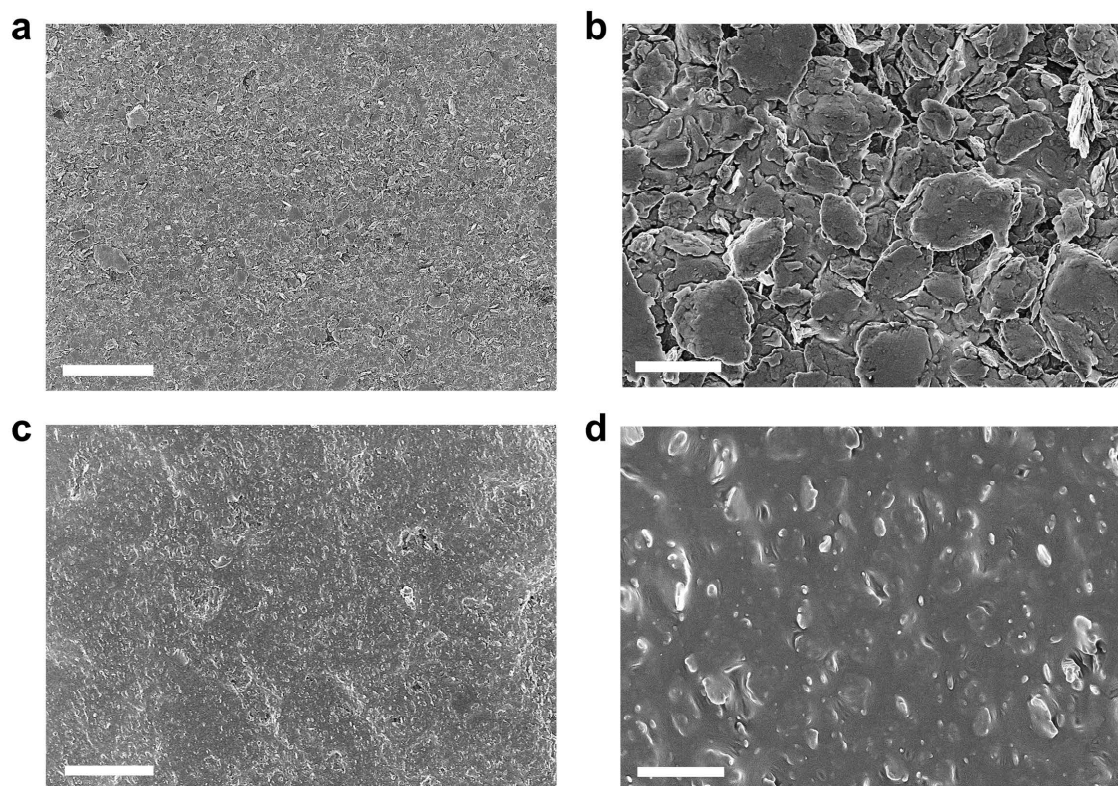


Figure S1. Surface morphology. a) and b) SEM images show the morphology of a uncoated cis-1,4-polyisoprene substrate at different magnifications. Scale bar: 50 μm (left) and 5 μm (right). c) and d) SEM images show the morphology of a cis 1,4-polyisoprene substrate coated with cross-linked PDMS layer at different magnifications. Scale bar: 50 μm (left) and 5 μm (right).

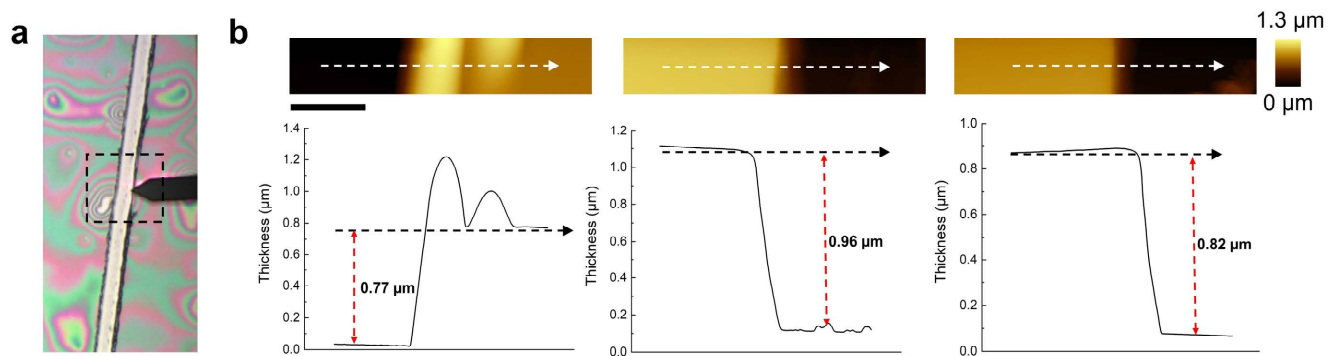


Figure S2. Measurement of the thickness of the PDMS binding layer. a) Optical image shows a scratch on the PDMS layer and the measuring position of atomic force microscopy (AFM). b) AFM results show the heights of the PDMS layer at three different positions. Scale bar: 2 μm.

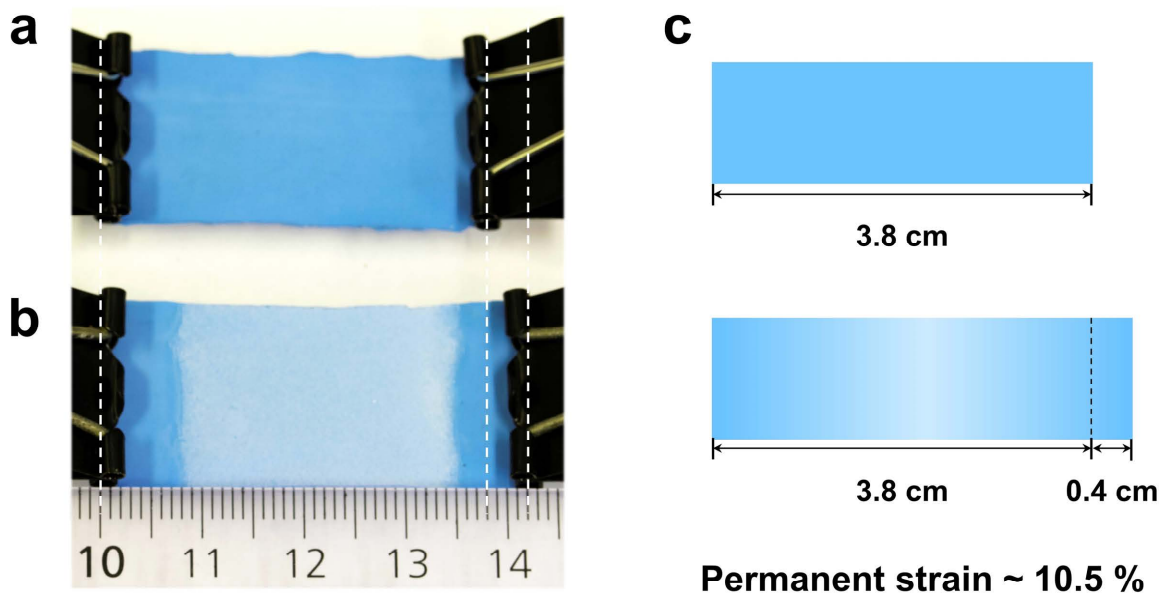


Figure S3. Remaining permanent strain of the nanofilament-structured and stretchable superamphiphobic (NFSS) surface after the preparation. a) Original cis-1,4-polyisoprene substrate. Tensile strain: 0%. b) The NFSS surface prepared from the substrate shown in a). White part in the middle shows the coating. Tensile strain: 0%. c) Scheme shows the length difference before and after treatment. The yield strain of the NFSS surface is around 10.5 %.

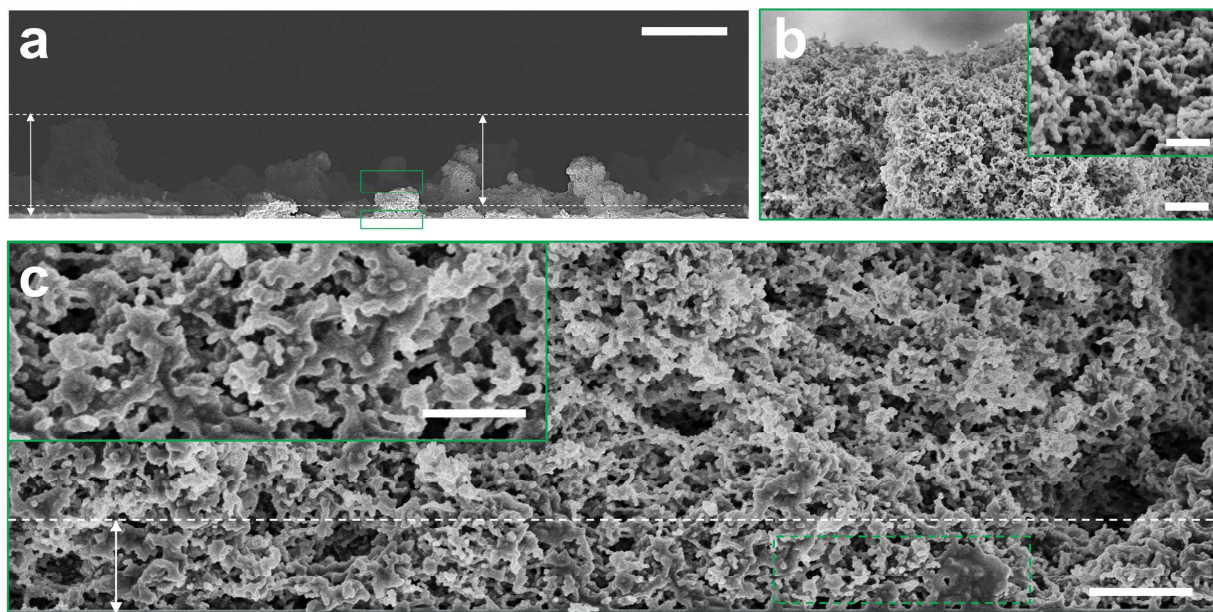


Figure S4. Characterization of the NFSS surface. a) SEM image shows the cross-section of the NFSS surface. Scale bar: 50 μm . b) SEM image shows the upper side of the NFSS surface. Scale bar: 1 μm . Inset shows the nanofilament structures. Scale bar: 500 nm. c) SEM image shows the bottom of the nanofilament cluster close to the NFSS surface. Scale bar: 2 μm . Inset shows the binding layer composed of the dense nanofilaments and cross-linked PDMS. Scale bar: 1 μm .

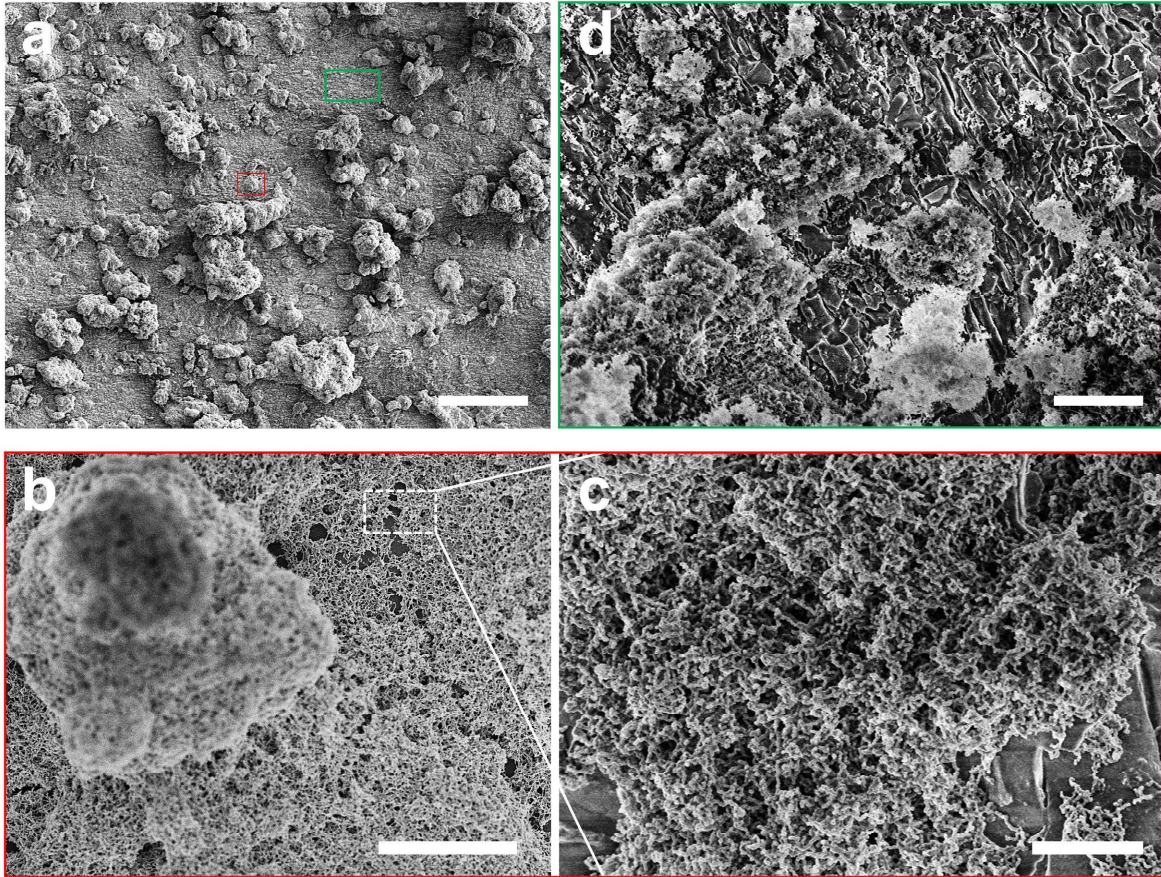


Figure S5. Morphology of the NFSS surface. a) The SEM images of the NFSS surface. Scale bar: 100 μm . b, c) The SEM images show the morphology of the red area (the feet of the cluster) marked in (a) at high magnification. Scale bar: 10 μm , 1 μm . d) The SEM image shows the morphology of the green area (the gap far away from the cluster) marked in (a) at high magnification. Scale bar: 2 μm .

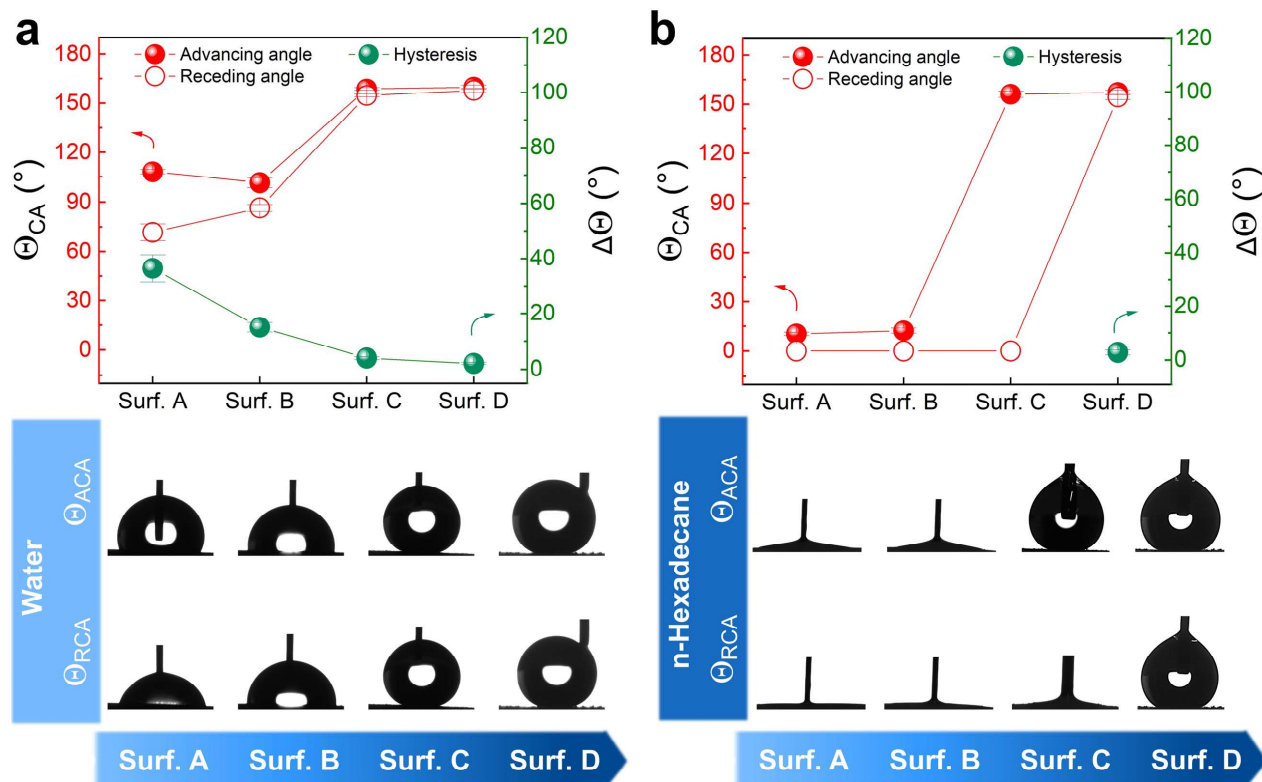


Figure S6. Dynamic contact angles of liquids on the stretchable surfaces when tensile strain $\varepsilon \approx 0\%$. Advancing and receding contact angle, and contact angle hysteresis (Θ_{ACA} , Θ_{RCA} and $\Delta\Theta$) of a) water and b) n-hexadecane were measured on four different stretchable surfaces. Tensile strain: 0 %. **Surf. A:** cis-1,4-polyisoprene substrate. **Surf. B:** cis-1,4-polyisoprene substrate with a cross-linked PDMS layer. **Surf. C:** cis 1,4-polyisoprene substrate spray-coated with silicon nanoparticles (diameter: 7 nm). **Surf. D:** the NFSS surface.

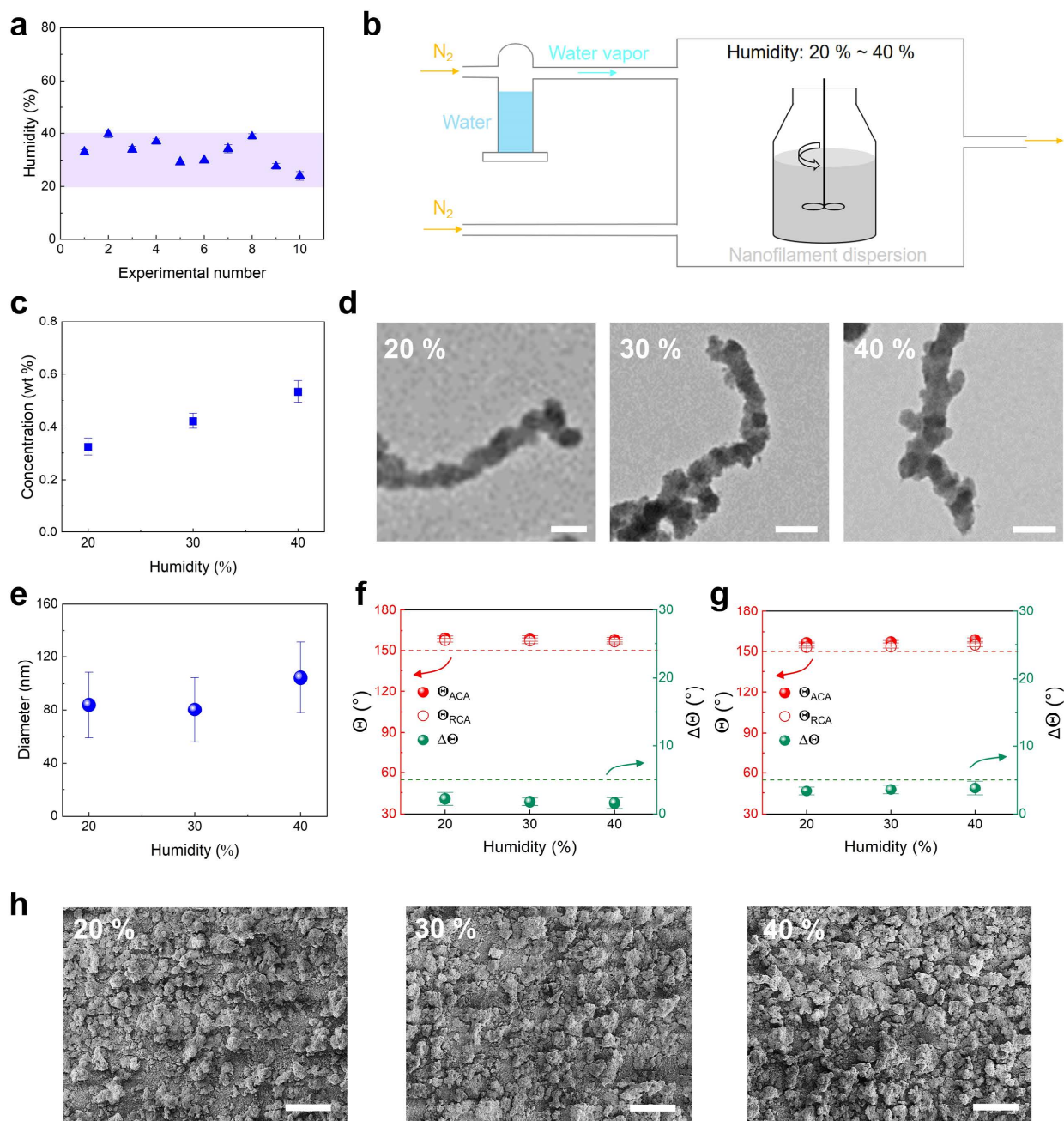


Figure S7. Influence of relative humidity on the reproducibility of NFSS surface. a) The values of the relative humidity in previous 10 experiments. b) The scheme to show the setup which is used to control the humidity when preparing the nanofilament dispersion. c) The concentration of the nanofilament dispersion when prepared in different humidity. The relative humidity was controlled to be 20%, 30%, and 40%. d) TEM (transmission electron microscopy) images of

nanofilament prepared in different humidity. e) The statistic value of the diameter of the silicone nanofilament prepared in different relative humidity. f) Θ_{ACA} , Θ_{RCA} and $\Delta\Theta$ of water on the NFSS surfaces ($\varepsilon = 200\%$) fabricated by nanofilament dispersions prepared at humidity of 20%, 30%, and 40%, in turn. g) Θ_{ACA} , Θ_{RCA} and $\Delta\Theta$ of n-hexadecane on the NFSS surfaces ($\varepsilon = 200\%$) fabricated by nanofilament dispersions prepared at humidity of 20%, 30%, and 40%, in turn. h) The SEM image to show the morphology of the NFSS surfaces fabricated by nanofilament dispersion prepared at different humidity.

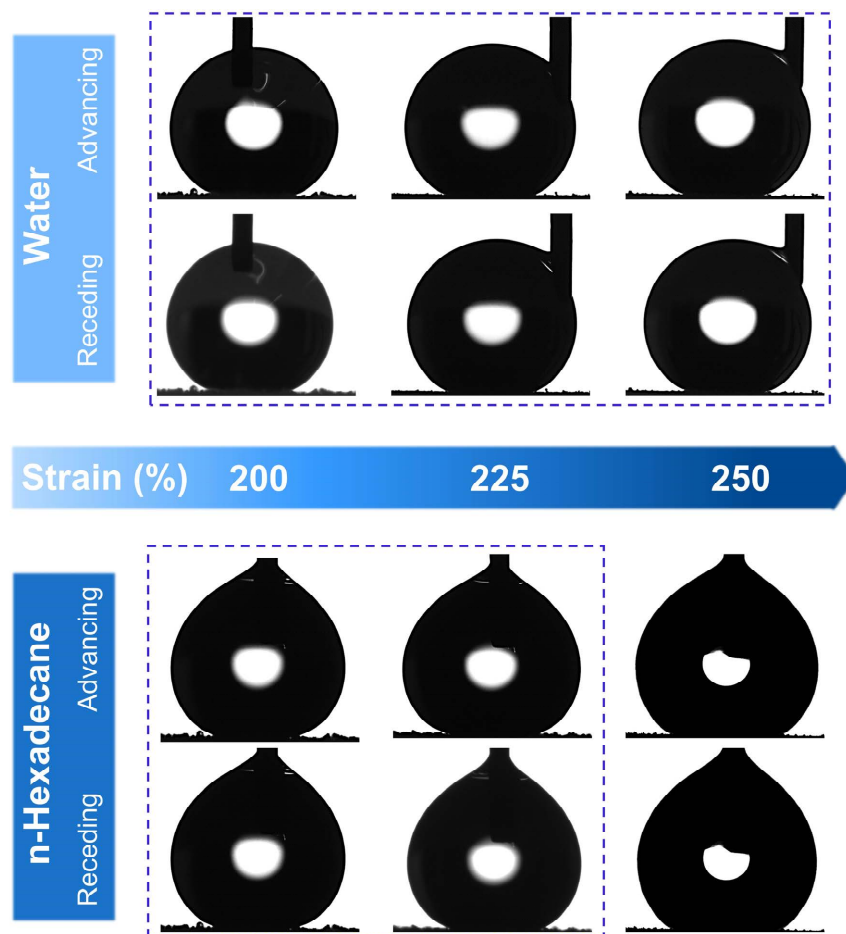


Figure S8. Optical images show the shapes of water and n-hexadecane drops during the advancing and receding of three-phase contact line on the NFSS surface. Volume: 10 μ L. Tensile strain \geq 200 %.

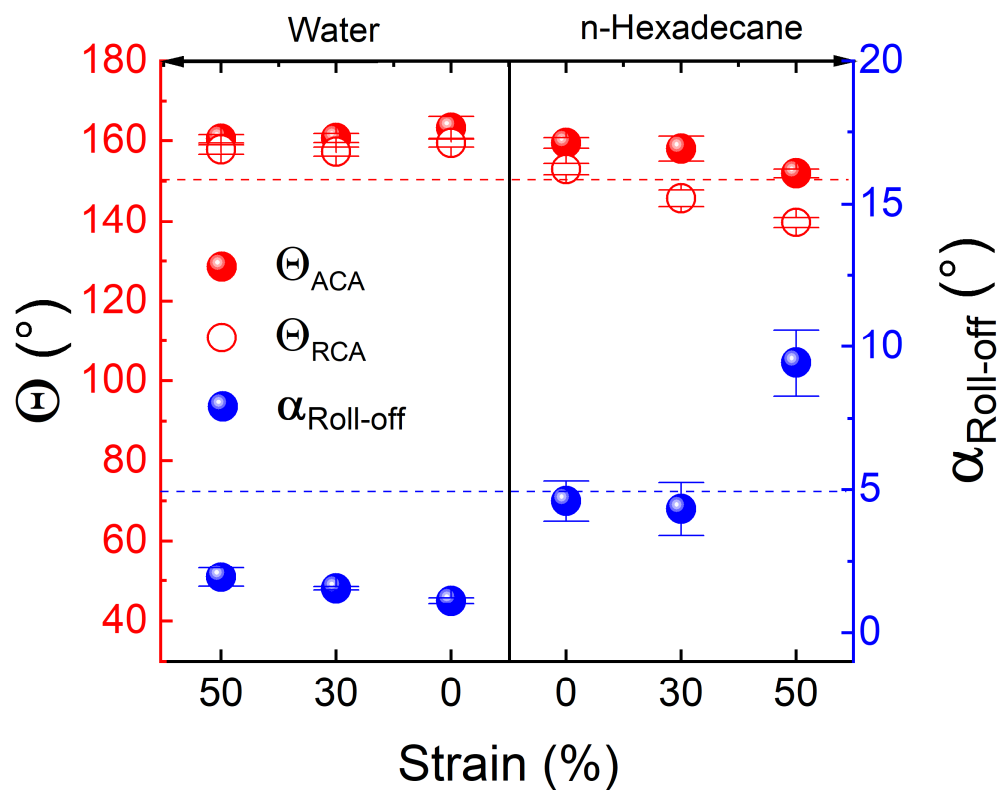


Figure S9. Advancing and receding contact angles (Θ_{ACA} and Θ_{RCA}) and roll-off angles ($\alpha_{roll-off}$) of water and n-hexadecane on the stretched NFSS surface which is prepared without pre-stretching of substrate. The tensile strains are 0%, 30% and 50%, in turn. Drop volume used in roll-off angle measurement was 10 μL .

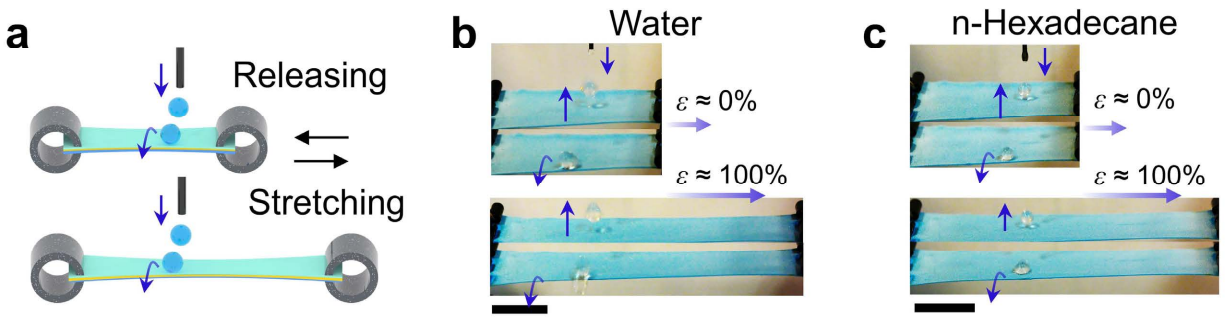


Figure S10. The stretch-release test. a) Schematic to illustrate a stretch-release test of the NFSS surface. Liquid drops were dropped intermittently during the test. b) Water and c) n-hexadecane drops impact and rebound rapidly from the surface during the stretch-release test with strain

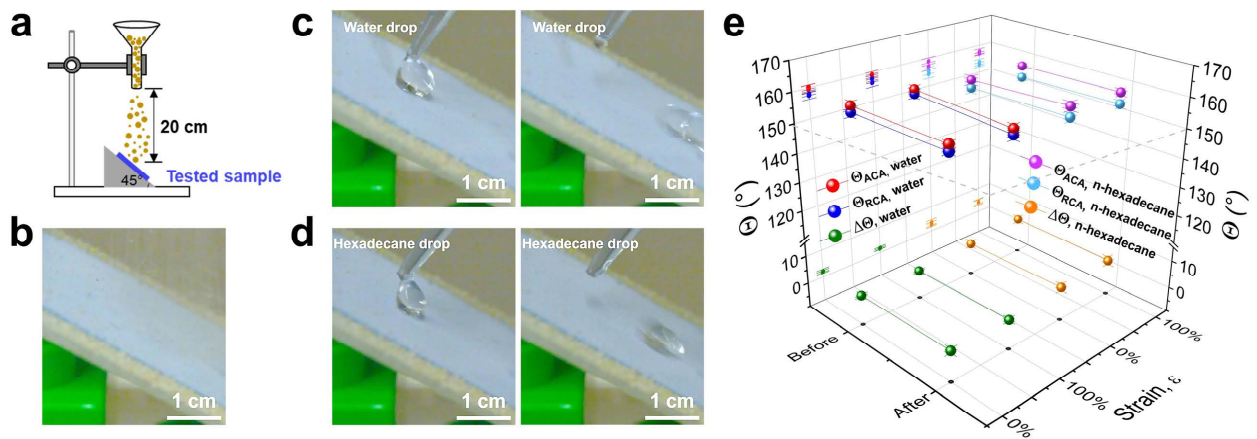


Figure S11. Sand abrasion test. a) The scheme showing the sand abrasion test. b) The appearance of the NFSS surface during the sand abrasion test. c) Images show sliding of water drop (volume: 30 μ L) on the surface after 5 min sand abrasion test. Tilted angle: 45°. d) Images show sliding of n-Hexadecane drop (volume: 20 μ L) on the surface after 5 min sand abrasion test. Tilted angle: 45°. e) Θ_{ACA} , Θ_{RCA} and $\Delta\Theta$ of water and n-hexadecane on the relaxed ($\epsilon = 0\%$) and stretched ($\epsilon = 100\%$) NFSS surface before and after 5 min sand abrasion test.

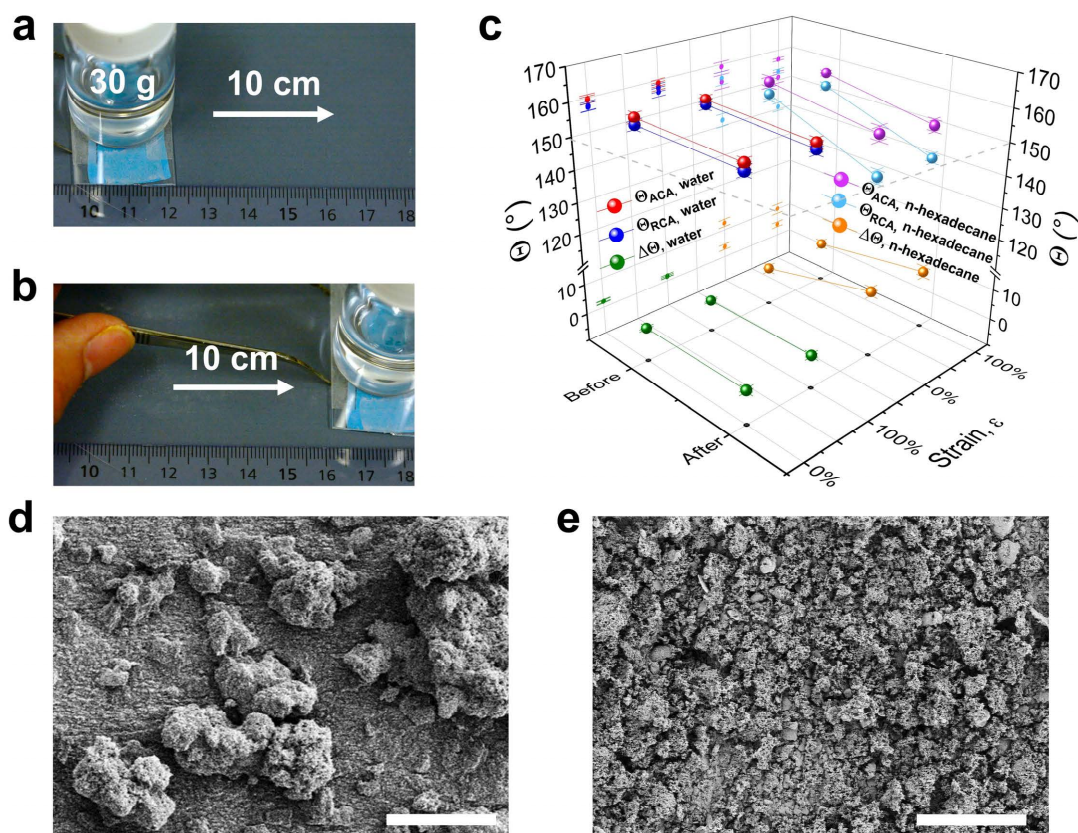


Figure S12. Sandpaper abrasion test. a, b) One cycle of the sandpaper abrasion test. c) Θ_{ACA} , Θ_{RCA} and $\Delta\Theta$ of water and n-hexadecane on the relaxed ($\varepsilon = 0\%$) and stretched ($\varepsilon = 100\%$) NFSS surface before and after 10 cycles of sand abrasion test. d) The SEM image to show the morphology of the NFSS surface before sandpaper abrasion test. Scale bar: 10 μm . e) The SEM image to show the morphology of the NFSS surface after 10 cycles of sandpaper abrasion test. Scale bar: 10 μm

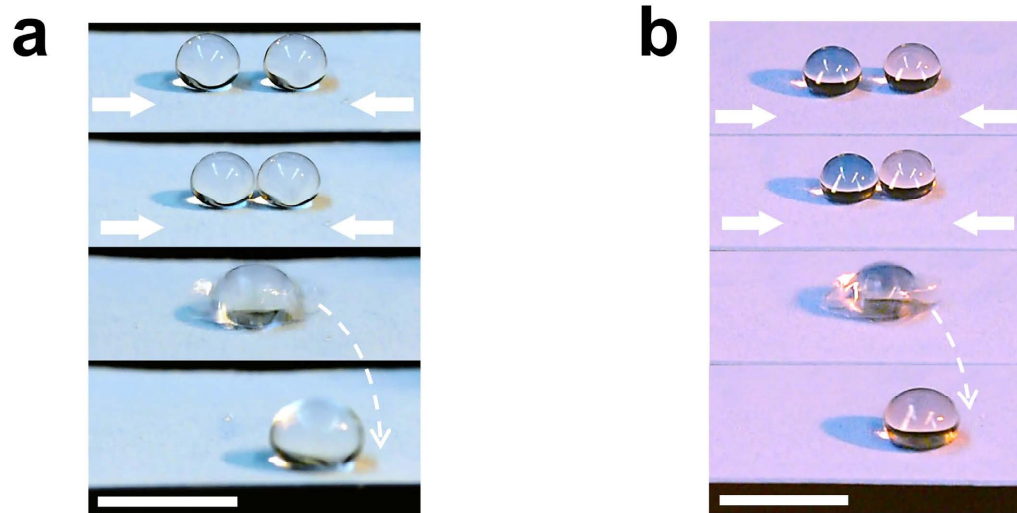


Figure S13. Coalescence of a) two water drops (15 μL) and b) two n-hexadecane drops (10 μL) on the NFSS surface. Scale bar: 5 mm.

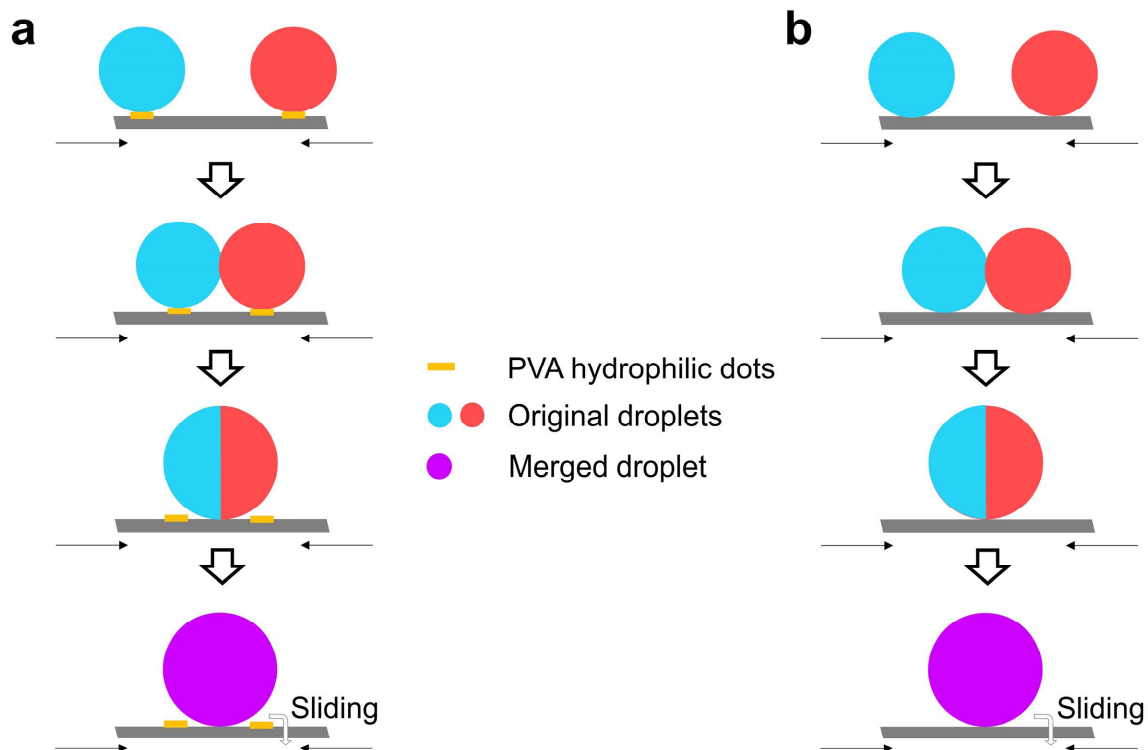


Figure S14. Schemes show the remote control of liquid drop coalescence by releasing the stretched NFSS surface. a) Coalescence of water drops. Since the ultra-low adhesion of the stretched NFSS surface to water, hydrophilic polyvinyl alcohol (PVA) dots are introduced on the surface to control the position of water drops. b) Coalescence of n-hexadecane drops. Each color represents a certain drop with specific component.

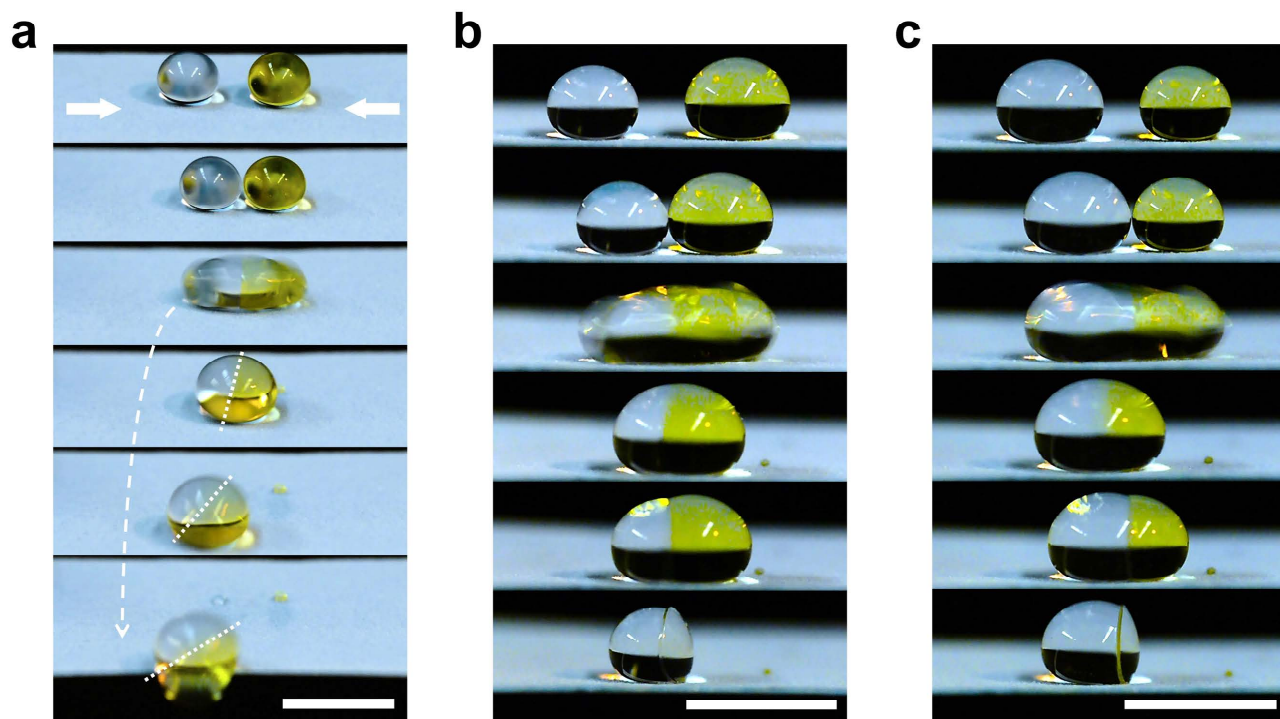


Figure S15. Synthesis of asymmetric hydrogels on the NFSS surface. a) One droplet (colorless, 15 μL) of alginate sodium aqueous solution and one droplet (yellow, 15 μL) of FeCl_3 aqueous solution merge and slide off the NFSS surface. White dot lines show the interface of two phases after merging. Yellow phase of the drop first rolling off the surface illustrates that the reaction of sodium alginate and FeCl_3 has happened. Scale bar: 5 mm. b) and c) Image series show the merging process of alginate sodium and FeCl_3 water aqueous droplets. The shape and size of the hydrogel can be controlled by the relative volume of the two drops. In b), volumes of the alginate sodium and FeCl_3 droplets are 20 μL and 30 μL , respectively. In c), volumes of the alginate sodium and FeCl_3 droplets are 30 μL and 20 μL , respectively. Scale bar: 5 mm.

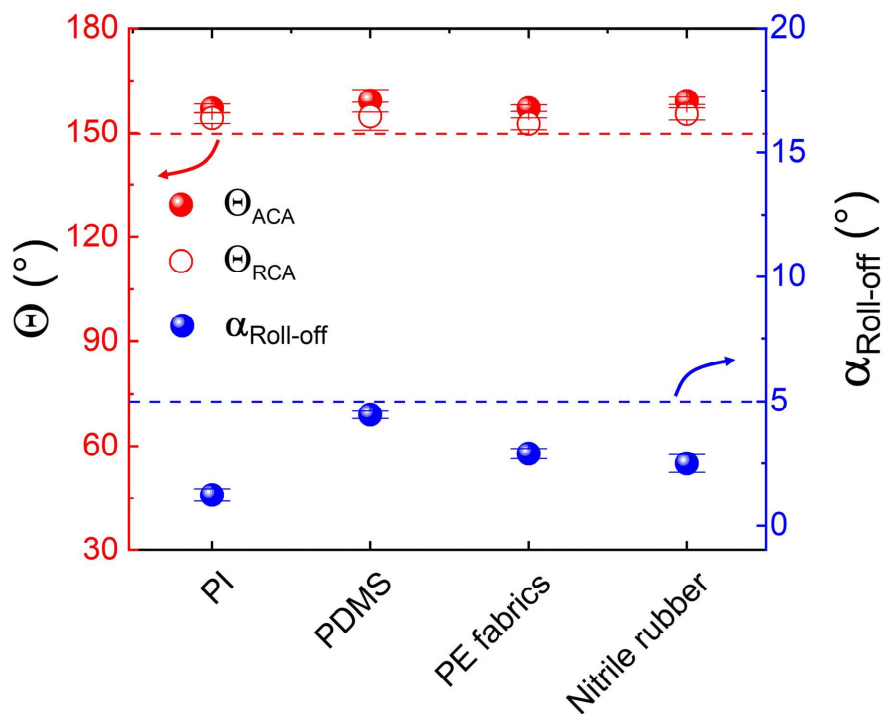


Figure S16. Advancing and receding contact angles (Θ_{ACA} and Θ_{RCA}) and roll-off angles ($\alpha_{roll-off}$) of n-hexadecane on the different coated substrates including cis-1,4-polyisoprene (PI), polydimethylsiloxane (PDMS), polyester (PE) fabrics and nitrile rubber when they are relaxed. All the substrates were spray-coated with NF by using our method. Drop volume used in roll-off angle measurement was 10 μ L.

Supplemental Movies:

Movie S1. The resistance of the NFSS surface to the impacting of water and n-hexadecane drops. Water (15 μL) and n-hexadecane (10 μL) drops releases from the syringe needle (diameter: 0.9 mm) and then slides on the NFSS surface during a stretch-release test. The release heights of drops are more than 1.5 cm. Scale bar: 1 cm.

Movie S2. Remotely controlling the coalescence of two n-hexadecane (10 μL) drops by releasing a stretched NFSS surface. Scale bar: 5 mm.

Movie S3. Remotely controlling the coalescence of two water (15 μL) drops by releasing a stretched NFSS surface. Scale bar: 5 mm.

Movie S4. Programmable controlling coalescence of four water (15 μL) drops by releasing a stretched NFSS surface. Scale bar: 5 mm.

Movie S5. Programmable controlling coalescence of four n-hexadecane (10 μL) drops by releasing a stretched NFSS surface. Scale bar: 5 mm.

2.2 X. Zhou et al. *Droplet*, 2022.

Chemically robust superhydrophobic surfaces with a self-replenish nano-scale liquid coating

Xiaoteng Zhou,¹ Pranav Sudersan,¹ Diego Diaz,¹ Benjamin Leibauer,¹ Chirag Hinduja,¹ Darvish Fahimeh,¹ Pravash Bista,¹ Lukas Hauer,¹ Manfred Wagner,¹ Werner Steffen,¹ Jie Liu,^{1,2,3} Michael Kappl,¹ Hans-Jürgen Butt¹

¹Max Planck Institute for Polymer Research, Ackermannweg 10, 55128, Mainz, Germany.

²Key Laboratory of Green Printing, Beijing National Laboratory for Molecular Science, Institute of Chemistry, Chinese Academy of Sciences, Beijing 100190, PR China

³School of Chemical Sciences, University of Chinese Academy of Sciences, Beijing 100190, PR China

Published in:

Droplet

Reproduced with permission from *Droplet*. 2023, e103. Copyright © 2023 The Authors. Published by John Wiley & Sons Australia, Ltd.

Author Contribution:

Xiaoteng Zhou, Jie Liu, Michael Kappl and Hans-Jürgen Butt designed the experiment. Xiaoteng Zhou, Pranav Sudersan and Michael Kappl did the AFM measurement. Xiaoteng Zhou and Diego Diaz performed the drop impact experiment. Xiaoteng Zhou and Darvish Fahimeh did the stability test after plasma treatment. Xiaoteng Zhou, Benjamin Leibauer and Manfred Wagner did the NMR measurement. Xiaoteng Zhou and Pravash Bista did the charge measurement. Xiaoteng Zhou and Lukas Hauer did the icing and melting experiment. Xiaoteng Zhou and Hans-Jürgen Butt perform the surface tension measurement. Xiaoteng Zhou and Chirag Hinduja did the DAFI measurement. All authors wrote the paper and have approved the final version of this manuscript.

Chemically robust superhydrophobic surfaces with a self-replenishing nanoscale liquid coating

Xiaoteng Zhou¹ | Pranav Sudersan¹  | Diego Diaz¹ | Benjamin Leibauer¹ | Chirag Hinduja¹ | Darvish Fahimeh¹ | Pravash Bista¹ | Lukas Hauer¹ | Manfred Wagner¹ | Werner Steffen¹ | Jie Liu^{1,2,3} | Michael Kappl¹ | Hans-Jürgen Butt¹ 

¹Max Planck Institute for Polymer Research, Mainz, Germany

²Key Laboratory of Green Printing, Beijing National Laboratory for Molecular Science, Institute of Chemistry, Chinese Academy of Sciences, Beijing, People's Republic of China

³School of Chemical Sciences, University of Chinese Academy of Sciences, Beijing, People's Republic of China

Correspondence

Jie Liu, Michael Kappl, and Hans-Jürgen Butt, Max Planck Institute for Polymer Research, Ackermannweg 10, 55128 Mainz, Germany. Email: liujie123@iccas.ac.cn, kappl@mpip-mainz.mpg.de and butt@mpip-mainz.mpg.de

Funding information

European Research Council (ERC) under the European Union's Horizon 2020 research and innovation program, Grant/Award Numbers: 883631, DYNAMO; German Research Society via the CRC 1194, Grant/Award Numbers: 265191195, C07N

Abstract

Due to poor chemical robustness, superhydrophobic surfaces become susceptible to failure, especially in a highly oxidative environment. To ensure the long-term efficacy of these surfaces, a more stable and environmentally friendly coating is required to replace the conventional aging-prone and unsustainable salinization layers. Here, soot-templated surfaces with re-entrant nanostructures are precoated with polydimethylsiloxane (PDMS) brushes. An additional nanometer-thick lubricant layer of PDMS was then applied to increase chemical stability. The surface is superhydrophobic with a nanoscale liquid coating. Since the lubricant layer is thin, ridge formation is suppressed, which leads to low drop sliding friction and fast drop shedding. By introducing a bottom "reservoir" of a free lubricant as an oil source for self-replenishing to the upper layer, the superhydrophobic surface becomes more stable and heals spontaneously in response to alkali erosion and O₂ plasma exposure. This design also leads to a higher icing delay time and faster removal of impacting cooled water drops than uncoated surfaces, preventing icing at low temperatures.

INTRODUCTION

Superhydrophobic surfaces have been proposed as promising materials for a variety of applications, including heat transfer,^{1,2} self-cleaning,³ fuel filters,⁴ water harvesting,⁵ anti-icing,^{6,7} and so forth. These surfaces mainly rely on hierarchical micro/nanostructures⁸⁻¹⁰ and low-surface-tension chemistry.^{11,12} A general challenge for these surfaces is the easily damaged surface structure and chemistry under physical contact or oxidation.¹³ Most recent studies mainly focus on preventing physical damages¹³; for example, a sacrificing coating layer¹⁴ and an "armor" surface frame³ are

designed. Rarely have strategies been reported to prevent the formation of chemical defects^{15,16} by reactant oxidization¹⁷ of the low-surface-tension silane coatings on these rough structures.¹⁸⁻²⁰

Generally, artificial superhydrophobic surfaces need to be modified with organosilanes,¹¹ such as fluorinated long-chain alkyl silanes²¹ or methylated medium-chain alkyl silanes,²² to lower the surface energy. These silanes limit the chemical stability of the surfaces because of a hydrolysis reaction between the Si-O bond in the silane and the OH⁻ in the solution.¹⁷ Moreover, atoms present in the side chain of the silanes can also be oxidized when exposed to plasma discharging.²³ This limits the use of these surfaces in

This is an open access article under the terms of the Creative Commons Attribution License, which permits use, distribution and reproduction in any medium, provided the original work is properly cited.

© 2023 The Authors. *Droplet* published by Jilin University and John Wiley & Sons Australia, Ltd.

spacecraft launch, water treatment, semiconductor manufacturing, and energy generation in which strong oxidizing environments exist. With respect to a low-temperature environment, the hydrophobic segment in the organosilane combined with the nanoroughness will provide more nucleation sites for the cooled water.^{24,25} This will result in a high nucleation rate and a low delay icing time, which will result in the impact drop being pinned on the cooled superhydrophobic surface.^{26,27} In addition, the widely used fluorinated silanes pose a threat to the environment and bioaccumulate in humans, animals, and plants. Therefore, fluorine-free alternatives are urgently needed.²⁸

By combining superhydrophobicity and so-called liquid-infused surfaces (LISs), we intend to make a step forward to overcome these limits. A LIS is a rough or porous surface that is infused with oil,²⁹ providing protection against corrosion³⁰ and enabling self-healing³¹ or self-replenishing.³² However, in contrast to superhydrophobic surfaces, they still show high normal adhesion, which requires significant effort to remove droplets and results in low drop velocity. Additionally, the depletion of the oil layer limits their functionality to a finite time or number of drops. Given the advantages of the liquid layer in stabilizing surface chemical properties, it is promising to apply a liquid layer as a coating for superhydrophobic surfaces. While some previous work has attempted to combine a liquid layer with micro-scale structures to create a lubricant-air interface,³³⁻³⁶ the resulting oil layer tends to have significant thickness (>1 μm). Consequently, an oil wedge is formed at the three-phase contact line, leading to a decreased drop shedding velocity. It is still a challenge to fabricate a superhydrophobic surface with high drop shedding velocities while also being chemically stable, self-replenishing, and icephobic.³⁷

Here, we propose a general strategy for creating chemically robust superhydrophobic surfaces by replacing the conventional solid coating with a replenishable liquid film. To combine the advantage of a liquid coating but prevent the formation of large oil menisci, a nanoscale liquid coating is successfully fabricated. By incorporating a precoated layer, a low-surface-tension liquid polydimethylsiloxane (PDMS) film can be subsequently stabilized with the help of the chemically identical interaction and the high roughness of the surface. The surface shows a high drop shedding velocity similar to that on a nonoil-coated superhydrophobic surface. Benefiting from the protection and replenishment of the flowable liquid coating, the superhydrophobic surface demonstrates outstanding stability, resisting alkaline corrosion and oxygen aging. Such a design, which combines superhydrophobicity and lubrication in one surface, significantly reduces lubricant depletion from the surface. The liquid coating, resulting in a smooth liquid-air interface, delays ice nucleation and accelerates liquid removal before freezing, enhancing the surface's performance at low temperature.

RESULTS AND DISCUSSION

The SiO_2 candle-soot-templated surface⁹ was prepared as a model surface with a nanoscopic re-entrant structure (Figure 1a). It is easy to prepare without the need for complex equipment. A large area of

similar coating can also be obtained by liquid flame spray using a well-designed setup.³⁸ The soot layer was typically $H_0 = 40 \mu\text{m}$ thick (Supporting Information: Figure S1). Liquid PDMS preferentially wets a smooth PDMS brush-modified surface,^{39,40} rather than fluorinated surfaces; on a smooth surface, PDMS forms a static contact angle of 6° rather than $\approx 50^\circ$ (Supporting Information: Figure S2). Thus, the soot-templated surface was modified with PDMS chains first.⁴¹ We call it a "PDMS brush," although the chains may be attached at random points of the chain and there may be multiple links. The nature of the bond is not clear. We assume that it is covalent because the PDMS chains cannot be removed by exposing them to a good solvent (Supporting Information: Section 1). We use the abbreviation PDMS-SH (PDMS brush-modified superhydrophobic) surface to refer to this surface. Since PDMS has a glass transition temperature of around -125°C , the brush is in an almost liquid-like state.⁴² Low concentrations of PDMS (viscosity: 100 cSt; M_w : 6000 g/mol) dissolved in toluene were spin-coated onto PDMS-SH surfaces (4000 rpm, 60 s). The liquid PDMS was chemically identical^{40,43} to the PDMS brush because of the same molecular weight and chemical structure. After solvent evaporation, due to mixing entropy, oil diffuses into the grafted PDMS and swells the brush (Figure 1a). This kind of surface has a similar mechanical stability as that reported for a superhydrophobic soot-templated surface (Supporting Information: Figure S4).⁹

After the preparation, we could observe a liquid nanofilm surrounding the nanostructures from the force measurement by atomic force microscopy (AFM) (Figure 1b,c). AFM is an effective tool to detect the presence of oil on the nanoscale features because it can locally probe capillary forces even on a rough surface⁴⁴ (Supporting Information: Section 2). The "jump-in distance" illustrates the thickness T of the fluid layer (Figure 1b). When the AFM tip approached a PDMS-SH surface, the tip jumped from an average distance of about 10 nm (Figure 1b, blue symbols). This value is the same order of magnitude as the brush thickness. Similar jump-in distances were observed on smooth PDMS-coated surfaces as reported before.⁴³ On the liquid-coated PDMS brush-modified superhydrophobic (L-PDMS-SH) (7.5%) surface, approaching force curves showed a long jump-in distance (Figure 1b, red symbols) before hard contact was established. The average thickness of the nanoscale oil layer was around 20 nm, and it has a wide range from 10 to 100 nm. These large jump-in distances demonstrate that the liquid swells the brush roughly by a factor of 2-3.

We used the quantitative imaging (QI) mode of the AFM, where a force-distance curve is obtained in each pixel of an image and the jump-in distance is extracted using a custom Python analysis script. From the resulting map (Figure 1c), we can see the oil distribution visually. For the PDMS-SH surface, the jump-in distance is lower than 10 nm over the whole surface, which illustrates a solid coating. For the L-PDMS-SH (7.5%) surface, we can see that the re-entrant structures are covered with a thin liquid layer. For a liquid-infused fluorinated superhydrophobic (L-F-SH, 7.5%) surface, the oil infused into the structure, but we could not detect continuous free PDMS on top (Supporting Information: Figure S7). We conclude that the oil can

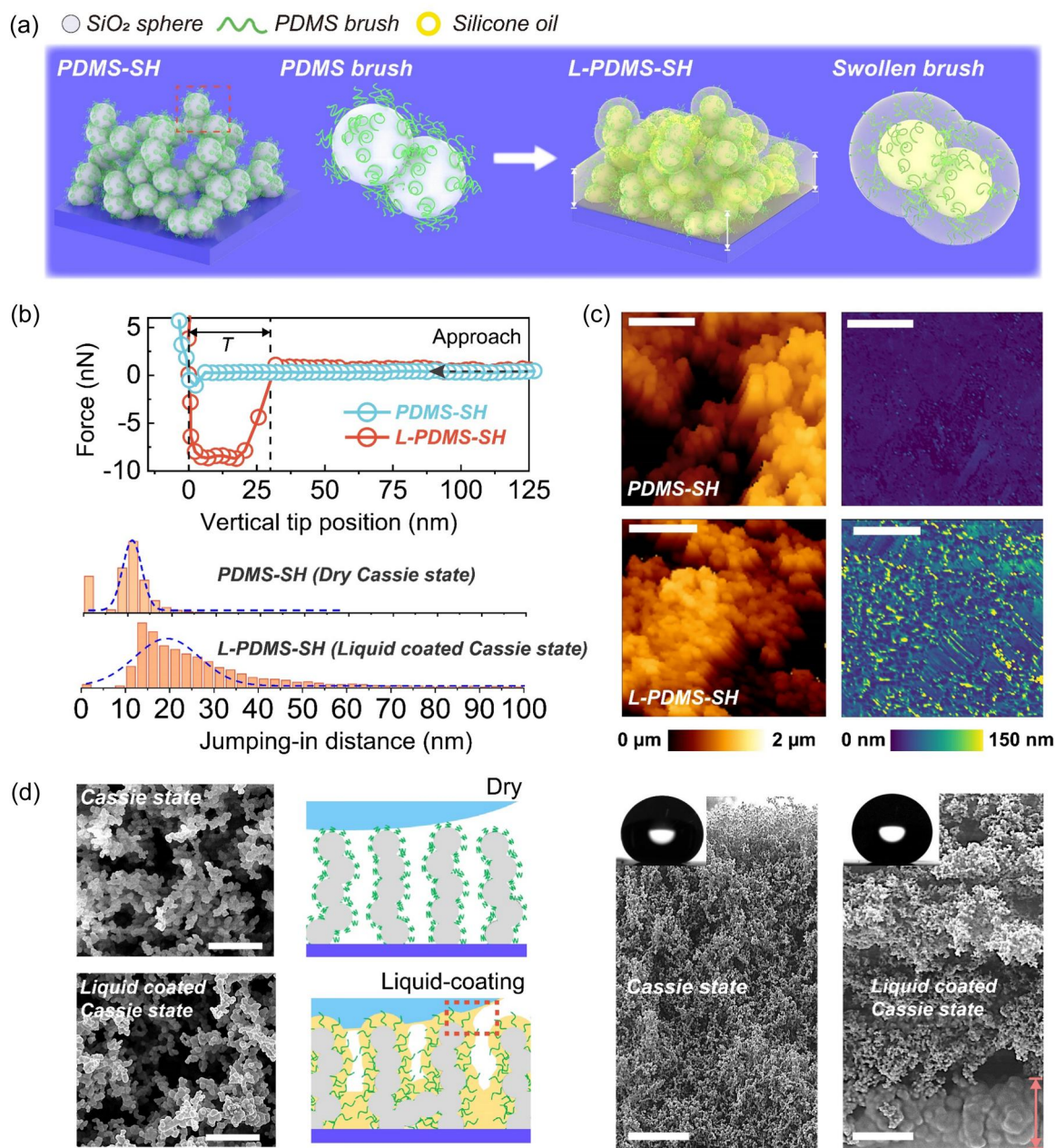


FIGURE 1 Liquid-coated polydimethylsiloxane brush-modified superhydrophobic (L-PDMS-SH) surface. (a) Schematic of the preparation and structures of PDMS brush-modified superhydrophobic (PDMS-SH) and the L-PDMS-SH surface. (b) Approaching force curve measured on PDMS-SH, L-PDMS-SH (7.5%) surfaces and histogram of the frequency count of jump-in distances on these surfaces. (c) Atomic force microscopy topography (left) of PDMS-SH, L-PDMS-SH (7.5%) surfaces, and the corresponding maps (right) of the distribution of liquid coating thickness. Scale bar: 500 nm. (d) Scanning electron microscopy images of a dry and a liquid-coated Cassie state. Scale bar top view (left): 10 μm ; cross-section view (right): 5 μm . The middle scheme illustrates the nanoscale liquid coating structure. The red dotted frame illustrates the neglectable nanoscale deformation near the contact line. The red arrow in the cross-section view indicates the thickness of the bottom oil reservoir.

only spontaneously cover the PDMS-coated surfaces because they are chemically identical but not the fluorinated ones.

Our oil layer in the PDMS brush is much thinner than previously reported liquid-coated surfaces.^{34,45,46} Since its thickness is only nanometers, it cannot be discerned in scanning electron microscopy (SEM) images (Figures 1d and 2). The morphology of the upper structure closely resembles that of the dry superhydrophobic surface.

A $\approx 5\text{-}\mu\text{m}$ -thick oil layer (bottom liquid "reservoir") is visible only at the lower portion of the surface in the cross-sectional view (Figure 1d). By assimilating the findings from AFM force curves, it can be inferred that a nanoscale oil layer envelops the nanosphere structures of the soot-templated surface.

The lubricating PDMS also forms a bottom oil layer as a "pool" underneath the nanostructures (Figure 2a). It can be used like a

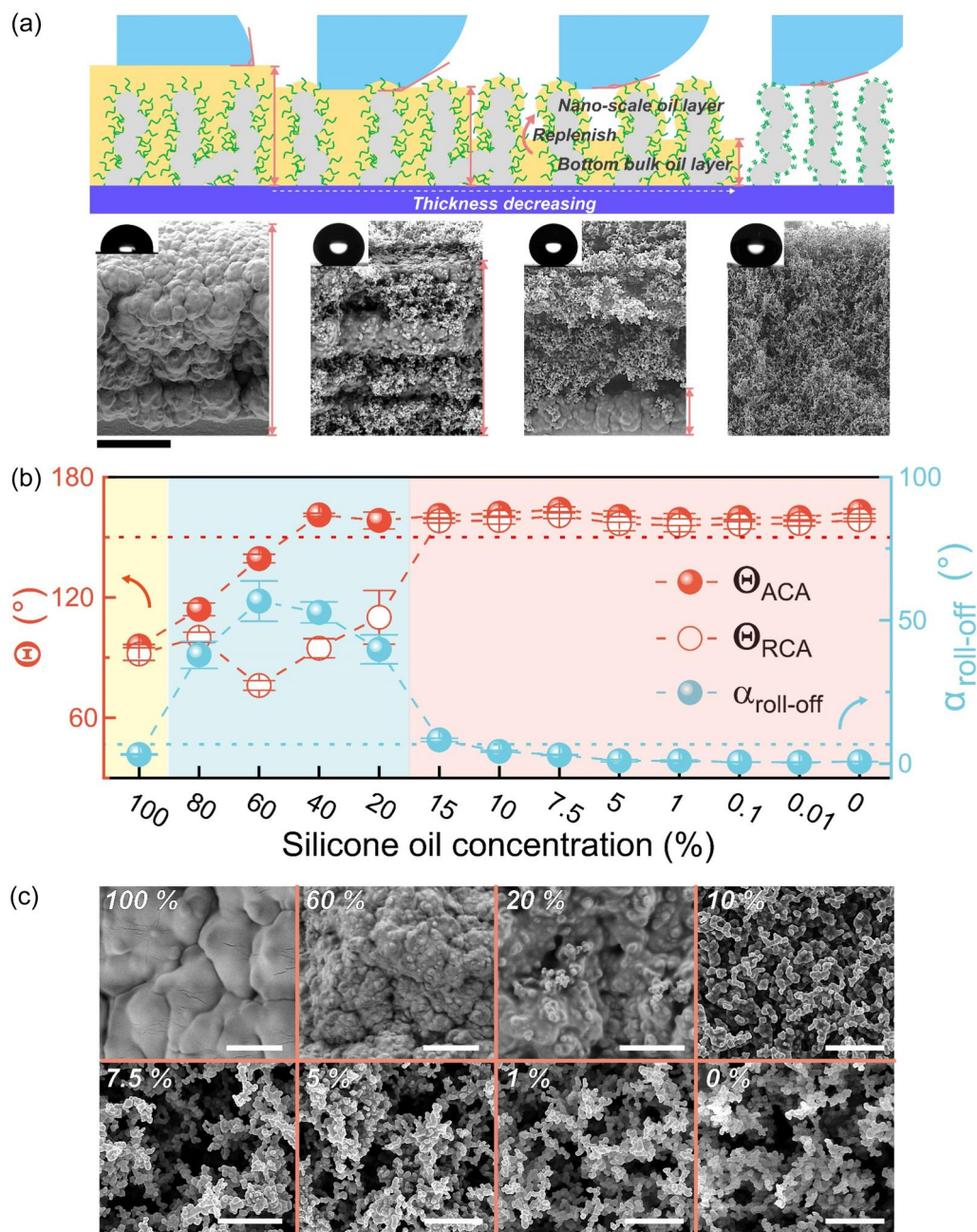


FIGURE 2 Wetting property transition. (a) Illustration of the oil structure in liquid-coated polydimethylsiloxane brush-modified superhydrophobic (L-PDMS-SH) surfaces resulting from the different concentrations of oil infused (from left to right: 100%, 20%, 7.5%, and 0%). Scanning electron microscopy (SEM) images show the cross-section morphologies of the surface with different bottom oil layer thicknesses; scale bar: 10 μ m. Inset images show the static contact angles of water drops on the corresponding morphology. (b) Advancing and receding contact angles (θ_{ACA} and θ_{RCA}) and roll-off angles ($\alpha_{roll-off}$) of 10 μ L of water on the L-PDMS-SH surfaces on infusing different concentrations of silicone oil. Red part (■): Superhydrophobic state. Blue part (■): Slippery Wenzel state. Yellow part (■): Slippery state. (c) SEM images of the top views of the L-PDMS-SH surfaces after infusing different concentrations of liquid polydimethylsiloxane (PDMS). Scale bar: 0%–7.5%, 1 μ m; 10% and 20%, 2 μ m; 60% and 100%, 10 μ m.

“gland” in animals for self-replenishing of the nanofilm on top when it is depleted. In this way, liquid-coated self-replenishing surfaces, denoted by L-PDMS-SH, are generated. We can adjust the thickness of the bottom oil layer by choosing different concentrations of PDMS-in-toluene solutions in spin-coating. On spin-coating 100% silicone oil, the whole soot-templated layer was full of liquid, which

can be considered as a LIS. On using the PDMS solutions, the thickness of the bottom oil layer decreased below the maximum height of the nanoscopic SiO_2 structures. During spin-coating, the whole soot-templated SiO_2 structure is filled with solution. After toluene evaporation, only silicone oil will leave, which results in a thinner bottom bulk oil layer than that when coating the surface with

pure oil. The wetting properties of L-PDMS-SH surfaces depend on the thickness of the bottom oil (Figure 2a,b) and the static contact angle is in agreement with the previous theoretical results (Supporting Information: Section 3). When the oil concentration was below 15%, the surface was superhydrophobic. The infusing oil viscosity did not affect the apparent advancing and receding contact angles, because the liquid layer is thin and their chemistry is almost similar (Supporting Information: Figure S7).³⁵

When the oil concentration ranged from 20% to 60%, no Cassie state was formed (Figure 2b) and it can be considered as a slippery Wenzel state as reported before.⁴⁶ When the surface was infused with pure oil, a slippery surface with a smooth oil-air interface was formed.

To visualize the interface of the L-PDMS-SH surfaces, which is related to the wetting property,⁴⁷ we infused the PDMS-SH surfaces with a mixture of vinyl-terminated PDMS ($M_w = 6000\text{--}8000$ g/mol, 100 cst; Gelest) and polymethylhydrosiloxane (Sigma-Aldrich) at a ratio of 9:1. Five microliters of 0.05 wt% and Pt catalyst (platinum-1,3-divinyl-1,1,3,3-tetramethyldisiloxane; Gelest) dissolved in toluene were added. The mixture was diluted into 60, 20, 10, 7.5, 5, and 1 wt% in toluene. The solutions were spin-coated immediately on the PDMS-SH surface and annealed at 80°C for 2 h to cross-link the mixture. Then, SEM images were taken in vacuum (Figure 2c). When the surface was infused with pure oil (100%), it was hard to see the re-entrant structure. Air gaps in the soot-templated structure start to appear after the oil concentration decreased to 20%. When the oil concentration decreased to 10%, some thick oil still remains outside the porous structure. For this reason, we use L-PDMS-SH surfaces with a solution concentration below 10% in the following tests. Once the infusing oil concentration was below 10%, the topography of the L-PDMS-SH surface was the same as that of the nooil-infused surface.

To further characterize difference in the wetting property, we carried out drop impact and drop sliding experiments. Four microliters of Milli-Q water drops were ejected from a needle controlled by a syringe pump at a height of 2 cm. The dimensionless Weber number We is 10.9 ($We = \rho U_0^2 D / \gamma$, where ρ is the density, U_0 is the impacting velocity, D is the diameter of the drop, and γ is the liquid-air surface tension). Drop impact was recorded using a Photron Fastcam Mini UX100 high-speed camera (5000 fps) with a $\times 2$ lens. Impact water drops can rebound from superhydrophobic PDMS-SH and L-PDMS-SH (7.5%) surfaces. However, the drop impact dynamics differed (Figure 3a and Supporting Information: Section 4). On PDMS-SH, the contact time $\tau = 10$ ms, while on the L-PDMS-SH (7.5%) surface, we observed a contact time $\tau = 18$ ms (Figure 3b). The restitution coefficient, $e = U_R / U_0$ (where U_R is the velocity at the moment of rebound), is higher for the PDMS-SH surface (Supporting Information: Figure S10) and drops disperse faster. The contact time of 10 ms for PDMS-SH agrees with the result obtained from the inverse of the first resonance frequency of drops. At the limit of low viscosity, the first resonance frequency is at an oscillation period $\tau = \pi \sqrt{\rho R^3 / 2\gamma} = \sqrt{3\pi\rho V / 8\gamma}$. Here, R is the initial radius of the drop, ρ is the density of the liquid, and V is the drop volume.⁴⁸⁻⁵⁰ Inserting $\gamma = 0.072$ N/m leads to $\tau = 8$ ms. On the

L-PDMS-SH surface, oil is transferred to the drop surface, reducing its surface energy. However, even if we take $\gamma = 0.058$ N/m, the calculated contact time is only $\tau = 9$ ms. Thus, more energy is dissipated on L-PDMS-SH than on PDMS-SH surfaces during the impact process. We suggest that the spreading of the oil layer on the drop's surface and the resulting Marangoni flow lead to this energy dissipation, resulting in a longer contact time.⁵¹

Water drops slide differently on L-PDMS-SH surfaces in three wetting states (Figure 3c,d). On PDMS-SH and L-PDMS-SH (5%) surfaces, water drops rolled over the surface at a low tilt angle ($< 5^\circ$) with high contact angles. For a 33 μL drop sliding over the L-PDMS-SH (5%) surface (tilting angle: 40°) for a distance of 4 cm, the maximum velocity was ≈ 0.8 m/s (Figure 3d). This velocity is comparable to that observed on a dry superhydrophobic surface (Supporting Information: Figure S12). Thus, drop friction on our nanoscopic liquid-infused surfaces is almost similar to dry superhydrophobic surfaces. At 20%, the advancing angle remained high and the receding contact angle decreased to around 90° (Figure 2b), resulting in a high sliding angle (Figure 3c). The maximum velocity after sliding 4 cm was 0.6 m/s, which is lower than that on a PDMS-SH surface. For the fully slippery state achieved by infusing pure PDMS, the sliding process was consistent with previous observations on LIS, showing a low sliding angle but low drop velocity. Furthermore, the increase in drop velocity with drop number (Figure 3d, right) indicates oil depletion typical for LIS. The main factor influencing drop movement and friction is the liquid layer thickness. For a micrometer-thick oil layer, a continuous meniscus wedge is formed, resulting in high dissipation caused by dragging this wedge over the surface (Supporting Information: Figure S13). For the nanoscale liquid layer, the formation of such a liquid wedge is suppressed, which results in less dissipation (Figure 1d). The friction force caused by dragging a liquid wedge across the surface is absent.^{52,53} Lower friction forces lead to a higher sliding velocity. The drop velocity on different surfaces can be theoretically determined by the energy dissipation based on previous models (Supporting Information: Section 4).⁵⁴

For the silane-modified superhydrophobic surface, OH^- or H^+ ions in the contact liquid cause hydrolysis of the Si-O bond (Figure 4a). Using oxygen plasma, atoms in the side chain can be oxidized. In our design, we added a flowable oil layer above the PDMS brush. It can act as a sacrificial layer to protect the swollen brush and improve the surface's chemical stability. This continuous oil layer can also be replenished by the deposited bottom oil, leading to long-term chemical stability.

To analyze the chemical stability of the surfaces, we measured the dynamic contact angles of an aqueous drop with different pH values on F-SH, PDMS-SH, and L-PDMS-SH (7.5%) surfaces first. The drops with different pH values were prepared by diluting 0.1 M H_2SO_4 aqueous (pH = 1) and 0.1 M KOH (pH = 14) to a certain concentration. They all showed receding contact angles above 150° and low roll-off angles (Supporting Information: Figure S14). However, in real applications, the surface needs to be stable for a long time. We conducted experiments in which we applied alkali KOH

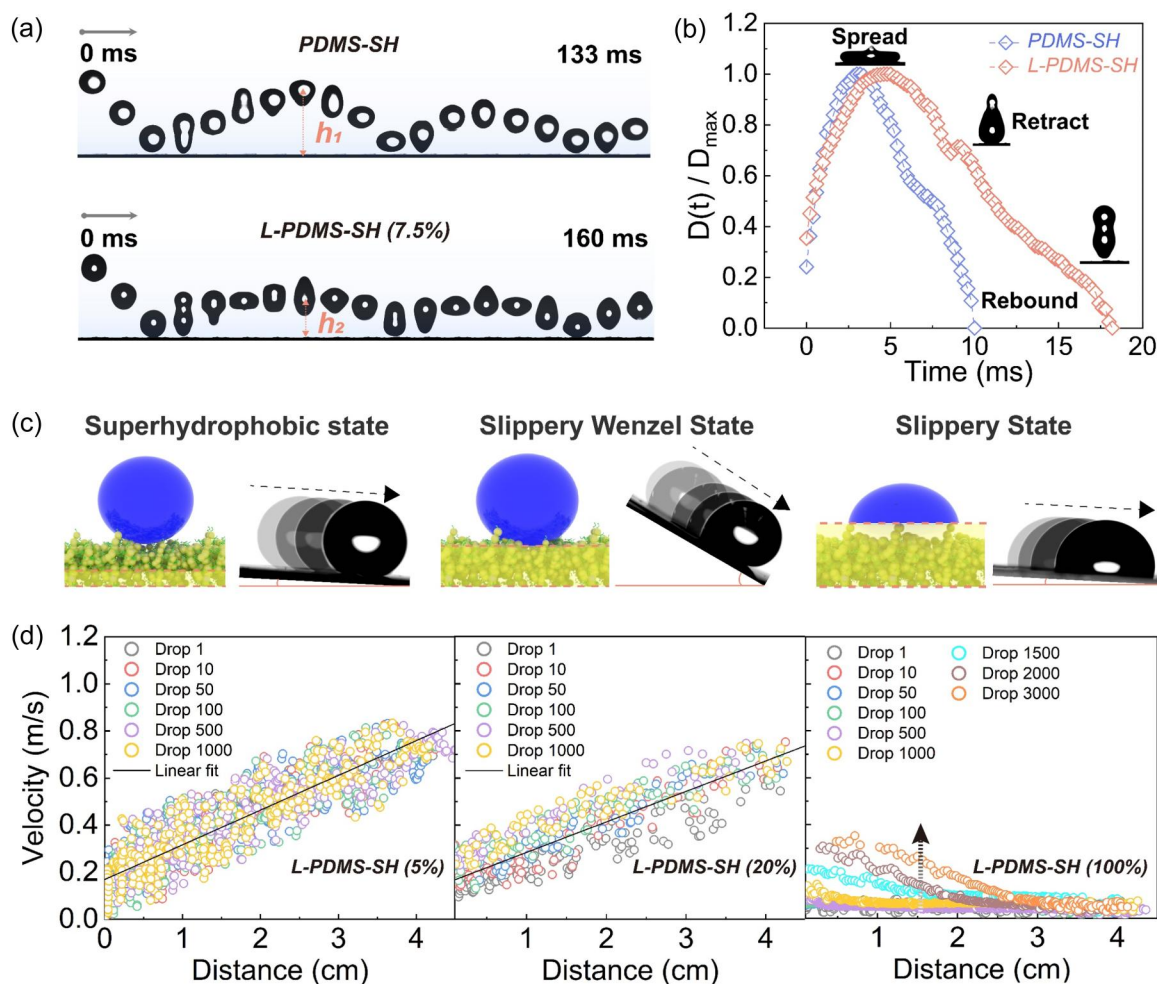


FIGURE 3 Drop dynamics. (a) Four microliters of drop impact on PDMS-SH and liquid-coated PDMS brush-modified superhydrophobic (L-PDMS-SH) (7.5%) surfaces ($We = 10.9$) and (b) time dependence of the scaled contact radius $D(t)/D_{max}$. (c) Three wetting states are indicated by the corresponding schematics and video sequences of 10 μL water drop sliding over L-PDMS-SH surfaces with infusing oil concentrations of 5%, 20%, and 100% (images were recorded at intervals of 0.2 s). (d) Drop velocity versus position on L-PDMS-SH in these three wetting states. The results were measured on a 40° tilted platform with 33 μL water drops. PDMS-SH, polydimethylsiloxane brush-modified superhydrophobic.

drops ($\text{pH} = 14$) to the surface and allowed them to slide for different time periods at a constant velocity (drop size: 45 μL ; Ismatec® Reglo digital miniflex pump; pump speed: 10 $\mu\text{L}/\text{s}$). Then, the contact angle of water was measured in the drop sliding path. F-SH and PDMS-SH surfaces lost their superhydrophobicity after ≈ 100 min (Figure 4b). For L-PDMS-SH (7.5%) surfaces, the surface failed after 800 min treatment, and was thus almost a factor 7 longer. This observation indicates that the oil coating and self-replenishment from the bottom layer prevent the alkali drop from contacting the solid part directly and prolongs the lifetime. This interpretation is supported by the observation that once the L-PDMS-SH fails, AFM experiments no longer showed a liquid layer on the surface (Supporting Information: Figure S15).

The chemical stability of the surface after acid ($\text{pH} = 1$) drop sliding was tested in the same way. Acid degradation for Si-O bonds has been reported to be much lower than that of alkali.¹⁷ Thus, the contact angle hysteresis on F-SH and L-PDMS-SH (7.5%) surfaces was still below 10° after 1000 min (Figure 4c) and the nanoscale oil layer on L-PDMS-SH

could be detected after 1000 min of acid treatment (Supporting Information: Figure S16). In contrast, contact angle hysteresis slightly increases on the PDMS-SH surface after 1000 min. That is because some PDMS chains on top were slowly degraded by the acid. Comparing these results, we know that the enhanced stability is because of the sacrificial nanoscale oil layer. The OH^- ions in the drop will react with the Si-O bond in the liquid part first. Then, because of the high degradation rate of alkali, the replenishment will meet its limitation and the nanoscale oil layer will be used out. The protected silane can be degraded as the other two surfaces after that, but this process extends the failure time considerably.

Plasma is known to activate the surface and change the interfacial chemical composition.⁵⁵⁻⁵⁷ We compared the wettability of L-PDMS-SH (7.5%), PDMS-SH, and F-SH surfaces after oxygen plasma treatment (power: 20 W; time: 30 s; Diener electronic GmbH). The results show that for F-SH, one cycle of plasma treatment was sufficient to make the surface superhydrophilic. It remained superhydrophilic for at least 24 h (Figure 4d). For L-PDMS-SH (7.5%), the

COLOR FIG

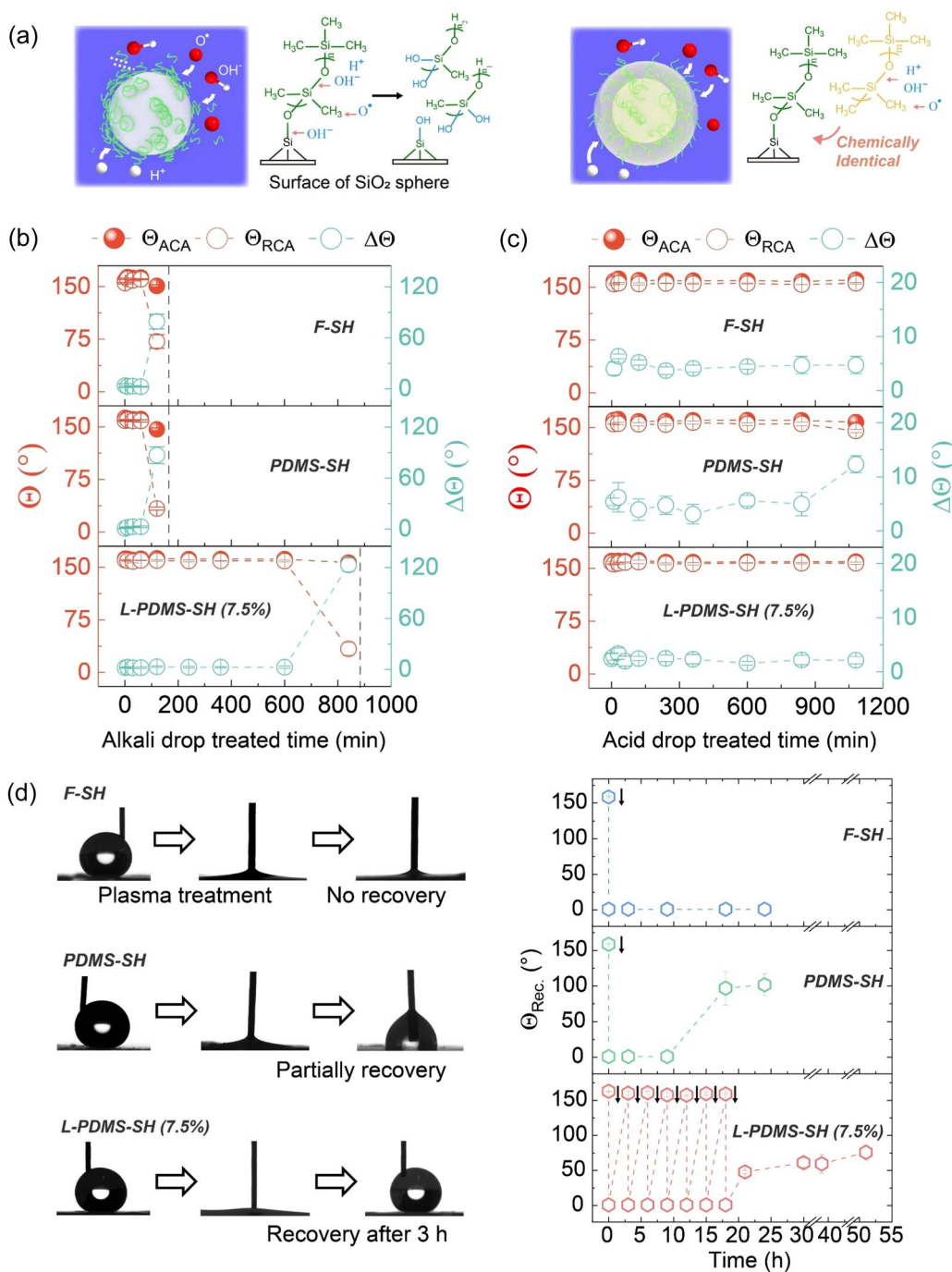


FIGURE 4 Enhanced chemical stability. (a) The diagram shows the possible mechanism of how the liquid coating protects the bonded organosilane from degradation in strong oxidation to enhance chemical stability. (b and c) Changes in advancing and receding contact angles (θ_{ACA} and θ_{RCA}) and hysteresis ($\Delta\theta$) of 10 μ L of water on the surfaces (b) after alkali drops and (c) after acid drops slide off fluorinated superhydrophobic surface (F-SH), polydimethylsiloxane brush-modified superhydrophobic (PDMS-SH), and liquid-coated PDMS brush-modified superhydrophobic (L-PDMS-SH) (7.5%) surfaces for different time periods (tilting angle = 50°, 15 drops/min). (d) Change in the receding contact angle of 10 μ L of water on F-SH, PDMS-SH, and L-PDMS-SH (7.5%) surfaces after O₂ plasma treatment (power: 20 W; time: 30 s). The black arrows inside represent plasma treatment carried out once.

receding contact angle decreased to zero after one plasma treatment. The AFM experiments demonstrated that the nanoscale oil layer still existed after plasma treatment (Supporting Information: Figure S17). However, on placing the surface at room temperature (25–30°C) for 3 h, it recovered. Water drops formed a Cassie state again. We

attribute this recovery to a self-replenishing process of the oil from the bottom. Oil from the bottom layer diffuses upward following the gradient in surface energy created by the plasma. These PDMS chains may also react with the SiO₂ surface, or they may be cross-linked during this process. Experimentally, we observed that after seven

cycles of plasma treatment, the surface no longer recovers to the superhydrophobic state even after 24 h.

We also characterized the wettability change of PDMS-SH after plasma treatment. The surface became superhydrophilic after one cycle of plasma treatment. After being placed at room temperature for 21 h, the water receding contact angle increased to more than 90° within 21 h, but the surface remained in the Wenzel state. Comparing this observation to the result on the L-PDMS-SH (7.5%) surface, we conclude that the recovery to the Cassie state after plasma treatment is caused by the flow and exchange of the bottom oil layer and the top oil nanofilm.

The chemical stability of the superhydrophobic L-PDMS-SH surface relies on the existence of the liquid coating and the replenishment by free PDMS from the bottom. For this reason, we further analyze the oil depletion. For the drop dynamics characterization, we can easily see the lubricate depletion by that if there is an obvious velocity change with the drop number increasing when the lubrication is high. However, for the designed liquid-coated superhydrophobic surface, the velocity change seems to be negligible. Silicone oil has a low surface tension $\gamma = 21 \text{ mN/m}$. When a water drop is placed on a silicone oil-infused surface, the oil spreads over

the water surface and covers it.⁵² As a result, a water drop sliding off this designed slippery superhydrophobic surface will also take some oil with it. Therefore, we need more sensitive methods to check this oil depletion. To test how fast oil is removed per drop, we measured the surface tension of the water collected after sliding over a liquid-coated superhydrophobic surface. In addition, we applied proton nuclear magnetic resonance (^1H NMR) to determine the amount of depleted oil in the collected water (Figure 5a).

The controlled sample for the oil depletion comparison that we use is a slippery smooth liquid-infused PDMS brush surface. This ensures continuous mobility of the oil layer throughout the experimental measurements. In the case of LIS where the depletion of oil volume becomes substantial after multiple drops slide on the surface, the presence of surface roughness introduces complexity in the oil depletion process. To measure the surface tension of water drops sliding over the L-PDMS-SH (7.5%) surface, $45 \mu\text{L}$ water drops were deposited at the top of inclined samples (tilting angle: 50°) by a pump at a speed of $10 \mu\text{L/s}$. The drops slid off the surface and were then collected in a beaker. After different numbers of drops slid over the surfaces, the beaker was placed in a Wilhelmy plate instrument (PT 11 mode of Dataphysics DCAT 25, Wilhelmy plate length:

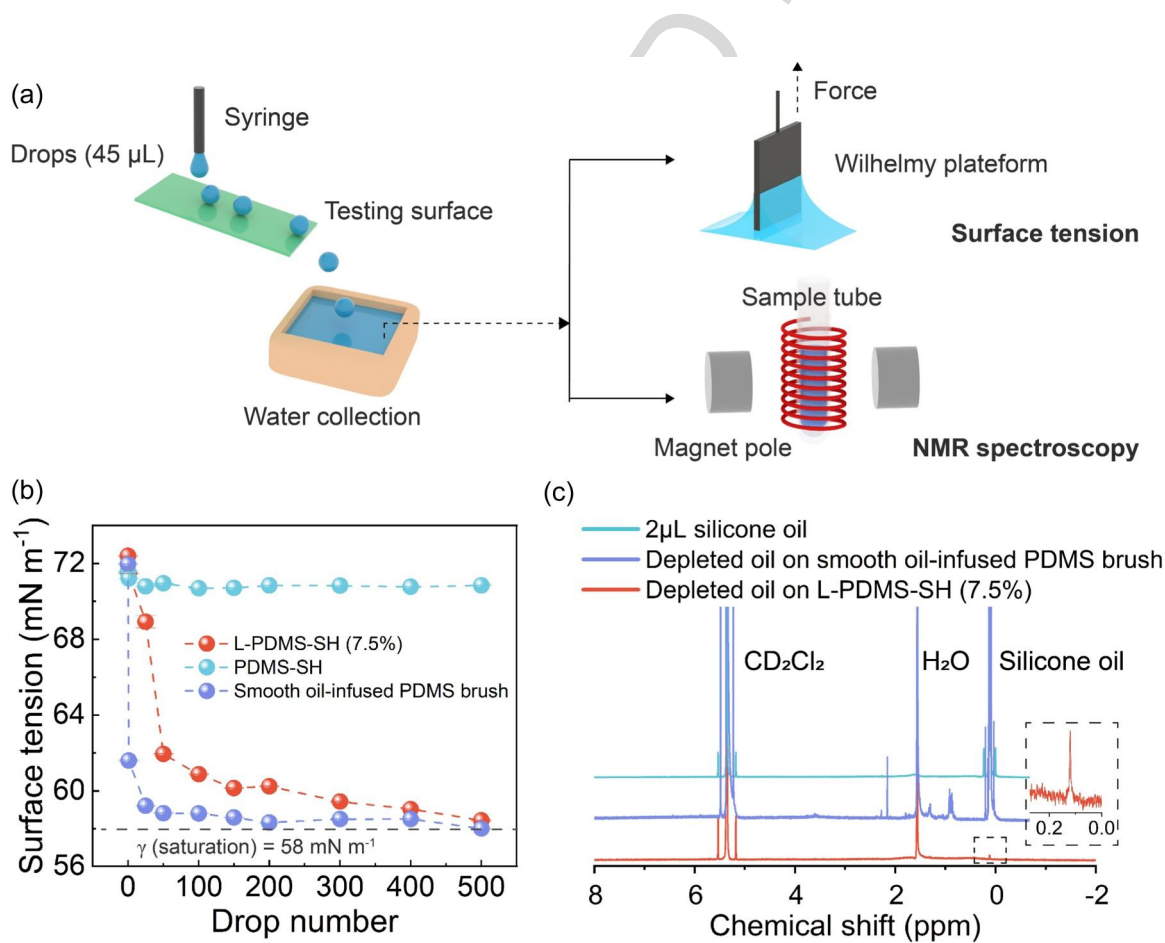


FIGURE 5 Oil depletion. (a) Schematic showing two methods to test the stability of a liquid nanofilm coating on the surface. (b) Interfacial surface tension changes of the collected water after drops slide off different surfaces. (c) Proton nuclear magnetic resonance (NMR) result showing the relative amount of depleted oil after 500 cycles of sliding of drops off the surfaces. L-PDMS-SH, liquid-coated polydimethylsiloxane brush-modified superhydrophobic; PDMS, polydimethylsiloxane; PDMS-SH, PDMS brush-modified superhydrophobic.

10 mm; width: 19.9 mm; thickness: 0.2 mm) and the surface tension was measured. The oil film will collect on top of the water and decrease the overall surface tension. To measure the interfacial tension of silicone-water plus silicone-air, we added 2 μL of silicon oil in a beaker filled with water. The interfacial tension for the interface in saturation was 58 mN/m (Figure 5b, black dashed line).

When the drop slid off the slippery smooth liquid-infused surface, the surface tension of the collecting water decreased to 62 mN/m even after one drop (Figure 5b). After collecting 50 drops, the surface tension of the water was close to the saturated surface tension. For the L-PDMS-SH (7.5%) surface, the surface tension of the collected water decreased more slowly. After 10 drops slid off the surface, the surface tension only changed from 72 to 69 mN/m. After 500 drops slid off the surface, it reached the saturated surface tension. This result illustrates that the oil depletion volume per sliding drop is lowered on the L-PDMS-SH (7.5%) surface compared to that on a smooth oil-infused surface.

We use ^1H NMR measurement to compare the total amount of depleted oil on these two surfaces. Five hundred water drops slid off the surface and were collected. The collected water was evaporated at 60°C under vacuum for 24 h. The remaining oil was then dissolved in deuterated dichloromethane (CD_2Cl_2) for the ^1H NMR measurement. As a control, we dissolved 2 μL of silicone oil in CD_2Cl_2 . The chemical shift of silicon oil was found to be around 0.1 ppm (^1H NMR) as reported before.⁵⁸ The spectra show that the relative peak integral of depleted oil from L-PDMS-SH (7.5%) (Figure 5c, inset) to that from the smooth tethered liquid surface was 1:22. The collected water drops that slid over the smooth oil-infused PDMS brush surface had a substantially higher amount of oil. During these experiments on the L-PDMS-SH (7.5%) surface, the thickness of oil changed substantially, after 500 drops slid over the surface (Supporting Information: Figure S18). This is because of the replenishing from the bottom oil “reservoir.” This kind of surface shows a longer lifetime when we extend it to include 10,000 drops (Supporting Information: Figure S19). These two results show that the lubricant is depleted more easily from the smooth surfaces than that from L-PDMS-SH (7.5%) surfaces. We suggest that this is because of the reduced contact area and sufficiently thin oil layer,⁵⁹ which is stabilized because it is chemically identical to the brush⁴⁰ and due to the considerable roughness of the surface.⁶⁰

To determine how oil depletion affects the bottom oil “reservoir” at the same time, we studied the electric charging of sliding drops (Supporting Information: Section 5). Water drops spontaneously acquire a charge when they slide on hydrophobic, insulating surfaces.^{61–63} The drop charge on the LIS was found to be affected by the bulk oil layer thickness.⁶⁴ We can determine if oil depletion will affect the thickness of the bottom oil layer on L-PDMS-SH surfaces by varying the charge of sliding drops (Supporting Information: Figure 20a). The increasing drop charge, when the number of drops is low, indicates that the bulk oil layer thickness decreases due to depletion on a slippery L-PDMS-SH (100%). However, this phenomenon cannot be observed when the infusing oil concentration is low, indicating that there is no loss (see Supporting Information: Figure 20b–d).

To test the icing delay time (the time interval between the surface cooling to a certain temperature and ice formation) on the surfaces, we placed 10 μL water drops on a cooling platform THMSG600 (Linkam Scientific Instruments) inside a closed, insulated chamber (Supporting Information: Figure S23). The humidity inside was controlled by mixing certain volumes of dry and wet nitrogen gas. The surface temperature was calibrated versus the temperature in the chamber (Supporting Information: Figure S24). The cooling platform could be cooled down to -20°C and heated up to 20°C at a rate of $0.5^\circ\text{C}/\text{s}$.

Figure 6a shows the freezing and melting process of one water drop on the L-PDMS-SH (7.5%) surface. When the characteristic tip of the spherical ice was observed, the drop was fully frozen.⁶⁵ The surface could remain superhydrophobic after this process. After 10 freezing/melting cycles, we measured the friction force required to move a 10 μL water drop on the surface using a drop adhesion force instrument.^{66,67} The result (Supporting Information: Section 6) shows that compared to that on PDMS-SH surface, the maximum force for a water drop on L-PDMS-SH (7.5%) to start moving did not change a lot after the 10 cycles of test. This means that the mobile oil layer can prevent defect formation due to the drop during the melting process. We have also measured the apparent contact area change of sessile water drops on cooling and heating the surface (Figure 6b). On flat fluorinated glass (F-glass), the contact area remained constant during freezing and melting. On superhydrophobic PDMS-SH and F-SH (fluorinated candle-soot-templated surface), the contact area increased during the freezing process, but it did not decrease after melting. The contact line was pinned. This observation indicates that some defects were generated by an ice/water mixture during the melting. Only for L-PDMS-SH (7.5%) did the contact area increase slightly before the freezing process. After melting, the drop contact area decreased to its original area. The results showed that the mobile contact line^{33,68} of the oil-infused PDMS brush can help to protect superhydrophobicity at low temperatures. Due to this mobility of the contact line, the surface can maintain its performance after more freeze/thaw cycles compared to previously reported work (Supporting Information: Figure S26).

On the L-PDMS-SH (7.5%) surface, freezing was delayed. We measured the delay time on four kinds of surfaces at a surface temperature of -15°C and a humidity of 20%. The tethered liquid nanofilm helps reduce the nucleation sites for the low-temperature water, so that the delay icing time on L-PDMS-SH (7.5%) surfaces was observed to be the longest before freezing (Figure 6c). The long delay in ice formation indicates a low ice nucleation rate.²⁶

In many applications, preventing icing from impacting cooled drops is important. We checked the drop impact process by placing these three surfaces on a Peltier with a surface temperature of -15°C . The high-speed camera, the Peltier, and the syringe were all stored in a refrigerator at 0°C and 20% humidity. A 0°C water drop was released from a syringe at a height of 0.5 cm. The PDMS-SH surface had a low icing delay time and many crystal sites so that the low-velocity cooled water drop did not rebound from the surface (Figure 6d). On the L-PDMS-SH (7.5%) surface, water drops easily

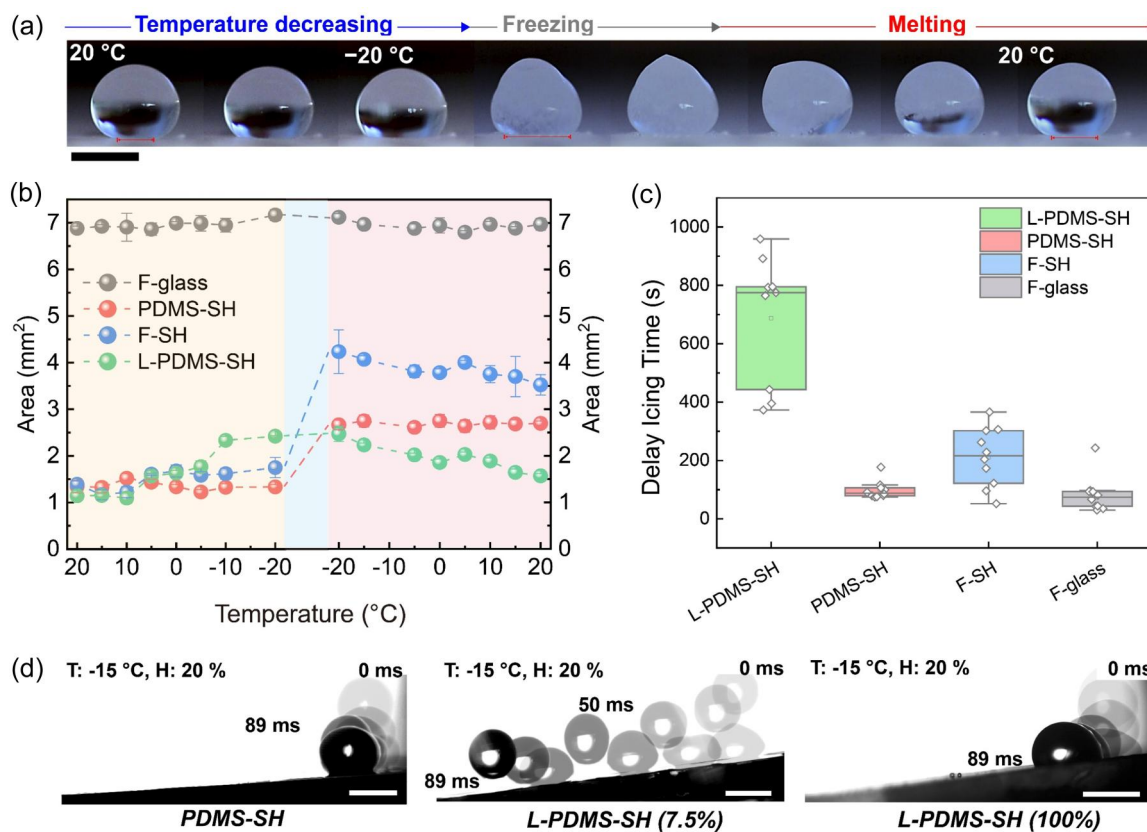


FIGURE 6 Improved icephobicity. (a) Image series showing the freezing and melting process of a 10 μL sessile water drop on the liquid-coated polydimethylsiloxane brush-modified superhydrophobic (L-PDMS-SH) (7.5%) surface. Scale bar: 2 mm. Surface temperature: -15°C ; humidity: 20%. (b) Contact area changes of a sessile water drop on four kinds of surfaces during the freezing and melting process. Yellow part (■): Cooling process. Blue part (■): Freezing process. Red part (■): Melting process. (c) Delay icing time of a sessile 10 μL water drop at -15°C on four different surfaces: L-PDMS-SH (7.5%), PDMS brush-modified superhydrophobic (PDMS-SH), fluorinated superhydrophobic surface (F-SH), and F-glass. (d) Drop impact on L-PDMS-SH (100%), PDMS-SH, and L-PDMS-SH (7.5%) surfaces in 89 ms, $We = 2.15$. Surface titling angle: 5° . Scale bar: 4 mm.

detach from this slightly tilting surface (titling angle: 5°) in a short time. For the surface in a slippery state, water drops will slide for a short distance at the beginning because of the initial energy. Water drops need quite a long time to slide over the surface (200 times longer than that on the superhydrophobic surface)⁵⁹ and it will be frozen on the surface in the end.

CONCLUSION

By coating the brush-modified nanostructure with liquid PDMS, we were able to create nanoscopic liquid-coated surfaces on which water drops form a Cassie state. The liquid nanofilm on top could be replenished from a micrometer-thick bottom oil layer hidden inside the nanostructure. The thickness and distribution of the oil-infused brush were obtained from AFM force measurements. The shedding velocity of liquid-coated surfaces was comparable to those observed on dry superhydrophobic surfaces. This liquid-coated superhydrophobic surface shows enhanced chemical stability based on the liquid nanofilm acting as a sacrificial and replenishable layer. After chemical

etching with an oxygen plasma, the surface recovered to the Cassie state due to the flow and exchange between the two-level oil layers. Oil depletion is quite low on the L-PDMS-SH (7.5%) surface compared to that on a slippery liquid-infused smooth or porous surface. The infused oil reduces the nucleation of cooled water drops and they have the highest icing delay time on the low-temperature liquid-coated superhydrophobic surface. Water drops can easily detach from this cooled surface. This new coating strategy helps us to fabricate robust superhydrophobic surfaces with high chemical stability, maintaining their superliquid repellency at low temperatures. This will be beneficial for the manufacture of long-term, self-cleaning, and corrosion-resistant devices used at low temperatures.

MATERIALS AND METHODS

Soot-templated surfaces were fabricated as described before⁹: glass slides ($4 \times 2 \text{ cm}^2$; EpreDia) were held 3 cm above the flame of a paraffin candle and moved back and forth for 30 s until they were coated with a black soot layer. The soot-coated glass substrates were

placed in a desiccator together with two open glass vessels containing 4 mL of tetraethoxysilane (TEOS, 98%; Sigma-Aldrich) and aqueous ammonia solution (25%; VWR Chemicals). The desiccator was closed and chemical vapor deposition of TEOS was carried out for 48 h. Then, the surfaces were annealed at 550°C for 2 h in air to remove the carbon cores. After treatment with oxygen plasma (5 min, 200 W, Femto low-pressure plasma system; Diener electronic GmbH) to increase reactivity, the slides were placed in 100 mL of silicon oil (100 cst, 6000 g/mol; Acros Organics) at 150°C for 24 h. Finally, they were immersed in a toluene environment for more than 10 min, and this process was repeated for three times to fully remove unbound PDMS. We call this PDMS layer “brush” here as in previous reports, although it is not clear if the bond to the substrate is really at the end of the chain and if the polymer chain conformation is highly stretched or not.

Silicon oil (100 cst, 6000 g/mol) was dissolved in toluene at concentrations of 100, 80, 60, 40, 20, 15, 10, 7.5, 5, 1, 0.1, 0.01, and 0 wt%. Then, 0.5 mL of these oil solutions was spin-coated (4000 rpm, 60 s) on the PDMS-SH surfaces. To evaporate the solvent, the surfaces were placed on a horizontal plate at 60°C for 1 h.

For comparison, we also prepared fluorinated surfaces. The candle-soot-templated surface was treated with oxygen plasma (5 min, 200 W) to increase reactivity. Then, the surface was placed in a vacuum desiccator containing a dish with 50 μL of 1H,1H,2H,2H-perfluorooctadecyltrichlorosilane (97%; Sigma-Aldrich). The desiccator was evacuated to 80–100 mbar. The reaction was allowed to proceed for 2 h. Finally, the surfaces were rinsed with ethanol to remove unbound silanes.

Silicon oil (100 cst) was dissolved in hexane in a weight ratio of 7.5 wt%. Hexane was used as a solvent because in penetrating the soot layer, toluene solutions were repelled. Then, 0.5 mL of this oil solution was spin-coated (4000 rpm, 60 s) on the fluorinated candle-soot-templated surface. The surface was placed on a horizontal plate at 60°C for 1 h to obtain the LIS.

Smooth lubricated PDMS brush surfaces were prepared as reported before.^{40,41,70} The glass slides were cleaned successively in hexane and alcohol with sonication for 3 min. Then, the glass slides were treated with oxygen plasma (5 min, 200 W). They were immersed in 100 mL of silicone oil (100 cst) at 150°C for 24 h. Then, the surfaces were rinsed with toluene three times. After that, silicon oil (100 cst) was spin-coated on the surfaces in 4000 rpm for 60 s. The oil-infused surfaces were then gently rinsed with ethanol ($\geq 99.8\%$; Honeywell) and Milli-Q water successively to remove nontethered oil.

To characterize the fluorinated surface, we also prepared samples on smooth glass slides. The glass slides were cleaned successively in hexane and alcohol with sonication for 3 min. Then, they were fluorinated as the F-SH surfaces.

The morphology of the surface was characterized by SEM (Zeiss LEO 1530 Gemini) at gun voltages of 1.5–3 kV using both the in-lens (for top view) and the SE2 detector (for cross-section view). To avoid charging, samples were sputtered with 7 nm Pt before measurement using a BalTec MED 020 modular high-vacuum coating system (argon pressure of 2×10^{-5} bar, current of 30 mA).

Advancing and receding contact angles as well as the roll-off angles of water on the surface were measured using an OCA 35 goniometer (DataPhysics Instruments). Side view videos of sessile drops were recorded on changing the volume of a sessile water drop gradually (0.5 $\mu\text{L}/\text{s}$) between 10 and 20 μL using a Hamilton syringe. Advancing and receding contact angles were determined by fitting an ellipse model to the contour images. Each data point is the average of at least three individual measurements on different areas of the surface.

The oil detection experiment was performed with cantilevers with a nominal resonance frequency of $f = 70$ kHz and a nominal spring constant of $k = 2$ N/m (Brucker OLTESPA). Spring constants were also measured using the thermal tune method. Samples were imaged using the JPK NanoWizard 4 AFM. The so-called QI mode was used to obtain force–distance curves at every point of the 128×128 pixel size scanning area ($3 \times 3 \mu\text{m}^2$ at a set point of 5 nN, a z length of 1 μm , and a time per pixel of 20 ms). To image the presence of oil on the samples, we looked at the instantaneous jump in the cantilever deflection signal on the approach cycle of the force–distance curves due to surface tension forces. The piezo position value at this point of the cantilever jump was subtracted from its position at the end of the approach cycle to obtain the “jump-in distance.” High values of jump-in distance indicate the presence of liquid on the sample surface. The jump-in distance was calculated for each force curve of the scan area automatically using a custom Python script (https://github.com/PranavSudersan/afm_surface_tension/blob/main/AFM_Liquid_Analyzer.ipynb).

^1H NMR measurement was used to determine the volume of depleted oil in the collected water. A 50 mL storage bottle was cleaned with Milli-Q water, ethanol, and acetone successively. After that, the bottle was heated at 60°C under vacuum to remove the residuals. The water drops sliding over the surface were collected in the bottle. The collected water was evaporated at 60°C for more than 24 h to obtain the depleted oil. The oil was then dissolved in CD_2Cl_2 (Deutero GmbH). The ^1H -NMR spectra were recorded on an AVANCE III Bruker NMR spectrometer (500 MHz) at 298 K with 16 scans and a relaxation delay of 12 s. The spectra were calibrated at 5.36 ppm with the remaining proton signal CHDCl_2 signal of the deuterated solvent.

Drop velocity was measured by a tilted platform as reported before⁷¹ by sliding 33 μL drops of distilled water (Thermo Fisher Scientific) over the surfaces. Drops were deposited at the top of a tilted sample by a grounded syringe needle (1.5 mm outer diameter), which was connected to a peristaltic pump (10 $\mu\text{L}/\text{s}$, MINIPULS 3; Gilson). The drops fell from a height of ≈ 5 mm, which is similar to the drop size to avoid drop rebounding. Drops were neutralized by a grounded copper wire before they landed on the surface. We imaged the drop with a frame rate of 1000 or 2000 per second on the side over a length of typically 4.5 cm with a high-speed camera (FASTCAM Mini UX100 [Photron] with a TitanTL telecentric lens, $\times 0.268$, 1 in., C-mount [Edmund Optics]). The videos were analyzed by an open drop-shape analysis from MATLAB. The dynamic contact angles were determined by applying a polynomial fit to every frame

of the images. Finally, we determined the drop velocity U by video analysis. All the measurements were performed at a temperature of $20 \pm 1^\circ\text{C}$ and humidity of 20%–40%.

ACKNOWLEDGMENTS

This project received funding from the European Research Council (ERC) under the European Union's Horizon 2020 research and innovation program (grant agreement no. 883631, DYNAMO). X. Z. is sponsored by the China Scholarship Council (CSC). We also acknowledge financial support from the German Research Society via the CRC 1194 (Project ID 265191195) project C07N (to C. H.). We are grateful for the technical help in SEM imaging provided by Gunnar Glasser.

CONFLICT OF INTEREST STATEMENT

The authors declare no conflict of interest.

ORCID

Pranav Sudersan  <http://orcid.org/0000-0003-2629-6535>

Hans-Jürgen Butt  <http://orcid.org/0000-0001-5391-2618>

REFERENCES

- Haechler I, Park H, Schnoering G, et al. Exploiting radiative cooling for uninterrupted 24-hour water harvesting from the atmosphere. *Sci Adv.* 2021;7:eabf3978.
- Schutzius TM, Jung S, Maitra T, Graeber G, Köhne M, Poulikakos D. Spontaneous droplet trampolining on rigid superhydrophobic surfaces. *Nature.* 2015;527:82-85.
- Wang D, Sun Q, Hokkanen MJ, et al. Design of robust superhydrophobic surfaces. *Nature.* 2020;582:55-59.
- Zhang W, Shi Z, Zhang F, Liu X, Jin J, Jiang L. Superhydrophobic and superoleophilic PVDF membranes for effective separation of water-in-oil emulsions with high flux. *Adv Mater.* 2013;25:2071-2076.
- Zhang S, Huang J, Chen Z, Lai Y. Bioinspired special wettability surfaces: from fundamental research to water harvesting applications. *Small.* 2017;13:1602992.
- Wang L, Tian Z, Jiang G, et al. Spontaneous dewetting transitions of droplets during icing & melting cycle. *Nat Commun.* 2022;13:378.
- Kreder MJ, Alvarenga J, Kim P, Aizenberg J. Design of anti-icing surfaces: smooth, textured or slippery? *Nat Rev Mater.* 2016;1:15003.
- Tuteja A, Choi W, Ma M, et al. Designing superoleophobic surfaces. *Science.* 2007;318:1618-1622.
- Deng X, Mammen L, Butt H-J, Vollmer D. Candle soot as a template for a transparent robust superamphiphobic coating. *Science.* 2012;335:67-70.
- Artus GRJ, Jung S, Zimmermann J, Gautschi HP, Marquardt K, Seeger S. Silicone nanofilaments and their application as superhydrophobic coatings. *Adv Mater.* 2006;18:2758-2762.
- Li L, Li B, Dong J, Zhang J. Roles of silanes and silicones in forming superhydrophobic and superoleophobic materials. *J Mater Chem A.* 2016;4:13677-13725.
- Ma M, Hill RM. Superhydrophobic surfaces. *Curr Opin Colloid Interface Sci.* 2006;11:193-202.
- Zhang W, Wang D, Sun Z, Song J, Deng X. Robust superhydrophobicity: mechanisms and strategies. *Chem Soc Rev.* 2021;50:4031-4061.
- Jin H, Tian X, Ikkala O, Ras RHA. Preservation of superhydrophobic and superoleophobic properties upon wear damage. *ACS Appl Mater Interfaces.* 2013;5:485-488.
- Chang F-M, Hong S-J, Sheng Y-J, Tsao H-K. High contact angle hysteresis of superhydrophobic surfaces: hydrophobic defects. *Appl Phys Lett.* 2009;95:0.
- Pierre-Gilles Gennes P-G, Brochard-Wyart F, Quéré D. *Capillarity and Wetting Phenomena: Drops, Bubbles, Pearls, Waves.* Springer; 2004.
- Ducom G, Laubie B, Ohannessian A, Chottier C, Germain P, Chatain V. Hydrolysis of polydimethylsiloxane fluids in controlled aqueous solutions. *Water Sci Technol.* 2013;68:813-820.
- Feng L, Yang Z, Zhai J, et al. Superhydrophobicity of nanostructured carbon films in a wide range of pH values. *Angew Chem Int Ed.* 2003;42:4217-4220.
- Wang C-F, Wang Y-T, Tung P-H, et al. Stable superhydrophobic polybenzoxazine surfaces over a wide pH range. *Langmuir.* 2006;22:8289-8292.
- Peng C, Chen Z, Tiwari MK. All-organic superhydrophobic coatings with mechanochemical robustness and liquid impalement resistance. *Nat Mater.* 2018;17:355-360.
- Chen L, Guo Z, Liu W. Outmatching superhydrophobicity: bio-inspired reentrant curvature for mighty superamphiphobicity in air. *J Mater Chem A.* 2017;5:14480-14507.
- Wu S, Du Y, Alsaid Y, et al. Superhydrophobic photothermal icephobic surfaces based on candle soot. *Proc Natl Acad Sci USA.* 2020;117:11240-11246.
- Flamm DL, Donnelly VM, Ibbotson DE. Basic chemistry and mechanisms of plasma etching. *J Vac Sci Technol B.* 1983;1:23-30.
- Vali G, DeMott PJ, Möhler O, Whale TF. Technical note: a proposal for ice nucleation terminology. *Atmos Chem Phys.* 2015;15:10263-10270.
- Liu K, Wang C, Ma J, et al. Janus effect of antifreeze proteins on ice nucleation. *Proc Natl Acad Sci USA.* 2016;113:14739-14744.
- Zhang R, Hao P, Zhang X, He F. Supercooled water droplet impact on superhydrophobic surfaces with various roughness and temperature. *Int J Heat Mass Transfer.* 2018;122:395-402.
- Schremb M, Roisman IV, Tropea C. Normal impact of supercooled water drops onto a smooth ice surface: experiments and modelling. *J Fluid Mech.* 2018;835:1087-1107.
- Wang Q, Sun G, Tong Q, Yang W, Hao W. Fluorine-free superhydrophobic coatings from polydimethylsiloxane for sustainable chemical engineering: preparation methods and applications. *Chem Eng J.* 2021;426:130829.
- Wong TS, Kang SH, Tang SKY, et al. Bioinspired self-repairing slippery surfaces with pressure-stable omniphobicity. *Nature.* 2011;477:443-447.
- Lee J, Shin S, Jiang Y, Jeong C, Stone HA, Choi C-H. Oil-impregnated nanoporous oxide layer for corrosion protection with self-healing. *Adv Funct Mater.* 2017;27:1606040.
- Li J, Ueda E, Paulssen D, Levkin PA. Slippery lubricant-infused surfaces: properties and emerging applications. *Adv Funct Mater.* 2019;29:1802317.
- Zhao H, Sun Q, Deng X, Cui J. Earthworm-inspired rough polymer coatings with self-replenishing lubrication for adaptive friction-reduction and antifouling surfaces. *Adv Mater.* 2018;30:1802141.
- Li X, Yang J, Lv K, et al. Salvinia-like slippery surface with stable and mobile water/air contact line. *Natl Sci Rev.* 2021;8:nwaa153.
- Dong Z, Schumann MF, Hokkanen MJ, et al. Superoleophobic slippery lubricant-infused surfaces: combining two extremes in the same surface. *Adv Mater Deerfield.* 2018;30:1803890.
- Launay G, Sadullah MS, McHale G, Ledesma-Aguilar R, Kusumaatmaja H, Wells GG. Self-propelled droplet transport on shaped-liquid surfaces. *Sci Rep.* 2020;10:14987.
- Jenner E, D'Urso B. Wetting states on structured immiscible liquid coated surfaces. *Appl Phys Lett.* 2013;103:0.
- Villegas M, Zhang Y, Abu Jarad N, Soleymani L, Didar TF. Liquid-Infused surfaces: a review of theory, design, and applications. *ACS Nano.* 2019;13:8517-8536.

- 1 38. Teisala H, Geyer F, Haapanen J, et al. Ultrafast processing of
2 hierarchical nanotexture for a transparent superamphiphobic coat-
3 ing with extremely low roll-off angle and high impalement pressure.
4 *Adv Mater.* 2018;30:1706529.
5 39. Lhermerout R, Davitt K. Contact angle dynamics on pseudo-brushes:
6 effects of polymer chain length and wetting liquid. *Colloids Surf A.*
7 2019;566:148-155.
8 40. Chen L, Park S, Yoo J, et al. One-step fabrication of universal
9 slippery lubricated surfaces. *Adv Mater Interfaces.* 2020;7:2000305.
10 41. Teisala H, Baumli P, Weber SAL, Vollmer D, Butt H-J. Grafting
11 silicone at room temperature—a transparent, scratch-resistant
12 nonstick molecular coating. *Langmuir.* 2020;36:4416-4431.
13 42. Zhao X, Khatir B, Mirshahidi K, Yu K, Kizhakkedathu JN, Golovin K.
14 Macroscopic evidence of the liquidlike nature of nanoscale
15 polydimethylsiloxane brushes. *ACS Nano.* 2021;15:13559-13567.
16 43. Leslie DC, Waterhouse A, Berthet JB, et al. A bioinspired
17 omniphobic surface coating on medical devices prevents thrombosis
18 and biofouling. *Nat Biotechnol.* 2014;32:1134-1140.
19 44. Peppou-Chapman S, Neto C. Depletion of the lubricant from
20 lubricant-infused surfaces due to an air/water interface. *Langmuir.*
21 2021;37:3025-3037.
22 45. Huang Y, Stogin BB, Sun N, Wang J, Yang S, Wong T-S. A switchable
23 cross-species liquid repellent surface. *Adv Mater.* 2017;29:1604641.
24 46. Dai X, Stogin BB, Yang S, Wong T-S. Slippery Wenzel state. *ACS*
25 *Nano.* 2015;9:9260-9267.
26 47. Wooh S, Vollmer D. Silicone brushes: omniphobic surfaces with low
27 sliding angles. *Angew Chem Int Ed.* 2016;55:6822-6824.
28 48. Okumura K, Chevy F, Richard D, Quéré D, Clanet C. Water spring: a
29 model for bouncing drops. *Europhys Lett.* 2003;62:237-243.
30 49. Deng X, Schellenberger F, Papadopoulos P, Vollmer D, Butt H-J.
31 Liquid drops impacting superamphiphobic coatings. *Langmuir.* 2013;
32 29:7847-7856.
33 50. Tsai P, Pacheco S, Pirat C, Lefferts L, Lohse D. Drop impact upon
34 micro- and nanostructured superhydrophobic surfaces. *Langmuir.*
35 2009;25:12293-12298.
36 51. Han X, Li W, Zhao H, Li J, Tang X, Wang L. Slippery damper of an
37 overlay for arresting and manipulating droplets on nonwetting
38 surfaces. *Nat Commun.* 2021;12:3154.
39 52. Smith JD, Dhiman R, Anand S, et al. Droplet mobility on lubricant-
40 impregnated surfaces. *Soft Matter.* 2013;9:1772-1780.
41 53. Keiser A, Keiser L, Clanet C, Quéré D. Drop friction on liquid-infused
42 materials. *Soft Matter.* 2017;13:6981-6987.
43 54. Olin P, Lindström SB, Pettersson T, Wågberg L. Water drop friction
44 on superhydrophobic surfaces. *Langmuir.* 2013;29:9079-9089.
45 55. Chen Q, Dai L, Gao M, Huang S, Mau A. Plasma activation of carbon
46 nanotubes for chemical modification. *J Phys Chem B.* 2001;105:618-622.
47 56. Liu S, Zhou H, Wang H, et al. Argon-plasma reinforced super-
48 amphiphobic fabrics. *Small.* 2017;13:0.
49 57. Ortiz-Ortega E, Hosseini S, Martinez-Chapa SO, Madou MJ. Aging of
50 plasma-activated carbon surfaces: challenges and opportunities.
51 *Appl Surf Sci.* 2021;565:150362.
52 58. Malmström J. Quantification of silicone oil and its degradation
53 products in aqueous pharmaceutical formulations by ¹H-NMR
spectroscopy. *J Pharm Sci.* 2019;108:1512-1520.
59. Badr RGM, Hauer L, Vollmer D, Schmid F. Cloaking transition of
droplets on lubricated brushes. *J Phys Chem B.* 2022;126:7047-7058.
60. Wong WSY, Hegner KI, Donadei V, Hauer L, Naga A, Vollmer D.
Capillary balancing: designing frost-resistant lubricant-infused sur-
faces. *Nano Lett.* 2020;20:8508-8515.
61. Helseth LE. Influence of salt concentration on charge transfer
when a water front moves across a junction between a
hydrophobic dielectric and a metal electrode. *Langmuir.* 2020;36:
8002-8008.
62. Yatsuzuka K, Mizuno Y, Asano K. Electrification phenomena of pure
water droplets dripping and sliding on a polymer surface. *J Electrostat.*
1994;32:157-171.
63. Stetten AZ, Golovko DS, Weber SAL, Butt H-J. Slide electrification:
charging of surfaces by moving water drops. *Soft Matter.* 2019;15:
8667-8679.
64. Li S, Bista P, Weber SAL, Kappl M, Butt H-J. Spontaneous charging of
drops on lubricant-infused surfaces. *Langmuir.* 2022;38:12610-12616.
65. Marín AG, Enríquez OR, Brunet P, Colinet P, Snoeijer JH.
Universality of tip singularity formation in freezing water drops.
Phys Rev Lett. 2014;113:054301.
66. Gao N, Geyer F, Pilat DW, et al. How drops start sliding over solid
surfaces. *Nat Phys.* 2018;14:191-196.
67. Hinduja C, Laroche A, Shumaly S, et al. Scanning drop friction force
microscopy. *Langmuir.* 2022;38:14635-14643.
68. Tan Y, Yang J, Li Y, et al. Liquid-pressure-guided superhydrophobic
surfaces with adaptive adhesion and stability. *Adv Mater.* 2022;34:
2202167.
69. Hao C, Li J, Liu Y, et al. Superhydrophobic-like tunable droplet
bouncing on slippery liquid interfaces. *Nat Commun.* 2015;6:7986.
70. Krumpfer JW, McCarthy TJ. Rediscovering silicones: “unreactive”
silicones react with inorganic surfaces. *Langmuir.* 2011;27:11514-11519.
71. Li X, Bista P, Stetten AZ, et al. Spontaneous charging affects the
motion of sliding drops. *Nat Phys.* 2022;18:713-719.

SUPPORTING INFORMATION

Additional supporting information can be found online in the Supporting Information section at the end of this article.

How to cite this article: Zhou X, Sudersan P, Diaz D, et al. Chemically robust superhydrophobic surfaces with a self-replenishing nanoscale liquid coating. *Droplet.* 2023;e103. doi:10.1002/dro2.103

Supporting Information

Chemically robust superhydrophobic surfaces with a self-replenish nano-scale liquid coating

Xiaoteng Zhou,¹ Pranav Sudersan,¹ Diego Diaz,¹ Benjamin Leibauer,¹ Chirag Hinduja,¹ Darvish Fahimeh,¹ Pravash Bista,¹ Lukas Hauer,¹ Manfred Wagner,¹ Werner Steffen,¹ Jie Liu,^{1,2,3} Michael Kappl,^{1*} Hans-Jürgen Butt^{1*}*

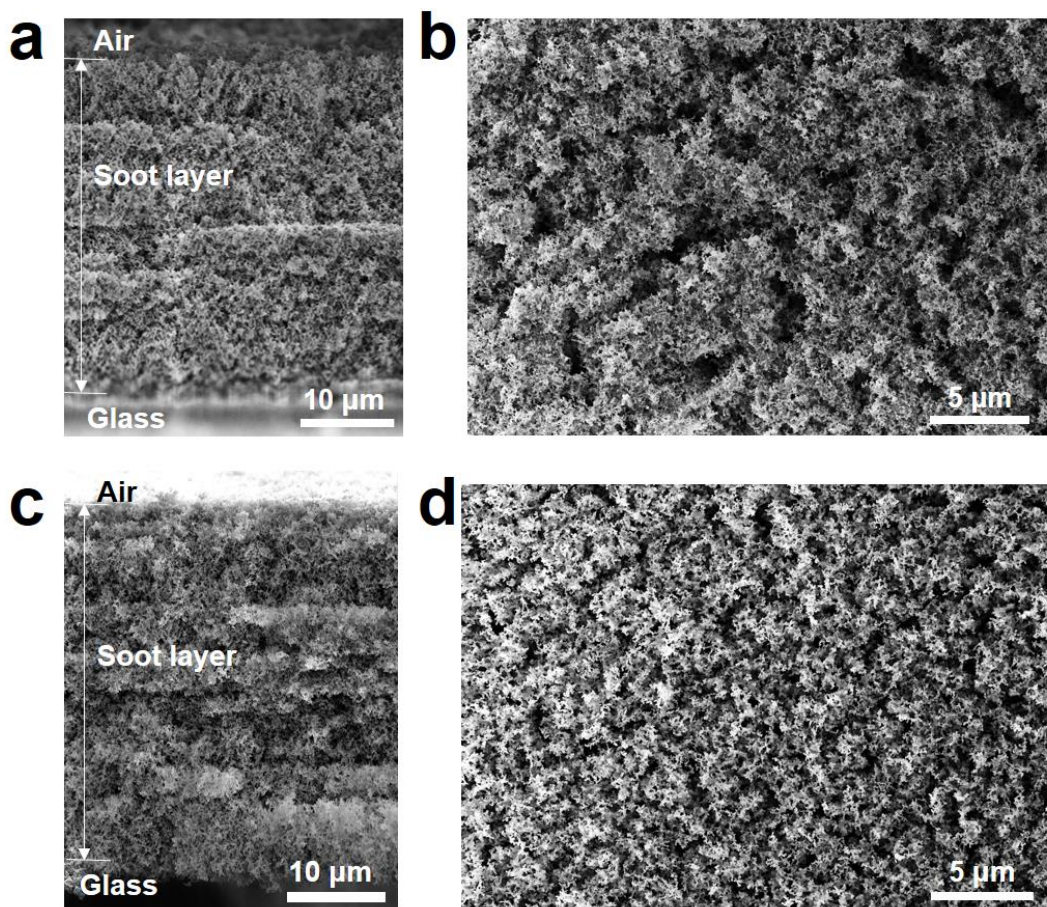
¹Max Planck Institute for Polymer Research, Ackermannweg 10, 55128, Mainz, Germany.

²Key Laboratory of Green Printing, Beijing National Laboratory for Molecular Science, Institute of Chemistry, Chinese Academy of Sciences, Beijing 100190, PR China

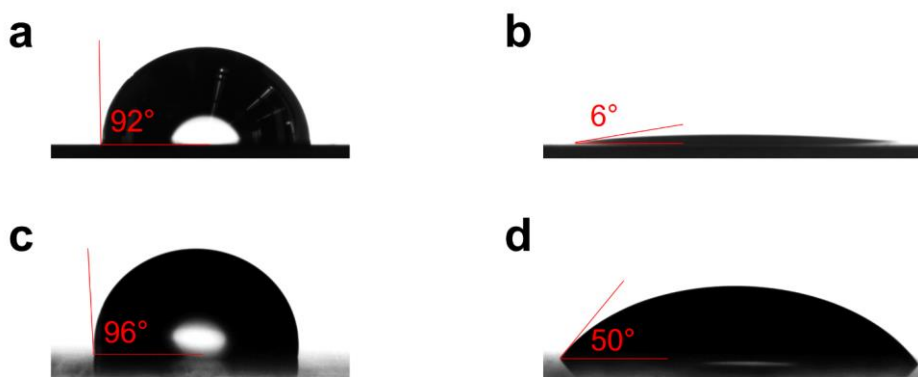
³School of Chemical Sciences, University of Chinese Academy of Sciences, Beijing 100190, PR China

*E-mail: liujie123@iccas.ac.cn, kappl@mpip-mainz.mpg.de, butt@mpip-mainz.mpg.de.

Keywords: wetting, liquid coating, drop dynamics, chemical stable, anti-icing



Supplementary Figure S1. **a** Cross-section and **b** top view of candle-soot templated SiO₂ surface before PDMS modification. **c** Cross-section and **d** top view of candle-soot template SiO₂ surface after PDMS modification (PDMS-SH surface).

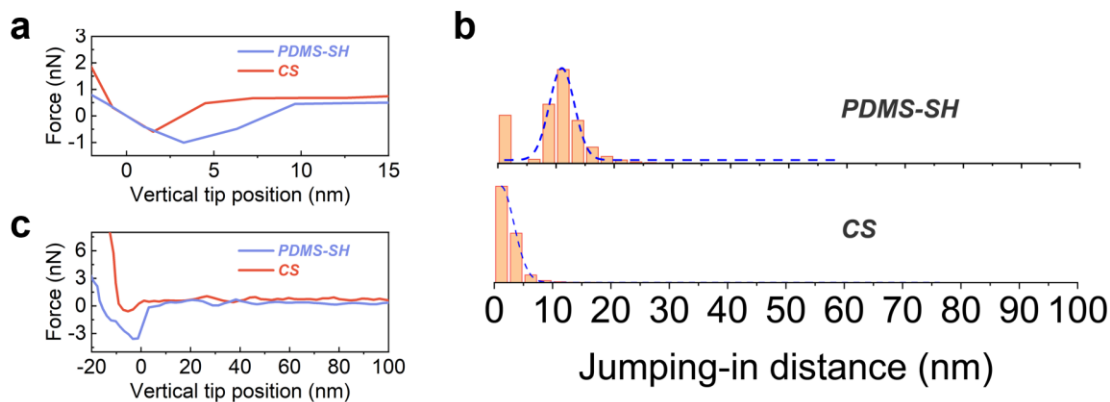


Supplementary Figure S2. **a, b** Static contact angle of **a** water and **b** 100 cSt silicone oil on a smooth PDMS brush-modified Si wafer. **c, d** Static contact angle of **c** water and **d** 100 cSt silicone oil on smooth fluorinated Si wafer.

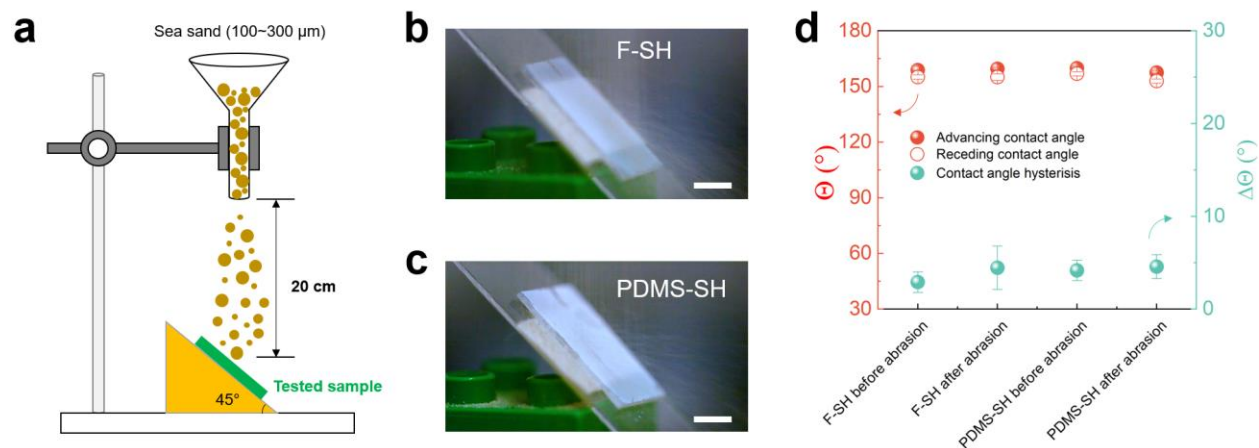
Supplementary Section 1. Characterization of the covalently bonded PDMS brush

It is thought to be covalent, because one cannot remove the PDMS layer by e.g. exposing it to a good solvent. In our preparation, we immerse the PDMS modified soot-template surface in toluene for more than 10 minutes and repeat this process 3 times.

From the jumping-in distance in the AFM approaching force curve, we can know the jumping distance measured on the PDMS coated surface is much higher than that measured on a pure soot-template surface (Figure S3a and b). The retracting force curve also shows an obvious soft retracting process compared to the pure soot-template structure (Figure S3c). From these results, we can conclude the PDMS coated soot-template surface has higher softness than that of a pure soot-template surface which illustrates a soft brush morphology of the coated layer.



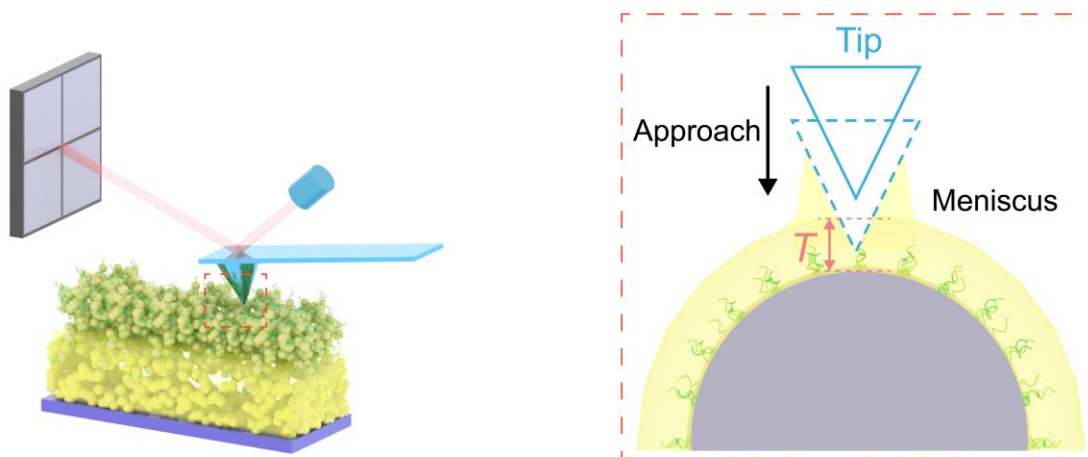
Supplementary Figure S3. (a) AFM approaching force curve measured on PDMS brush modified soot templated surface (PDMS-SH) surface and pure candle-soot-template (CS) surface. (b) The histogram of the frequency count of jump-in distances on PDMS-SH and CS surfaces (c) AFM retracting force curve measured on PDMS-SH and CS surfaces



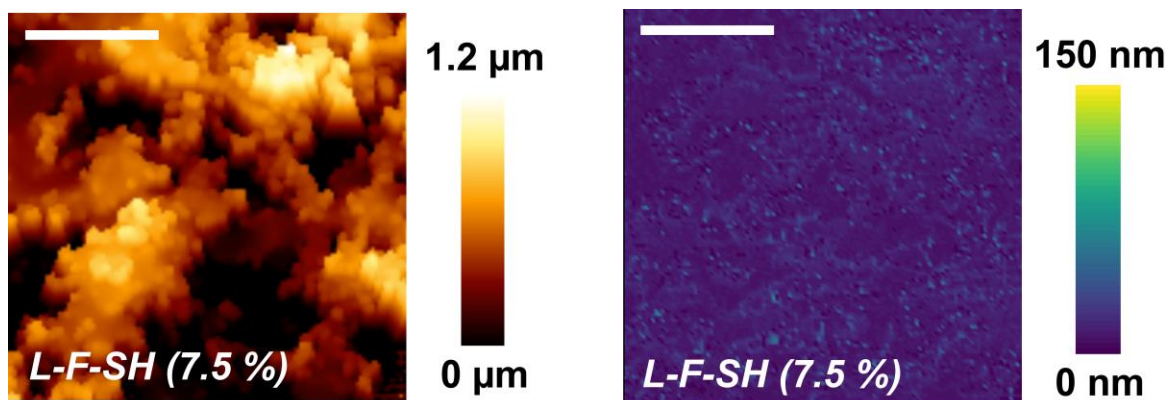
Supplementary Figure S4. Mechanical resistance quantified by sand abrasion. (a) The scheme showing the sand abrasion test. (b) (c) The appearance of the (b) F-SH and (c) PDMS-SH during the sand abrasion test, scale bar: 1 cm. d) Advancing and receding contact angles, and contact angle hysteresis $\Delta\theta$ of water on these two surfaces before and after 5 min sand abrasion test.

Supplementary Section 2. AFM force measurement

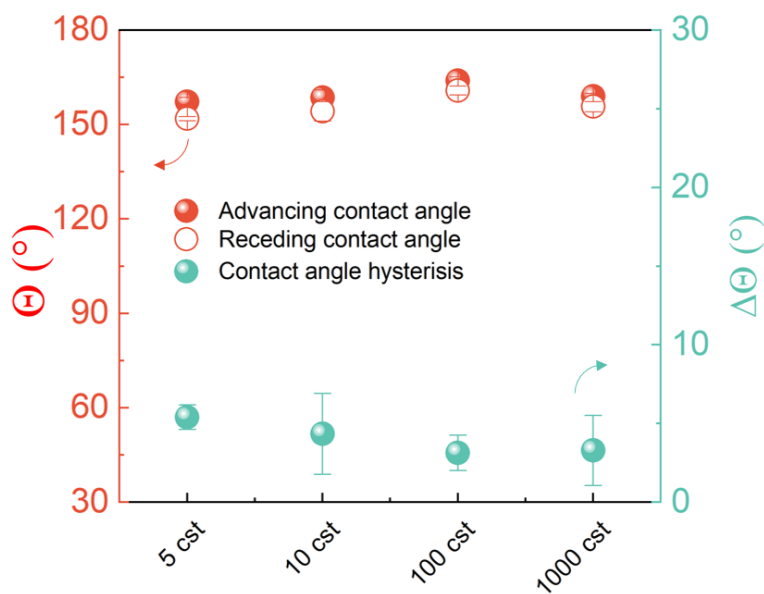
In an AFM force experiment, the tip is constantly moved up and down. During the lower part of this cycle, it contacts the topmost nanoscopic structures of the L-PDMS-SH surface. When the tip contacts the top of the oil-infused PDMS brush, a meniscus is formed between the tip and liquid, which leads to an attractive capillary force (Supplementary Fig. S5). This force remains attractive while the tip further penetrates the liquid layer. When it has fully penetrated the liquid and contacts the solid SiO_2 , the tip starts to deflect in the opposite direction, reflected by a sharp increase in force. The “jump-in distance” is measured by calculating the difference between the piezo position value at this point of the cantilever jump and at the end of the approach cycle. It can illustrate the thickness T of the fluid layer.



Supplementary Figure S5. The scheme to show the method to measure the force between the cantilever tip and the oil on top of the surface by atomic force microscopy (AFM).



Supplementary Figure S6. The AFM topography of the L-F-SH (7.5%) surface and the map illustrates the two-dimension distribution of the jump-in distance of the approaching force curve in the corresponding area. Scale bar: 500 nm.



Supplementary Figure S7. Advancing and receding contact angles, and contact angle hysteresis $\Delta\theta$ of water on L-PDMS-SH surfaces with infusing 7.5 % oil/toluene mixtures. The oil viscosities in these mixtures are 5 cst, 10 cst, 100 cst and 1000 cst, respectively.

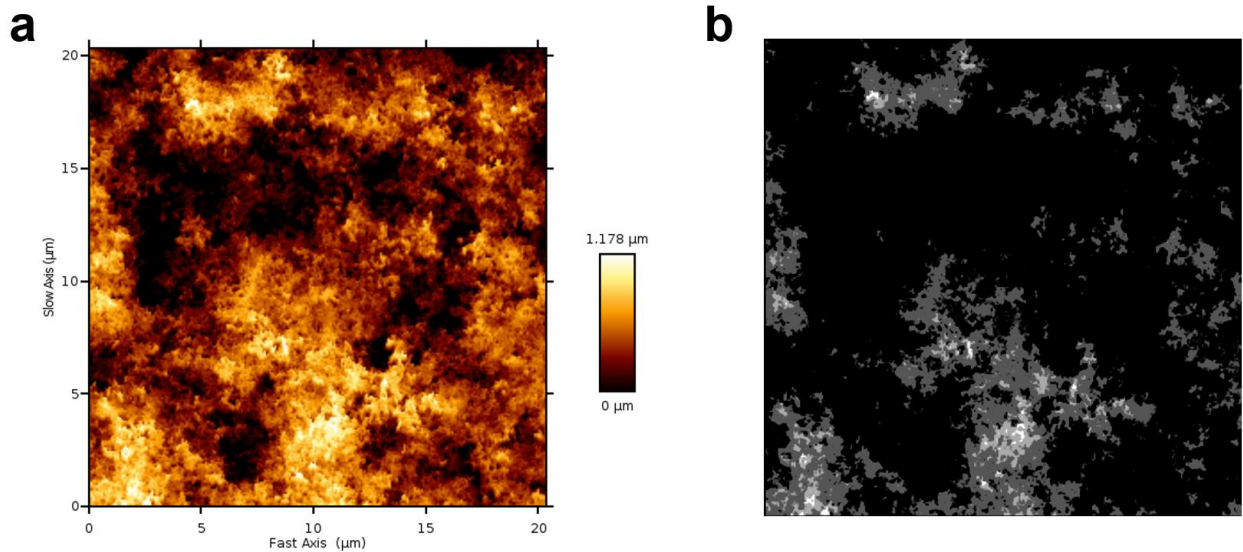
Supplementary Section 3. Prediction of the static contact angle

A reminiscent of the Cassie–Baxter equation $\cos \theta^* = f_l \cos \theta_l - (1 - f_l)$ to evaluate the apparent equilibrium contact angle θ^* . Here, f_l is the solid surface area fraction (which is covered by oil) and θ_l is the contact angle of water on a flat oil infused surface. We neglect the deformation of the oil-infused PDMS brush. The whole soot structure is covered by an oil infused PDMS layer. For this reason, we can assume that the fraction f_l is equal to the solid fraction f_s , estimated from AFM images (Supplementary Figure S8). The average solid fraction measured by a binary process of the AFM morphology image is around 0.24 and θ_l is around 106° . The calculated contact angle θ^* is $\approx 165^\circ$. It agrees with the contact angle measurement for the drops on the surface in a superhydrophobic state.

However, if the bottom oil layer is too thick (Figure 2a when silicone oil concentration is above 60%), the air gap between the structure disappears. The drop on the surface will not be in a Cassie–Baxter state. In this state the contact angle hysteresis is so large, that an estimation of the equilibrium contact angle does not make sense. A measured static

contact angle is somewhere between the receding and advancing contact angle, depending on how a drop is placed.

For slippery state drop (100 % sample), the static contact angle on them will be similar to a water drop on a silicone oil surface which is 100° . This value agrees with one calculated with the modified Young's equation (McHale et al., Langmuir 2019, 35, 11, 4197–4204) $\cos \theta = \frac{\gamma_o - \gamma_{wo}}{\gamma_w}$ of $\theta = 101^\circ$. Here, $\gamma_o = 21$ mN/m is the surface tension of the silicon oil, $\gamma_{wo} = 35$ mN/m is the interfacial tension of silicon oil-water, and $\gamma_w = 72$ mN/m is the surface tension of water.

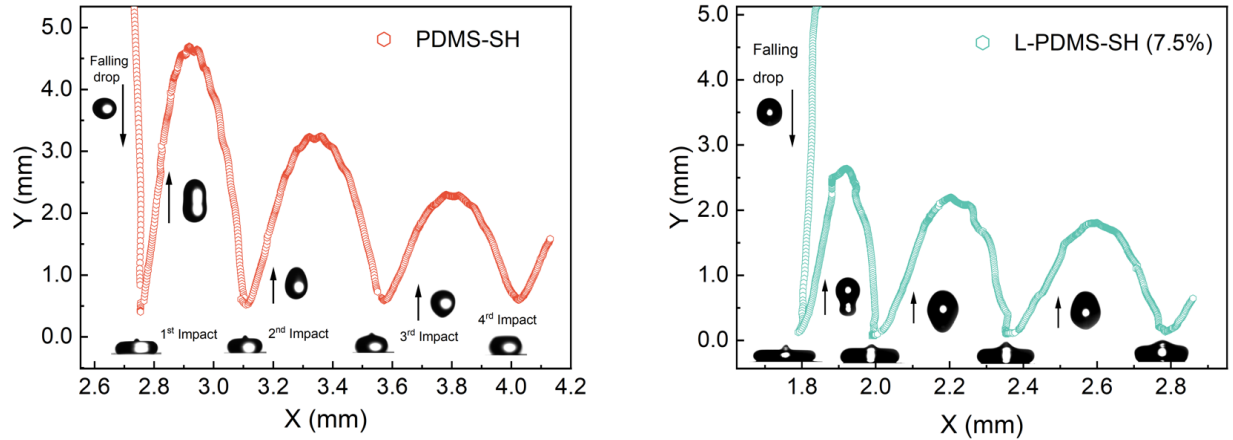


Supplementary Figure S8. (a) AFM morphology image of the candle-soot template surface in a $20 \mu\text{m} \times 20 \mu\text{m}$ area. (b) An 8-bit image to show the solid fraction at the interface by a binary process to the image by ImageJ.

Supplementary Section 4. Drop dynamics

Tracking the drop mass center position

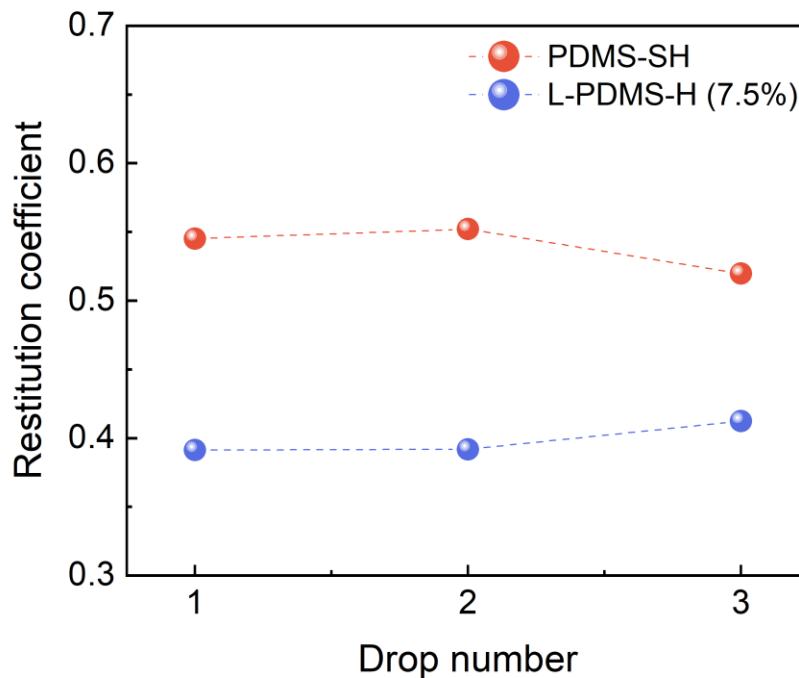
An algorithm in MATLAB software was developed to track the drop mass center position during the impact at each frame of the high-speed videos. The algorithm considers that the drop mass center coincides with the centroid of the drop. The tracking process serves additionally to know the velocity of the moving drop at each frame.



Supplementary Figure S9. Position of the center of mass of a drop rebounding from **a** PDMS-SH (Left) and **b** L-PDMS-SH (Right).

Restitution coefficient

The restitution coefficients for PDMS-SH and L-PDMS-SH were calculated by $e = U_R/U_0$, where U_R is the rebounding velocity, immediately after impact, and U_0 is the impact speed.



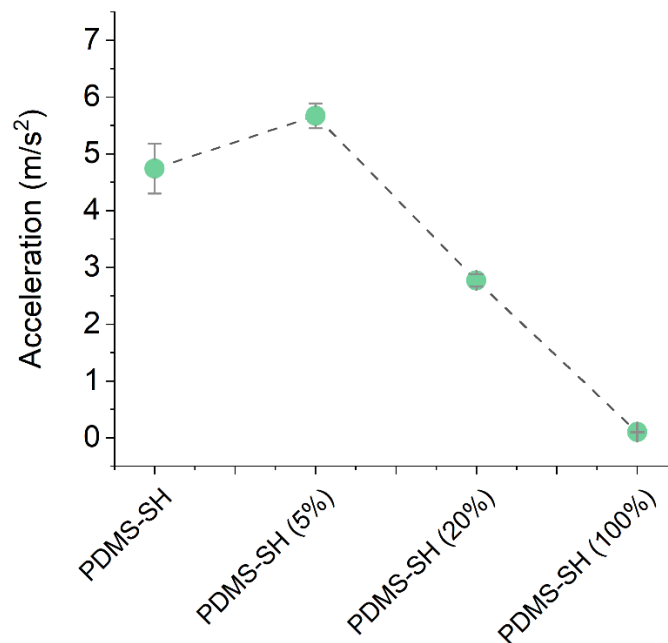
Supplementary Figure S10. Restitution coefficient versus the drop number when water drop impact on PDMS-SH and L-PDMS-SH surfaces.

Evaluation of the drop velocity

For superhydrophobic surface, the velocity can be predicted as Pontus reported^[1] due to the acceleration a that $a = g \sin \alpha - b_{sh} g Bo^{-1/2}$, α is the surface tilting angle, g is the gravitational acceleration, b_{sh} is the friction coefficient and Bo is the Bond number.

Inspired by this, we can add one more idea when drops sliding off the L-PDMS-SH surfaces (Figure 2a). The equation of motion is in general: $\frac{m}{k} \dot{U} = mg \sin \alpha - \beta U$. Here, \dot{U} is the drop velocity, k is a factor which takes the inertia of the drop into account. It is 5/7 for a perfectly rolling sphere and 1 for perfectly sliding drop without rolling component.

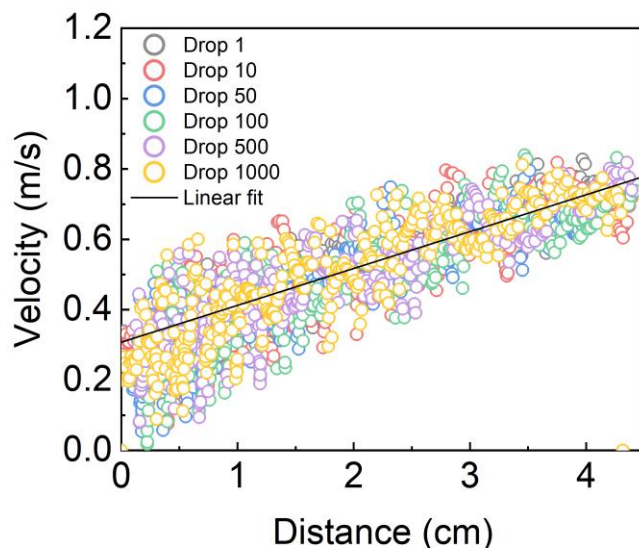
This equation is solved by $U = U_0(1 - e^{-t/\tau}) \Rightarrow \dot{U} = \frac{U_0}{\tau} e^{-t/\tau}$, (U_0 : final steady state velocity). $\frac{m}{k} \frac{U_0}{\tau} e^{-t/\tau} = mg \sin \alpha - \beta U_0(1 - e^{-t/\tau}) \Rightarrow U_0 = \frac{mg \sin \alpha}{\beta}$ and $\frac{m}{k} \frac{U_0}{\tau} e^{-t/\tau} = \beta U_0 e^{-t/\tau} \Rightarrow \tau = \frac{m}{k\beta}$. The initial acceleration is $\dot{U}(t=0) = kg \sin \alpha$. For drops at 40° tilt, the expected initial acceleration is 5 m/s² for rolling sphere and 6.3 m/s² for perfectly sliding drop.



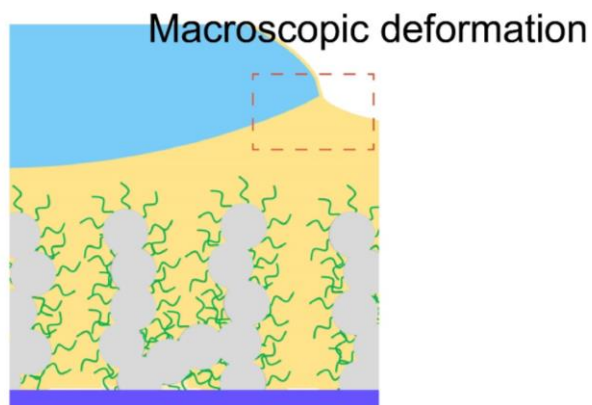
Supplementary Figure S11. The initial acceleration of 33 μ L water drops moving at 40° tilting angle on four different surfaces.

The measured initial acceleration of moving water drops on PDMS-SH and PDMS-SH (5%) surfaces was $\approx 5 \text{ m/s}^2$ (Supplementary Figure S11), highly agrees with the calculation. If the drop is in a slippery Wenzel state, the drop will contact the bottom oil layer. It will result in more friction. Therefore, the initial acceleration is smaller.

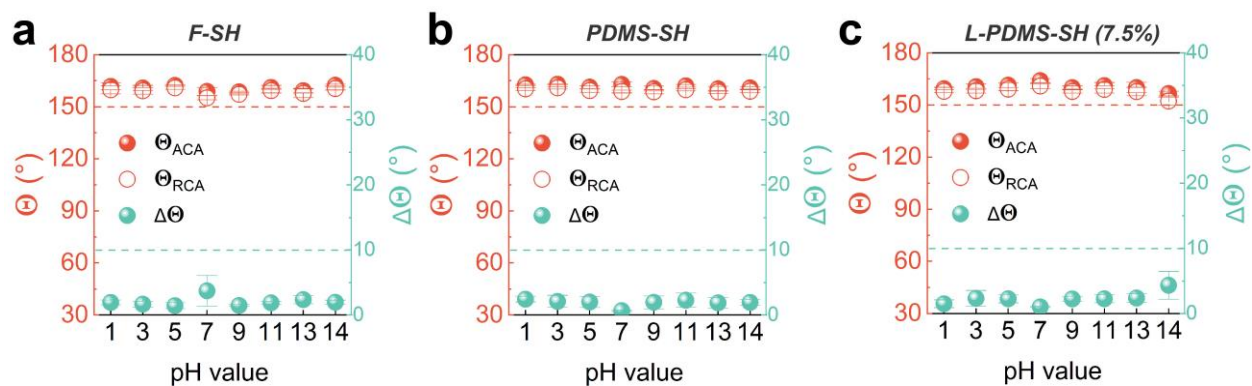
For a smooth slippery state drop (Figure 2a, yellow area), the magnitude of the velocity data agrees with the model of Keiser et al. [2] before $U = \frac{(\rho g)^{2/3} R^3}{\gamma_0^{1/2} \beta \eta_0} \sin^{3/2} \alpha$, when the oil viscosity is bigger than that of water. Here, ρ is the drop density, γ_0 is the oil surface tension, η_0 is the oil viscosity, V is the drop volume, R is the radius of the drop, $\beta = \ln \frac{l}{h}$, with l being the meniscus size and h being the oil layer thickness, is the numerical factor reflecting the singular dissipation at the wedge tip. We estimate it to be an order of 10 according to the reference.[2] For an apparent contact angle of 90° drop, it is related to the drop volume V by $R = \left(\frac{3V}{2\pi}\right)^{1/3}$. Then, we can the equation: $U = \frac{(\rho g)^{3/2} V}{2\pi\sqrt{3}\beta\eta_0\gamma_0^{1/2}} \sin^{3/2} \alpha$, to calculate the steady drop velocity on such smooth slippery surface. The calculated value is around 0.02 m/s which agrees with the experimental result (0.04 m/s).



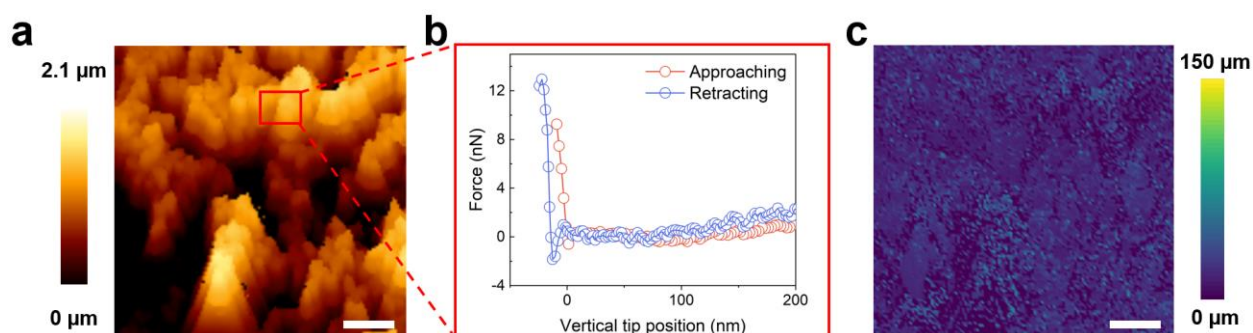
Supplementary Figure S12. Drop velocity versus slide distance when water drops slide over the PDMS-SH surface for a 4 cm distance.



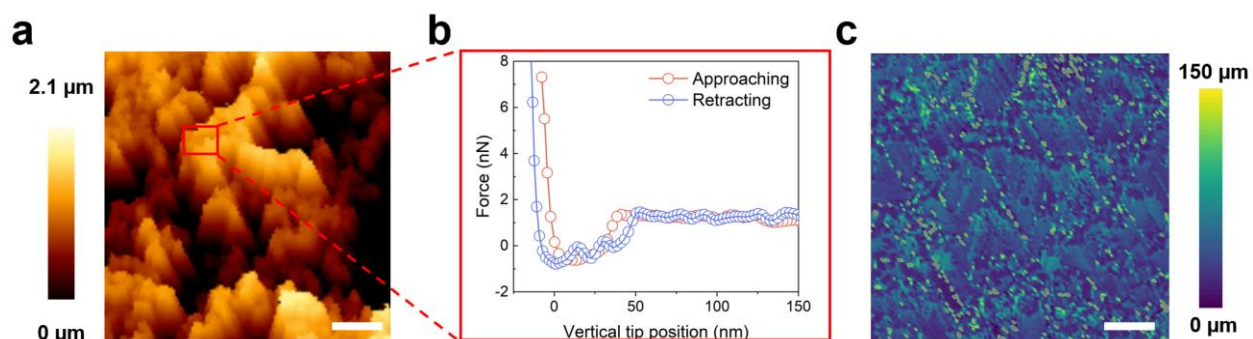
Supplementary Figure S13. The middle scheme illustrates the elastic deformation near the three-phase contact line when the liquid coating thickness is in macroscopic scale.



Supplementary Figure S14. Advancing and receding contact angles (Θ_{ACA} and Θ_{RCA}) and contact angle hysteresis ($\alpha_{roll-off}$) of 10 μ L drops with different pH values on **a** F-SH, **b** PDMS-SH and **c** L-PDMS-SH (7.5%) surfaces.

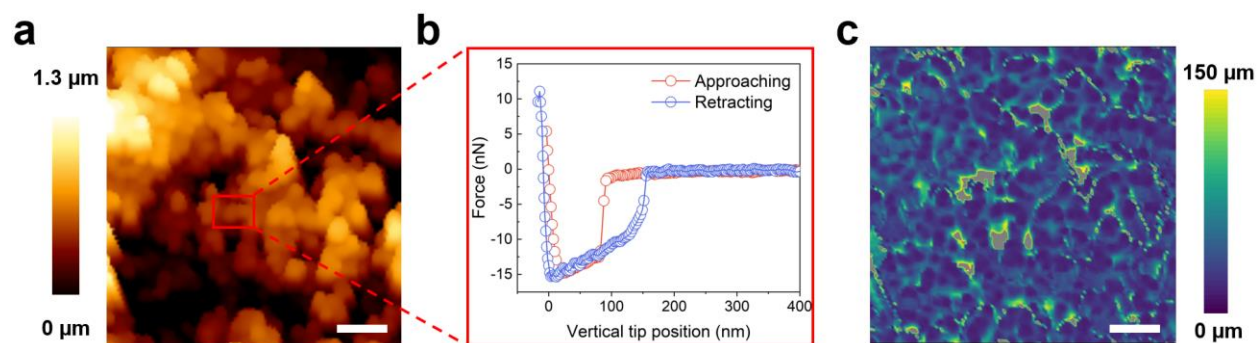


Supplementary Figure S15. Verification of absence of infused nano-scale oil layer on L-PDMS-SH (7.5%) surface after around 1000 min of alkali treatment. **a** AFM image of the surface topography. **b** The force curve was measured in the indicated area. **c** Map of jump-in distances in the approaching force curve on the surface. Scale bar: 500 nm.

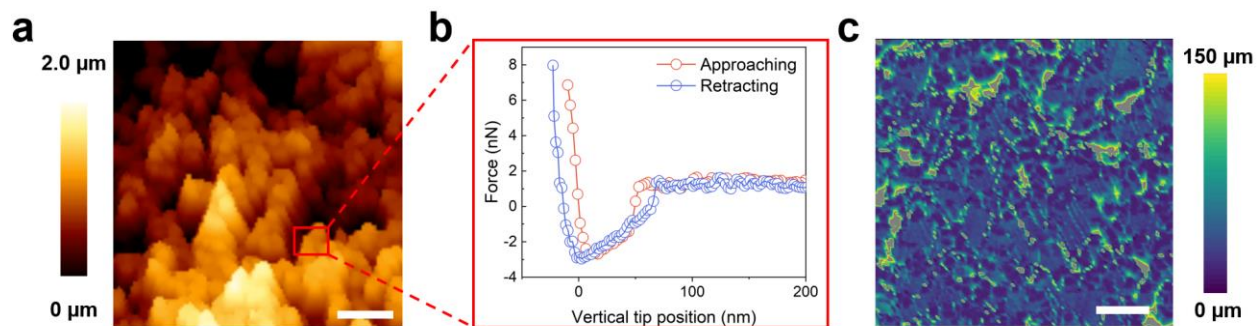


Supplementary Figure S16. The nano-scale infused oil layer on L-PDMS-SH (7.5%) surface after around 1000 min of acid treatment. **a** AFM image of the surface topography.

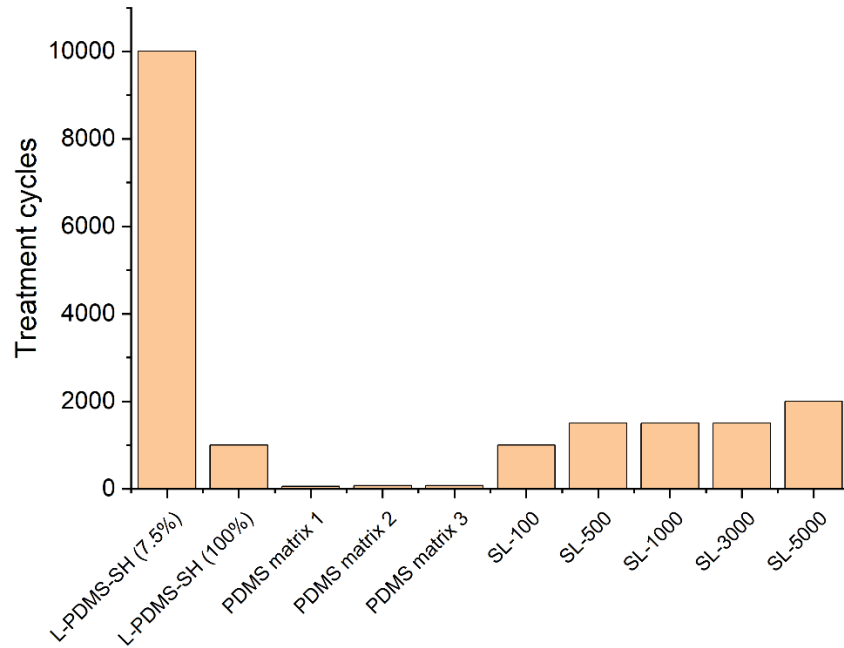
b The force curve was measured in the indicated area. **c** Map of jump-in distances in the approaching force curve on the surface. Scale bar: 500 nm.



Supplementary Figure S17. The nano-scale infused oil layer on L-PDMS-SH (7.5%) surface after plasma treatment once. **a** AFM image of the surface topography. **b** The force curve was measured in the indicated area. **c** Map of jump-in distances in the approaching force curve on the surface. Scale bar: 500 nm.



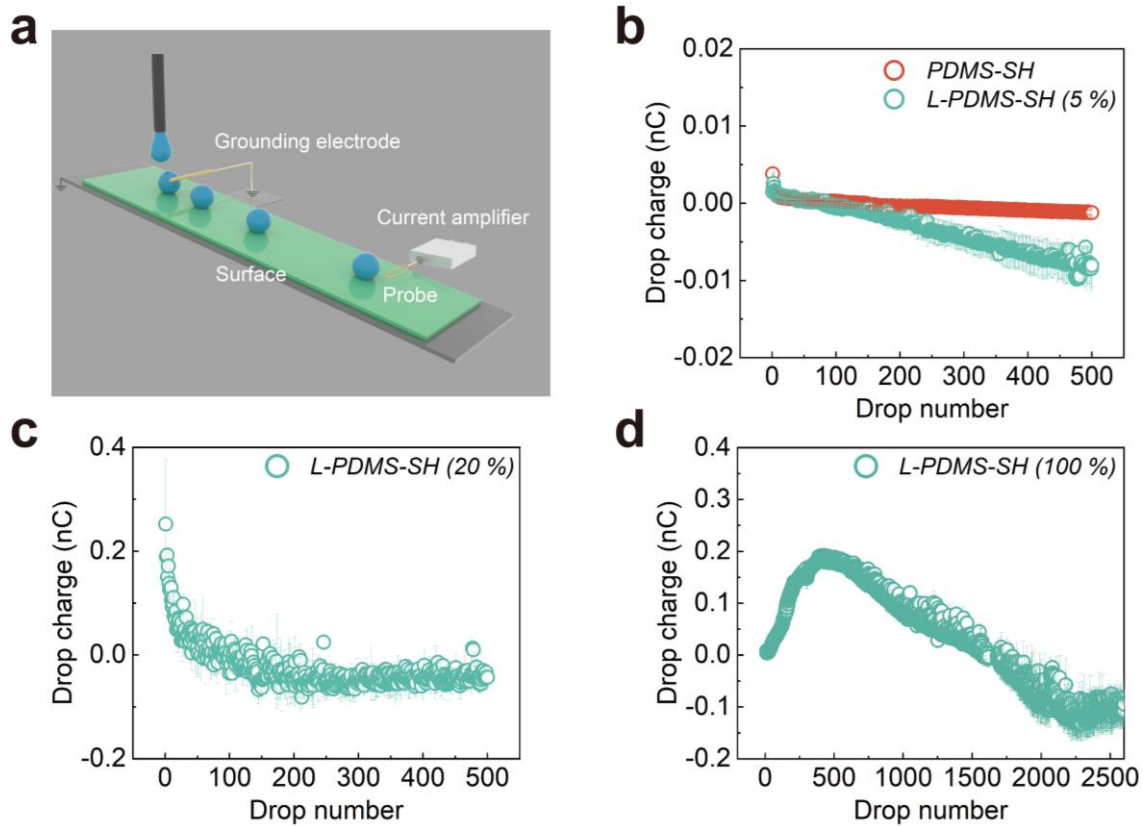
Supplementary Figure S18. The nano-scale infused oil layer on L-PDMS-SH (7.5%) surface after 500 drops sliding off. **a** AFM image of the surface topography. **b** The force curve was measured on the indicated area. **c** Map of jump-in distances in the approaching force curve on the surface. Scale bar: 500 nm.



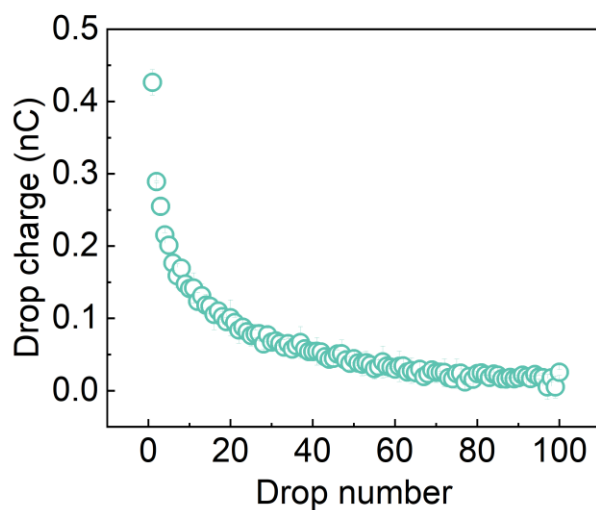
Supplementary Figure S19. Maximum treatment cycles for different liquid infused or liquid coated surfaces to maintain their original wetting property.

Supplementary Section 5. Drop charge

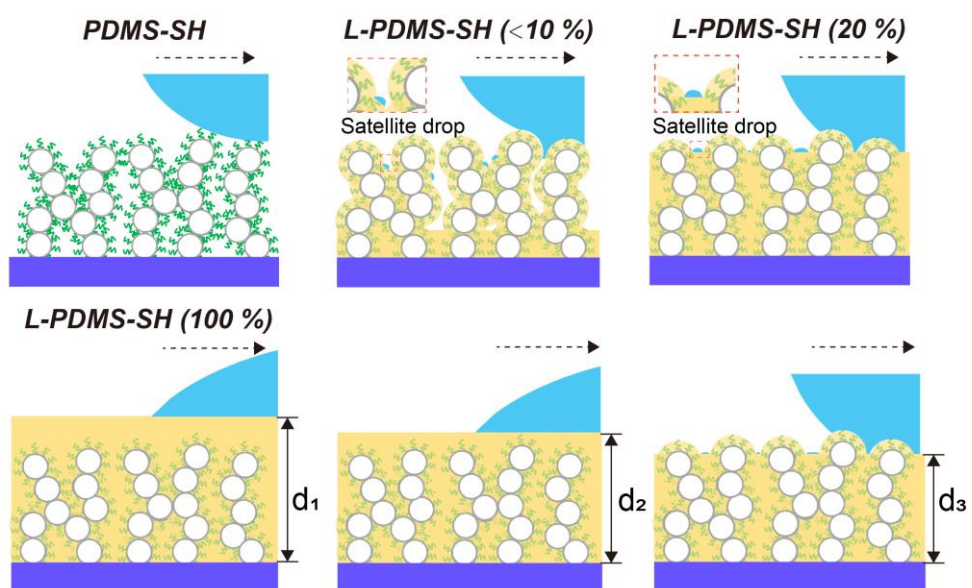
Drop charges of series of 500-2500 drops (45 μL , interval between drops: 2 s) were measured with a tilted plate setup (Supplementary Fig. S20a) at a tilt angle of 40° at $25 \pm 1^\circ\text{C}$ and relative humidity of 20-30%.^[3] After placing water drops on the top part of the surface, drops were discharged by touching a grounded electrode. After 4 cm sliding, a second electrode connected to an amplifier measured the discharge current (response time: 0.8 ms, DDPCA-300, FEMTO). A current spike was recorded for every drop. The drop charge was calculated by integrating the current over the first 2 ms. On L-PDMS-SH surfaces, charging depended critically on the thickness of the bottom oil layer (Supplementary Fig. S20b-d). For a thin bottom oil layer (5%, thickness $\approx 11 \mu\text{m}$), drops charges were similar to charging on PDMS-SH surfaces. The first drops were weakly positively charged, starting at $Q \approx +0.002 \text{ nC}$. For the PDMS-SH surface drops kept a constant charge of 0.0004 nC (almost 0) up to more than 500 drops. For the L-PDMS-SH surface drop charge further became negative and decreased to -0.008 nC after 500 drops slid off the surface. Compared to smooth hydrophobic PDMS brush coated surfaces (Supplementary Fig. S21), the first drop charging and the saturation charge was low, presumably because of the small real contact area in the Cassie state. For L-PDMS-SH (100%) which can be considered as a SLIPS, we observed no charging for the first drop and then positively charged drops with Q up to $+0.2 \text{ nC}$. This agrees with earlier observations on smooth liquid-infused surface.⁴² After 500 drops, the drop charges like a normal, flat hydrophobic surface. That's because the bulk oil layer thickness decreasing because of the depletion (we can also see this in the velocity change in Fig. 3d). And after that, the charging process behaves like that on L-PDMS-SH (20%) in a slippery Wenzel state (Supplementary Figure S20d). Thus, drops are in the Wenzel state, but the oil behaves like a solid PDMS layer. Then charging decreases, indicating that the real contact area decreases. At very high drop number, negative drop charge was observed in all cases. Why drops charge negatively is not clear yet. Until now we only observed negative water drops on surfaces with amino coatings.^[4] We assume that's because some satellite drop exist after the drop leaving from the lubricate layer on a rough structure as reported before^[5] (Supplementary Fig. S22).



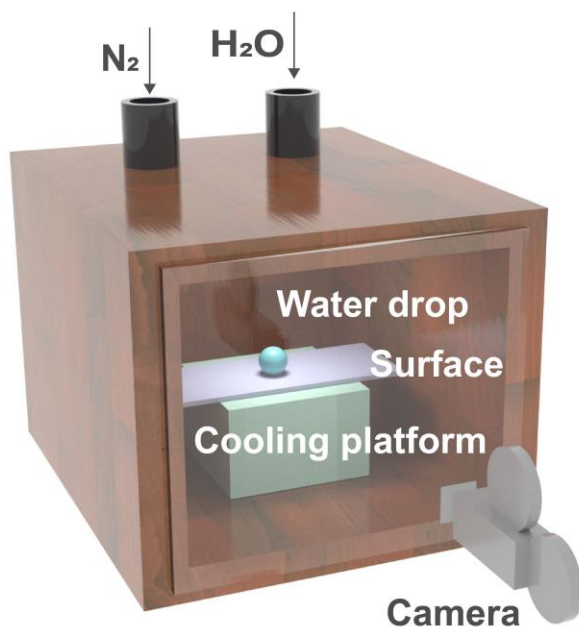
Supplementary Figure S20. **a** The scheme of the experimental setup for water drops slide electrification measurement. **b-d** Water drop charge on the PDMS-SH and L-PDMS-SH (5 %, 20 % and 100 %) surfaces versus drop number.



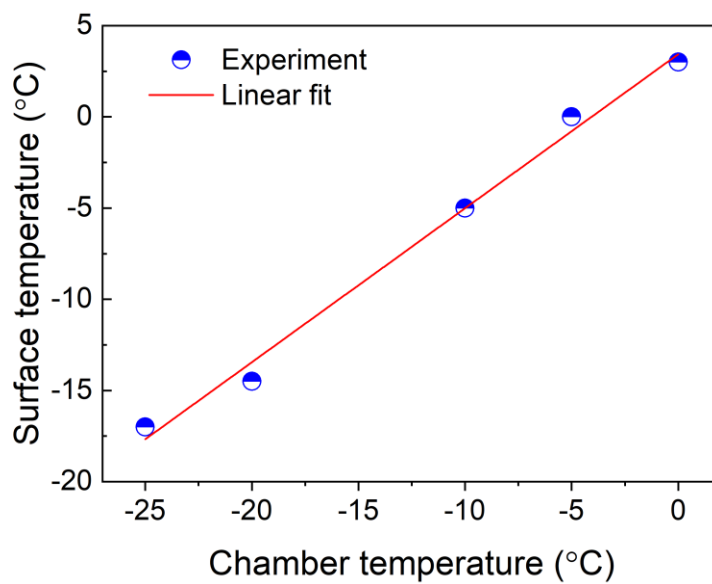
Supplementary Figure S21. Water drops slide electrification on different L-PDMS-SH surfaces.



Supplementary Figure S22. The diagrams to illustrate the surface state of the L-PDMS-SH surfaces after drops slide off.



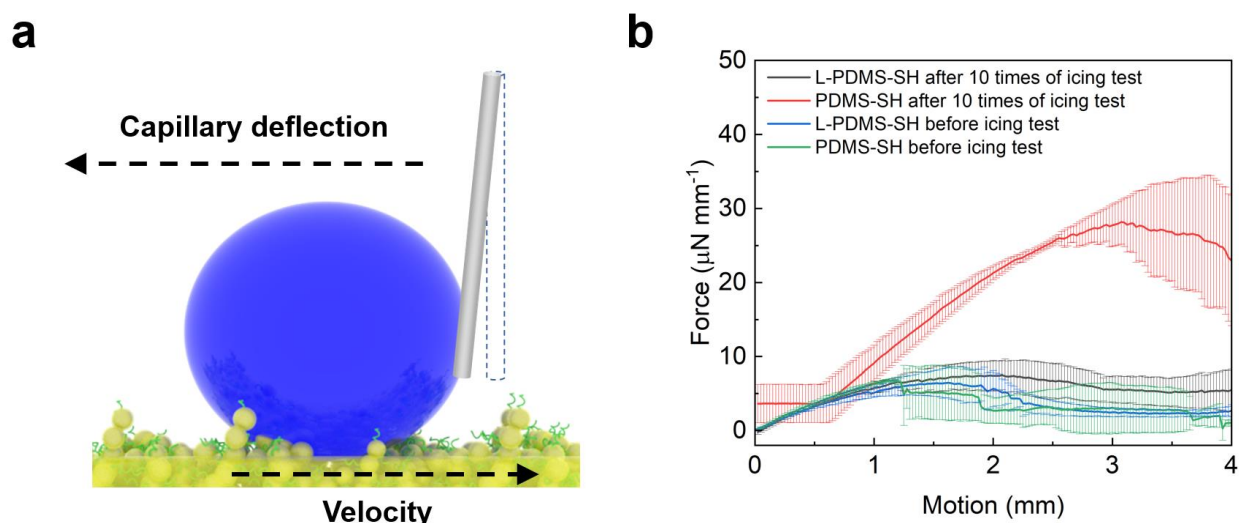
Supplementary Figure S23. The scheme to show the setup to monitor the sessile water drop freezing on the surface.



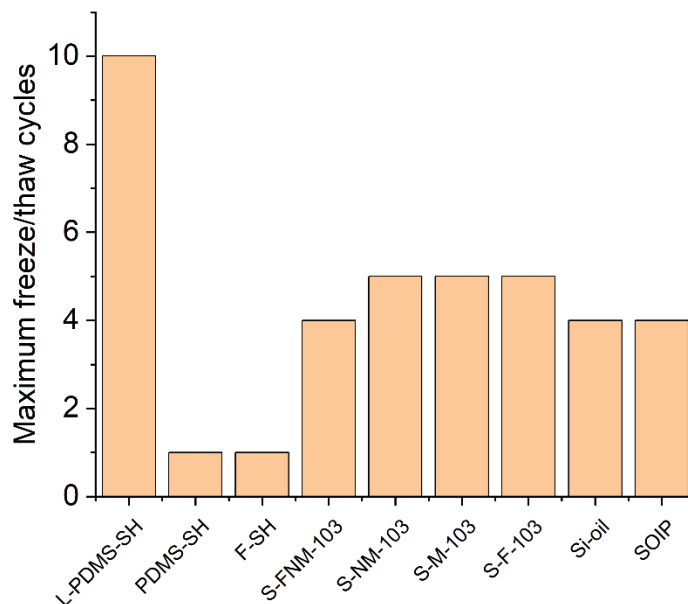
Supplementary Figure S24. Calibration curve of chamber temperature versus surface temperature.

Supplementary Section 6. Drop adhesion force measurement

DAFI (drop adhesion force instrument) measurement: The lateral adhesion force during a constant velocity movement of a water drop has been measured using the drop adhesion force instrument (DAFI). The device (Supplementary Figure S19a) consists of a motorized linear stage to which the substrate is attached, a cantilever, and a side view camera.^[6] The liquid drop was held by the cantilever while the solid substrate moves continuously with a constant predefined velocity. The force was calculated by the capillary deflection.



Supplementary Figure S25. a The scheme to show the setup for DAFI measurement. **b** Drop adhesion force curves of 10 μL water drop on L-PDMS-SH (7.5%) surface before and after 10 cycles of icing and melting process.



Supplementary Figure S26. Maximum freeze/thaw cycles for different liquid infused or liquid coated surfaces to maintain their original wetting property.

References

- [1] P. Olin, S. B. Lindström, T. Pettersson, L. Wågberg, *Langmuir* **2013**, *29*, 9079.
- [2] A. Keiser, L. Keiser, C. Clanet, D. Quéré, *Soft Matter* **2017**, *13*, 6981.
- [3] A. Z. Stetten, D. S. Golovko, S. A. L. Weber, H.-J. Butt, *Soft Matter* **2019**, *15*, 8667.
- [4] W. S. Y. Wong, P. Bista, X. Li, L. Veith, A. Sharifi-Aghili, S. A. L. Weber, H. J. Butt, *Langmuir* **2022**, *38*, 6224.
- [5] S. Adera, J. Alvarenga, A. V. Shneidman, C. T. Zhang, A. Davitt, J. Aizenberg, *ACS Nano* **2020**, *14*, 8024.
- [6] C. Hinduja, A. Laroche, S. Shumaly, Y. Wang, D. Vollmer, H.-J. Butt, R. Berger, *Langmuir* **2022**.

2.3. J. Liu, Y. Sun, X. Zhou et al. *Adv. Mater.*, 2021.

One-Step Synthesis of a Durable and Liquid-Repellent Polydimethylsiloxane Coating

Jie Liu, Yuling Sun, Xiaoteng Zhou, Xiaomei Li, Michael Kappl, Werner Steffen, Hans-Jürgen Butt

Max Planck Institute for Polymer Research, Ackermannweg 10, 55128, Mainz, Germany.

Published in:

Advanced Materials

Reproduced with permission from *Advanced Materials* 2021, 33, 2100237. Copyright © 2021 The Authors. *Advanced Materials* published by Wiley-VCH GmbH.

Author Contribution:

Jie Liu, Yuling Sun, Xiaoteng Zhou and Hans-Jürgen Butt designed and performed experiments. Jie Liu, Yuling Sun, Xiaoteng Zhou, Xiaomei Li and Michael Kappl contributed new reagents/analytic tools. Jie Liu, Yuling Sun, Xiaoteng Zhou and Xiaomei Li analyzed the data. All authors wrote the paper and have given approval to the final version of the manuscript.

One-Step Synthesis of a Durable and Liquid-Repellent Poly(dimethylsiloxane) Coating

Jie Liu,* Yuling Sun, Xiaoteng Zhou, Xiaomei Li, Michael Kappl, Werner Steffen, and Hans-Jürgen Butt*

Coatings with low sliding angles for liquid drops have a broad range of applications. However, it remains a challenge to have a fast, easy, and universal preparation method for coatings that are long-term stable, robust, and environmentally friendly. Here, a one-step grafting-from approach is reported for poly(dimethylsiloxane) (PDMS) brushes on surfaces through spontaneous polymerization of dichlorodimethylsilane fulfilling all these requirements. Drops of a variety of liquids slide off at tilt angles below 5°. This non-stick coating with autophobicity can reduce the waste of water and solvents in cleaning. The strong covalent attachment of the PDMS brush to the substrate makes them mechanically robust and UV-tolerant. Their resistance to high temperatures and to droplet sliding erosion, combined with the low film thickness (≈ 8 nm) makes them ideal candidates to solve the long-term degradation issues of coatings for heat-transfer surfaces.

Rapid removal of liquid droplets from surfaces is of great concern in practical applications and fundamental research such as water harvesting,^[1] heat transfer,^[2] liquid manipulation,^[3] and so on. For drops to slide off surfaces easily even at low tilt angles, a low contact angle hysteresis is required. Very low roll-off angles can be found on super-liquid-repellent surfaces. Combination of topographic features and low surface energy chemistry, in particular combining re-entrant or double re-entrant textures with surface fluorination, has been the typical strategy for fabricating super-liquid-repellent surfaces.^[4] This strategy requires that liquids are supported on topographic features and an air layer is maintained underneath. This so-called Cassie state is, however, only metastable and can collapse under external forces leading to a Cassie-to-Wenzel transition. Furthermore, the surface textures tend to be fragile and the frequent use of fluorinated chemicals to decrease the surface energy raises concerns on their health and environmental impact.^[5] Another type

of liquid-repellent surface, slippery liquid-infused porous surface (SLIPS), repels liquids through dynamic liquid/liquid/vapor contact-line motion.^[6] The required slippery liquid must be both immiscible with and not be leached out by the contacting liquid medium to avoid lubricant loss and contamination. Ensuring the long-term robustness of such coatings and their wetting performance remains challenging.^[7] Therefore, other methods to create surfaces with good liquid repellency are desirable.


An alternative strategy, covalently attaching flexible macromolecules brushes such as PDMS and perfluorinated polyether onto smooth surface was proposed to repel liquids.^[8] The idea is that the high

mobility of the flexible macromolecules allows them to act as a liquid-like lubricating layer to liquids with a broad range of surface tensions.^[8c] Due to the covalent attachment to the surface, these molecular structures cannot be dissolved or displaced by the contacting liquids. Specifically, surfaces coated with PDMS brushes exhibit excellent resistance to high temperature treatment, photodegradation, and even scratching.^[8a,9] In addition, since the layers are only a few nanometers thick, they are transparent, do not influence the appearance of coated surfaces, and have little impact on heat conductivity. Preparation of PDMS brushes can be traced back to 1970, when Vermeulen et al. deposited a low-liquid-adhesion PDMS brush layer on glass surface with a vapor-phase reaction for 16 h.^[10] However, grafting polymers from surfaces is generally based on complex and time-consuming preparative procedures, limiting their use in practical applications.

McCarthy et al. systematically investigated new strategies to fabricate PDMS brushes on surfaces.^[11] They proposed to use dimethyldimethoxysilane (DMDMS) as monomer to polymerize PDMS brushes with sulfuric acid as catalyst.^[8a] After rinsing the surface with a copious amount of solvent to remove residual oligomer and acid, PDMS brushes with low liquid adhesion form on the silicon (or glass) surface after drying the reactive solution (includes DMDMS, sulfuric acid, and isopropyl alcohol) for some time. Compared to McCarthy's method, we developed a simpler approach to graft PDMS brushes on surfaces with no catalyst required. Furthermore, we characterized the stability of PDMS brushes under tape-peeling, sonication, drop sliding corrosion, heating, UV degradation, acid corrosion, and more. McCarthy et al. only investigated the effect of heating at 100 °C.

Dr. J. Liu, Dr. Y. Sun, X. Zhou, X. Li, Dr. M. Kappl, Prof. W. Steffen, Prof. H.-J. Butt

Max Planck Institute for Polymer Research
Ackermannweg 10, Mainz D-55128, Germany
E-mail: liujie@mpip-mainz.mpg.de; butt@mpip-mainz.mpg.de

 The ORCID identification number(s) for the author(s) of this article can be found under <https://doi.org/10.1002/adma.202100237>.

© 2021 The Authors. Advanced Materials published by Wiley-VCH GmbH. This is an open access article under the terms of the Creative Commons Attribution License, which permits use, distribution and reproduction in any medium, provided the original work is properly cited.

DOI: 10.1002/adma.202100237

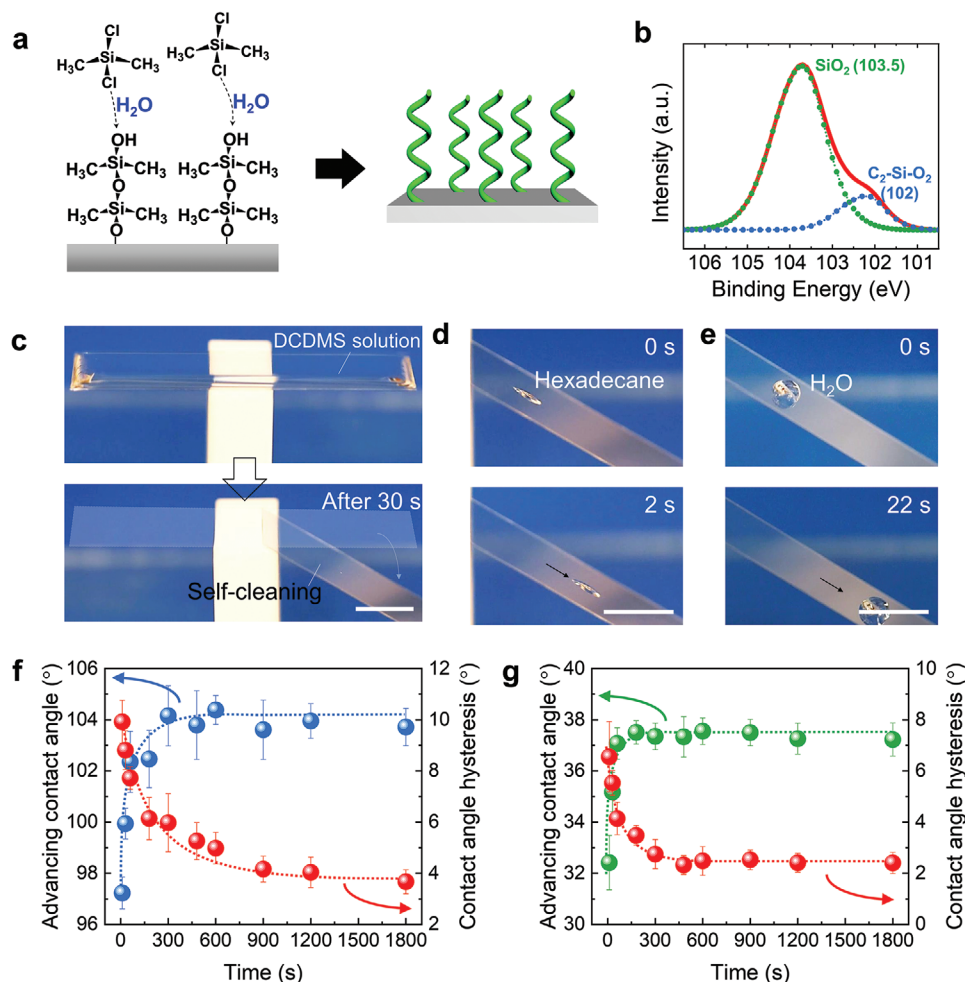


Figure 1. Ultrafast processing of PDMS brushes. a) Schematic illustration of the formation of PDMS brushes from dichlorodimethylsilane (DCDMS) monomers. b) Si 2p peaks (red line) measured by X-ray photoelectron spectroscopy (XPS) of the PDMS brushes grafted onto a silicon wafer. The fit indicates the presence of O–Si–O (green line) and –O–Si(CH₃)₂–O– (blue line) bonds. Reaction time: 30 min. The sample was washed with toluene for five times. c) Autophobicity of PDMS brushes on glass: after 30 s grafting time, the reactant can be fully removed by simple tilting. d) Sliding of *n*-hexadecane on the PDMS-brushes-coated glass slide. Liquid volume: 5 μ L. e) Sliding of water on the PDMS-brushes-coated glass slide. Liquid volume: 10 μ L. Scale bar (c–e): 1 cm. f) Advancing contact angle (θ_{ACA}) and contact angle hysteresis ($\Delta\theta$) of water as function of grafting time. g) Advancing contact angle and contact angle hysteresis of *n*-hexadecane as function of grafting time.

Here, we report a further simplified processing method, using a fast one-step approach to prepare PDMS brushes that exhibit autophobicity and low contact angle hysteresis for a broad range of liquids. PDMS brushes are synthesized directly on the desired surface through polymerization of reactive silane monomers (dichlorodimethylsilane, DCDMS) without initiator. Polymerization of DCDMS happens under hydrolysis of water.^[12] Reacting with water, the Si–Cl group of DCDMS is hydrolyzed to Si–OH. When a silicon wafer pretreated with oxygen plasma is rinsed in DCDMS/toluene solution, DCDMS attaches spontaneously and fast to the surface via reaction of the Si–OH or Si–Cl group with hydroxyl groups on the surface. Further condensation reactions between Si–OH and Si–OH or Si–Cl at the surface will follow, finally forming PDMS brushes (Figure 1a).^[13] The high reactivity of DCDMS promotes the fast grafting process of PDMS brush.

With this recipe, PDMS brushes were fabricated by immersing the substrate, in our case silicon wafer (used as

substrate in the following if not otherwise stated) or glass, into a toluene solution containing DCDMS (0.24×10^{-3} M). We maintained a saturated concentration ($c_{\text{water}} \approx 0.024 \times 10^{-3}$ M) of water in toluene at room temperature. X-ray photoelectron spectroscopy (XPS) of PDMS brushes on silicon wafers revealed the existence of the –O–Si(CH₃)₂–O– (≈ 102 eV) in addition to the previously existing SiO₂ (Figure 1b). This proves the successful grafting of poly(dimethylsiloxane) (PDMS) molecules. Grafting of brushes occurs synchronously on the whole surfaces in a homogeneous solution, therefore the final surface is smooth with low roughness; AFM images of PDMS surface show a roughness of $R_a \approx 0.1$ nm (Figure S1, Supporting Information).

Conveniently, the PDMS brushes are autophobic in the sense that the reactant solution itself can be easily removed. When for example coating a glass slide by covering its top with DCDMS solution for 30 s (Figure 1c), the reactant solution was easily removed by simply tilting the surface. No residual stains were left (Movie S1 and Figure S2, Supporting Information). The

induced self-repellency toward the reactant solution implies that no extra washing step is necessary to clean the surface, which reduces solvent waste. The fast coating process makes the glass surface repellent to liquids with both low (hexadecane) and high (water) surface tensions. “Repellent” here means that hexadecane and water droplets easily run off a tilted surface (Figure 1d,e).

The advancing (θ_{ACA}) and receding (θ_{RCA}) contact angles as well as contact angle hysteresis ($\Delta\theta = \theta_{ACA} - \theta_{RCA}$) of water and hexadecane drops were used to illustrate the liquid repellency (Figure 1f,g). Within a reaction time of 30 s, the contact angle hysteresis of the silicon wafer decreased to $\Delta\theta = 9^\circ$ for water and $\Delta\theta = 5^\circ$ for hexadecane (water: $\theta_{ACA} = 100^\circ$, $\theta_{RCA} = 91^\circ$ and hexadecane: $\theta_{ACA} = 35^\circ$, $\theta_{RCA} = 30^\circ$). For a longer grafting time (>15 min), PDMS brushes become thicker (Figure S3, Supporting Information) and the contact angle hysteresis of water was reduced to less than 5° . According to the stretching length (L) of the PDMS molecules, the molecular weight of the brushes can be roughly estimated. The length of $-\text{Si}-\text{O}-$ is around 1.61 Å. By dividing the stretching length by the length per monomer we get the minimal number of monomers per chain. When the grafting time is 30 min ($L = 13 \pm 1$ nm), the molecular weight of the PDMS brushes must be larger than 3000 g mol^{-1} . The reaction rate can be accelerated by increasing the concentration of DCDMS (Figure S4, Supporting Information). It turned out that the water concentration plays an important role in the grafting process. The higher concentration of water can effectively accelerate the reaction and reduce grafting time (Figure S5, Supporting Information).

Contact angle hysteresis has an important physical significance: It is directly linked to the lateral adhesion and the tilt angle α required to let the drop slide off the surface:^[14]

$$\sin \alpha = \frac{k w^\circ}{g V \rho} (\cos \theta_{RCA} - \cos \theta_{ACA}) \quad (1)$$

Here, $k \approx 1$ is a geometrical factor, w is the width of the contact area of the drop, γ is the surface tension of the liquid, $g = 9.81 \text{ m s}^{-2}$ is the acceleration of gravity and ρ is the density of the liquid. Since contact angle hysteresis is relatively low, drop shapes of small drops can be well described by a spherical cap model. In this aspect, a natural length scale for drops is the capillary length $\kappa = \sqrt{\gamma/g\rho}$, which for water is 2.7 mm. In the spherical drop model, the width of the drop is twice the contact radius a . The contact radius is given by the drop volume: $\alpha = \sin \theta \left(\frac{3V}{\pi\beta} \right)^{1/3}$ with $\beta = (1 - \cos \theta)^2 (2 + \cos \theta)$. Here θ is the mean contact angle. Therefore,

$$\sin \alpha = \frac{2\gamma \sin \theta}{g V^{2/3} \rho} \left(\frac{3}{\pi\beta} \right)^{1/3} (\cos \theta_{RCA} - \cos \theta_{ACA}) \quad (2)$$

That implies that reducing the contact angle hysteresis decreases the lateral adhesion and thus the sliding angle. Due to the $V^{-2/3}$ scaling, large drops easily slide down tilted planes while small drops tend to stick. Therefore, we used small drops (5 μL) to test our surfaces.

Silicon wafers coated with PDMS brushes show low sliding angles for liquids with a broad range of surface tensions.

An *n*-hexane ($\gamma = 18.4 \text{ mN m}^{-1}$) sessile drop slides down from the PDMS brushes tilted by 2° (Figure 2a). An ethanol ($\gamma = 22.1 \text{ mN m}^{-1}$) and a toluene ($\gamma = 28.4 \text{ mN m}^{-1}$) droplet slide easily off the surface with a tilting angle of 5° . For comparison, a surface coated with 1H,1H,2H,2H-perfluorooctyltrimethoxysilane shows a higher lateral adhesion to liquids than PDMS brushes: an *n*-hexadecane droplet slides on PDMS brushes but remains stationary on a fluorinated surface when $\alpha = 5^\circ$ (Figure S6, Supporting Information). The lateral adhesion forces (f) of water droplets (5 μL) on PDMS brushes ($f = 18.9 \pm 1 \mu\text{N}$) was much lower than that on the fluorinated surface ($f = 60.0 \pm 3 \mu\text{N}$) when the relative speed between droplet and surface was $250 \mu\text{m/s}$ (Figure S7, Supporting Information). Contact angle hysteresis measurements show that liquids such as ethanol, isopropyl alcohol (23.0 mN m^{-1}), hexadecane (27.5 mN m^{-1}), toluene, dimethylformamide (DMF) (37.1 mN m^{-1}), dimethyl sulfoxide (DMSO) (43.5 mN m^{-1}), diiodomethane (50.8 mN m^{-1}), and water (72.8 mN m^{-1}) all present a low lateral adhesion to the surface with $\Delta\theta < 5^\circ$ (Figure 2b). The sliding angles of the liquid droplets are studied versus the volume (5, 10, and 20 μL) (Figure 2c). 10 μL droplets independent of the type of liquid slide at $\alpha < 5^\circ$. The roll-off angles observed for liquids with different surface tension and drops with different volumes agree with theoretical predictions of Equation (2). The PDMS-brush-coated surface repels low and high viscosity liquids such as poly(propylene glycol) ($M_n \approx 725$, viscosity: 115 cP), poly(ethylene glycol)-*block*-poly(propylene glycol)-*block*-poly(ethylene glycol) ($M_n \approx 2000$, viscosity: 325 cP), and poly(ethylene glycol)-*block*-poly(propylene glycol)-*block*-poly(ethylene glycol) ($M_n \approx 4400$, viscosity: 1200 cP) (Figure S8, Supporting Information).

For practical applications, robustness and durability of surface coatings is of critical importance. In a first test, sonication (45 kHz, 60 W) of our grafted PDMS brushes for 6 h in toluene did not alter the wetting properties for both water and hexadecane (Figure 2d). This resistance to sonication cleaning excludes the possibility that the low adhesion is caused by embedded, non-grafted silicone monomer or oligomer.^[9a,15] The contact angle hysteresis of water and hexadecane on the PDMS brushes starts to slightly increase after 7 h of sonication. Nevertheless, the hysteresis is still not larger than 10° even after 18 h sonication. In contrast, on a 1H,1H,2H,2H-perfluorodecyltriethoxysilane modified surface contact angle hysteresis increased from 18° to 29° after 1 h sonication (Figure S9a, Supporting Information).

In a second test, a Scotch tape (3M 810) was homogeneously pressed onto a PDMS brush grafted silicon wafer (load: 11.5 kPa, duration: 20 s) and then peeled off (Figure 2e). The peeling force (F_{peeling}) of the tape on silicon wafer ($F_{\text{peeling}} = 110 \pm 12 \text{ N m}^{-1}$) was markedly reduced by PDMS brushes ($F_{\text{peeling}} = 4 \pm 1 \text{ N m}^{-1}$). Eighty adhesion-peeling cycles did not influence the repellency of both water and hexadecane; the contact angle hysteresis remained below 5° for both liquids. After 300 peel-test cycles, the advancing and receding contact angles of water decreased from 103° and 99° to 97° and 84° , respectively; contact angle hysteresis increased from 4° to 13° . In contrast, wetting performance for hexadecane was not altered even after 300 peel-tests. Compared to the mechanical stability of the PDMS brushes, the fluorinated surface rapidly lost their hydrophobicity. The receding contact angle of water decreased from 99° to 78° and

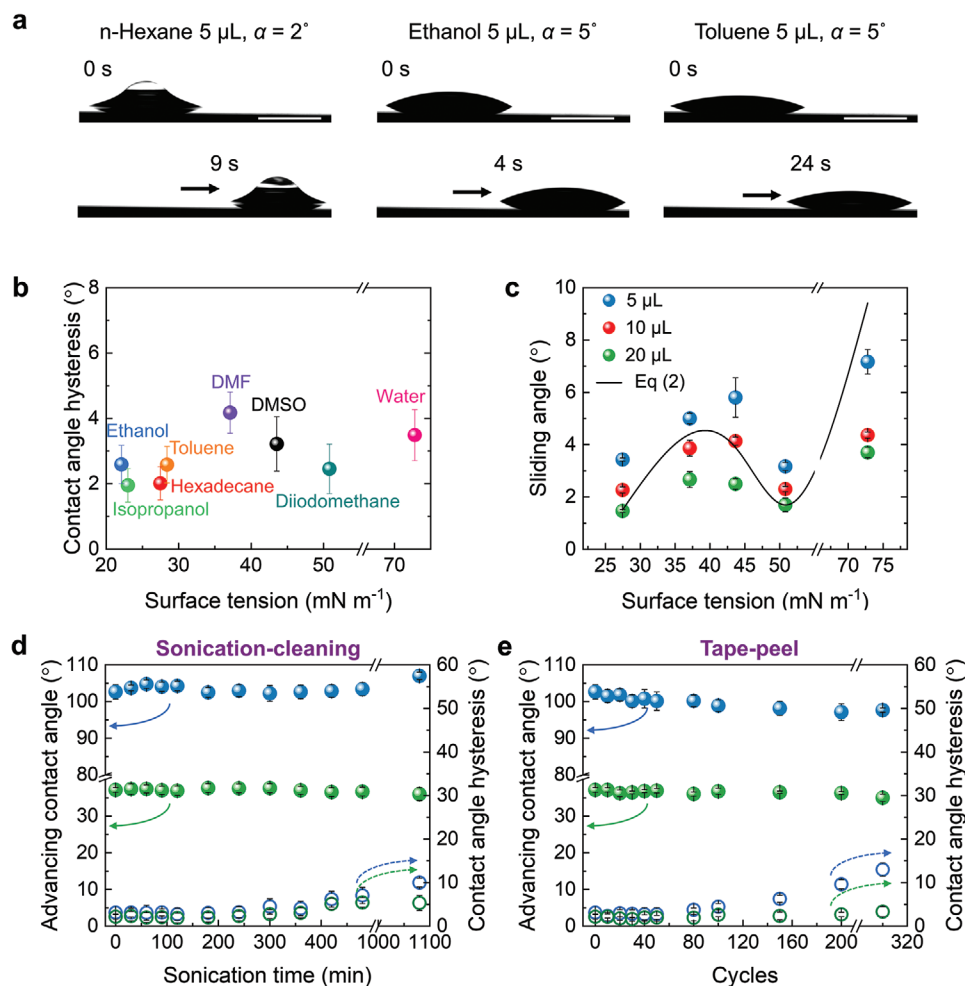


Figure 2. Robust liquid-repellent PDMS brushes. a) Time-sequence images of hexane (left), ethanol (middle), and toluene (right) droplets sliding down a tilted silicone brush surface. To increase visibility of the hexane drop, a small air bubble was injected on the top of hexane droplet. Scale bar: 2 mm. b) Contact angle hysteresis of various liquids on PDMS brushes. Grafting time: 30 min. c) Sliding angle of drops of various liquids (from left to right: *n*-hexadecane, DMF, DMSO, diiodomethane, water) on PDMS brushes. The black line shows sliding angles of liquid drops (10 μL) versus surface tension plotted according to Equation (2). The mean, advancing, and receding contact angles were measured values of the five kinds of liquids. d) Water (θ_{ACA} : \bullet and $\Delta\theta$: \circ) and *n*-hexadecane (θ_{ACA} : \bullet and $\Delta\theta$: \circ) repellency of the PDMS brushes versus sonication-washing time. e) Water (θ_{ACA} : \bullet and $\Delta\theta$: \circ) and *n*-hexadecane (θ_{ACA} : \bullet and $\Delta\theta$: \circ) repellency of the PDMS brushes resisting tape-peeling tests.

the contact angle hysteresis increased from 18° to 25° after 100 peel-tests (Figure S9b, Supporting Information).

A temperature-tolerance test was carried out to study the durability of our PDMS brushes (Figure 3a,b) for heat transfer applications. The coating can resist long term heat treatment at 100°C in air, as advancing and receding contact angles of water and hexadecane on PDMS brushes remained constant for at least 32 days. When the temperature was increased to 250°C , the advancing contact angle of water increased from 104° to 107° and remained constant for 15 days. $\Delta\theta$ of water increased slightly during this time, reaching 8° after 15 days of heat treatment. So even at such high temperatures, little loss of wetting properties was observed. Contact angles changed more in the case of *n*-hexadecane but contact angle hysteresis still remained very low ($\Delta\theta = 3^\circ$). The decrease of the contact angle of *n*-hexadecane might be caused by the reaction between end groups ($-\text{OH}$) at 250°C , causing the loss of the molecular mobility of the brushes.^[8a,11]

In heat transfer, especially condensation heat-transfer, maintenance of a low lateral adhesion of droplets is a key factor to enhance condensation rates.^[2a] The PDMS brushes exhibit a constant and low water adhesion independent of temperature in a wide temperature window (0°C to 70°C) (Figure S10, Supporting Information). A droplet sliding erosion test was designed to characterize the durability of PDMS brushes under high temperature (70°C) water vapor treatment (Figure S11, Supporting Information). The water vapor was prepared by heating water at 200°C to obtain water steam, and then the steam was cooled to 70°C on the surfaces during which condensed droplets formed. As shown in Figure 3c, even after 40 h of treatment (flow rate: $0.8 \pm 0.1 \text{ L min}^{-1}$), the advancing contact angle of water on the PDMS brushes did not change. Only the contact angle hysteresis increased from 4° to 7° . For the 1H,1H,2H-perfluorooctyltrimethoxysilane coated surface as a control, the initial contact angle hysteresis was much higher ($\Delta\theta = 18^\circ$). After 20 h of treatment, the advancing contact

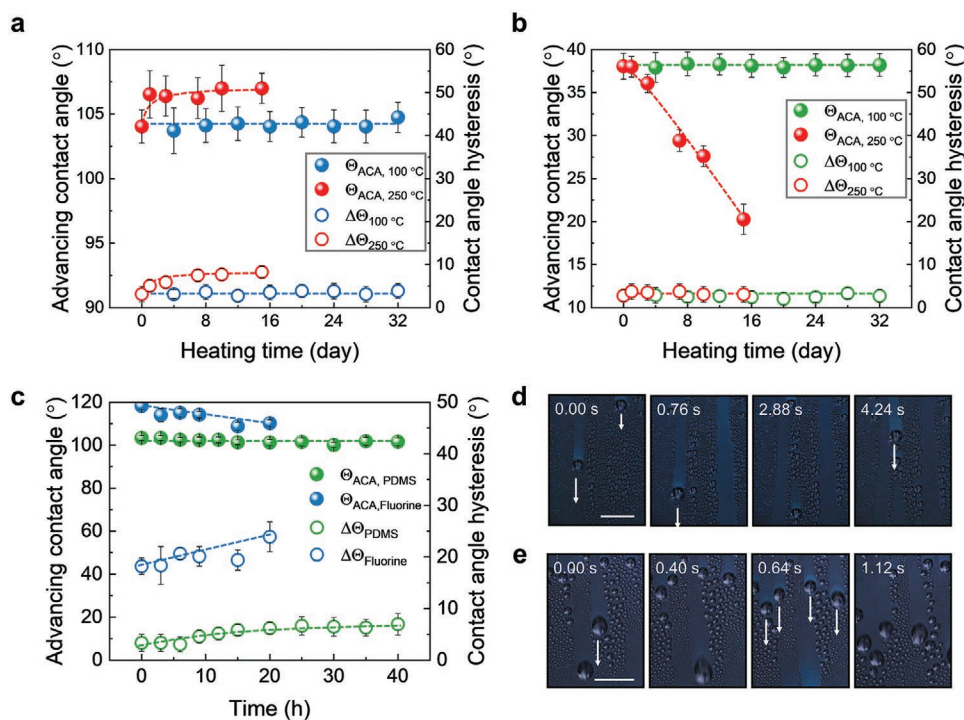


Figure 3. Durability of the PDMS brushes under high-temperature and water vapor treatment. a) Water repellency of the PDMS brushes versus aging time at 100 °C and 250 °C. b) Hexadecane repellency of the PDMS brushes versus aging time at 100 °C and 250 °C. c) Durability of wetting property of water on PDMS brushes and fluorinated surface under water vapor treatment at 70 °C. d) Image sequence shows sliding of condensed water droplets during water vapor treatment. Vapor temperature: 70 °C. e) Image sequence shows sliding of condensed toluene droplets during toluene vapor treatment. Vapor temperature: 70 °C. Scale bar in (d,e): 0.5 cm.

angles decreased from 118° to 109°, accompanied by the contact angle hysteresis increase from 18° to 24°. This deterioration indicates degradation or partial removal of the fluorination layer under the sliding of condensing water droplets. The reason is that the fluorinated surface has a much higher adhesion to water droplets than the PDMS brushes. This leads to a higher peeling force loaded to the fluorinated molecules from water droplets; thus the molecules are more easily detached from the surface. In addition, the higher thickness of the PDMS brush layer ensures its better stability than the fluorinated layer. Thus, our PDMS brushes are significantly more stable than fluorinated silane coated surfaces.

Condensed water droplets are expected to move easily due to the low hysteresis of water on PDMS brushes. Rather than reporting the tilt angle at defined volume, we measured the sizes of water droplets on different vertical surfaces ($\alpha = 90^\circ$ fixed tilt angle) such as PDMS brushes, silicone oil impregnated PDMS brush surface (liquid-impregnated surface, SLIPS), and fluorinated surface (Figure S12a, Supporting Information). Condensed water droplets slid off the vertical PDMS brushes with a diameter (D) around 1.2 mm, a little bit larger than that on SLIPS ($D = 1.0$ mm). In contrast, the minimum sliding size of water drops on fluorinated surface is much bigger ($D = 2.3$ mm). Therefore, the mass transfer efficiency of water on these three surfaces should differ greatly. Water-collection efficiency (water volume slid off per square meter surface) was measured when we cooled the surfaces to 0 °C (room temperature: 20 ± 1 °C, relative humidity: $80 \pm 5\%$) (Figure S12b,

Supporting Information). PDMS brushes present the similar water-collection efficiency with the SLIPS in 1 h. Cloaking of the droplets by the oil on SLIPS reduces the coalescence of water droplets^[16], resulting in condensed droplets sliding earlier on PDMS brushes than on SLIPS. Requiring a comparatively large drop size for sliding (Figure S12a, Supporting Information), no water was collected on fluorinated surfaces within 1 h condensation time as the droplet remained pinned.

Depending on application, not only water may be used as heat transfer medium. Due to their excellent liquid repellency to a broad range of liquids, PDMS-brush-coated surfaces could be used in heat and mass transfer in different situations.^[17] Besides repellency to condensate water (Figure 3d), condensed liquids with low-surface-tension such as toluene can also slide fast and easily on the PDMS brushes (Figure 3e, Movie S2, Supporting Information).

The fast and spontaneous grafting reaction of PDMS brushes on surfaces allows using various coating methods such as dip-coating, drop-casting, or spray coating to form PDMS brushes. We applied the reaction solution with a soaked textile or paper to modify large areas in a controlled way (Figure 4a). As an example, a paper (80 g m^{-2}) was used to hold the solution and spread the coating solution on the surface. In this way, the coating area was increased 16 times compared to the drop-casting method. After grafting PDMS brush for 3 min, toluene droplets rapidly slid on the surface (Figure S13, Supporting Information).

Transparency of coatings is required in many applications.^[18] Good transparency of the PDMS brushes opens the possibility

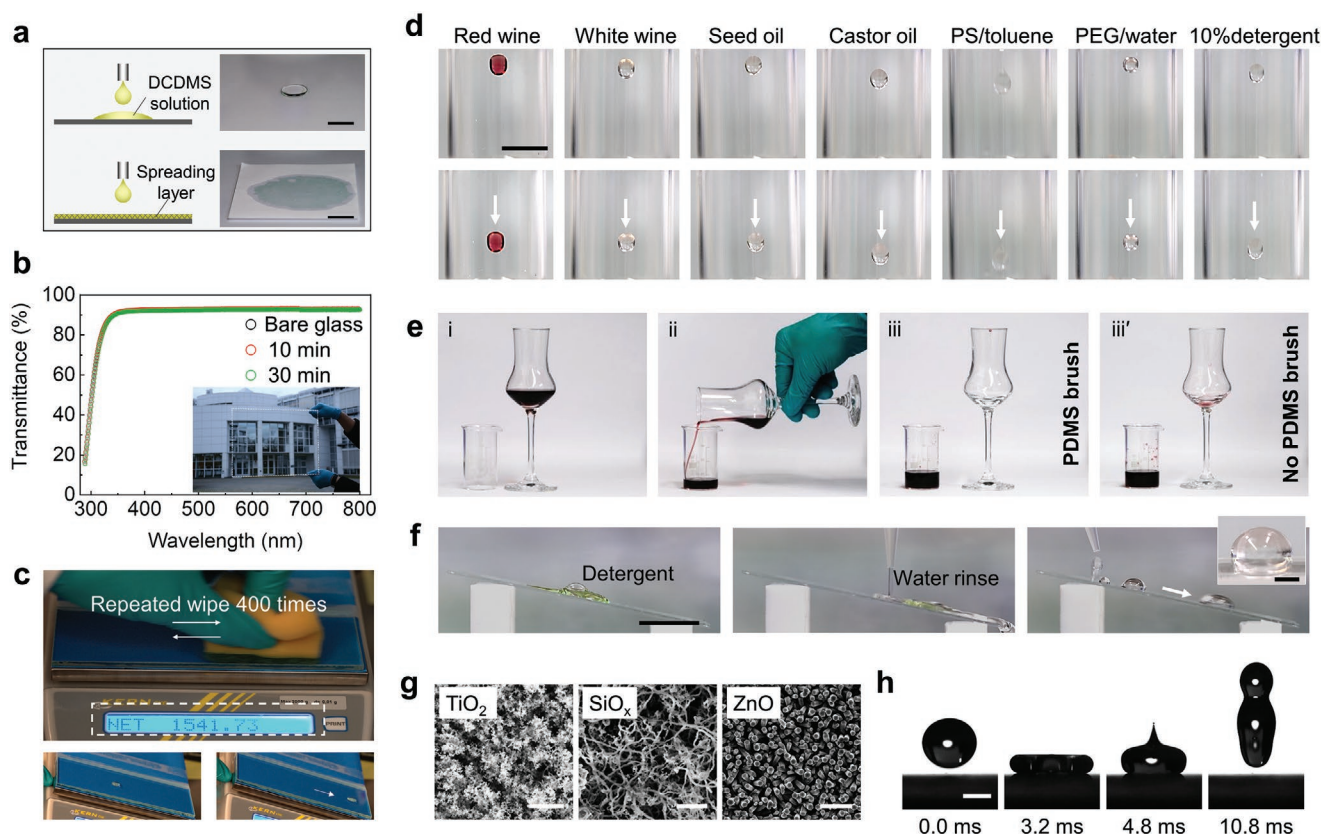


Figure 4. Applications of PDMS brushes. a) A window glass plate (soda-lime glass, $20 \times 10 \text{ cm}^2$) was covered with a piece of commercial paper (80 g m^{-2}). Then the reactant solution ($200 \mu\text{L}$) was applied. The paper was used to hold the reaction solution and promote its spreading on the surface. Scale bar: 2 cm. b) UV-vis spectra show the film transmittance as a function of modification time. The inset shows a window glass ($30 \times 20 \text{ cm}^2$) coated for 30 min. c) Wearing tolerance of PDMS brushes on window glass ($15 \times 7 \text{ cm}^2$). Grafting time: 3 min. d) Images show sliding of various liquids on coated glass. Liquids from left to right: red wine, white wine, seed oil, castor oil, polystyrene solution in toluene (1 wt%), poly(ethylene glycol) aqueous solution (50 wt %), and detergent aqueous solution (10 wt%). Scale bar: 1 cm. e) Pouring of red wine from wine glass and no staining on the coated surface (iii). A layer of wine stayed on the glass surface after pouring (iii'). f) Washing of concentrated detergent (0.3 mL) on a coated glass with water flux (25 mL). Grafting time: 3 min. Scale bar: 2 cm. Inset shows a water drop after the detergent was removed. Scale bar: 2 mm. g) Metal-oxide surfaces with nanostructures. Surfaces from left to right: titanium dioxide (TiO_2) nanotexture, silicone nanofilament (SiO_x), and zinc oxide nanopillars (ZnO). Scale bars (left to right): 500 nm, 500 nm, 1 μm . h) Impacting and bouncing of a $5 \mu\text{L}$ water droplet shows superhydrophobic performance of TiO_2 hierarchical surface after grafting with PDMS brushes in 3 min. Dropping height: 2 cm. Scale bar: 1 mm.

to coat surfaces without changing their outward appearance. The overlapped UV/Vis spectra of the glass (thickness: 1 mm) coated with PDMS brushes with different thickness indicates no transparency loss was caused by the brush layer (Figure 4b). This is mainly attributed to the nanoscale thickness of the brush layer and its refractive index close to glass (silicone oil: 1.4, window glass: 1.5).

Wear tolerance is a key feature in practical applications. One potential application we investigated preliminarily is preparing low-adhesion and wash-free liquid containers based on to the liquid-repellent performance of PDMS brushes. To test how robust the surface is against wear, a piece of window glass (soda-lime glass, size: $15 \times 7 \text{ cm}^2$) was coated with PDMS brushes with a reaction time of 3 min (Figure 4c). The coated window glass was subjected to wear by a hand-held commercial scouring pad on a balance so that we can record the applied pressure during forward/backward stroke cycles. The average pressure during wearing test was $6.6 \pm 1.2 \text{ kPa}$. After wearing the brush-coated glass for 400 stroke cycles, water droplets can

still easily slide on the surface. The PDMS-brush-coated surface kept its repellency to both water and *n*-hexadecane even after it was slightly destroyed by rubbing with sandpaper (1000 mesh) under the pressure of 1.1 kPa (Figure S14, Supporting Information). In addition, a water jet with a velocity of 4.7 m s^{-1} was applied to impact the surface three times for 1 s (Figure S15, Supporting Information). After the treatment, the wetting property of the surface remains unchanged with $\Delta\theta_{\text{water}} = 4^\circ \pm 1^\circ$ and $\Delta\theta_{\text{hexadecane}} = 2.7^\circ \pm 1^\circ$.

Liquid adhesion on surfaces causes waste of water or solvents for cleaning. A glass bottle coated with PDMS brushes presents low sliding adhesion to liquids such as wine, plant oil, polymer solutions, and detergent (Figure 4d). After coating a layer of PDMS brushes, red wine drops can easily slide down the surface (Figure 4e). This indicates that much less wine drops will stain the inner surface of the coated glass after drinking, and therefore reduces the waste of water in cleaning. In contrast, a thin layer of wine always stains the bare glass. The easy sliding of oils such as castor oil and seed oil reduces

waste of cooking oil attached to their bottles (Figure 4d). In addition, cleaning of chemical reaction containers in the lab is a daily nuisance. Chemicals left on the surface need a lot of solvent to clean, because even little residues may spoil following reactions. This problem can be reduced by coating surface with PDMS. For example, glass coated with PDMS brushes presents good repellency to a polystyrene in toluene solution (1 wt%) and poly(ethylene glycol) (PEG) aqueous solution (50 wt%) (Figure 4d). The surface kept this antifouling benefit even when it was placed outdoor for 21 days (Figure S16, Supporting Information).

Furthermore, to clean dirty surfaces, a detergent solution is usually used. However, remaining stains of detergent after drying raise concerns on their health impact. Removing detergent stains requires a lot of water. We demonstrate that aqueous detergent solutions (10 wt%) easily slide off PDMS brushes (Figure 4d). Even when a coated glass was stained with a concentrated detergent, it can be completely cleaned by washing with a water flow (Figure 4f; and Movie S3, Supporting Information). The complete removal of the detergent from the surface was inferred from the shape ($\theta \approx 101^\circ$) of water drop and fast sliding of water drops on the surface after washing. It is noted that the mass of water needed to clean detergent on PDMS brushes is maximum 50% of that needed to clean hydrophilic glass surface, and it is hard to know if the hydrophilic surface is clean completely or not. Surfaces coated with PDMS brushes also present tolerance to UV illumination (Figure S17, Supporting Information), making them especially suitable for outdoor applications. Its resistance to acid benefits its application in corrosion resistance (Figure S18, Supporting Information).

PDMS brushes can become a substitute to decrease surface energy also of other materials than glass. Three metal oxide surfaces such as titanium dioxide (TiO_2) nanotexture, silicon oxide (SiO_x) nanofilament, and zinc oxide (ZnO) nanorod were prepared according to previous studies.^[9b,19] All these surfaces are easily and rapidly coated with PDMS brushes and became superhydrophobic in 3 min (Figure 4g). After modification, water drops easily rebound completely from such surfaces (Figure 4h). However, this method still has shortcomings. Since surface hydroxyl groups are required, and since HCl is produced during synthesis, it is of limited use on wood and metals such as steel, copper or gold (Figure S19, Supporting Information). Only aluminum, with its oxide layer, becomes moderately hydrophobic.

In conclusion, a fast one-step approach to coat poly(dimethylsiloxane) brushes through direct polymerization of dichlorodimethylsilane on surfaces was reported. This cheap and green coating exhibits low lateral adhesion to liquids including the reaction solution itself. To reduce the amount of material required to form a PDMS brush, we hold the reaction solution by a porous spreading layer (a paper). Using paper also allows coating of defined areas. The auto-phobic performance provides possibilities to apply PDMS brush coatings to liquid containers, which avoids loss of products due to incomplete emptying and reduces waste of water and solvents for subsequent cleaning. The strong tolerance of PDMS brushes to high temperature treatment and UV illumination as well as wear resistance makes them suitable to

prolong the service time of hydrophobic surfaces used in heat transfer.

Experimental Section

Fabrication and Characterization of the PDMS Brushes: Dichlorodimethylsilane (DCDMS, Sigma–Aldrich) was dissolved in 40 mL of toluene. The toluene was saturated with water (0.024×10^{-3} M). The molar ratios of DCDMS to water were controlled to be 5:1, 10:1, and 20:1 to determine the best reaction condition. The solution was swirled to mix for about 30 s and allowed to stand for 5 min at room temperature before use. Oxygen-plasma-treated silicon wafer (10 cm diameter, N-type doped with phosphor, (100) oriented, 525 μm thick) or soda-lime glass was submerged in the reactive solution for a certain time (from 30 s to 1 h) to get PDMS-brush-coated surfaces. The wetting properties of the surfaces were investigated using a contact angle measurement device equipped with a side camera (IDS uEye camera) and a goniometer. XPS was conducted using a Kratos Axis UltraDLD spectrometer (Kratos, Manchester, UK) to characterize the element composition of the silicone brush.

Fabrication of the Fluorinated Surfaces and Liquid-Impregnated Surfaces: An oxygen-plasma-treated silicon wafer was coated with 1H,1H,2H,H-perfluorooctyltrimethoxysilane (Sigma–Aldrich) under vacuum for 12 h. The surface was further heat treated at 120 °C for 2 h to obtain hydrophobicity. Liquid-impregnated surfaces were prepared by spin-coating (4000 rpm, time: 60 s) a layer of silicone oil (100 cSt, 10 wt% in hexane, Sigma–Aldrich) on PDMS brushes (grafting for 30 min).

Droplet-Sliding Erosion Assays: A dual control system was established to characterize the durability of PDMS brushes under high temperature (70 °C) and high humidity water vapor treatment (Figure S11, Supporting Information). A nitrogen flow was passed through boiling water in a bottle with one inlet and one outlet. The wet nitrogen was heated to 200 °C in a spiral circular copper tube. Surfaces (fluorinated surface and PDMS brushes) were treated with the heated water vapor. By changing the distance between surface and outlet, the vapor temperature can be controlled. The temperature of the vapor was monitored by a mercury thermometer with measuring range of 200 °C. The durability of the surfaces was demonstrated by measuring the wetting performance of the surfaces with different treating time.

Coating PDMS Brushes on Various Surfaces: Titanium dioxide (TiO_2) hierarchical surfaces (composed of 99 wt% TiO_2 and 1 wt% SiO_2) were prepared via liquid flame spray.^[19a] Hydrogen (50 L min^{-1}) and oxygen (15 L min^{-1}) were used as combustion gases to achieve a turbulent, high temperature flame (>2500 °C). Tetraethyl orthosilicate (TEOS, 98% pure, Alfa Aesar) and titanium (IV) isopropoxide (TTIP, 97% pure, Alfa Aesar) were dissolved in isopropyl alcohol. The overall Si + Ti atomic concentration in the precursor solution was 50 mg mL^{-1} . The ratio of silicon to titanium was 1/99 in precursor solution. Silicone nanofilament was prepared from trichloromethylsilane (TCMS).^[19b] After immersing an oxygen-plasma-treated glass in TCMS solution in toluene (water content: 260 ppm) for 6 h, the surface was coated with nanofilaments. The surface was further washed with hexane three times. The ZnO nanorod surfaces were prepared by spin coating (speed: 4000 rpm, time: 60 s) of zinc acetate dihydrate (0.75 M) in 2-methoxyethanol and monoethanolamine (0.75 M).^[9b] Sintered the surface at 350 °C for 30 min in order to get a ZnO thin layer. ZnO nanorods were further grown for 2 h in an aqueous solution containing zinc nitrate (0.025 M) and hexamethylenetetramine (0.025 M) at 90 °C. PDMS brushes were coated for 3 min after oxygen plasma treatment. After oxygen plasma treatment, all the surfaces were coated with PDMS brushes.

Supporting Information

Supporting Information is available from the Wiley Online Library or from the author.

Acknowledgements

The research leading to these results has received funding from the European Research Council under the European Union's Seventh Framework Programme (FP7/2007-2013)/ERC grant agreement n°883632 (H.J.B., W.S.) and the Deutsche Forschungsgemeinschaft (DFG) Priority Program 2171 (X.L.). The authors would like to express their gratitude to Prof. Doris Vollmer and Dr. Hao Lu for their fruitful suggestions.

Open access funding enabled and organized by Projekt DEAL.

Conflict of Interest

The authors declare no conflict of interest.

Author Contributions

J.L. and Y.S. contributed equally to this work. J.L., Y.S., and H.-J.B. designed and performed research; J.L., Y.S., X.Z., X.L., and M.K. contributed new reagents/analytic tools; J.L. and Y.S. analyzed data; J.L., M.K., W.S. and H.-J.B. wrote the paper. All authors have given approval to the final version of the manuscript.

Data Availability Statement

The data that support the findings of this study are available from the corresponding author upon reasonable request.

Keywords

adhesion, liquid-repellency, poly(dimethylsiloxane), polymer brushes, wetting

Received: January 11, 2021

Revised: February 22, 2021

Published online: May 6, 2021

- [1] K.-C. Park, P. Kim, A. Grinthal, N. He, D. Fox, J. C. Weaver, J. Aizenberg, *Nature* **2016**, 531, 78.
 [2] a) H. J. Cho, D. J. Preston, Y. Zhu, E. N. Wang, *Nat. Rev. Mater.* **2016**, 2, 16092; b) S. Daniel, M. K. Chaudhury, J. C. Chen, *Science* **2001**, 291, 633.
 [3] X. Wang, Z. Wang, L. Heng, L. Jiang, *Adv. Funct. Mater.* **2019**, 30, 1902686.
 [4] a) T. L. Liu, C.-J. C. Kim, *Science* **2014**, 346, 1096; b) X. Deng, L. Mammen, H.-J. Butt, D. Vollmer, *Science* **2012**, 335, 67;

- c) A. Tuteja, W. Choi, M. Ma, J. M. Mabry, S. A. Mazzella, G. C. Rutledge, G. H. McKinley, R. E. Cohen, *Science* **2007**, 318, 1618; d) S. Pan, R. Guo, M. Björnalm, J. J. Richardson, L. Li, C. Peng, N. Bertleff-Zieschang, W. Xu, J. Jiang, F. Caruso, *Nat. Mater.* **2018**, 17, 1040.
 [5] Y. Zushi, J. N. Hogarh, S. Masunaga, *Clean Technol. Environ.* **2012**, 14, 9.
 [6] a) T.-S. Wong, S. H. Kang, S. K. Y. Tang, E. J. Smythe, B. D. Hatton, A. Grinthal, J. Aizenberg, *Nature* **2011**, 477, 443; b) P. Kim, M. J. Kreder, J. Alvarenga, J. Aizenberg, *Nano Lett.* **2013**, 13, 1793; c) J. D. Smith, R. Dhiman, S. Anand, E. Reza-Garduno, R. E. Cohen, G. H. McKinley, K. K. Varanasi, *Soft Matter* **2013**, 9, 1772.
 [7] D. Wang, Q. Sun, M. J. Hokkanen, C. Zhang, F.-Y. Lin, Q. Liu, S.-P. Zhu, T. Zhou, Q. Chang, B. He, Q. Zhou, L. Chen, Z. Wang, R. H. A. Ras, X. Deng, *Nature* **2020**, 582, 55.
 [8] a) L. Wang, T. J. McCarthy, *Angew. Chem., Int. Ed.* **2015**, 55, 244; b) S. Wooh, D. Vollmer, *Angew. Chem., Int. Ed.* **2016**, 55, 6822; c) D. F. Cheng, C. Urata, M. Yagihashi, A. Hozumi, *Angew. Chem., Int. Ed.* **2012**, 51, 2956; d) S. Huang, J. Li, L. Liu, L. Zhou, X. Tian, *Adv. Mater.* **2019**, 31, 1901417; e) X. Zhao, M. A. R. Khandoker, K. Golovin, *ACS Appl. Mater. Interfaces* **2020**, 12, 15748; f) M. Liu, Z. Wang, P. Liu, Z. Wang, H. Yao, X. Yao, *Sci. Adv.* **2019**, 5, eaaw5643.
 [9] a) H. Teisala, P. Baumli, S. A. L. Weber, D. Vollmer, H.-J. Butt, *Langmuir* **2020**, 36, 4416; b) S. Wooh, N. Encinas, D. Vollmer, H.-J. Butt, *Adv. Mater.* **2017**, 29, 1604637; c) J. Liu, L. Ye, S. Wooh, M. Kappl, W. Steffen, H. J. Butt, *ACS Appl. Mater. Interfaces* **2019**, 11, 27422.
 [10] W. J. Herzberg, J. E. Marian, T. Vermeulen, *J. Colloid Interface Sci.* **1970**, 33, 164.
 [11] J. W. Krumpfer, T. J. McCarthy, *Langmuir* **2011**, 27, 11514.
 [12] A. Mitra, D. A. Atwood, *Encyclopedia of Inorganic Chemistry*, Wiley, New York **2006**.
 [13] W. J. Herzberg, W. R. Erwin, *J. Colloid Interface Sci.* **1970**, 33, 172.
 [14] a) C. Furmidge, *J. Colloid Interface Sci.* **1962**, 17, 309; b) D. A. Olsen, P. A. Joyner, M. D. Olson, *J. Phys. Chem.* **1962**, 66, 883; c) C. Antonini, F. Carmona, E. Pierce, M. Marengo, A. Amirfazli, *Langmuir* **2009**, 25, 6143.
 [15] P. J. Rossky, *Faraday Discuss.* **2010**, 146, 13.
 [16] C. P. Collier, J. B. Boreyko, G. Polizos, P. G. Datskos, S. A. Sarles, *Proc. Natl Acad. Sci. USA* **2014**, 111, 7588.
 [17] a) S. Sett, P. Sokalski, K. Boyina, L. Li, K. F. Rabbi, H. Auby, T. Foulkes, A. Mahvi, G. Barac, L. W. Bolton, N. Miljkovic, *Nano Lett.* **2019**, 19, 5287; b) K. Khalil, D. Soto, T. Farnham, A. Paxson, A. U. Katmis, K. Gleason, K. K. Varanasi, *Joule* **2019**, 3, 1377.
 [18] a) V. F. Petrenko, S. Peng, *Can. J. Phys.* **2003**, 81, 387; b) K. Golovin, D. H. Lee, J. M. Mabry, A. Tuteja, *Angew. Chem., Int. Ed.* **2013**, 52, 13007; c) X. Deng, L. Mammen, Y. Zhao, P. Lellig, K. Mullen, C. Li, H. J. Butt, D. Vollmer, *Adv. Mater.* **2011**, 23, 2962.
 [19] a) H. Teisala, F. Geyer, J. Haapanen, P. Juuti, J. M. Makela, D. Vollmer, H. J. Butt, *Adv. Mater.* **2018**, 30, 1706529; b) G. R. J. Artus, S. Jung, J. Zimmermann, H. P. Gautschi, K. Marquardt, S. Seeger, *Adv. Mater.* **2006**, 18, 2758.

ADVANCED MATERIALS

Supporting Information

for *Adv. Mater.*, DOI: 10.1002/adma.202100237

One-Step Synthesis of a Durable and Liquid-Repellent
Poly(dimethylsiloxane) Coating

Jie Liu, Yuling Sun, Xiaoteng Zhou, Xiaomei Li, Michael Kappl, Werner Steffen, and Hans-Jürgen Butt**

One-Step Synthesis of a Durable and Liquid-Repellent Poly(dimethylsiloxane) Coating

Jie Liu^{1,*}, Yuling Sun¹, Xiaoteng Zhou, Xiaomei Li, Michael Kappl, Werner Steffen, Hans-Jürgen

Butt*

Max Planck Institute for Polymer Research, Ackermannweg 10, D-55128, Mainz, Germany.

¹These authors contributed equally: Jie Liu and Yuling Sun.

*E-mail: liujie@mpip-mainz.mpg.de; butt@mpip-mainz.mpg.de

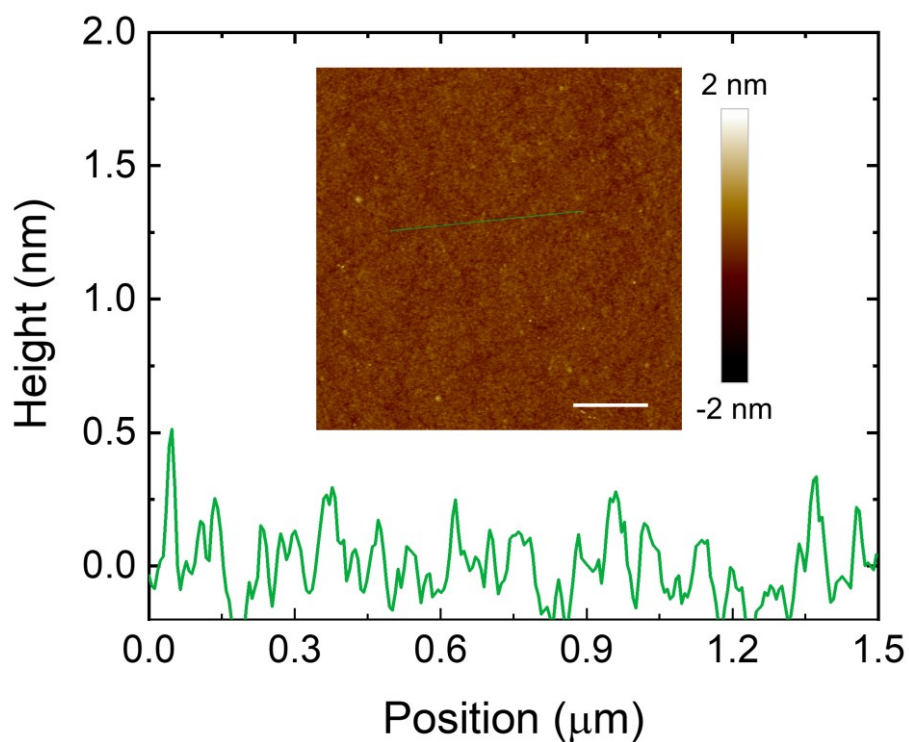


Figure S1 Morphology of PDMS brushes on silicon wafer. Image measured by atomic force microscope (AFM) in tapping mode. This shows the smooth surface of PDMS brushes with a low roughness of 0.1 nm (Ra) over an area of $3 \times 3 \mu\text{m}^2$. Scale bar: 600 nm. Reaction time: 30 min. The vertical profile of the PDMS along the labelled green line indicates a homogeneous PDMS brush layer formed on silicon wafer.

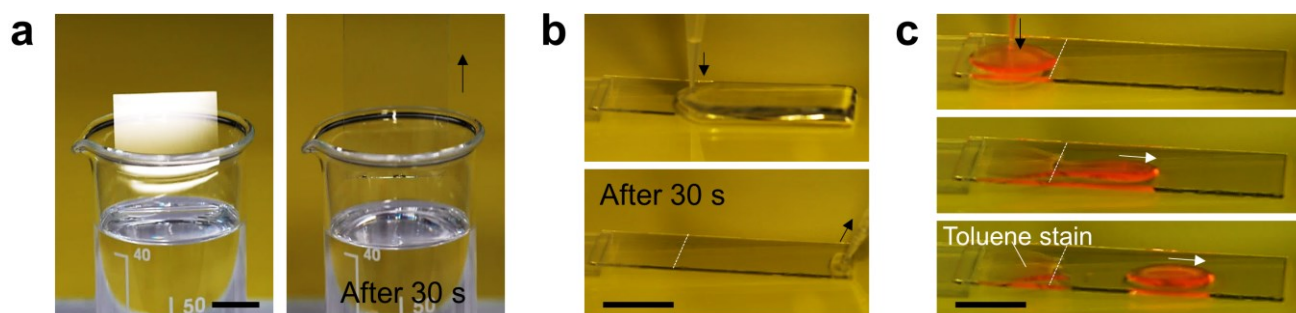


Figure S2 Easy fabrication of PDMS brushes. a) Fabrication of PDMS brushes on a glass slide by dip-coating. No DCDMS solution stains stay on the glass slide when pulling it from the solution after coating for 30 s. Scale bar: 1 cm. b) Fabrication of PDMS brushes on a glass slide by drop-casting. The reactive solution was easily removed without leaving stains. Scale bar: 2 cm. c) Images show toluene sliding on PDMS brush coated glass. In contrast to coated part, placement of drop occurs on upper, uncoated part. Toluene was labelled with Nile red. Scale bar: 2 cm.

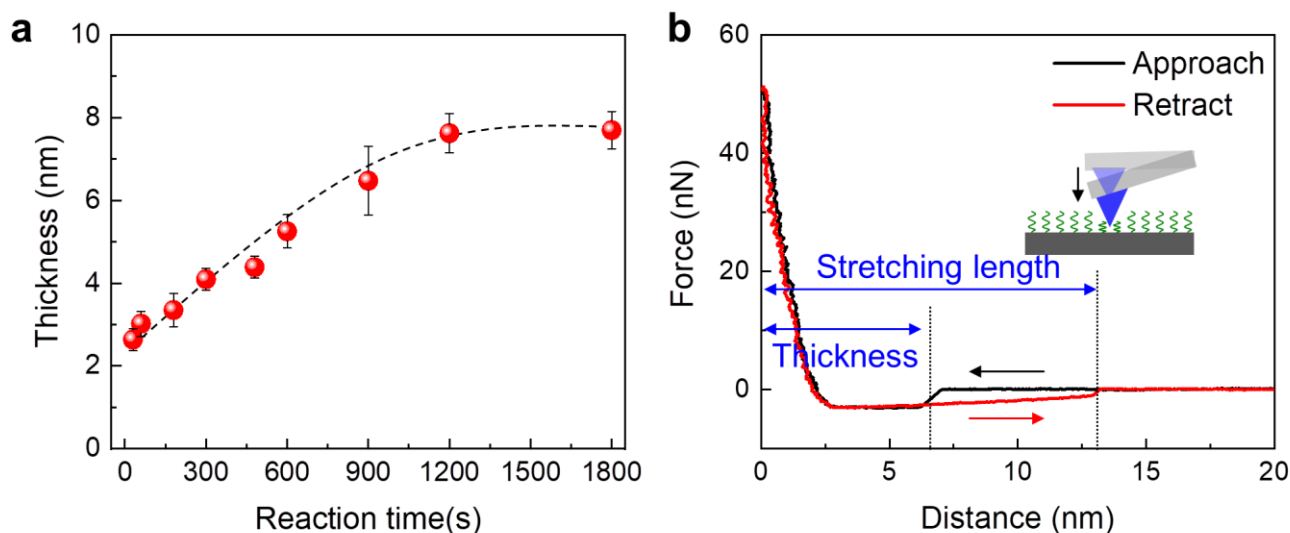


Figure S3 Thickness evolution of the PDMS brushes versus grafting time. a) The thickness of PDMS brushes on silicon wafers can be controlled from 2 nm to 8 nm. Each data point was calculated from 200 measurements. b) The thickness of PDMS brushes was extracted from force spectroscopy measurements with an atomic force microscope (NanoWizard IV, JPK Instruments, Berlin, Germany)^[1]. The cantilever mounted on the piezoelectric translator of the AFM can be controlled to approach or retract from surface with a constant velocity. The deflection of the cantilever was measured as a function of the piezo displacement with a split photodiode during approach and retraction. The resulting detector signal versus piezo position curves were converted to force versus distance curves (force curves) by the following procedure: first, a linear fit of the zero-force line was subtracted from the force curve. Second, the cantilever deflection sensitivity was determined by fitting the linear compliance region of the force curve corresponding to the portion of the measurement during probe contacting with a rigid substrate (clean silicon wafer without PDMS brush). We subsequently obtained force curves by subtracting the cantilever deflection from the piezo position to obtain correct position values and multiplying the deflection (obtained by dividing the detector signal value by the cantilever deflection sensitivity) by the spring constant of the cantilever to obtain force values. The black line shows the force between the probe and surface while approaching. At a distance of about 6-7 nm, an attractive force is observed, leading to negative

deflection of the cantilever. This event indicates the contact between tip and upper end of the PDMS layer, leading to attractive van der Waals and capillary forces between tip and layer. As the tip pushes further into the layer, forces become more and more repulsive, until a hard contact is reached (vertical force line). The PDMS brush thickness was determined as the distance between jump-in event and hard contact. At the same time, when the tip presses the PDMS brushes, some PDMS molecules can physically be attached to the tip. Recording the force loaded on the tip when withdrawing the tip from the surface, a stretching length (L) of PDMS molecules was defined, $L = 13 \pm 1$ nm. We assume that the molecular chain is completely straightened under stretching. The length of $-\text{Si}-\text{O}-$ is around 1.61 Å. By dividing the stretching length by the length per monomer we get the minimal number of monomers per chain. Therefore, the molecular weight of the PDMS brushes must be larger than 3000 ± 200 g/mol.

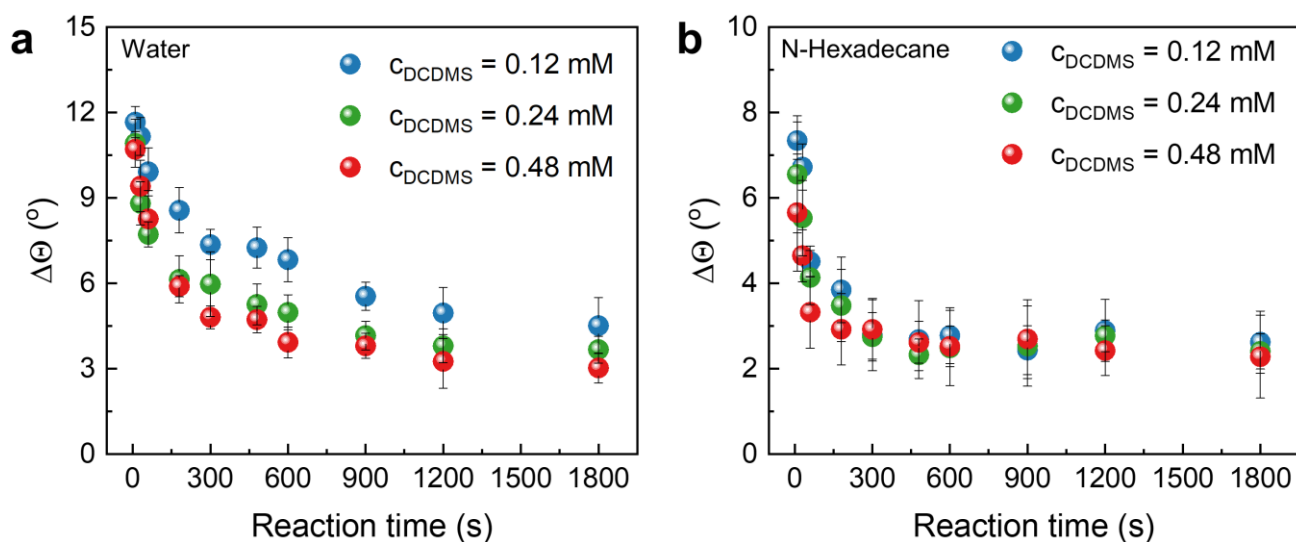


Figure S4 Influence of DCDMS concentration on grafting kinetics of PDMS brushes on silicon wafer. a) Contact angle hysteresis ($\Delta\Theta = \Theta_{\text{ACA}} - \Theta_{\text{RCA}}$) of water on PDMS brushes as function of grafting time and DCDMS concentration. b) Contact angle hysteresis ($\Delta\Theta$) of n-hexadecane on PDMS brushes as function of grafting time and DCDMS concentration. The water concentration (c_{water}) in toluene was 0.024 mM. The DCDMS concentration (c_{DCDMS}) was 0.12 mM (blue), 0.24 mM (green), or 0.48 mM (red). The grafting kinetics is accelerated with higher DCDMS concentration.

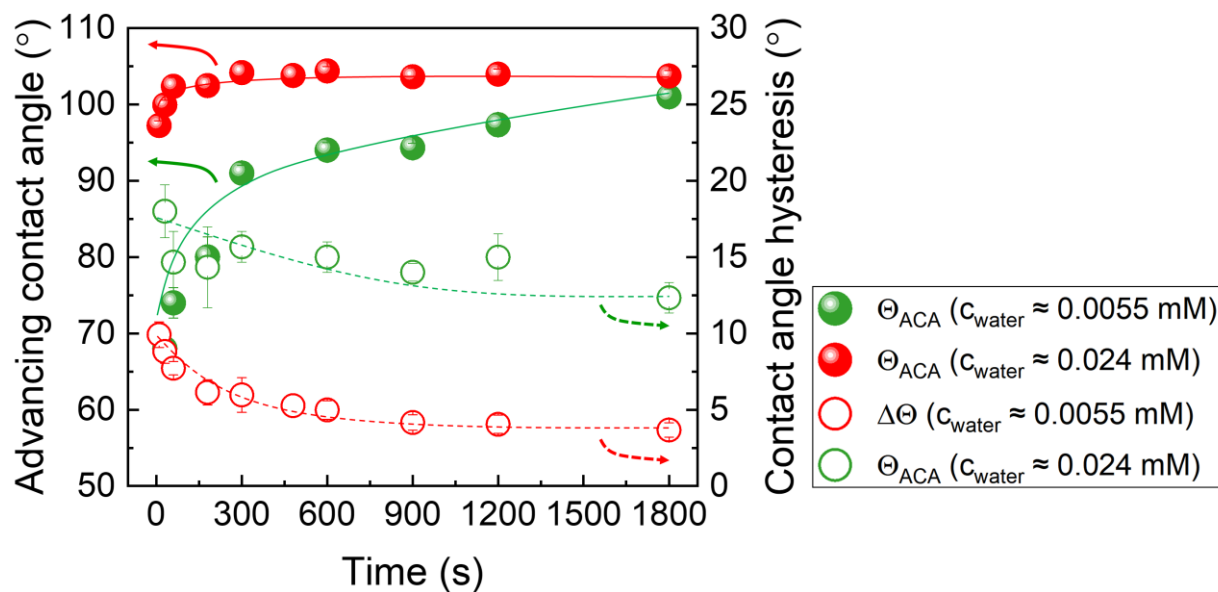


Figure S5 Influence of water concentration on the grafting process of PDMS brush. With a low water concentration (0.0055 mM) in toluene, the grafting speed is much slower than that when the water concentration is 0.024 mM. After reacting for 30 min, the PDMS brushes prepared from a low water concentration exhibit contact angle hysteresis of $\Delta\Theta \approx 13^\circ$ which is much higher than $\Delta\Theta \approx 4^\circ$ of the brushes grafted from $c_{\text{water}} \approx 0.024 \text{ mM}$. Therefore, the higher concentration of water can effectively accelerate the reaction and reduce grafting time.

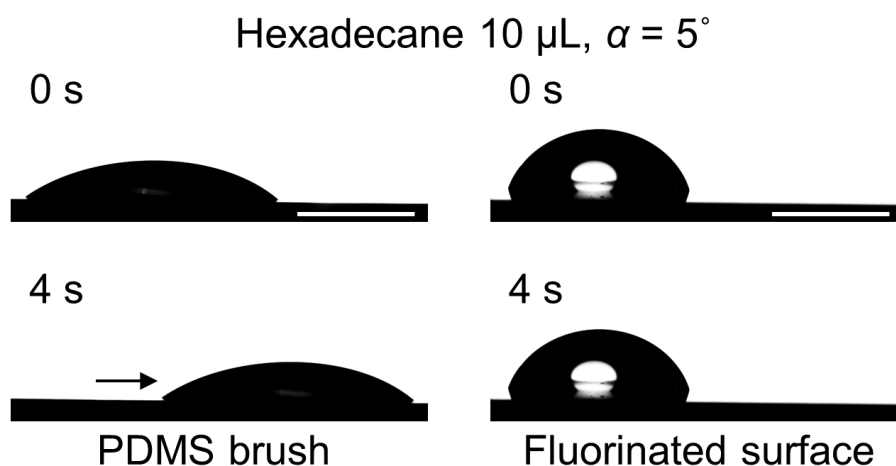


Figure S6 Sliding of n-hexadecane on hydrophobic coatings. 10 μL n-hexadecane droplet slides more easily on PDMS brushes than on the fluorinated surface. The fluorinated surface was modified with 1H,1H,2H,2H-perfluorooctyltrimethoxysilane. Tilt angle: 5° . Scale bar: 2 mm.

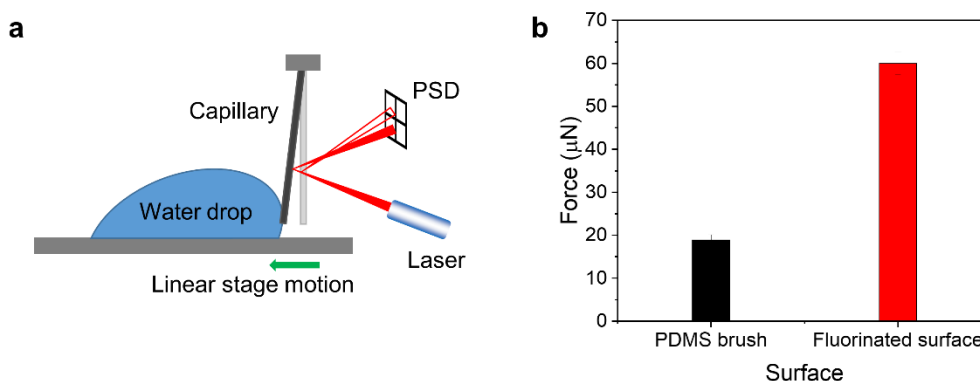


Figure S7 Measurement of lateral adhesion force of water droplet on surfaces. a) A drop of liquid is placed on a solid substrate mounted on a linear stage driven by a step motor.^[2] A laser beam incident on the capillary is reflected to a position-sensitive detector (PSD). The contact width between the drop of liquid and the solid surface (orthogonal to the direction of motion) and contact length (parallel to the direction of motion) are simultaneously monitored by cameras (not shown). b) The lateral adhesion force of a water droplet (5 μL) on PDMS brushes and fluorinated surface. The relative moving velocity of the drop is 250 $\mu\text{m/s}$.

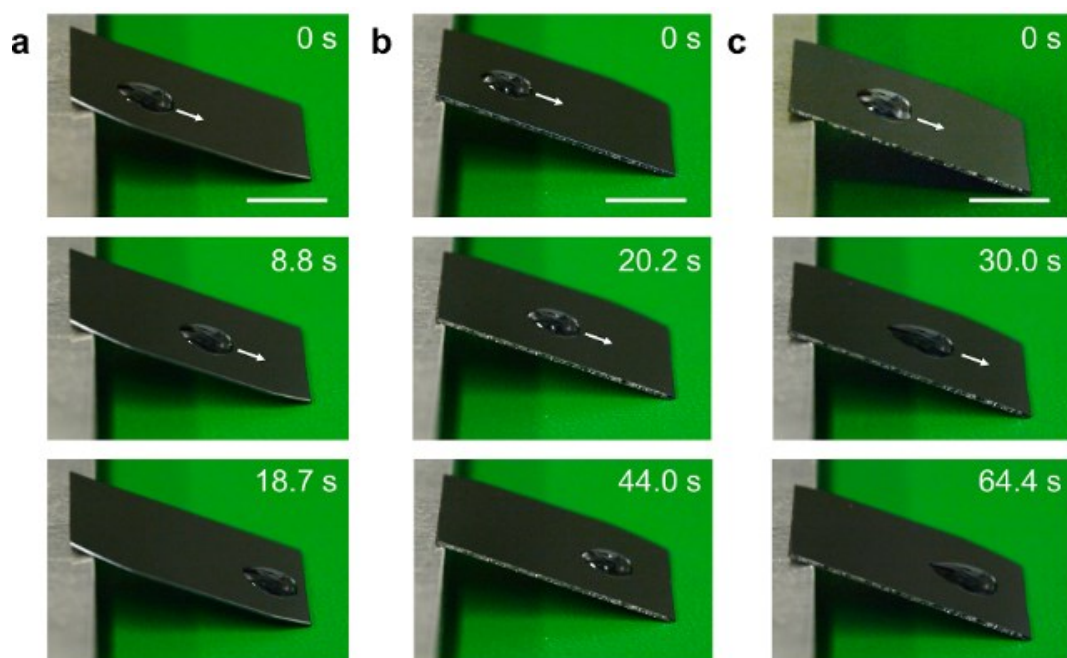


Figure S8 Sliding of liquid drops (30 μ L) with high viscosity on the PDMS brush coated surface.

The liquids are (a) poly(propylene glycol) (Mn \sim 725, viscosity: 115 cP), (b) poly(ethylene glycol)-block-poly(propylene glycol)-block-poly(ethylene glycol) (Mn \sim 2,000, viscosity: 325 cP), (c) poly(ethylene glycol)-block-poly(propylene glycol)-block-poly(ethylene glycol) (Mn \sim 4,400, viscosity: 1,200 cP). Tilt angle: 20°. Scale bar: 1 cm.

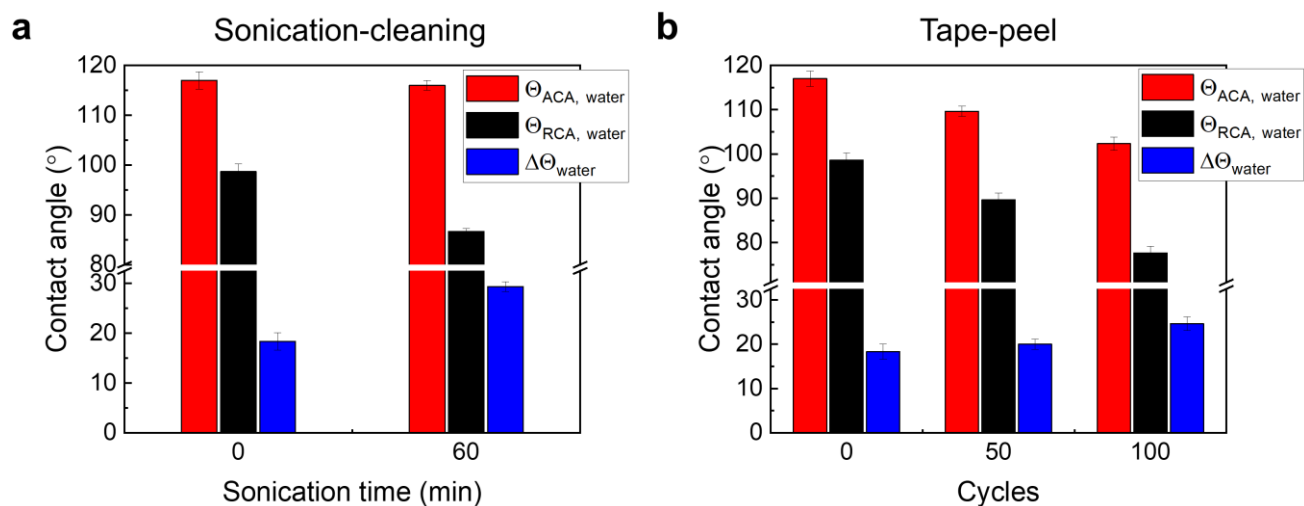


Figure S9 Mechanically robustness of fluorinated surface resisting sonication and tape-peel treatments. a) Advancing (Θ_{ACA}), receding (Θ_{RCA}) contact angle, and contact angle hysteresis ($\Delta\Theta$) of water on the fluorinated surface as function of sonication-cleaning time. The fluorinated surface was coated with 1H,1H,2H,2H-perfluorooctyltrimethoxysilane. b) Advancing (Θ_{ACA}), receding (Θ_{RCA}) contact angle, and contact angle hysteresis ($\Delta\Theta$) of water on the fluorinated surface as function of tape-peel test cycles. The receding contact angle of water decreases from 99° to 78° and the contact angle hysteresis increases from 18° to 25° after 100 peel-tests.

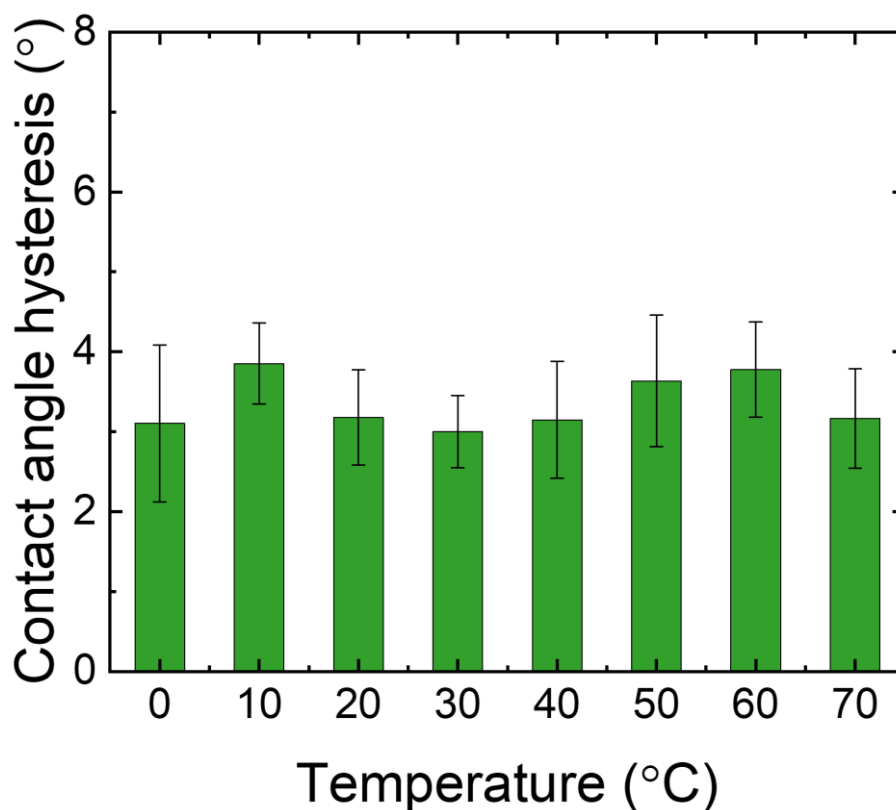


Figure S10 Stable wetting performance of PDMS brushes independent of temperature. Contact angle hysteresis of water on PDMS brushes was measured in a wide temperature window (from 0 °C to 70 °C). The test was done in a closed chamber with saturated water vapor, so that the evaporation or condensation effects of water have less influence on the wetting property measurements. The PDMS brushes exhibit a constant and low water adhesion independent of temperature.

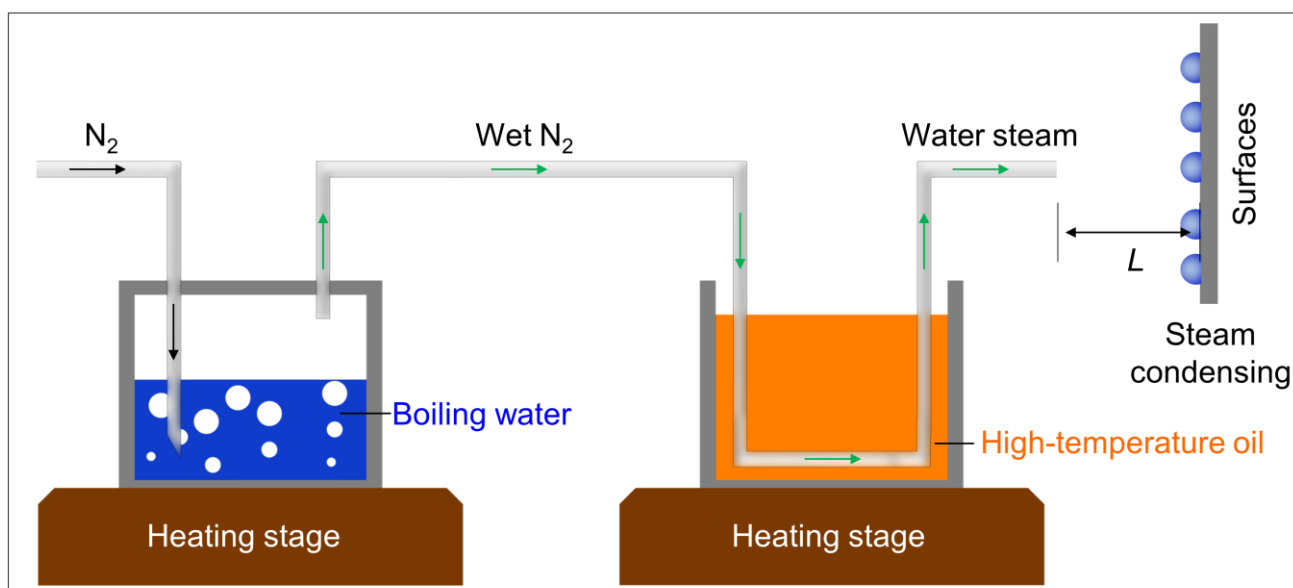


Figure S11 Schematic of the drop sliding erosion test. The setup was used to characterize the durability of PDMS brushes under high temperature (70 °C) and supersaturated water vapor treatment. Nitrogen was bubbled through boiling water with a flux of $0.8 \pm 0.1 \text{ L min}^{-1}$. Then, the wet nitrogen was heated to 200 °C in a spiral circular copper tube. The PDMS brush coated surface was located in front of the outlet of the N₂ flux. Through changing the distance between surface and outlet, the vapor temperature can be controlled. The vapor temperature at the position of surface was determined by a mercury thermometer with a measuring range of 200 °C.

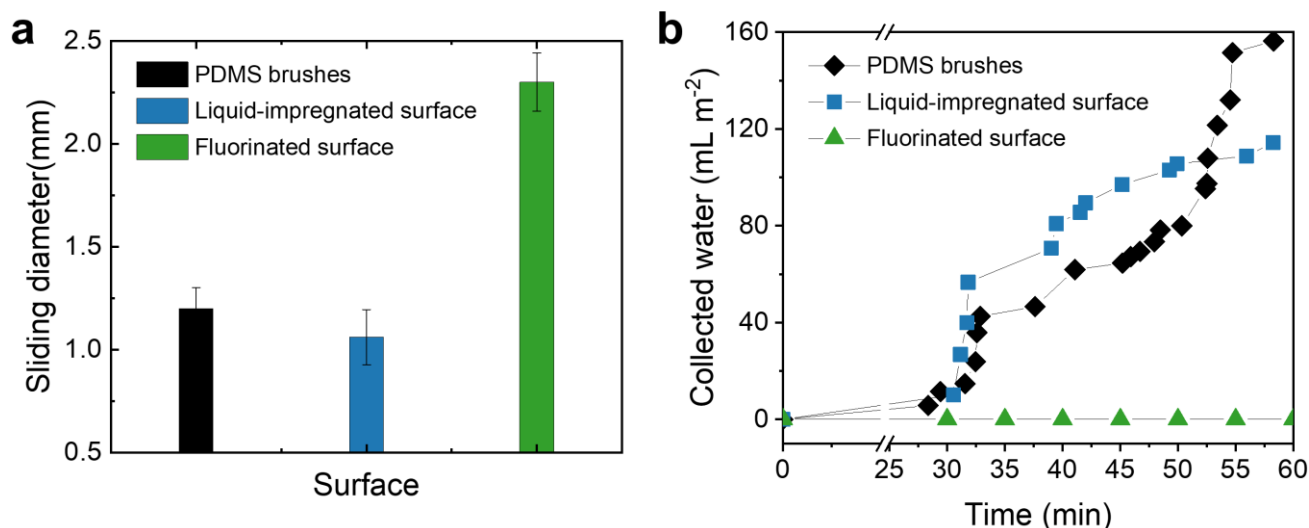


Figure S12 Mobility of condensed water droplets on PDMS brushes. a) The minimal sliding sizes of water droplets on different vertical surfaces ($\alpha = 90^\circ$ fixed tilt angle) such as PDMS brushes, silicone oil impregnated PDMS brush surface (liquid-impregnated surface), and fluorinated surface. Condensed water droplets slid off the vertical PDMS brushes with a diameter (D) around 1.2 mm, a little bit smaller than that on liquid-impregnated surface ($D = 1.0$ mm). In contrast, the minimal sliding size of water drops on the fluorinated surface is much bigger ($D = 2.3$ mm). b) Water-collection efficiency (water volume slid off per square meter surface) on different vertical surfaces such as PDMS brushes, liquid-impregnated surface, and fluorinated surface at 0°C (room temperature: $20 \pm 1^\circ\text{C}$, relative humidity: $80 \pm 5\%$). PDMS brushes present the highest water-collection efficiency in one hour. Requiring big droplets for sliding, no water was collected by sliding at the bottom of the fluorinated surfaces when condensed for 1 hour.

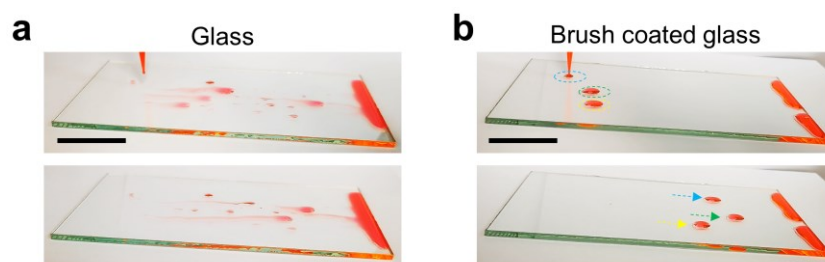


Figure S13 Large-scale fabrication of PDMS brushes on glass. a) Optical images show the pinning effect of toluene drops on window glass ($20 \times 10 \text{ cm}^2$) plate without PDMS brushes. b) Optical images show the sliding of toluene drops on window glass plate after coating PDMS brushes. Toluene drops are labeled with Nile red. Scale bar (a and b): 4 cm.

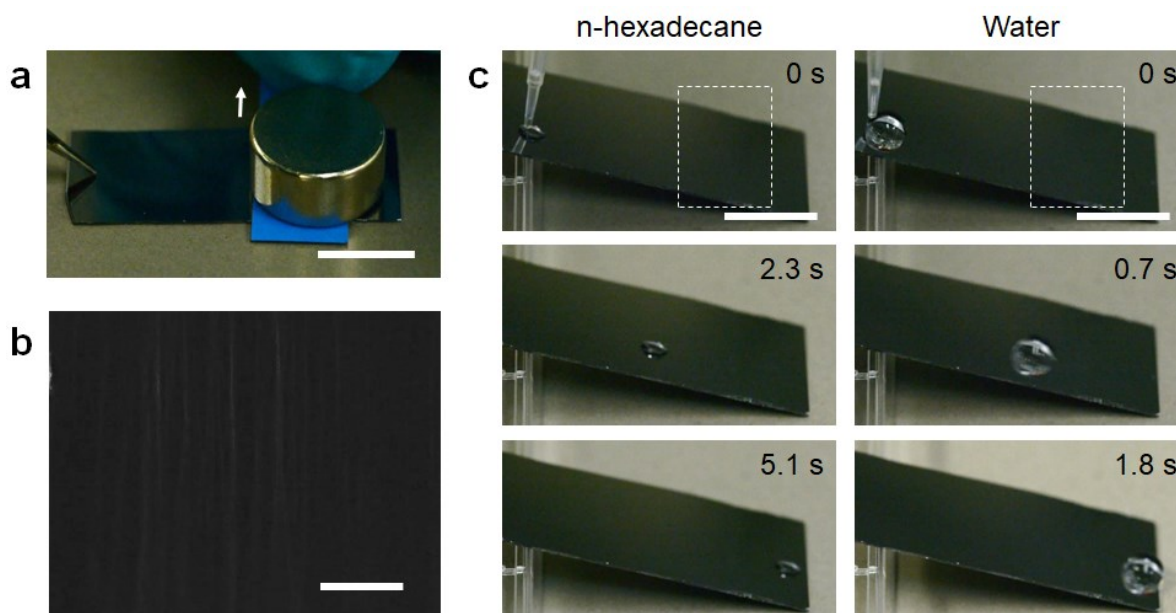


Figure S14 Abrasion test. a) A PDMS brush coated silicon wafer was rubbed with a sandpaper (1000 mesh) under the pressure of 1.1 kPa along the direction of the arrow. Scale bar: 1 cm. b) Digital image shows the scratches on the surface after abrasion for two times. Scale bar: 1 mm. c) Sliding of n-hexadecane ($5 \mu\text{L}$) and water ($10 \mu\text{L}$) droplets on the surface after sand paper (1000 mesh) abrasion. The dashed frame marks out the abrasion position. Scale bar: 1 cm.

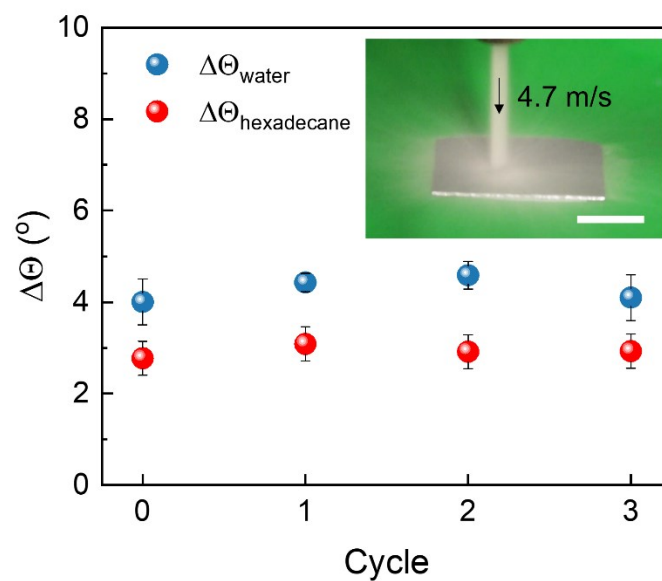


Figure S15 Stability of the surface resisting water jet impact. A water jet with mean velocity of 4.7 m/s was applied to impact the surface three times for 1 s. After the treatment, the wetting property of the surface remains unchanged with $\Delta\Theta_{\text{water}} = 4^\circ \pm 1^\circ$ and $\Delta\Theta_{\text{hexadecane}} = 2.7^\circ \pm 1^\circ$. Inset shows the impacting of water jet on the surface. Scale bar: 1 cm.

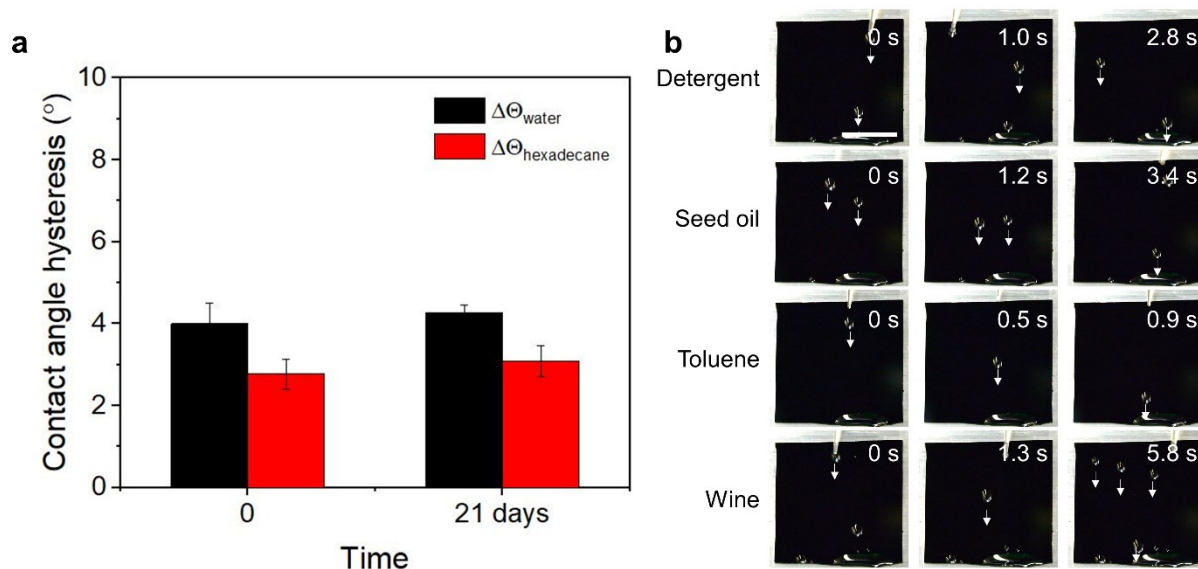


Figure S16 Real outdoor environment test. a) Contact angle hysteresis ($\Delta\Theta$) of water and n-hexadecane on PDMS brush coated silicon wafer after being placed in real outdoor environment for different time. b) Images show the sliding of various liquid drops on the PDMS brush coated surface after 21 days outdoor. Scale bar: 2 cm.

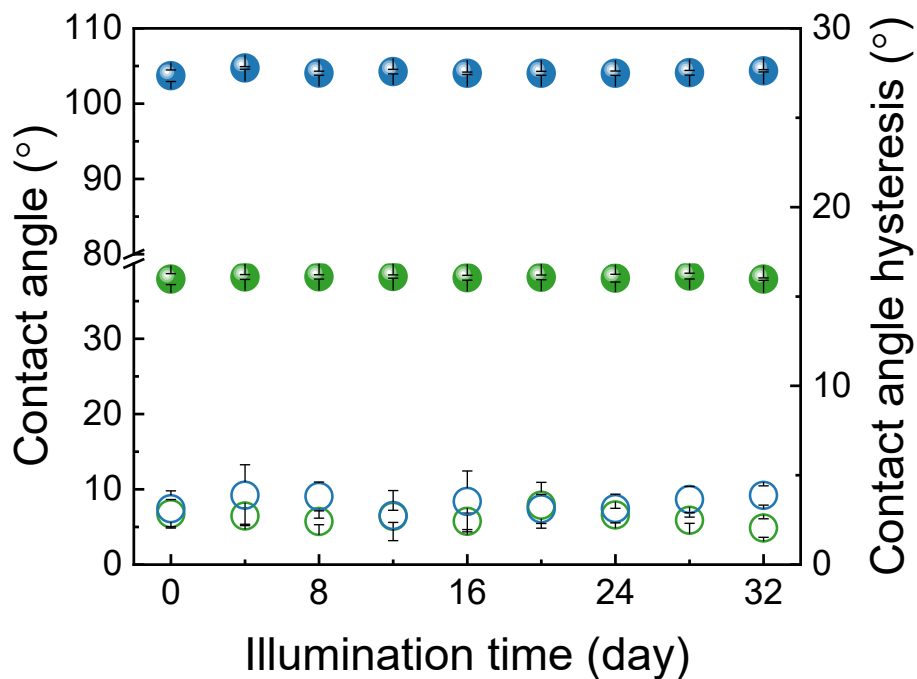


Figure S17 UV illumination resistance of PDMS brushes. Water (Θ_{ACA} : ● and $\Delta\Theta$: ○) and n-hexadecane (Θ_{ACA} : ● and $\Delta\Theta$: ○) repellency of the PDMS brushes versus UV illumination time. PDMS brushes present perfect wetting performance for at least 32 days under UV illumination. Wavelength: 365 nm. Intensity: 5 mW cm⁻².

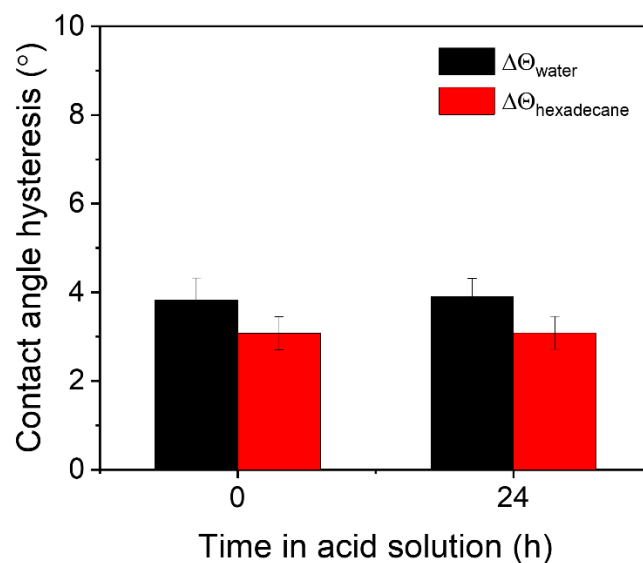


Figure S18 Stability of PDMS brushes in acid solution. HCl solution with pH = 1 was used. The surface is very stable even after immersing in acid solution for 24 hours. The wetting property remains the same with the original one. However, the surface is not stable and becomes hydrophilic after being immersed in the base solution. This might be caused by the chemical composition of the PDMS brushes, in which $-\text{Si}-\text{O}-$ can react with the OH^- .

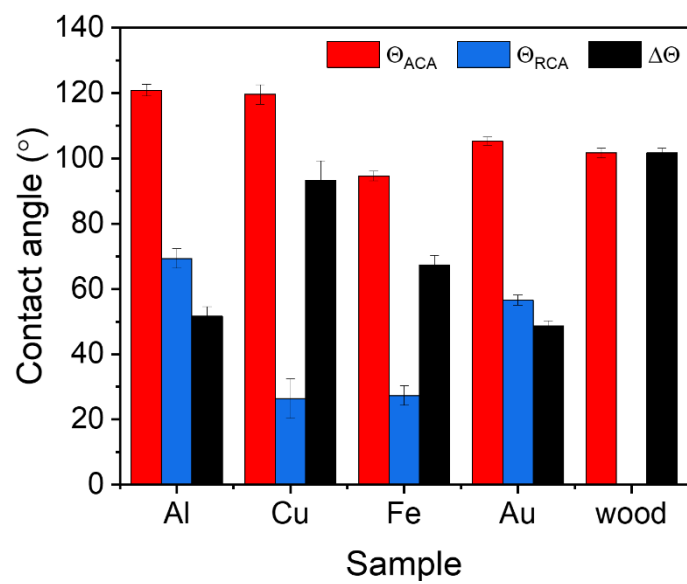


Figure S19 Advancing and receding contact angles (θ_{ACA} and θ_{RCA}) and contact angle hysteresis ($\Delta\theta$) of water on various surface coated with PDMS brushes.

Movie S1 Fast and spontaneous grafting of PDMS brushes on glass surface. No residual stains were left. The induced self-repellency towards the reactant solution implies that no extra washing procedures are necessary to clean the surface, which reduces solvent waste.

Movies S2 Dropwise condensation of toluene on PDMS brushes. Condensed toluene can slide fast and easily on the PDMS brushes.

Movie S3 Washing of detergent stain on the PDMS brushes. The detergent can be completely cleaned by washing with less water flux. After cleaning water droplets slide easily on the surface.

Reference

- [1] J. Ally, E. Vittorias, A. Amirfazli, M. Kappl, E. Bonaccorso, C. E. McNamee, H. J. Butt, *Langmuir* **2010**, *26*, 11797.
- [2] N. Gao, F. Geyer, D. W. Pilat, S. Wooh, D. Vollmer, H.-J. Butt, R. Berger, *Nat. Phys.* **2017**, *14*, 191.

2.4. X. Zhou et al. *Submitted, 2023.*

Thickness of nano-scale polydimethylsiloxane layers determines the motion of sliding water drops

Xiaoteng Zhou,¹ Yongkang Wang,^{1,2} Xiaomei Li,¹ Pranav Sudersan,¹ Katrin Amann-Winkel,^{1,3} Kaloian Koynov,¹ Yuki Nagata,¹ Rüdiger Berger,¹ Hans-Jürgen Butt¹

1. Max Planck Institute for Polymer Research, Ackermannweg 10, 55128, Mainz, Germany.
2. School of Mechanical Engineering, Southeast University, 211189, Nanjing, China.
3. Institute for Physics, Johannes Gutenberg University Mainz, Staudingerweg 10, 55128 Mainz, Germany.

Submitted to:

Advanced Materials

Author Contribution:

Xiaoteng Zhou and Hans-Jürgen Butt designed the experiment. Xiaoteng Zhou, Pranav Sudersan, and Rüdiger Berger did the AFM related measurement and analysis. Xiaoteng Zhou, Yongkang Wang and Yuki Nagata did the SFG measurement and analysis. Xiaoteng Zhou and Katrin Amann-Winkel did the X-ray measurement and analysis. Xiaoteng Zhou and Xiaomei Li did the drop velocity measurement and analysis. Kaloian Koynov did the diffusion time measurement by fluorescence correlation spectroscopy (FCS). All authors wrote the paper and have approved the final version of this manuscript.

1
2
3
4 **Thickness of nano-scale poly(dimethylsiloxane) layers determines the**
5 **motion of sliding water drops**
6
7

8
9 Xiaoteng Zhou,¹ Yongkang Wang,^{1,2} Xiaomei Li,¹ Pranav Sudersan,¹ Katrin Amann-
10 Winkel,^{1,3} Kaloian Koynov,¹ Yuki Nagata,¹ Rüdiger Berger,¹ Hans-Jürgen Butt^{1,*}
11
12
13
14

15
16 1. Max Planck Institute for Polymer Research, Ackermannweg 10, 55128, Mainz, Germany.
17

18 2. School of Mechanical Engineering, Southeast University, 211189, Nanjing, China.
19

20 3. Institute for Physics, Johannes Gutenberg University Mainz, Staudingerweg 10, 55128 Mainz,
21 Germany.
22
23

24
25
26
27 *E-mail: butt@mpip-mainz.mpg.de.
28
29

30
31
32 **Keywords:** wetting, liquid-like coating, drop friction, interfacial water, microfluid.
33
34
35
36
37
38
39
40
41
42
43
44
45
46
47
48
49
50
51
52
53
54
55
56
57
58
59
60
61
62
63
64
65

1
2
3
4 **Abstract**
5
6

7 Layers of nanometer thick polydimethylsiloxane (PDMS) are widely applied as hydrophobic
8 coatings because of their environmentally-friendly and chemically-inert properties. In applications
9 such as heat exchangers or fog harvesting, low water drop friction on surfaces is required. While
10 the onset of motion (static friction) has been studied, our knowledge of dynamic friction needs to
11 be improved. Which processes lead to energy dissipation and cause friction? This knowledge is
12 important to minimize drop friction. Here, we measured the dynamic friction of drops on PDMS
13 layers of different thicknesses and architecture, covering the whole available velocity regime. The
14 layer thickness L turned out to be a predictor for drop friction. 4-5 nm thick PDMS layer showed
15 lowest dynamic friction. A certain minimal layer thickness is necessary to form homogeneous
16 surfaces and reduce the attractive interaction between water and the substrate. The increase in
17 friction above $L = 4-5$ nm is attributed to the PDMS meniscus formed at the contact line. When
18 the contact line moves, the meniscus is dragged. Energy is dissipated due to chain stretching and
19 viscous dissipation. AFM force and friction measurements support this interpretation. The effect
20 is enhanced with increased viscosity of PDMS layer caused by entanglement of the chains.
21
22
23
24
25
26
27
28
29
30
31
32
33
34
35
36
37
38
39
40
41
42
43
44
45
46
47
48
49
50
51
52
53
54
55
56
57
58
59
60
61
62
63
64
65

Introduction

Environmentally-friendly polydimethylsiloxane (PDMS) coatings are often used to fabricate hydrophobic surfaces.^[1] These surfaces can help to reduce interfacial friction,^[2] and exhibit anti-fouling and anti-icing properties.^[3] One way to coat PDMS is by chemically anchoring PDMS chains to substrates,^[4] which prevents surface depletion.^[5] In this case, one end of the polymer chain is fixed on the substrates by the covalent bond, the rest of the chain is free to rotate, bend, and stretch due to the low glass transition temperature ($<-100^{\circ}\text{C}$) of PDMS.^[6] Such surfaces are called covalently attached liquid surfaces (CALs)^[1] or an omniphobic liquid-like surface.^[6] Limited by the length of the polymer chain and its tendency to pack randomly, the film thickness of CALS is typically a few nanometers in size.

When a liquid drop is placed on a soft layer, the surface tension of the liquid exerts a tensional force at the contact line.^[7] As a result, the layer is locally deformed. When the drop moves over the surface, this deformation moves with the drop and energy is dissipated. In contrast to micrometer-thick PDMS layers, viscoelastic deformation at the contact line is minimal and less energy is dissipated on a nanoscopic layer than on thick PDMS layers.^[8] This liquid-like behavior in combination with low viscoelastic energy dissipation in thin layers makes PDMS CALS a promising coating for use in applications such as fluid manipulation, in heat exchangers, and in microfluidic applications.^[9] In engineering applications, it is important that drops move fast, with little resistance.^[10] Here, we study the dynamic drop friction of water drops on PDMS CALS. The aim is to identify conditions minimizing drop friction.

The static friction force F is typically measured by placing a water drop on a solid surface and then tilting the surface until the drop starts sliding off at a tilt angle α . Low roll-off angles α indicate low static friction.^[11] The reason for such low roll-off angles is low contact angle hysteresis. Drops slide off surfaces once the gravitational force, $mg \sin \alpha$ (m is the drop mass, $g = 9.81 \text{ m/s}^2$) exceeds the capillary force F_0 , which is the main component of the static friction force:

$$F \approx F_0 = \gamma k (\cos \Theta_R^0 - \cos \Theta_A^0) \quad (1)$$

Here, w is the width of the drop's contact area, γ is the surface tension of the liquid, and $k \approx 1$ is a geometrical drop shape factor, Θ_A^0 and Θ_R^0 are the static advancing and receding contact angles. The difference between Θ_A^0 and Θ_R^0 determines the onset of sliding. Because of the capillary force in equation (1) low roll-off angles of a tiny drop ($< 100 \mu\text{L}$) imply low contact angles hysteresis $\Theta_A^0 - \Theta_R^0$.

1
2
3
4 Nanoscopic PDMS coatings often lead to particularly low contact angle hysteresis.^[1, 6] Grafting-
5 to^[12] and grafting-from^[13] methods have been developed to coat surfaces such as glass, Si wafers
6 or textured structures with nanometer thick layers of PDMS. Different preparations result in
7 different architectures of the polymer layers.^[1, 6] In previous work, the onset of sliding was
8 correlated with the reduced grafting density, $\Sigma = \sigma\pi R_g^2$.^[14] Here, σ is the grafting density in m^{-2} and
9 R_g is the radius of gyration of the polymer in a melt. Empirically, the layer thickness was found to
10 help predict the static friction changing.^[1, 6] Gresham *et al.* found that the static friction is minimal
11 at 2-5 nm layer thickness.^[14] In order to achieve low friction, grafted chains should fully cover the
12 substrate with a homogeneous brush. Moreover, the chain length needs to be long enough to
13 display its full liquid mobility.
14
15
16
17
18
19
20
21

22 In this study, we focused on dynamic friction. Dynamic friction $F(U)$ is the force required to move
23 a drop at a given velocity U . In a steady state it is related to energy dissipation (that is the work
24 done to move the drop per unit time P) by $P = F(U) \times U$. Only when a drop is moving, can it
25 dissipate energy. As far as we know, dynamic friction forces $F(U)$ have neither been
26 systematically measured on PDMS layers, nor have the relevant energy dissipation processes
27 been identified. To analyze which processes, dissipate energy and cause friction, we needed to
28 look at dynamic friction. The questions we addressed were: What is the ideal layer thickness and
29 architecture to achieve the lowest drop friction? Is the layer thickness a sufficient descriptor of
30 dynamic drop friction or does the architecture of the brush influence drop friction? What is the
31 energy dissipation processes in thin PDMS layers during drop movement?
32
33
34
35
36
37
38

39 To answer these questions, we investigated how coating thickness and architecture influence
40 drop sliding. Three methods of coating surfaces with PDMS were applied (Table 1), including one
41 grafting-from method and two grafting-to methods. Grafting-from leads to PDMS chains anchored
42 at one end to the solid substrate.^[1] In one grafting-to method we allowed the PDMS chain with
43 one functional end to bind to the surface. Both methods led to polymer brushes. In the second
44 grafting-to method, the PDMS chains were able to spontaneously bind to the substrate and could
45 have more than one adsorption point. This is usually called pseudo-brush.^[15] To test the different
46 PDMS coatings, we imaged water drops sliding down tilted surfaces and obtained the friction
47 force by solving the equation of motion. Layer thicknesses were measured by atomic force
48 microscopy, X-ray reflectivity and ellipsometry. The layer mobility variation, which results in the
49 friction difference, was also characterized by AFM friction measurements and by using
50 fluorescence correlations spectroscopy (FCS). In addition, the interfacial water structure and
51 microscopic polymer structure was explored using sum-frequency generation (SFG).
52
53
54
55
56
57
58
59
60
61

Experimental Section

Si wafers as substrates: To reduce the contribution of electrostatic interactions^[16], P-doped silicon wafers were used as substrates. Silicon wafers (orientation: <1-0-0>, resistivity: $\sim 10^{-20} \Omega \text{ cm}$, polished, SiMat Inc.) were cleaned by sonication in hexane and ethanol for 3 min. Subsequently, the wafers were treated with oxygen plasma (Femto low-pressure plasma system, Diener electronic GmbH, Germany) for 5 min at 200 W to enhance their reactivity and generate surface hydroxyl groups.

Fabrication of PDMS layers by grafting-to methods using methyl-terminated PDMS: Wafers were immersed in 20 mL methyl-terminated liquid PDMS (Sigma–Aldrich), with different molecular weights ($M_w = 1350, 3500, 6000, 14000, 18500, 30000$ and $117000 \text{ g mol}^{-1}$) in an oven at 150°C for 24 hours. To reduce the influence of free silicon oil or other adsorbed organic molecules, PDMS surfaces were carefully rinsed before use. The wafers were washed with toluene at least three times to remove free PDMS.^[12a, 12c] The samples were named as GT_ M_w e.g. GT_1350 and GT_117000.

Fabrication of PDMS brushes coatings by grafting-from methods: A reactive solution was prepared by dissolving 1.4 mL of dichlorodimethylsilane (DCDMS, Sigma–Aldrich) in 40 mL of water-saturated toluene. The silicon wafers, previously treated with oxygen plasma, were immersed in the reactive solution for either 10 seconds or 30 minutes to allow the DCDMS to polymerize starting from surface hydroxyl groups. Afterwards, the samples were washed three times in toluene to remove any unreacted monomers. The samples were named GF_10s and GF_30min. The molecular weight of such a brush is evaluated by a fitting due to its linear structure (Supplementary Section 1).

Fabrication of PDMS layer by grafting using chlorine terminated PDMS: Silicon wafers were immersed in a PDMSC (polydimethylsiloxane-chlorine terminated, Sigma–Aldrich) liquid. Afterwards, the wafers were placed in a sealed container inside an oven at 120°C for 12 hours. Finally, the samples were washed three times with toluene, creating sample GT_SCT.

Wetting properties measurement by goniometer: Static advancing and receding contact angles as well as the roll-off angles of water on the surface were measured by an OCA 35 goniometer (DataPhysics Instruments, Germany). Side view videos of sessile drops were recorded when changing the volume of a sessile water drop gradually ($1.0 \mu\text{L}\cdot\text{s}^{-1}$) between 10 and 20 μL using a Hamilton syringe. Static advancing and receding contact angles were determined by fitting an

1
2
3
4 ellipse model to the contour images. Roll-off angles of the water drop on surfaces were
5 characterized by goniometer with a 33 μL drop by titling the platform at a speed of 0.1°/s. Each
6 data point is the average of at least 3 individual measurements on different areas of the surface.
7
8
9

10 **Table 1. The abbreviation and properties of the PDMS layer coated on the Si wafer.**

	Units [†]	M _w (g/mol) [†]	Θ_{A}^0 (°)*	Θ_{R}^0 (°)*	Method
GT_1350	18	1350	102	95	Grafting-to ^[12a]
GF_10s	22	1750	104	98	Grafting-from ^[13a]
GF_30min	38	2800	105	101	Grafting-from
GT_3500	46	3500	106	101	Grafting-to
GT_6000	80	6000	108	106	Grafting-to
GT_14000	186	14000	108	103	Grafting-to
GT_18500	246	18500	110	108	Grafting-to
GT_SCT	127	9500	108	106	Grafting-to ^[12d]
GT_30000	400	30000	109	104	Grafting-to
GT_117000	1560	117000	107	76	Grafting-to

11
12
13
14
15
16
17
18
19
20
21
22
23
24
25
26
27
28
29
30
31
32
33
34
35
36
37
38
39
40
41
42
43
44
45
46
47
48
49
50
51
52
53
54
55
56
57
58
59
60
61
62
63
64
65

[†]The obtaining of the units and M_w are described in Supplementary Section 1. * Θ_{A}^0 and Θ_{R}^0 are the static advancing and receding contact angles measured by goniometer.

Tilted plate experiments: To characterize dynamic wetting, we conducted the tilted plate experiment as previously reported.^[16] 33 μL drops of distilled water (<1 $\mu\text{S}/\text{cm}$, Gibco, Thermo Fisher Scientific) were deposited at the top of a tilted platform by a grounded syringe needle (1.5 mm outer diameter), which was connected to a peristaltic pump (MINIPULS 3, Gilson). Before every experiment, the surface was neutralized by an ionizing air blower for 5 min (Aerostat PC ionizing air blower, Simco-Ion). The drops fell from a height of ≈ 5 mm which was similar to the drop size itself to avoid drop re-bouncing. The drops were neutralized by a grounded copper wire immediately after they landed on the surface. We imaged the drops from the side with a frame rate of 1000 or 2000 per second over a slide length of typically 4.5 cm using a FASTCAM Mini UX100 (Photron) with a TitanTL telecentric lens ($\times 0.268$, Edmund Optics). The videos were analyzed by open drop-shape analysis programmed in MATLAB. The dynamic contact angles were determined by applying a polynomial fit to each frame of the images. In the end, we analyzed the drop velocity U , dynamic contact angles at the front (advancing contact angle, Θ_{A}) and rear (receding contact angle, Θ_{R}), and the length of the drops. All the measurements were done at 20 ± 1 °C and at 20–40% relative humidity.

1
2
3
4 *Atomic force microscope (AFM) measurements:* The layer thickness, thickness distribution
5 mapping, and chain length measurements were performed with cantilevers having a nominal
6 resonance frequency of $f = 70$ kHz and a nominal spring constant of $k_z = 2 \text{ N} \cdot \text{m}^{-1}$ (Brucker
7 OLTESPA). Spring constants were determined by the thermal tune method.^[17] Samples were
8 imaged using the JPK NanoWizard 4 AFM. The “Quantitative Imaging” (QI) mode was used to
9 obtain force-distance curves at every point of the 128×128 pixels with a scanning area of $3 \times 3 \mu\text{m}^2$
10 at a set point force of 5 nN (Vertical movement 1000 nm, time per pixel 20 ms). To determine the
11 PDMS film thickness and obtain information about the PDMS chain length we recorded force-
12 piezo displacement curves, briefly called “force curves”. In the approach stage of force curves,
13 we calculated the difference in piezo-position of the point where the tip first touched the surface
14 and was pulled onto the film and the point where attractive and repulsive sample forces balanced.
15 At this point there is no net force acting on the tip. This distance is called jump-in distance $L_{\text{jump-in}}$.
16 Accordingly, we determined the “PDMS chain length” in the retracting cycle. We calculated the
17 difference in piezo-displacement for the point where attractive and repulsive forces balance and
18 the point where the tip snaps off the surface, i.e., detaches from the PDMS chains. We call it
19 “jump off distance” $L_{\text{jump-off}}$. It is important to note that this value may be lower than the real chain
20 length because the point where the tip attaches from the PDMS chain may not be the end of the
21 chain. The jump-in and jump-off distances were calculated for each force curve of the scan area
22 automatically using a custom Python script
23 (https://github.com/PranavSudersan/afm_surface_tension/blob/main/AFM_Liquid_Analyzer.ipynb)
24 b).

25
26
27
28
29
30
31
32
33
34
35
36
37
38
39
40 *X-ray reflectivity (XRR):* X-ray reflectivity measurements were applied to measure the thickness
41 of the PDMS layers. X-rays impinged on the sample at grazing incidence angles and probe
42 scattering angles slightly above total reflection. At the interfaces of a film (PDMS, substrate), the
43 electron density changes. The reflected X-ray intensity is measured as a function of 2θ . Kissing-
44 fringes appear due to interference of the reflected X-rays at the different interfaces, the period of
45 the fringes is inversely proportional to the thickness of the film.^[18] Here, we used a Rigaku
46 SmartLab Instrument with a rotating Cu-Anode, at an X-ray energy of 8.04 keV. The measured
47 XRR data were analyzed using the software package (SmartLab Studio II).^[19]

48
49
50
51
52
53
54 *Ellipsometry measurement:* The thickness of PDMS layers was measured by an ellipsometer
55 (Nanofilm EP3, 658 nm. Laser 50 mW) using a $10\times$ lens and by fitting, using a dispersion model.^[20]
56 The fitting parameters for the silicon wafer (refractive index: 3.836) and PDMS (refractive index:
57
58
59
60
61
62
63
64
65

1
2
3
4 1.428) were kept constant. The native SiO₂ layer (refractive index: 1.457) on the Si wafer was
5 measured as 1.6 ± 0.1 nm. The error reflects the variation within a series of measurements.
6

7
8 *Characterization of PDMS layers:* We measured the thickness of the PDMS layers using three
9 independent methods (Figure 1a and Supplementary Section 2): AFM force curves utilizing the
10 jump-in distance,^[21] X-ray reflectivity (XRR),^[18] and ellipsometry.^[20] We sorted the layer according
11 to average thickness from these measurements. The results from the three thickness
12 measurement techniques were in good agreement up to $L=6$ nm. For thicker layers, the difference
13 in results obtained with different methods increased. One possible reason for the different results
14 could be a non-uniform thickness of layers. To further analyze the thickness distribution across
15 the surface, the AFM QI™ mode was utilized to map the surface thickness distribution using force
16 curves (Supplementary Figure S2b). Typically, the thickness at different locations on one sample
17 varied by ≈2 nm.
18

19
20 *AFM friction measurement:* The measurement was performed with a JPK NanoWizard 4. We
21 calibrated the cantilever spring constant k_z and the sensitivity S_z in the lateral direction using a
22 non-contact method reported by Mullin und Hobbs.^[22] We used PPP-CONT-W (NANOSENSORS,
23 width: 50 μm, length: 450 μm, nominal resonance frequency: 13 kHz) as sensors. Friction is
24 measured in liquid using the contact mode. The applied normal force was adjusted from 30 to
25 10 nN. Initially, the AFM tip was brought in contact with the PDMS surface in water at a high
26 normal force (30 nN). Then the friction force was measured over a scan size of 10 μm at a tip
27 velocity of 10 μm/s (scan rate: 1 Hz). The normal load was then lowered subsequently to 20 nN
28 and 10 nN and the friction force was measured again. All measurements were carried out at 24 °C,
29 measured inside the acoustic housing of the AFM.
30

31
32 *Fluorescence correlation spectroscopy (FCS) measurement:* FCS experiments were performed
33 on a commercial confocal microscope (LSM 880, Carl Zeiss, Jena, Germany) using a C-
34 Apochromat 40x/1.2 W (Carl, Zeiss, Jena, Germany) water immersion objective. A HeNe laser (λ
35 = 633 nm) fiber coupled to the LSM 880 was used for the excitation of the terrylene diimide (TDI)
36 dyes. The emission light in the spectral range 650-700 nm was detected using a spectral detection
37 unit (Quasar, Carl Zeiss, Jena, Germany). A glass coverslip coated with a PDMS layer infiltrated
38 with TDI molecules was mounted in an Attofluor® stainless steel chamber (Thermo Fisher
39 Scientific, Waltham, MA, USA). The TDI dye molecules were infiltrated into the PDMS layer by
40 adding a hexane solution on top, followed by hexane evaporation and vacuum annealing at 70°C
41 overnight. The chamber was then filled with 1 mL MiliQ water so that the PDMS layer was
42 completely covered by water. The confocal detection volume was placed over the PDMS layer
43

and FCS autocorrelation curves were recorded for 150 seconds in repetitions of 30 seconds. The experiments were performed multiple times at 3-7 different lateral positions on the layer. The experimental autocorrelation curves were fitted with an analytical equation for a two-dimensional Brownian motion:^[23]

$$G(\tau) = 1 + \left[1 + \frac{f_T}{1-f_T} e^{-\tau/\tau_T} \right] \cdot \frac{1}{N} \cdot \sum_{i=1}^m \frac{f_i}{1 + \frac{\tau}{\tau_{D,i}}} \quad (2)$$

Here f_T and τ_T are the fraction and the decay time of the triplet state, respectively, and N denotes the average number of fluorescent species in the observation volume. f_i is the fraction of the fluorescent species possessing the diffusion time $\tau_{D,i}$. The diffusion coefficient D_i of the i -th species is related to their diffusion time through $D_i = r_0^2/4\tau_{D,i}$ where r_0 is the radial dimension of the confocal volume. The fits were done using the ZEN 3.0 software (Carl Zeiss, Jena, Germany).

Heterodyne-detected sum-frequency generation (HD-SFG) measurements: We used the non-collinear HD-SFG setup, the details of which are described elsewhere.^[24] In short, a Ti:Sapphire regenerative amplifier laser system (Spitfire Ace, Spectra-Physics, centered at 800 nm, ~40 fs pulse duration, 5 mJ pulse energy, 1 kHz repetition rate) was employed in this setup. A part of the output was guided to a grating-cylindrical lens pulse shaper to produce a narrowband visible pulse (10 μ J pulse energy, FWHM = ~10 cm^{-1}). The other part of the output was used to generate a broadband infrared (IR) pulse (3.5 μ J pulse energy, FWHM = 530 cm^{-1}) through an optical parametric amplifier (Light Conversion TOPAS-C) with a silver gallium disulfide (AgGaS₂) crystal. The IR and visible beams were first focused into a 200 nm-thick ZnO deposited on a 1 mm-thick CaF₂ window to generate a local oscillator (LO) signal.^[25] Subsequently, the IR, visible, and LO beams were re-focused by using a pair of off-axis parabolic mirrors. These beams overlapped spatially and temporally at the sample position at the angles of incidence of 33°, 38°, and 37° respectively. We used a fused silica glass plate with a 1.5 mm thickness for phase modulation of the LO signal. The SFG signal from the sample interfered with the SFG signal from the LO, generating the SFG interferogram, which was then dispersed in a spectrometer (Shamrock 303i, Andor Technology) and detected by an EMCCD camera (Newton, Andor Technology).

The samples of the PDMS brushes were modified on the SiO₂ substrates (25 mm diameter with a thickness of 2 mm, PI-KEM Ltd.) for the HD-SFG measurement. HD-SFG spectra were measured in an N₂ atmosphere to avoid spectral distortion due to water vapor. The measurement was conducted in the *ssp* polarization combination, where *ssp* denotes s-polarized SFG, s-polarized visible, and p-polarized IR beams. To control the height of the samples, we used a

1
2
3
4 height displacement sensor (CL-3000, Keyence). The peak area of the C-H peaks was obtained
5 by fitting the $\text{Im}\chi^{(2)}$ spectra with Lorentz curves. The complex-valued spectra of second-order
6 nonlinear susceptibility ($\chi^{(2)}$) of the SiO_2 -PDMS brush/water interfaces were obtained via the
7 Fourier analysis of the interferogram and normalization with that of the SiO_2 -PDMS brush/gold
8 interface. The interferogram of the SiO_2 -PDMS brush/gold interface was collected immediately
9 before the sample measurement to ensure a precise and stable reference phase. The phase of
10 gold was determined based on the fact that the $(\text{Im}\chi^{(2)})$ spectrum of the SiO_2 -PDMS brush/ D_2O
11 interface shows a flat zero line.
12
13
14
15
16
17
18
19
20

21 RESULTS AND DISCUSSION

23 Static wetting phenomena

24 PDMS brush/ pseudo-brush coated surfaces with different thicknesses (Figure 1a) were prepared
25 as described in the Experimental Section. To characterize their wetting properties, we measured
26 the static advancing and receding contact angles of water on horizontal surfaces by gradually
27 changing the drop volume at a rate of 1 $\mu\text{L/s}$ in a goniometer. The static advancing Θ_A^0 and
28 receding contact angles Θ_R^0 increased slightly up to a layer thickness of ≈ 4 nm (Table 1, Figure
29 1b). In parallel, the contact angle hysteresis, $\Delta\Theta = \Theta_A^0 - \Theta_R^0$, remained constant at $\Delta\Theta \approx 5^\circ$. Only
30 at very high M_w (more than 100 kg/mol), did it increase again (Figure 1b). These results agree
31 with earlier reports.¹ Accordingly, the roll-off angles of 10 μL water drops were between 2° to 4°
32 (Figure 1c) except for $M_w = 117$ kg/mol. By means of the static advancing and receding contact
33 angles, we can calculate the capillary force required to start sliding (equation 1). We call it “static
34 friction force”.^[11] To enable a comparison with other reports we plotted the static friction force
35 divided by the width of the drop in Figure 1c. When inserting measured contact angles into
36 equation (1), the slight difference in contact angle hysteresis on different surfaces when the
37 thickness is below 10 nm did not result in a significant correlation with the thickness (Figure 1c,
38 red points).
39
40
41
42
43
44
45
46
47
48
49
50
51

52 Coating thickness determines drop velocity and dynamic drop friction

53 A constant roll-off angle indicates that the acceleration a drop undergoes in a tilted plate
54 experiment is constant for different PDMS thicknesses. We expected that the velocity change of
55
56
57
58
59
60
61
62
63
64
65

1
2
3
4 drops sliding down would also be identical (except for $M_w = 117$ kg/mol). However, the velocities
5
6 of drops moving down tilted surfaces (Figure 1d) varied by up to a factor of 2 across the different
7
8 PDMS-coated surfaces (Figure 1e). At 60° tilt and 4 cm slide distance, water drops reached a
9
10 velocity of 0.36 m/s on GT_6000. In contrast, on GT_SCT it was only 0.18 m/s and on GT_30000
11
12 0.22 m/s. When plotting such drop velocity versus the PDMS layer thickness a peak velocity value
13
14 was observed around a coating thickness of 5 nm (Figure 1f). This peak velocity at $L \approx 5$ nm was
15
16 detected at a range of tilt angles (30° to 60°). We do not show results for lower titling angles
17
18 because the drop velocity variation was too low. This thickness-dependent phenomenon was
19
20 observed on PDMS-coated surfaces irrespective of the specific preparation. The surface
21
22 roughness was indistinguishable for all layers prepared (Supplementary Figure S3). We conclude
23
24 that the polymer layer thickness is the main predictive parameter for drop velocity. We further
25
26 conclude that the dynamic friction force and thus energy dissipation depends on the PDMS layer
27
28 thickness. Energy dissipation is minimal around a thickness of 5 nm.

29
30 To analyze where the low energy dissipation at intermediate layer thickness comes from, we
31
32 measured dynamic advancing and receding contact angles (Θ_A and Θ_R) using the tilting platform
33
34 at low and high drop velocities. Equation (1) can also be used to evaluate the dynamic drop friction
35
36 per unit width,^[11] provided the dynamic contact angles (Θ_A and Θ_R)^[26] are inserted. To obtain
37
38 dynamic contact angles over a wide range of velocities, experiments were carried out at tilt angles
39
40 between 30° and 60°. The advancing contact angle remained constant with velocity for all the
41
42 samples (~120°). In contrast, the receding contact angles on different surfaces decreased with
43
44 increasing drop velocity. They decreased by up to 20° ($L = 8.3$ nm) when the drop velocity reached
45
46 more than 0.35 m/s (Figure 1g). For thin and thick PDMS layers, the receding contact angle
47
48 decreased more with velocity than for a layer thickness around 5 nm (Figure 1h). Thus, the
49
50 reduced energy dissipation for 5 nm thick films is primarily situated at the receding contact line.

51
52 To further analyze dynamic drop friction, we determined drop friction forces F acting on drops by
53
54 evaluating the equation of motion as described before:^[26]

$$55 \quad F = mg \sin \alpha - m^* \frac{dU}{dt} \quad (3)$$

56
57 Here, $m^* \approx 1.05m$ is an effective mass, which considers a rolling component of drop motion.^[16]
58
59 $m^* \frac{dU}{dt}$ represents the inertia of the drop. We extracted the drop position from the side view videos
60
61 and calculated the velocity so that we could solve the equation of motion and obtain F versus U .
62
63 This analysis is only an approximate method because m^* depends slightly on velocity and we
64
65 assumed that the drop is always in a steady state shape, without any vibrations.

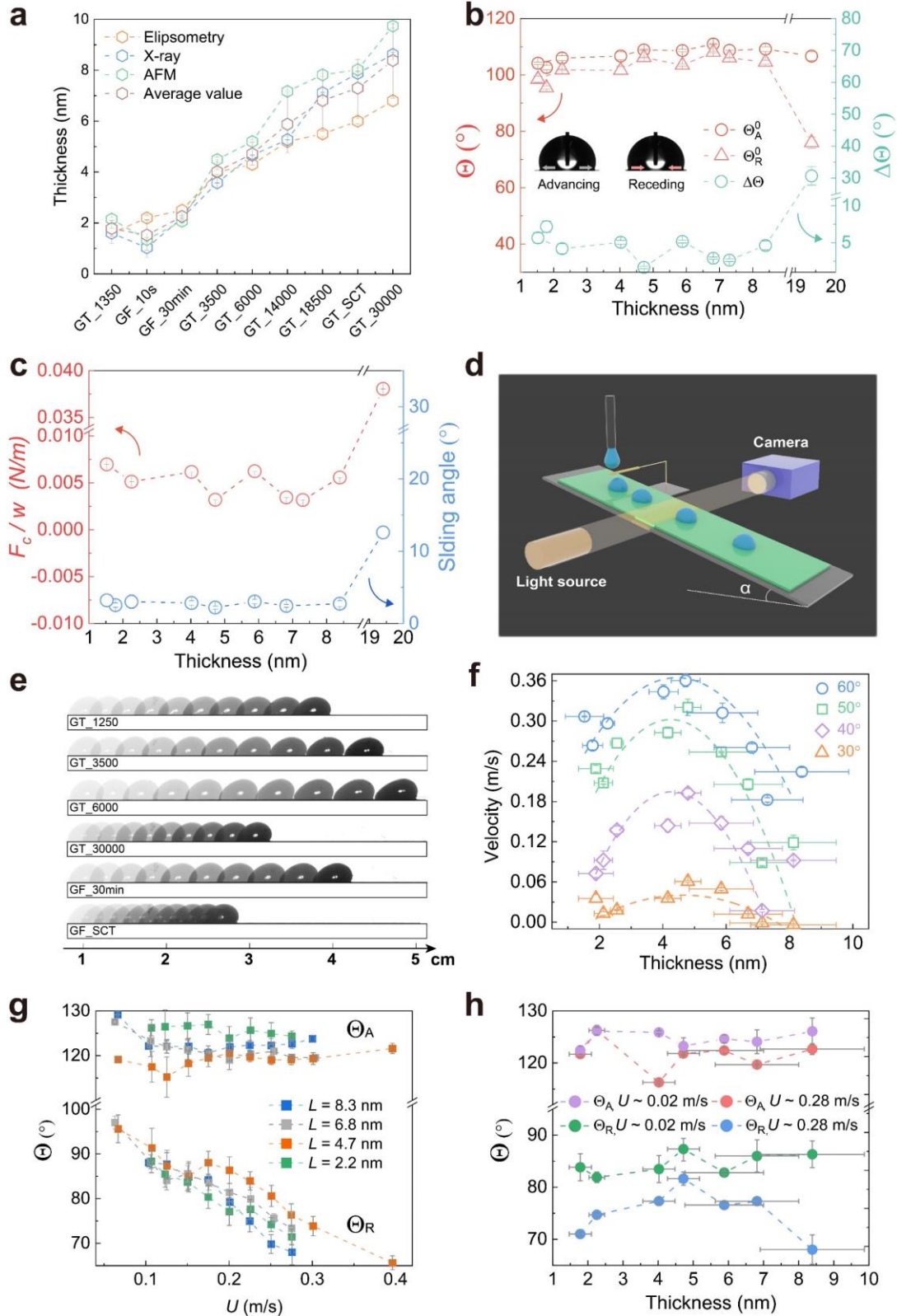


Figure 1. Characterization of PDMS-coated surfaces and motion of water drops. (a) Thickness values from three independent methods and average values corresponded to the

1
2
3
4 different samples. (b) The static advancing (Θ_A^0) and receding (Θ_R^0) contact angles measured by
5 goniometer with a goniometer when both the advancing and receding contact line start to move
6 versus the PDMS layer thickness and the corresponding contact angle hysteresis of a 10 μ L water
7 drop. (c) Capillary force in unit width at the three-phase contact line calculated by equation (1).
8 The drop width w was set to twice that of the drop contact radius.^[16] (d) The scheme of the tilted
9 plate setup for drop velocity measurements and dynamic contact angles. (e) Sequences of video
10 side images of drops on different PDMS-coated surfaces. The time interval between images was
11 15 ms, the tilting angle was 60°. (f) Drop velocity versus PDMS layer thickness after 4 cm drop
12 sliding at tilting angles of 60°, 50°, 40°, 30°. The dashed lines are to guide the eye. (g) Dynamic
13 advancing (Θ_A) and receding contact angles (Θ_R) versus drop velocity for different layer
14 thicknesses. (h) Dynamic advancing (Θ_A) and receding contact angles (Θ_R) measured by the titled
15 plate versus layer thickness at a velocity of 0.02 and 0.28 m/s.

16
17
18
19
20
21
22
23
24
25
26
27
28
29
30
31
32
33
34
35
36
37
38
39
40
41
42
43
44
45
46
47
48
49
50
51
52
53
54
55
56
57
58
59
60
61
62
63
64
65

When plotting drop friction versus velocity (Figure 2a), the force starts at a certain threshold given by equation 1. Then it increased approximately linearly. The results can be fitted by:^[26]

$$F = F_0 + \beta w \eta U \tag{4}$$

Here, F_0 is a threshold force which needs to be exceeded to initiate drop motion (equation 1). β is a dimensionless friction coefficient. When plotting the F-vs-U slopes for various PDMS thickness, a minimum friction coefficient at 4.7 nm was observed (Figure 2a and b). Although the surface chemistry was the same for all samples, the measured friction coefficient confirms that energy dissipation is significantly higher for both thin and thick layers as compared to layers of ≈ 5 nm thickness.

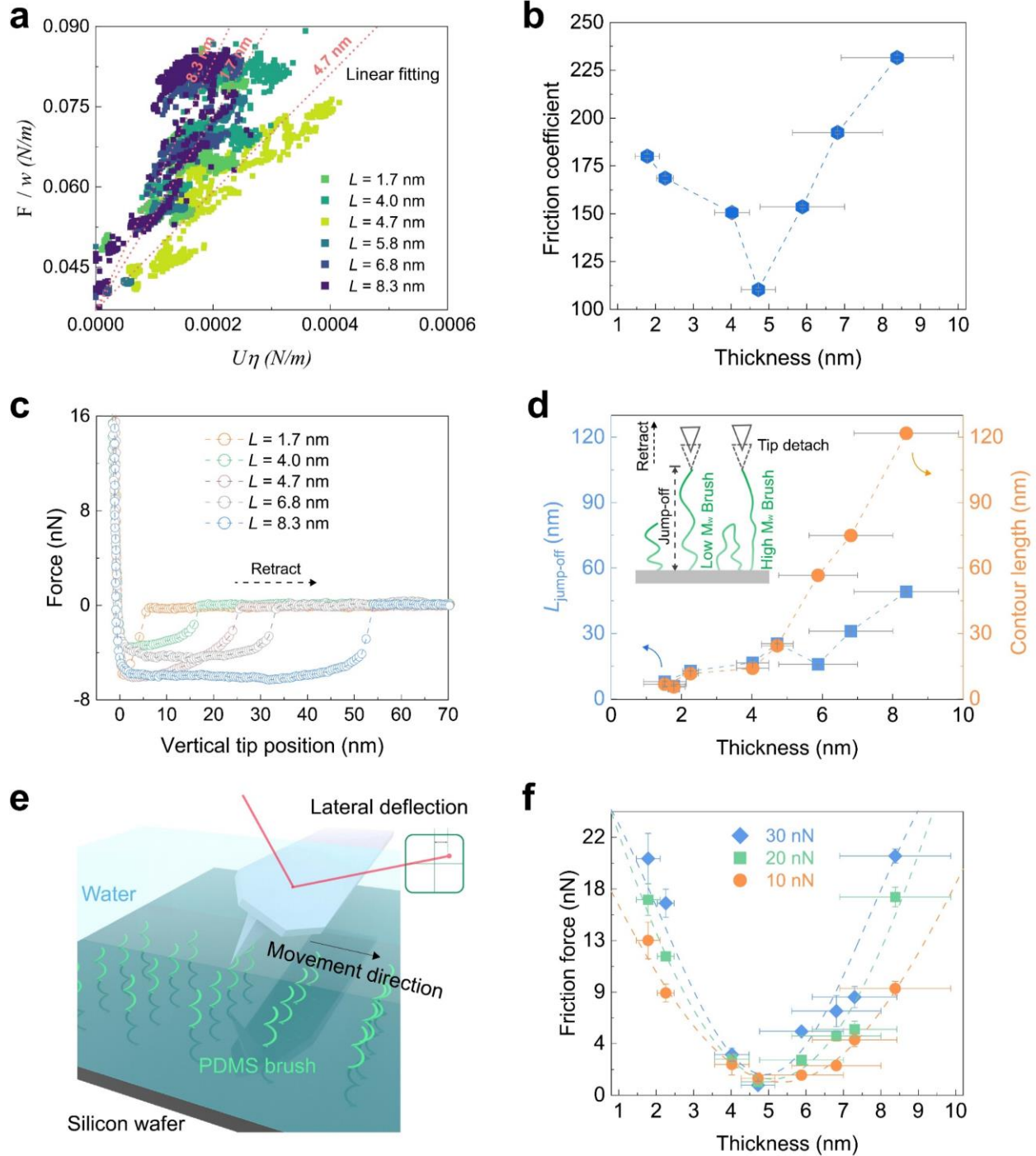


Figure 2. Friction of moving water drops. (a) Linear fitting of the friction force (F) as a function of velocity. (b) The slope of the linear fitting (friction coefficients) for the reference force plotted versus the coating thickness. (c) AFM retracting force curves obtained on various PDMS brush surfaces. (d) The disparity between the “jump-off distance” $L_{\text{jump-off}}$ and contour lengths of the polymer chains. (e) The scheme to show the AFM measurement of the friction on PDMS brush

1
2
3
4 surfaces in a water environment. (f) Friction force versus the thickness when the load force is 10
5 nN, 20 nN and 30 nN (dash lines are guides for the eye by Gaussian peak fitting).
6
7
8
9

10 Hypothesis to explain minimum in friction

11
12 What are the possible explanations for the observed minimum in the dependence of the friction
13 on the PDMS layer thickness? While interpreting their data on $\Theta_A^0 - \Theta_R^0$ and static friction,
14 Gresham *et al.*^[14] concluded that “*the PDMS chains must be sufficiently long and densely packed*
15 *to uniformly coat the silicon wafers substrates, but not so tightly packed that chain entanglement*
16 *compromises mobility.*” In the same way, we assume that the thickness-dependent architecture^[27]
17 of the PDMS layer will significantly influence drop sliding and dynamic friction. Thus, we used
18 FCS^[28] to monitor the diffusion of small tracer molecules in the PDMS layers. The mobility of tracer
19 molecules is influenced by the heterogeneity and effective viscosity of the PDMS layer.
20
21
22
23
24
25

26 In an FCS experiment, the fluctuations of fluorescent light intensity caused by the diffusion of
27 fluorescent tracers through a small observation volume ($<1 \mu\text{m}^3$) were measured using a confocal
28 microscope. A correlation analysis of these fluctuations provided information on the diffusion time
29 τ_D that the tracers needed to cross the observation volume and similarly information on their
30 diffusion coefficient and the mobility/viscosity of the environment.^[28] Here, we studied the diffusion
31 of small ($\sim 1 \text{ nm}$) terylene diimide (TDI) dyes dispersed in a PDMS brush as described in the
32 Experimental Section. For the FCS experiments the brushes were covered with water to better
33 mimic the contact angle hysteresis and the drop sliding experiments. It should be noted, however,
34 that no TDI molecules were observed in the water because they are hydrophobic and remained
35 in the PDMS layer. Typical autocorrelation curves and their corresponding fits with equation (2)
36 are shown in Figure 3a. The diffusion times for all PDMS layers are plotted versus layer thickness
37 in Figure 3b. The diffusion time τ_D shows a minimum for layers with intermediate thickness of
38 around 5 nm. TDI tracers diffused relatively quickly in such layers. Due to the high mobility of
39 these PDMS layers the tracers experienced low local (nano) viscosity. For thicker layers the
40 diffusion time increased, indicating lower mobility of the PDMS chains probably due to increased
41 grafting density and entanglements. The diffusion time was highest and the mobility lowest in the
42 very thin brushes.
43
44
45
46
47
48
49
50
51
52
53
54
55

56 As the autocorrelation curves measured in the very thin brushes could not be represented well
57 with single component fits, a two-component model ($m=2$ in equation 2) was used. The second
58 component has only a small fraction (f_2 in eq.2) of 5-10% of the amplitude in the autocorrelation
59
60
61
62
63
64
65

curve. The corresponding diffusion time, $\tau_{D,2}$ was several orders of magnitude slower than $\tau_{D,1}$. This extremely slow process is related to a temporal absorption of the TDI tracers to the glass substrate. Its presence clearly indicates lower grafting density and inhomogeneities in the coating.

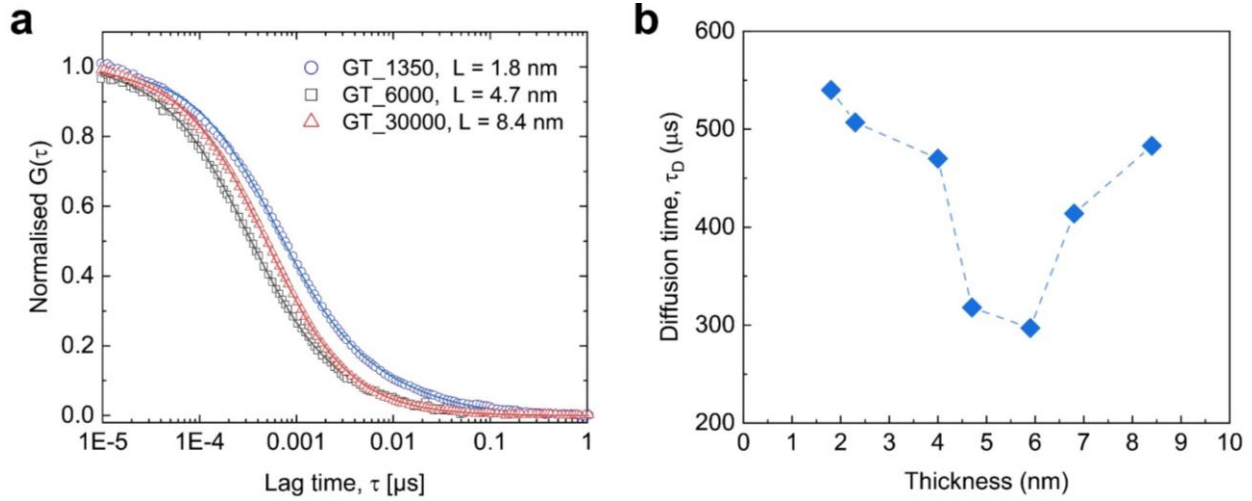


Figure 3. FCS measurements of tracer diffusion in PDMS layers. (a) Typical autocorrelation curves and their corresponding fits for PDMS layer with low, medium, and high thickness. (b) Diffusion time of TDI tracers versus PDMS layer thickness.

Further to the discussion of the reasons for the observed minimum in the dependence of the friction on the PDMS layer thickness (Figure 2b), we noted that the inhomogeneities evident in the FCS experiments for PDMS layers with thickness ≤ 4 nm can affect not only tracer mobility, but also Such inhomogeneity are highly affect the drop friction e.g. on a series of rigid octyltrichlorosilane (OTS) surfaces as recently reported.^[29] Inhomogeneity leads to local pinning of the contact line and energy dissipation during drop sliding. Energy is dissipated as heat when at a specific point the stretched contact line points de-pins and jumps back to the original position. In addition, we suggest that a decreasing van der Waals interaction between the substrate and the brush plays a role (**Figure 4**). Water interacts more strongly with the native oxide layer on the silicon wafer than with PDMS; this is one reason why the contact angle of water on Si wafers is lower than on PDMS. With increasing layer thickness, the distance between the surface of the Si wafer and water increases. As a result, the attraction between the Si wafer and water decreases. The initial increase in velocity can be attributed to the progressive thickening of the PDMS, thereby reducing the substrate effect. This reduced van der Waals force would also explain the increase in contact angles Θ_A and Θ_R for $L \leq 4$ nm.

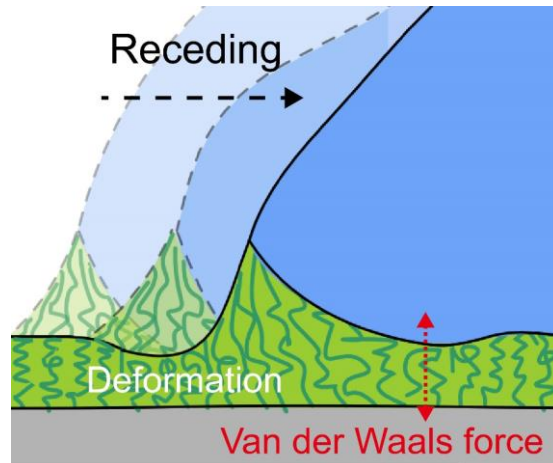


Figure 4. The interaction between the drop and the substrate. A schematic representation to show the van der Waals force between a water drop and the inhomogeneous layer on the substrate and the deformation near the three-phase contact line due to the drag of brush chains by the drop surface tension.

Why does the friction coefficient increase again for $L > 5$ nm (Figure 2b)? We argue that the effect is mainly caused by the formation and shifting of the meniscus at the contact line (Figure 4). The thicker the PDMS layer, the larger the PDMS meniscus, the more energy that is dissipated in drop motion. This effect is enhanced by the increasing viscosity of the PDMS layer caused by entanglement of the chains (Figure 4). In prior research, it has been observed that energy dissipation of good solvent moving on PDMS brushes is caused by a possible elastic deformation at the contact line.^[15, 30] For poor solvent like water, energy is still dissipated because the PDMS chains in the meniscus are elastically stretched.^[31] When they relax back to their initial configuration the energy is dissipated as heat. The maximal deformation increases with layer thickness and thus more energy is dissipated in the case of thicker layers. Therefore, viscous shear between the chains during the process of meniscus formation is directly dissipated. A third factor is the increase in interfacial areas (PDMS-air and water-PDMS), which may result in an interfacial energy change.

An important yet unsolved question concerns hydrodynamic viscous dissipation in the wedge of the water drop. On flat, infinitely rigid and homogeneous solid surfaces viscous dissipation due to flow of the liquid near the contact line is thought to be the dominating energy dissipation process.^[9a, 32] Based on a flow field calculated by C. Huh & L.E. Scriven,^[33] Kim *et al.* calculated the energy dissipation per unit contact line caused by wedge dissipation: $\Phi_w = 4c(\theta)\eta U^2 \ln(\Lambda/\lambda)$ with $c(\theta) = \sin^2 \theta / 2(\theta - \sin \theta \cos \theta)$.^[34] Here, θ is the contact angle. Λ is a macroscopic length

1
2
3
4 scale of typically 1 mm (size of the drop or capillary length) and λ is a cutoff length; below a length
5
6 scale λ the usual no-slip boundary condition is relaxed. It is typically set to the order of 1 nm. Thus,
7
8 viscous dissipation in the wedge critically depends on the boundary condition near the contact
9
10 line. This boundary condition can change when the substrate is flexible enough. Elastic substrates
11
12 react by deforming due to large local shear stress. It is not yet clear how deformation influences
13
14 viscous dissipation in the drop. A change of a factor of 10 in the cutoff length λ would change
15
16 energy dissipation by a factor of 2.3.

17 **AFM experiments**

18
19 To support the hypothesis of energy dissipation by nanoscopic ridge formation we further
20
21 analyzed the retracting part of AFM force curves. The main question is: Could the work done to
22
23 form and move a nanoscopic meniscus of PDMS along the contact line account for the energy
24
25 dissipation leading to dynamic drops friction? When retracting the AFM tip from the PDMS layer
26
27 (Figure 2c), the attractive force (F_{att}) typically increased to $F_{att} = 3-6$ nN. Then it remained relatively
28
29 constant up to a characteristic jump-off distance $L_{jump-off}$. The jump-off happened at a distance
30
31 between 6 nm (GT_1350) and 50 nm (GT_30000). We compared the jump-off distance to the
32
33 contour length of the polymer chains calculated from the molecular weight. Up to $L \approx 5$ nm, the
34
35 jump-off distance agreed with the calculated chain length (Figure 2d). For thicker layers, the
36
37 measured jump-off distance was 2-3 times lower than the contour length. The AFM retracting
38
39 curves did not show any stretching of single chains, which would lead to an order of magnitude
40
41 of lower forces.^[35] This can be explained by the fact that these chains can be attached in their
42
43 middle section, and in the case of longer chains even more attachment points can be formed.
44
45 Thus, they behave more like a molten film. We interpreted the attractive forces as the stretching
46
47 of a PDMS meniscus formed by bundles of polymer chains (Supplementary Figure S4). Since
48
49 PDMS is nearly incompressible, it behaves like a molten film.

50
51 The meniscus formed on a retracting AFM tip has similarities to the meniscus formed at a contact
52
53 line. The difference is the radial symmetry for the AFM tip while the symmetry is along a line for
54
55 the drop. To convert the work done by the AFM to a similar work at the contact line, we first
56
57 needed to convert the force of the tip to a similar force exerted by the surface tension of water at
58
59 the contact line. To reach an attractive force of F_{att} by the surface tension of water one would need
60
61 a contact line of length l given by $F_{att} = \gamma l \sin \theta$, θ is the contact angle of tip on the brush. Here, for
62
63 simplicity and because the contact angles are of the order of 90° , we set $\sin \theta = 1$. Thus, to reach
64
65 an attractive force of 3-6 nN, the contact line of a water drop would need to be $l = 42 - 83$ nm long.

1
2
3
4 To compare the AFM experiments to drop friction we needed to calculate the work carried out to
5 form the meniscus. The work required to form the meniscus with an AFM tip W_{att} can be estimated
6 from the integral underneath the force-vs-distance curve (Figure 2d). It varied from $W_{att} \approx 4 \times 10^{-17}$
7 J for a 4 nm thick PDMS layer to 3×10^{-16} J for 8 nm thick layers. The corresponding work done at
8 the contact line per unit length would be $w_m = W_{att}/l$. Interpreting F_{att} as the mean force applied
9 during retraction, we get $W_{att} = F_{att} L_{jump-off}$. Thus, $w_m = F_{att} L_{jump-off} / (F_{att}/\gamma) = L_{jump-off} \gamma$. This work per
10 unit length for the formation of a meniscus increased because $L_{jump-off}$ increases with the
11 thickness of the PDMS layer (Figure 2f). w_m increased from 1.2 nN for 4 nm thickness to 3.5 nN
12 for $L = 8.4$ nm. In conclusion, the AFM experiments confirm that for thicker PDMS layers more
13 energy is required to form the meniscus than for thinner layers.
14
15
16
17
18
19
20
21

22 Is the energy dissipated by the formation of a meniscus sufficiently high to account for drop friction?
23 The typical scaled friction force of a drop on PDMS surface was $F/w = 0.06$ N/m (Figure 2a). In
24 case energy dissipation is only caused by forming and shifting the meniscus, the equivalent of
25 one meniscus needs to be formed every lateral distance Δx estimated by $\Delta x = 2w_m w/F$; the factor
26 2 accounts for the front and rear side of the drop. Inserting typical values, we obtain $\Delta x = 40$ nm
27 for 4 nm thickness and 117 nm for 8.4 nm thickness. Thus, if sliding of two menisci by 40 nm or
28 117 nm, respectively, dissipates as much energy as their formation, viscoelastic deformation of
29 the PDMS layer contributes substantially to drop friction.
30
31
32
33
34
35

36 To support our view on energy dissipation, we measured friction force using AFM tips (Figure 2e).
37 Similar to the contact line of a moving drop, the tip will deform the PDMS layer locally. The PDMS
38 will form a meniscus around the tip which will shift when the tip is moved laterally over the surface.
39 The main difference is the different symmetry. Underneath a drop the polymer layer is deformed
40 along a line. In the AFM experiments it is deformed around a central point. In addition, a load is
41 applied by the AFM tip while the contact line of a drop only applies a tensional force. The AFM
42 experiments were carried out underwater (Figure 2e). The applied loads ranged from 30 nN to 10
43 nN. Initially, the AFM tip was brought into contact with the PDMS surface at a load of 30 nN. Then
44 friction force was measured by calibrating the lateral deflection of the cantilever tip over a 10 μ m
45 distance (Figure 2d and Supplementary Figure S5). Then the load was reduced to 20 nN and 10
46 nN, and the friction force was measured again (Figure 2f). At low layer thickness (< 3 nm), the
47 friction force was high. High friction illustrates more torsion when the tip slides on the coating.
48 This is because of the low mobility of the polymer chain that is affected by the uncovered substrate
49 or the possible stretching of the polymer chain. Given this, a pronounced minimum in the friction
50 force was observed for all applied loads, irrespective of the specific architecture of the layer. Once
51
52
53
54
55
56
57
58
59
60
61
62
63
64
65

1
2
3
4 the thickness exceeded ≈ 6 nm, the friction increased again with thickness. If we divide the lowest
5
6 AFM friction force by the equivalent length of a contact line of the order of 50 nm,^[36] the friction
7
8 force per unit length is around 0.1 N/m, which agrees with the drop friction we measured in
9
10 magnitude.

11
12 In addition to the effects proposed by Gresham *et al.*²² and by our group, other factors may be of
13
14 significance. Our understanding of drop friction is certainly not yet complete. One gap in our
15
16 knowledge is our poor understanding of dynamic processes at the interface on a molecular scale.
17
18 For this reason, we carried out additional experiments to learn more about how the structure of
19
20 water at the PDMS-water interface affects the drop friction.

21 **Sum-frequency generation spectroscopy (SFG)**

22
23 To understand the interfacial water organization at the polymer-water interface on different
24
25 samples, we carried out the HD-SFG measurement at the interface of water and the PDMS layer
26
27 supported by a SiO₂ substrate (Figure 5a and Supplementary Figure S6). The $\text{Im}\chi^{(2)}$ spectra
28
29 (Figure 5b) shows the broad O-H stretch of water features spanning from 2950 cm⁻¹ to 3550 cm⁻¹
30
31 as well as the C-H stretch modes of the terminal -CH₃ group of the polymer (antisymmetric C-H
32
33 stretch mode at 2940 cm⁻¹ and symmetric C-H stretch mode at 2880 cm⁻¹).^[37]

34
35 The O-H stretch $\text{Im}\chi^{(2)}$ bands are positive irrespective of PDMS layer thickness, indicating that the
36
37 water dipole moment points up from the bulk water to the PDMS layer. However, the spectral
38
39 areas of the $\text{Im}\chi^{(2)}$ bands vary with the thickness. To quantify the spectral area in the $\text{Im}\chi^{(2)}$ bands,
40
41 we integrated the spectra from 3000 cm⁻¹ to 3500 cm⁻¹. The data is shown in Figure 5c revealing
42
43 that the peak area is maximized at a thickness of 4.7 nm. The large (small) peak area of the O-H
44
45 stretch mode indicates more (less) ordering of the interfacial water. Thus, the SFG data suggests
46
47 that the interfacial water is the most ordered for the sample with a thickness of 4.7 nm, because
48
49 the water-polymer interaction is the strongest. This correlation of water ordering seen in SFG
50
51 measurement of the O-H band and drop friction may indicate that molecular level interaction of
52
53 water-polymer reduced the drop friction.

54
55 How can the water-polymer interface alter the SFG signal and drop friction? To answer this
56
57 question, we first obtained the ratio of the symmetric stretch peak area vs. the antisymmetric
58
59 stretch peak area. The ratio of the symmetric/antisymmetric stretch peak area is an indicator of
60
61 the structural alignment of the polymer at the interface,^[38] smaller (larger) ratio of the
62
63 symmetric/antisymmetric peak area indicates that the terminal -CH₃ group is randomized
64
65 (ordered). In the case of the polymer with a thickness of ~ 5 nm, the ratio is minimal, manifesting

1
2
3
4 that the terminal -CH₃ group of the PDMS is more ordered for the sample with its thickness of ~5
5 nm (Figure 5d). When the PDMS layer thickness is smaller than 5 nm, the surface is more
6 randomized. The polymer chains are more or less self-organized. When the PDMS layer
7 thickness is larger than 5 nm, the polymer chains are again more disordered, as the terminal of
8 the polymer chains are too long to support their ordered structure (Figure 5 c and d).
9

10
11
12
13 When the polymer thickness is ≤ 4 nm, the ordering of both the polymer interface and interfacial
14 water is enhanced. This means that the polymer phase and water regions are well disentangled.
15 In contrast, for $L > 4$ nm, the ordering of the polymer interface and interfacial water is reduced.
16 This strongly suggests that at the water-polymer interfaces, the tails of the polymer and water are
17 entangled, reducing the specific ordering along the surface normal (Supplementary Figure S7).
18 Such entangling of the polymer and interfacial water microscopically increases the effective
19 contact area of the polymer and water, resulting in an increase in friction.
20
21
22
23
24
25
26
27
28
29
30
31
32
33
34
35
36
37
38
39
40
41
42
43
44
45
46
47
48
49
50
51
52
53
54
55
56
57
58
59
60
61
62
63
64
65

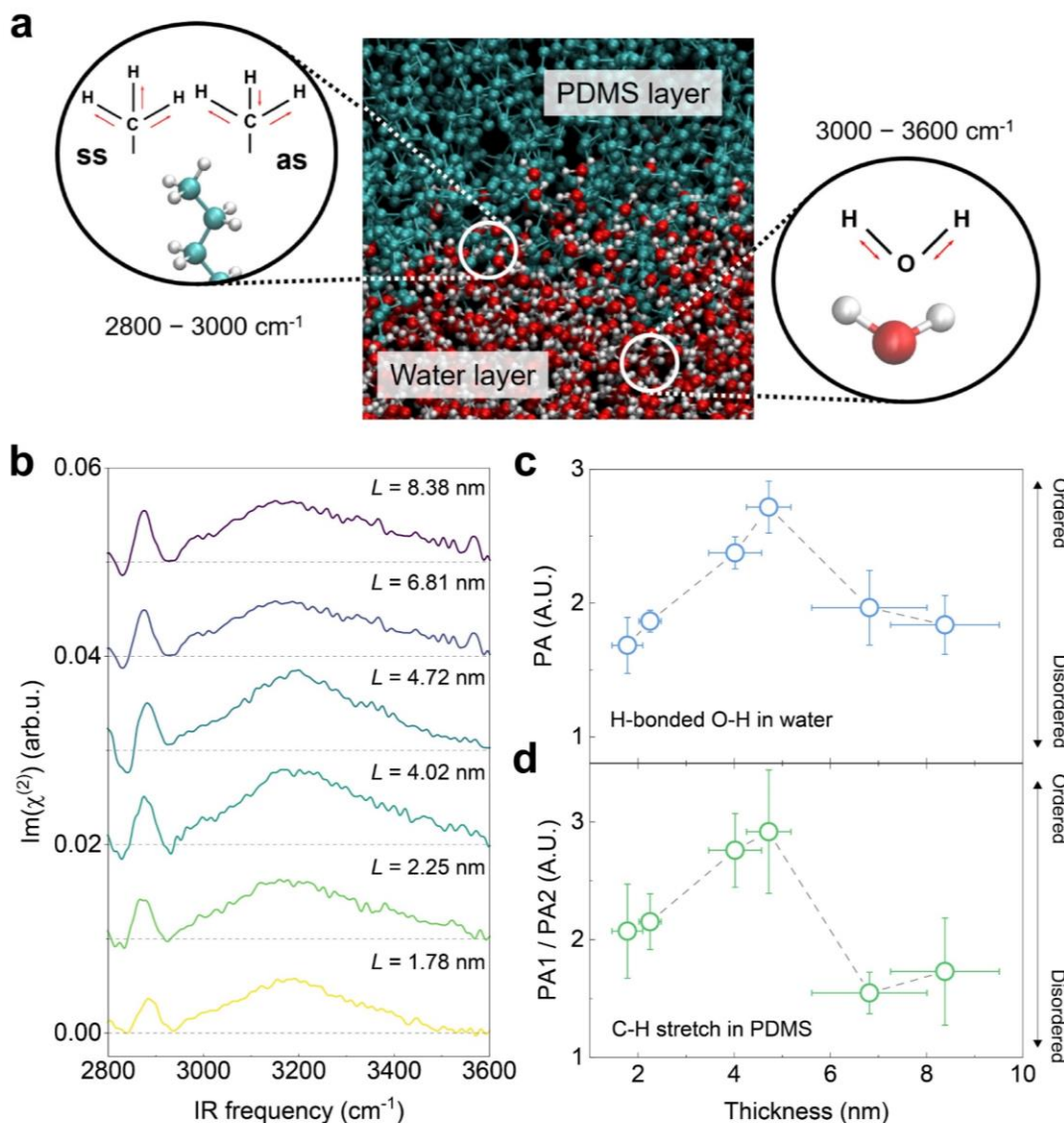


Figure 5. The impact of coating thickness variations on the interfacial water. (a) Schematic of the PDMS/water interface. The red, green, and white spheres indicate oxygen, carbon, and hydrogen atoms, respectively. Atoms other than carbon atoms are removed from the PDMS layer for simplicity. The vibrational mode probed by the SFG spectroscopy is also illustrated. Symmetric stretch and antisymmetric stretch modes are denoted as “ss” and “as”, respectively. (b) SFG stretching spectra obtained at the SiO₂-supported PDMS/water interface for various PDMS brush surfaces. (c) Changes in peak area of the O-H stretch mode $Im\chi^{(2)}$ signatures spanning from 2950 to 3400 cm⁻¹ in (b) versus thickness of the coating thickness. A higher value illustrates more ordered water molecule at the interface. (d) The ratio of symmetric (PA1) to antisymmetric (PA2) stretches peak area of C-H bonds in (b) versus the coating thickness. A higher value illustrates a more ordered polymer tail at the interface.

Conclusions

In this work, we focus on the dynamic friction of water drops moving on a nanoscopic PDMS layer. The energy dissipation depends on the thickness L of the layers. The lowest dynamic friction is achieved at a brush thickness of 4.7 nm. We explain the increasing friction below $L \leq 4$ nm with a decreasing homogeneity of the surface: inhomogeneities and defects hinder the smooth motion of the contact line. We further suggest that below ≈ 4 nm thickness the van der Waals interaction between the substrate and water increases the interaction between substrate and the water drop. When the thickness is high (> 5 nm), viscoelastic deformation of the PDMS layer may start to dominate. The vertical component of the surface tension of water leads to the formation of a meniscus at the contact line. This meniscus moves with the drop and energy is dissipated. AFM experiments showed that this effect becomes stronger for thicker layers. It may be enhanced by an increasing effective viscosity due to entanglement of PDMS chains. SFG measurements showed a decrease in the ordering of the polymer interface and interfacial water when the thickness is smaller or larger than 5 nm, suggesting that the polymer and water are microscopically more entangled at the interface. Such microscopic entangling of water and polymer interface increases the effective contact area of the polymer and water, resulting in increased friction.

Author Contributions

X.Z. and H.-J.B. designed the experiment. X.Z., P. S., and R. B. conducted the AFM related measurement and analysis. X.Z., Y.W. and Y.N. conducted the SFG measurement and analysis. X. Z. and K.A. carried out the X-ray measurement and analysis. X.Z. and X.L. conducted the drop velocity measurement and analysis. K. K. performed the fluorescence correlation spectroscopy measurement and analysis. X.Z., Y.W., X.L., P. S., K.A., Y.N., R. B. and H.-J.B. wrote the paper. All authors have approved the final version of this manuscript.

Acknowledgement

This project received funding from the European Research Council (ERC) under the European Union's Horizon 2020 research and innovation program (grant agreement No 883631, DYNAMO). X.Z. is sponsored by the China Scholarship Council (CSC). The authors acknowledge financial support by the German Research Society (DFG) via the Priority Programme 2171 Dynamic wetting of flexible, adaptive, and switchable surfaces (Grant No. BE 3286/6-1: X.L., R.B., H.-J.B.). We would like to thank Stefan Weber and Doris Vollmer for fruitful discussions.

References

- [1] I. J. Gresham, C. Neto, *Advances in Colloid and Interface Science* **2023**, 315, 102906.
- [2] H. Barrio-Zhang, É. Ruiz-Gutiérrez, S. Armstrong, G. McHale, G. G. Wells, R. Ledesma-Aguilar, *Langmuir* **2020**, 36, 15094.
- [3] a)H. Zhang, M. Chiao, *Journal of Medical and Biological Engineering* **2015**, 35, 143; b)K. Golovin, A. Dhyani, M. D. Thouless, A. Tuteja, *Science* **2019**, 364, 371.
- [4] S. T. Milner, T. A. Witten, M. E. Cates, *Macromolecules* **1988**, 21, 2610.
- [5] a)B. Zhao, W. J. Brittain, *Progress in Polymer Science* **2000**, 25, 677; b)D. Daniel, J. V. I. Timonen, R. Li, S. J. Velling, M. J. Kreder, A. Tetreault, J. Aizenberg, *Phys. Rev. Lett.* **2018**, 120, 244503.
- [6] L. Chen, S. Huang, R. H. A. Ras, X. Tian, *Nature Reviews Chemistry* **2023**, 7, 123.
- [7] a)B. Andreotti, J. H. Snoeijer, *Annual Review of Fluid Mechanics* **2020**, 52, 285; b)P. G. de Gennes, *Reviews of Modern Physics* **1985**, 57, 827.
- [8] a)A. Carré, J.-C. Gastel, M. E. R. Shanahan, *Nature* **1996**, 379, 432; b)M. Zhao, J. Dervaux, T. Narita, F. Lequeux, L. Limat, M. Roché, *Proc. Natl. Acad. Sci. USA* **2018**, 115, 1748.
- [9] a)D. Bonn, J. Eggers, J. Indekeu, J. Meunier, E. Rolley, *Reviews of Modern Physics* **2009**, 81, 739; b)H. Song, D. L. Chen, R. F. Ismagilov, *Angew. Chem. Int. Ed.* **2006**, 45, 7336.
- [10] a)F. Chen, Y. Wang, Y. Tian, D. Zhang, J. Song, C. R. Crick, C. J. Carmalt, I. P. Parkin, Y. Lu, *Chem. Soc. Rev.* **2022**, 51, 8476; b)E. Y. Bormashenko, *Wetting of Real Surfaces*, De Gruyter, Berlin, Boston **2019**; c)F. B.-W. Pierre-Gilles Gennes, David Quéré, *Capillarity and Wetting Phenomena: Drops, Bubbles, Pearls, Waves*, Springer New York, NY **2004**.
- [11] N. Gao, F. Geyer, D. W. Pilat, S. Wooh, D. Vollmer, H.-J. Butt, R. Berger, *Nat. Phys.* **2018**, 14, 191.
- [12] a)H. Teisala, P. Baumli, S. A. L. Weber, D. Vollmer, H.-J. Butt, *Langmuir* **2020**, 36, 4416; b)N. Singh, H. Kakiuchida, T. Sato, R. Hönes, M. Yagihashi, C. Urata, A. Hozumi, *Langmuir* **2018**, 34, 11405; c)J. W. Krumpfer, T. J. McCarthy, *Langmuir* **2011**, 27, 11514; d)K. Fazle Rabbi, J. Y. Ho, X. Yan, J. Ma, M. J. Hoque, S. Sett, N. Miljkovic, *Adv. Funct. Mater.* **2022**, 32, 2112837; e)A. Viallat, J. P. Cohen-Addad, A. Pouchelon, *Polymer* **1986**, 27, 843; f)N. Celik, S. Akay, F. Sahin, G. Sezer, E. Dagaslan Bulucu, M. Ruzi, H.-J. Butt, M. S. Onses, *Adv. Mater. Interfaces* **2023**, 10, 2300069.
- [13] a)J. Liu, Y. Sun, X. Zhou, X. Li, M. Kappl, W. Steffen, H.-J. Butt, *Adv. Mater.* **2021**, 33, 2100237; b)L. Wang, T. J. McCarthy, *Angew. Chem. Int. Ed.* **2016**, 55, 244.
- [14] I. Gresham, S. Lilley, A. Nelson, K. Koynov, C. Neto, *Angew. Chem. Int. Ed.* **2023**, n/a, e202308008.
- [15] R. Lhermerout, H. Perrin, E. Rolley, B. Andreotti, K. Davitt, *Nat. Commun.* **2016**, 7, 12545.
- [16] X. Li, P. Bista, A. Z. Stetten, H. Bonart, M. T. Schür, S. Hardt, F. Bodziony, H. Marschall, A. Saal, X. Deng, R. Berger, S. A. L. Weber, H.-J. Butt, *Nat. Phys.* **2022**, 18, 713.
- [17] I. A. Soldatenkov, *Journal of Friction and Wear* **2008**, 29, 7.
- [18] M. F. Toney, C. M. Mate, K. A. Leach, D. Pocker, *J. Colloid Interface Sci.* **2000**, 225, 219.
- [19] M. Yasaka, presented at *The Rigaku Journal*, **2010**.
- [20] J. Sancho-Parramon, M. Modreanu, S. Bosch, M. Stchakovsky, *Thin Solid Films* **2008**, 516, 7990.
- [21] S. Li, Y. Hou, M. Kappl, W. Steffen, J. Liu, H.-J. Butt, *Adv. Mater.* **2022**, n/a, 2203242.
- [22] N. Mullin, J. K. Hobbs, *Review of Scientific Instruments* **2014**, 85, 113703.
- [23] N. Kahya, P. Schwille, *Molecular Membrane Biology* **2006**, 23, 29.
- [24] Y. Wang, T. Seki, X. Liu, X. Yu, C.-C. Yu, K. F. Domke, J. Hunger, M. T. M. Koper, Y. Chen, Y. Nagata, M. Bonn, *Angew. Chem. Int. Ed.* **2023**, 62, e202216604.
- [25] H. Vanselous, P. B. Petersen, *J. Phys. Chem. C* **2016**, 120, 8175.
- [26] X. Li, F. Bodziony, M. Yin, H. Marschall, R. Berger, H.-J. Butt, *Nat. Commun.* **2023**, 14, 4571.
- [27] B. Zuo, H. Zhou, M. J. B. Davis, X. Wang, R. D. Priestley, *Phys. Rev. Lett.* **2019**, 122, 217801.
- [28] K. Koynov, H.-J. Butt, *Current Opinion in Colloid & Interface Science* **2012**, 17, 377.

- 1
2
3
4 [29] S. Lepikko, Y. M. Jaques, M. Junaid, M. Backholm, J. Lahtinen, J. Julin, V. Jokinen, T. Sajavaara, M.
5 Sammalkorpi, A. S. Foster, R. H. A. Ras, *Nature Chemistry* **2023**.
6 [30] R. Lhermerout, K. Davitt, *Colloids and Surfaces A: Physicochemical and Engineering Aspects* **2019**,
7 566, 148.
8 [31] D. Long, A. Ajdari, L. Leibler, *Langmuir* **1996**, 12, 1675.
9 [32] J. H. Snoeijer, B. Andreotti, *Annual Review of Fluid Mechanics* **2013**, 45, 269.
10 [33] C. Huh, L. E. Scriven, *J. Colloid Interface Sci.* **1971**, 35, 85.
11 [34] H.-Y. Kim, H. J. Lee, B. H. Kang, *J. Colloid Interface Sci.* **2002**, 247, 372.
12 [35] S. Al-Maawali, J. E. Bemis, B. B. Akhremitchev, R. Leecharoen, B. G. Janesko, G. C. Walker, *The*
13 *Journal of Physical Chemistry B* **2001**, 105, 3965.
14 [36] J. Eggers, H. A. Stone, *J. Fluid Mech.* **2004**, 505, 309.
15 [37] a) I. V. Stioekin, H. D. Jayathilake, A. N. Bordenyuk, A. V. Benderskii, *J. Am. Chem. Soc.* **2008**, 130,
16 2271; b) L. Wang, T. Ishiyama, A. Morita, *J. Phys. Chem. A* **2017**, 121, 6701.
17 [38] N. Takeshita, M. Okuno, T.-a. Ishibashi, *Physical Chemistry Chemical Physics* **2017**, 19, 2060.
18
19
20
21
22
23
24
25
26
27
28
29
30
31
32
33
34
35
36
37
38
39
40
41
42
43
44
45
46
47
48
49
50
51
52
53
54
55
56
57
58
59
60
61
62
63
64
65

Thickness of nano-scale poly(dimethylsiloxane) layers determines the motion of sliding water drops

Xiaoteng Zhou,¹ Yongkang Wang,^{1,2} Xiaomei Li,¹ Pranav Sudersan,¹ Katrin Amann-Winkel,^{1,3} Kaloian Koynov,¹ Yuki Nagata,¹ Rüdiger Berger,¹ Hans-Jürgen Butt^{1,*}

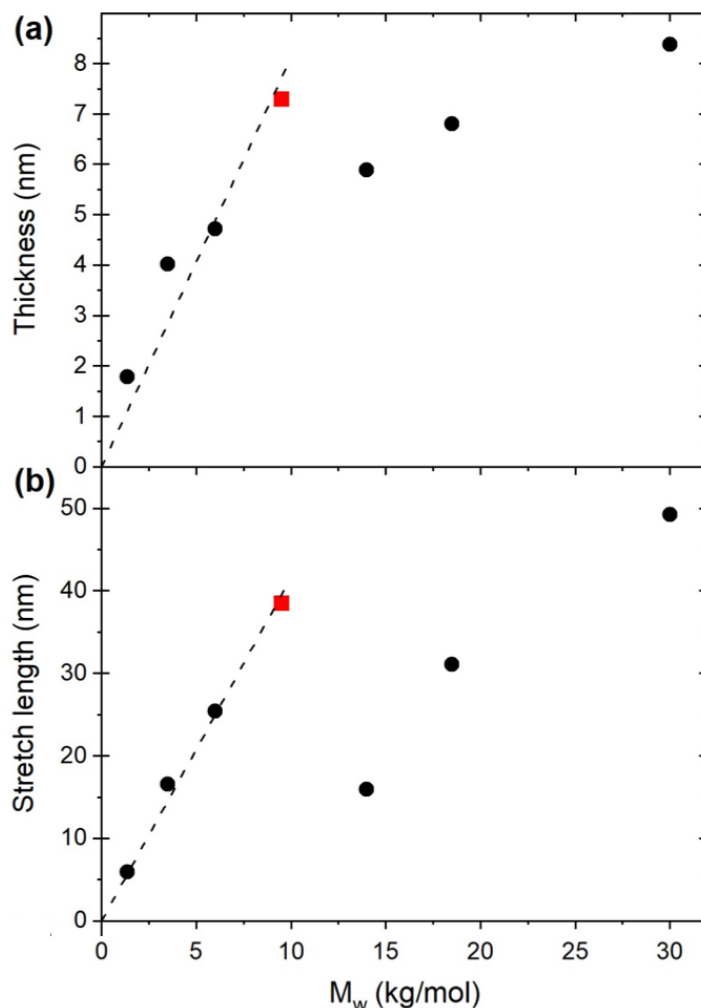
1. Max Planck Institute for Polymer Research, Ackermannweg 10, 55128, Mainz, Germany.
2. School of Mechanical Engineering, Southeast University, 211189, Nanjing, China.
3. Institute for Physics, Johannes Gutenberg University Mainz, Staudingerweg 10, 55128 Mainz, Germany.

*E-mail: butt@mpip-mainz.mpg.de.

Keywords: wetting, liquid-like coating, interfacial water, friction, microfluid.

Supplementary Section 1. Molecular weight estimation for grafting-from method.

For the grafting-from methods, GF_10s and GF_30 min, we do not know the molecular weight of the PDMS chains. To estimate it we used two methods. First, we plotted the molecular weights of all known samples versus their thickness (Figure S1a). For low molecular weights, the results could be fitted with a linear function.^[1] The point obtained with the SCT polymer lies above the curve obtained for the grafted to samples. The reason is most likely that for the Krumpfer method, PDMS chains do not necessarily attach the end.^[2] We deliberately included the thickness obtained with the SCT polymer because it is end-grafted, like the grafting-from samples. Then, we used the linear fitting to get the molecular weight of the GF_10s and GF_30 min samples. Second, using AFM retracting force curves, we obtain the maximal stretching distances in retracting force curves (Figure 2e, Figure S1b). Again, we used the three low-molecular weight PDMS layers formed by the Krumpfer method and the SCT PDMS layer to calibrate. The molecular weights of GF_10s and GF_30min were obtained as 1.6 and 2.8 kg/mol, respectively (Supplementary Figure S1).

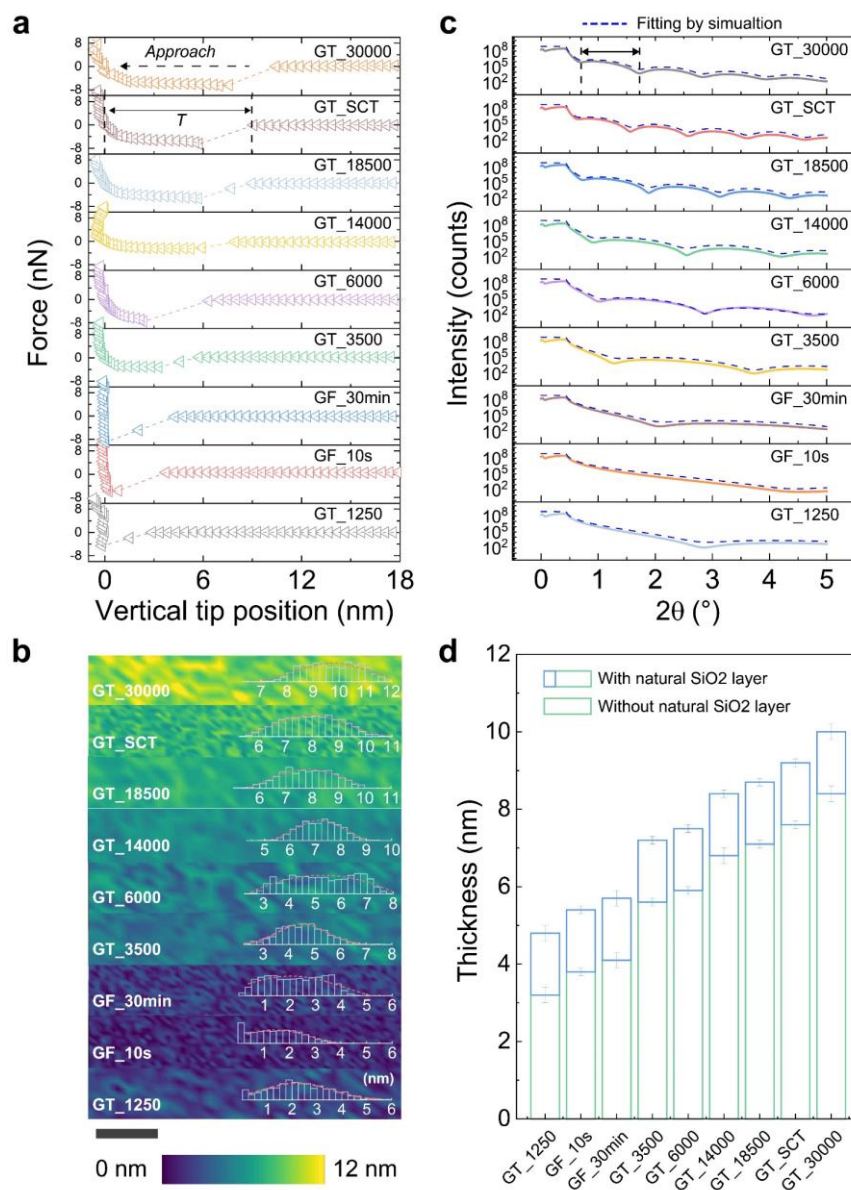


Supplementary Figure S1. (a) Mean layer thickness versus molecular weight for samples prepared by “grafting-to” (Krumpfer method, black circles) and from the end-functionalized PDMS (SCT, red squares). The linear fit (dashed) calculated for the four samples with low molecular weight was used to estimate the molecular weight of the grafting-from samples. (b) Mean stretch distance from AFM retracting curves.

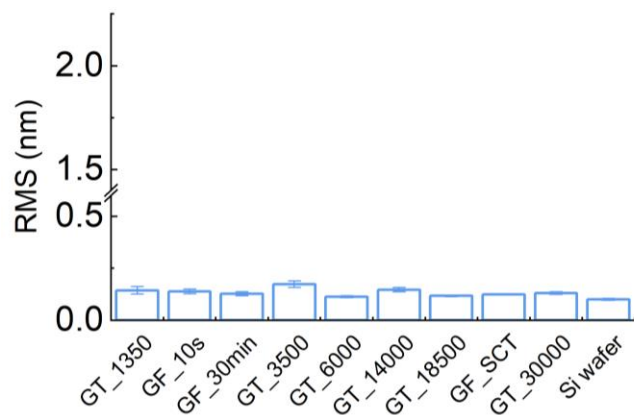
Supplementary Section 2. Thickness measurement

The thickness of the PDMS layer was measured by three independent methods: AFM force curves utilizing the jump-in distance (Figure S2a),^[3] X-ray reflectivity (XRR) (Figure S2c),^[4] and ellipsometry (Figure S2d).^[5] The thickness distribution was characterized by the AFM QI mode (Figure S1b).

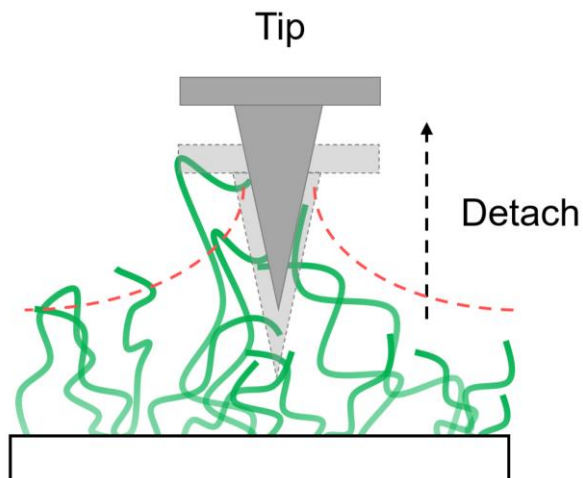
Commonly, bulk Si wafers are covered with native silicon dioxide layers of ≈ 2 nm thickness.^[6] Here, we verified this value by the ellipsometry and measured a thickness of around 1.7 nm. This value is used for fitting the PDMS thickness as measured by XRR and ellipsometry.



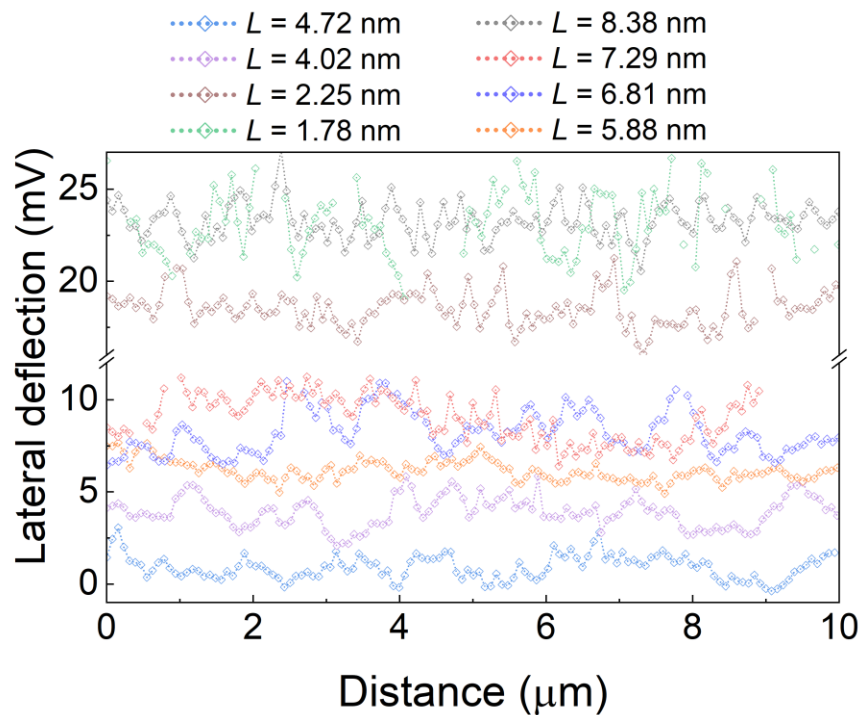
Supplementary Figure S2. Thickness measurement. (a) AFM measurement: Approaching force curves on different PDMS-coated surfaces. (b) Maps of the jump-in distance measured by AFM. (c) X-ray curves measured by the X-ray reflectivity (XRR) changing. (d) Ellipsometry measurements of the thickness of PDMS brush.



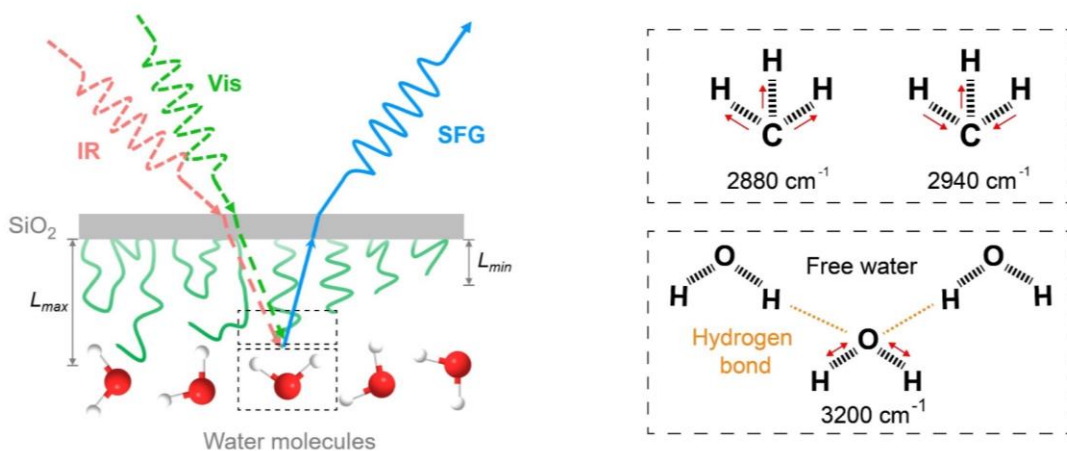
Supplementary Figure S3. Root-mean square (RMS) surface roughness measured by atomic force microscopy (AFM) in a $2\ \mu\text{m} \times 2\ \mu\text{m}$ area.



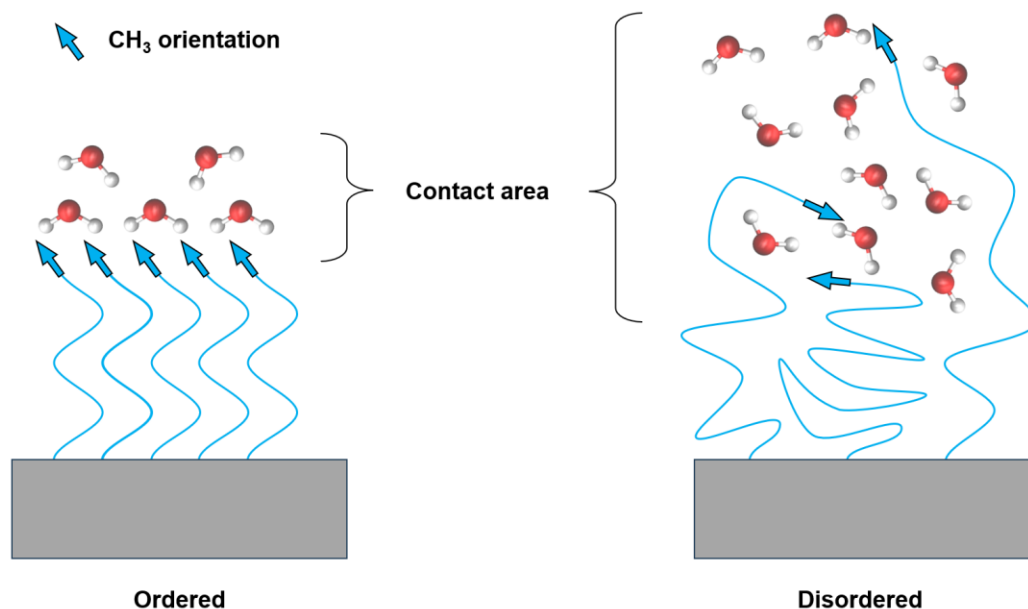
Supplementary Figure S4. The scheme shows the attractive forces caused by the stretching of a PDMS meniscus formed by bundles of polymer chains when the tip of cantilever detaches from the PDMS brush surface.



Supplementary Figure S5. The lateral deflection corresponding to torsion of the AFM-cantilever for a scan size of $10 \mu\text{m}$. The setpoint force was adjusted to 30 nN for these measurements.



Supplementary Figure S6. Schematic representation of the measurement conducted using SFG (Sum Frequency Generation) spectroscopy and the wavelengths for different vibrations. In the experiment for practical reasons the the water is underneath the PDMS layer.



Supplementary Figure S7. Schematic representation of the the ordered and disordered water and polymer tail at the interface detected by (Sum Frequency Generation) spectroscopy. Left ordered case consistent with smaller SFG amplitude of water's O-H signal and right disordered case as is observed from the high ratio of the SFG C-H stretch PAs (symmetric vs. anti-symmetric C-H stretch modes) and stronger SFG amplitude of water's O-H signal.

References

- [1] K. U. Kirst, F. Kremer, T. Pakula, J. Hollingshurst, *Colloid and Polymer Science* **1994**, 272, 1420.
- [2] J. W. Krumpfer, T. J. McCarthy, *Langmuir* **2011**, 27, 11514.
- [3] S. Li, Y. Hou, M. Kappl, W. Steffen, J. Liu, H.-J. Butt, *Adv. Mater.* **2022**, n/a, 2203242.
- [4] M. F. Toney, C. M. Mate, K. A. Leach, D. Pocker, *J. Colloid Interface Sci.* **2000**, 225, 219.
- [5] J. Sancho-Parramon, M. Modreanu, S. Bosch, M. Stchakovsky, *Thin Solid Films* **2008**, 516, 7990.
- [6] D. Metzler, C. Li, C. S. Lai, E. A. Hudson, G. S. Oehrlein, *Journal of Physics D: Applied Physics* **2017**, 50, 254006.

Chapter 3. Conclusion and outlook

In this thesis, we focus on the evaluating and improving the liquid-repellency of soft PDMS-coated surfaces. By using the fundamental wetting theory, we understand and reduce the friction coming from the energy dissipation when drop moves on these surfaces. There are three main conclusions for this thesis:

1. In **Chapter 2.1**, we prevent the induced deformation or swelling when water or low-surface tension liquids are placed on a highly stretchable PDMS-coated substrate by a two-level structured polymerized organosilicon coating. Such superamphiphobic coating isolates the soft PDMS layer from the liquid. The liquid cannot contact the soft substrate directly even in a stretched state. Therefore, the surface can maintain its super-liquid-repellency even when the surface is stretched to a strain of 250%.
2. In **Chapter 2.2**, a liquid-infused superhydrophobic surface with a nano-scale liquid layer is prepared. Compared to previous liquid-infused surfaces, by decreasing the lubricant layer to a nano-scale, ridge formation caused by the elastowetting is suppressed which leads to low drop sliding friction and fast drop shedding. Due to the liquid layer, the surface also have an improved chemical stability and anti-icing performance at low temperatures.
3. In **Chapter 2.3 and 2.4**, a new grafting-from method is studied to fabricate covalently attached liquid surfaces (CALs). Mixing this method and other grafting-to processes, we investigate how such nano-scale coating layer thickness affects the drop motion. A coating thickness (4-5 nm) is determined to have the lowest drop friction when it slides off these surfaces.

The newly designed liquid repellent surfaces have potential in fabricate waterproof stretchable electronics, anti-fouling artificial skin and further study on efficient heat transfer process of these applications. Moreover, understanding the layer effect when drop moving on a soft thin polymer surface hold significant implications for future research focusing on the influence of nano-scale polymer coatings on drop sliding, microfluidics and heat transfer process on polymer packaging circuits.

Chapter 4. Acknowledgement

During my Ph. D. studies, the challenges posed by the COVID-19 pandemic were significant. Thankfully, with the collective support of many, I successfully completed my Ph. D. as anticipated.

I would like to extend my sincere gratitude, firstly, to my supervisor, Hans-Jürgen Butt, for his invaluable guidance in establishing a robust foundation in my research field and for his assistance in crafting the manuscripts and thesis.

I also wish to express my appreciation for the assistance provided by Michael Kappl, Rüdiger Berger, and Kaloian Koynov. Their contributions inspired me to explore novel approaches and construct a compelling scientific narrative.

My heartfelt thanks go to Diego Diaz, Pranav Sudersan, Leibauer Benjamin, and Lukas Hauer. Despite our diverse nationalities, your generosity and willingness to help resolve the challenges I encountered were greatly appreciated.

I am indebted to Jie Liu and Wendong Liu for their guidance when I initially arrived at the institute. Their mentorship was instrumental in my academic journey.

I would like to acknowledge Xiaomei Li and Zhongyuan Ni for their continuous inspiration in seeking innovative problem-solving strategies.

Special gratitude is extended to my friend, Shiyao Li, and his partner, Xiaoyu Wei, who not only cared for my previous cat but also committed to accompanying him in Germany in the future.

I must express my deep appreciation to my parents and my grandfather, who provided unwavering support and companionship via the internet during the challenging times of the pandemic.

I am deeply appreciative of the support provided by Lin Ma, who stood by my side during the most challenging phases of my Ph. D. journey, offering solace and camaraderie through online chats.

Chapter 5. Curriculum vitae

Personal details

Xiaoteng Zhou

Supervisor: Hans-Jürgen Butt

Department of Physics at Interface

Max Planck Institute for Polymer Research

Ackermannweg 10

D-55128 Mainz, Germany

OrcidID: <https://orcid.org/0000-0002-0666-8402>

Google scholar (H-index:8): <https://scholar.google.com/citations?hl=en&user=4dVGSi4AAAAJ>

Male; born, 27/10/1994, Nanyang, Henan (P. R. China).

Nationality: Chinese (CN).

Education

Undergraduate:

University of Science and Technology Beijing; Material chemistry, 2012-2016

Graduate:

Tsinghua University; MSc in Material Science and Engineering, 2016-2019

Max Planck Institute for Polymer Research, Ph. D. student in Physics at Interface, 2019-now

Research interests

My Ph.D. study focuses on the wetting phenomenon and the interfacial force on soft liquid repellent surfaces e.g. soft polymer brush surfaces, stretchable super liquid repellent surfaces, and liquid repellent polymer coatings. Understanding the wetting process on these soft and deformed interfaces will be meaningful in developing applications in surgery, tissue engineering,

flexible electronics, and soft robotics. AFM (atomic force microscopy), SEM (scanning electron microscopy), CLSM (confocal laser scanning microscopy), high-speed cameras and goniometers are commonly used in my research process.

Chapter 6. List of publications and contributions

Selected publications

Zhou X., Wang Y., Li X., Sudersan P., Amann-Winkel K., Koynov K., Nagata Y., Berger R., & Butt, H. J. (2023) Thickness of nano-scale poly(dimethylsiloxane) layers determines the motion of sliding water drops. *Advanced Materials*, submitted.

Zhou X., Díaz D., Ni Z., Liu J., Kappl M., & Butt, H. J. Split of drops impacting on irregular sharp surfaces. Prepared.

Zhou X., Sudersan P., Diaz D., Benjamin L., Hinduja C., Fahimeh D., Bista P., Hauer L., Wagner M., Steffen W., Liu J., Kappl M., & Butt, H. J. (2023) Chemically robust superhydrophobic surfaces with a self-replenish nano-scale liquid coating. *Droplet*, accepted.

Zhou, X., Liu, J., Liu, W., Steffen, W., & Butt, H. J. (2022). Fabrication of Stretchable Superamphiphobic Surfaces with Deformation-Induced Rearrangeable Structures. *Advanced Materials*, 34(10), 2107901.

Díaz, D., Li, X., Bista, P., **Zhou, X.**, Darvish, F., Butt, H. J., & Kappl, M. (2023). Self-generated electrostatic forces of drops rebounding from hydrophobic surfaces. *Physics of Fluids*, 35(1), 017111.

Liu, J., Sun, Y., Ma, R., **Zhou, X.**, Ye, L., Mailänder, V., ... & Butt, H. J. (2022). Mechanically Robust and Flame-Retardant Superhydrophobic Textiles with Anti-Biofouling Performance. *Langmuir*, 38(42), 12961-12967.

Zhou, X., Sun, Y., & Liu, J. (2021). Designing anti-icing surfaces by controlling ice formation. *Advanced Materials Interfaces*, 8(17), 2100327.

Liu, J., Sun, Y., **Zhou, X.**, Li, X., Kappl, M., Steffen, W., & Butt, H. J. (2021). One-step synthesis of a durable and liquid-repellent poly (dimethylsiloxane) coating. *Advanced Materials*, 33(23), 2100237.

Award

Finalist (8) of Langmuir award in 97th ACS Colloid and Surface Science Symposium.

Conference contributions

Oral talk 'Fabrication of Stretchable Superamphiphobic Surfaces' in 51st Conference of the German Colloid Society, Berlin, Germany. (Sep. 2022)

Poster 'Stretchable Superamphiphobic Surfaces' in 36th European Colloid & Interface Society Conference, Crete, Greece. (Sep. 2022)

Oral talk acceptance in 97th ACS Colloid and Surface Science Symposium Raleigh, NC, USA. (Jun. 2023. Traveling is canceled because of the visa problem.)

Oral talk 'Fabrication of Stretchable Superamphiphobic Surfaces' in 6th International Conference on Droplets, Beijing, China. (Aug. 2023)

Oral talk acceptance for SPP 2171 Workshop "Wetting of Flexible, Adaptive, and Switchable Substrates", Berlin, Germany. (Dec. 2023)

Oral talk and poster application for APS March Meeting 2024 "Thickness of nano-scale poly(dimethylsiloxane) layers determines the motion of sliding water drops", Minneapolis, USA. (Mar. 2024)